UNIVERSITY OF CALIFORNIA

Santa Barbara

Impacts of Climate Variability on Surface Energy and Water Budgets in sub-Saharan Africa

A dissertation submitted in partial satisfaction of the

requirements for the degree Doctor of Philosophy

in Geography

by

Laura Suzanne Harrison

Committee in charge:

Professor Joel Michaelsen, Chair

Professor Leila Carvalho

Professor Phaedon Kyriakidis

Dr. Chris Funk, University of California Santa Barbara

Dr. Christopher Still, Oregon State University

December 2014

The dissertation of Laura Suzanne Harrison is approved.

_____

Chris Funk

_____

Christopher Still

_____

Phaedon Kyriakidis

_____

Leila Carvalho

_____

Joel Michaelsen, Committee Chair

December 2014

Impacts of Climate Variability on Surface Energy and Water Budgets in sub-Saharan Africa

by

Laura Suzanne Harrison

ACKNOWLEDGEMENTS

I am grateful for support from many people.

My parents Mike and Carol instilled in me an eternal desire to learn about the natural world. They also taught me that when presented with difficult tasks it is good to meet them with realistic optimism. Big achievements take many small steps, so evaluating potential routes and rewards is the best way to start. My sister Julie and her family taught me to enjoy some of the good things in life along the way.

My husband Chris never stops inspiring me. We experienced my PhD together, and along the way he supported me with patience, comfort, and an intelligent outlook. I will always be grateful for the happiness he brings me. Along those lines, I can't resist acknowledging our pup Leo for the many laughs this past year.

The UCSB Climate Hazards Group and the USAID Famine Early Warning System Network financially supported much this research and my graduate education. They also provided me the opportunity to conduct research in a very rewarding setting. With these groups I applied research skills to important issues in the developing world and interacted with a spectrum of stakeholders, including USGS and NASA researchers, African farmers, and government policymakers.

Support also came from the UCSB Geography Department. I have worn many hats in the Geography Department and have seen it in constant change, always trying to improve itself. This perpetual metamorphosis and its skillful faculty, researchers, staff, and students have made it a fantastic center for learning.

My committee did a good job providing scientific direction and motivation for in depth analysis. Joel Michaelsen, the committee chair, taught me to shed bias before approaching data. He also taught me to look for larger themes that can turn analysis into knowledge. Chris Funk, the director of the Climate Hazards Group, showed me that the key to linking research to helping people is to design projects thoughtfully and to communicate results clearly.

Finally, I am grateful for the beauty in this world. Acts of love can be found all around us- the trick is allowing yourself to see them. My mentors Pete Peterson and Leila Carvalho helped me learn how to take notice during turbulent times. I have found many moments of peace from the view of the Santa Ynez range from Ellison Hall. Only 30 miles to the north (as the bird flies) brings you to the Sisquoc River, which Chris and I have explored from its headwaters to its finish. It is one of my favorite desolate sanctuaries and has been a great point of reference for our place in nature and history.

To these people and these things, thank you.

VITA OF LAURA SUZANNE HARRISON

December 2014

EDUCATION

Doctor of Philosophy in Geography, University of California, Santa Barbara
Dissertation: Impacts of Climate Variability on Surface Energy and Water Budgets in sub-Saharan Africa. December 2014.

Master of Arts in Geography, University of California, Santa Barbara
Thesis: Historical and Future Temperature Impacts on Maize Phenology and Stress Risk in Mozambique. December 2009.

Bachelor of Science in Physical Geography, University of California, Santa Barbara
June 2006.

PEER-REVIEWED PUBLICATIONS

Harrison, L., Michaelsen, J., Funk, C., Husak, G. (2011). Effects of temperature changes on maize production in Mozambique. *Clim Res* 46:211-222. 2011.
http://www.int-res.com/abstracts/cr/v46/n3/p211-222/

Grace, K., Harrison, L., Michaelsen, J., Pedreros, D., Husak, G. (2012). Using high resolution satellite imagery to estimate cropped area in Guatemala and Haiti. *Applied Geography* DOI:10.1016/j.apgeog.2011.05.014. 2012.
http://www.sciencedirect.com/science/article/pii/S014362281100097X

USGS Fact Sheet on temperature effects on phenology (October 2011). Using observed warming to identify hazards to Mozambique maize production.
http://pubs.usgs.gov/fs/2011/3110/pdf/fs2011-3110.pdf

PRESENTATIONS

(Invited) Harrison, L. (2014). Identifying sources of surface heating: Attribution of recent events in east Africa. UCSB Climate Research meeting. SB, CA. 12 Sep.

(Invited) Harrison, L., Michaelsen, J., Funk, C., Husak, G. (2013). Identifying food security hotspots by intersecting climate and vegetation trends with livelihoods. Association of American Geographers Annual Meeting. Los Angeles, CA. 11 Apr.

(Invited) Mahowald, N., Harrison, L., Shukla, S., Funk, C., Can earth system models be used for impact studies? (2012). Presented at 2012 Fall Meeting, American Geophysical Union. San Francisco, CA. 3-7 Dec.

(Poster) Harrison, L., Michaelsen, J., Funk, C., Carvalho, L., Still, C., McNally, A., Peters-Lidard, C. (2012). Identifying surface response to drought and heat with a land surface model

and NDVI. Presented at 2012 Fall Meeting, American Geophysical Union. San Francisco, CA. 3-7 Dec.

Harrison, L., Michaelsen, J., Funk, C., Tarnavsky, E., Marshall, M., Brown, M. (2012) Vulnerability to near-term warming in the Sahel. U.S. Geological Survey FEWS NET Science Meeting. Santa Barbara, CA. 2-3 Oct.

(Poster) Harrison, L., Michaelsen, J., Funk, C., Tarnavsky, E., Marshall, M., Brown, M. (2011). High resolution projections of cropping season atmospheric evaporative demand in the African Sahel. World Climate Research Programme Open Science Conference. Denver, CO. 24-28 Oct.

Harrison, L., Michaelsen, J., Funk, C., Tarnavsky, E., Marshall, M., Brown, M. (2011). Temperature-driven PET Projections. American Meteorological Society Annual Meeting. Seattle, WA. 23-28 Jan.

(Invited) Harrison, L., Michaelsen, J., Funk, C., Husak, G. (2010). Warmer Season, Faster Growth. Quantifying temperature trends and projections as relevant to maize production in Mozambique. UCSB Climate Research meeting. SB, CA. 5 Feb.

Harrison, L., Michaelsen, J., Funk, C., Husak, G. (2009). Variation in Maize Phenology and Climatic Inputs: Yield implications of the past and future. Association of American Geographers Annual Meeting. Las Vegas, NV. 22-27 Mar.

WORKSHOPS

NCAR Community Earth System Modeling Tutorial (2013)
Tutorial included lectures on simulating the climate system and practical sessions on running the CESM, modifying components, and analyzing data. National Center for Atmospheric Research, Boulder, CO. 12 - 16 August.

Conservation Agriculture with Trees in Niger (2011)
Workshop was about agroforestry as a basis for food security and environmental resilience in Niger and the Sahel. Organized by World Agroforestry Centre and African Forest Forum. Field visit to Zinder and Maradi and Workshop at Palais des Congrès, Niamey, Niger. 12 – 20 January.

POSITIONS

Associate Instructor (Jun 2014-Aug 2014)
Geography 3A: Oceans and Atmosphere
Introduction to the oceans and atmosphere and their role in the Earth's climate and its weather patterns. Focus on the flows of solar energy through the ocean and atmosphere systems. Human impacts of the Earth's climate are also introduced. Teaching Assistant: Corbin Hodges.

Graduate Student Researcher (Jan 2008- Dec 2014)
Climate Hazards Group (CHG) http://chg.geog.ucsb.edu/research/index.html. CHG is a UCSB partnership with the U.S. Geological Survey as part of the Famine Early Warning System Network (FEWS NET).
Personal contributions:

- Observed and projected climate impacts on crop production and livelihoods in sub-Saharan Africa.
- Scientific support for climate change adaptation planning
- Climate trend analysis with in situ and remotely sensed observations
- Land surface, crop water balance and cropped area modeling
- Scientific data programming and support
- Africa hazards monitoring

Graduate Student Teaching Assistantships
Geog 3A Oceans and Atmosphere. Summer 2013 with Sarah Harris
Geog 110 Intro to Meteorology. Spring 2009 with Dr. Leila Carvalho
Geog 148 Geography of California. Fall 2007 with Dr. Joel Michaelsen

Graduate Student Reader (Spring 2010)
Labs for Geog 210C. Climate data analysis and spatial interpolation techniques.

Undergraduate Assistant, UCSB Dept. of Geography (May 2006-July 2007)
Full-time staff position. Provided support to the Undergraduate program and provided guidance to students.

AWARDS AND CERTIFICATIONS

Summer Teaching Institute for Associates (Nov 2014)
STIA is a program designed to promote effectiveness and scholarship in college and university teaching. STIA Associates completed interactive online activities, attended face-to-face workshops, and participated in UC faculty-led mentoring meetings. Specific topics included student learning and assessments, teaching methods, and course planning. May-September 2014.

Fellowship on Hazards (Jun 2013)
Awarded by the California Institute for Research on Hazards and the UCSB Earth Research Institute to support research that increases our understanding and forecasting of natural hazards.

2013 CESM tutorial financial support (Aug 2013)
Awarded from the National Center for Atmospheric Research.

Dangermond Travel Award (Oct 2011)
Full support to attend the World Climate Research Programme Open Science Conference. Denver, CO 24-28 Oct. 2011

ABSTRACT

Impacts of Climate Variability on Surface Energy and Water Budgets in sub-Saharan Africa

by

Laura Suzanne Harrison

According to the IPCC Fifth Assessment Report, climate change will exacerbate current climate and non-climate stressors on agricultural systems in sub-Saharan Africa. This will adversely impact food security and the wellbeing of communities. Small-scale farmers grow more than 90 percent of the food produced in the region and many households depend on productive local growing conditions to support for their families. A better understanding of recent and near future climate constraints is important for identifying future food security risks and locally-appropriate adaptation strategies.

This dissertation research examines impacts of weather and climate on vegetation productivity in geographically diverse areas of east Africa and the semi-arid Sahel. The focus of this research is how surface energy and water budgets respond to variations in rainfall and temperature. It asks the following questions: Where will warmer temperature pose a hazard to rainfed agriculture in the Sahel in the next 20 years? What environment and weather conditions led to above average surface temperature during the recent decade in east Africa? How have declines in rainfall since the 1980s impacted vegetation productivity and hydrology in Tanzania? The research incorporates a variety of earth observation data, including historical records from in situ, model-derived, and satellite-observed sources and

projections from global climate models. A major contribution is the identification of specific areas, mainly in semi-arid climate zones, where increases in temperature and decreases to rainfall have large negative impacts on vegetation productivity. The research also presents new methods for evaluating land-atmosphere interactions in the context of hazards to vegetation.

TABLE OF CONTENTS

Introduction

In this dissertation we examine impacts of climate variability and climate change in sub Saharan Africa. We use a geographic approach to identify how surface energy and water budgets in arid, semi-arid, and wet climate regions respond to variations in rainfall, temperature, and weather. Our main focus is how vegetation productivity can be impacted by these changes. The analysis period is from the last 30 years, when earth observation data are most plentiful, to 20 years in the future. We use a variety of earth observation data including historical records from in situ, model-derived, and satellite-observed sources and projections from global climate models.

The motivation for this research is the importance of vegetation productivity for food security in Africa. There are four main components to food security: Availability of food, access to food (purchasing power), personal health to utilize nutrients, and how consistent of these factors are through time (Gregory et al., 2005). In the three study areas we examine, the African Sahel and two areas in east Africa, many households depend on productive growing conditions for generating income or for producing their own food (Thurlow and Wobst, 2003; Sissoko et al., 2011). Understanding climate and land surface interactions in the recent historical era can support efforts to improve food security. Our capacity to anticipate food availability or access problems at local to regional scales would be improved by better knowledge of the weather conditions that cause yield reductions in particular areas. Understanding historical climate constraints to vegetation productivity provides a frame of reference for evaluating potential impacts of future climate change. The information may help planners identify strategies to improve resilience in particular communities. Solutions

might involve improved economic, political, and agricultural policies, crop insurance programs, improved seeds, or conservation-oriented farming techniques (Brown and Funk, 2008; Garrity et al., 2010). If climate variability becomes more pronounced and widespread, as models project, disruptions to food production will become more frequent and more severe in sub-humid and semi-arid areas of Africa (Schmidhuber and Tubiello, 2007).

How climate variability and climate change impact people is inherently a geographic problem. Geography is based on the idea that places are both connected and unique. Places have physical qualities that are connected to a larger system, but each has a unique combination of physical and social characteristics. If rainfall or temperature changed by the same amount in every place on earth, different places would be impacted in different ways. The same magnitude reduction to rainfall is a larger proportion of the water budget in drier areas. The same increase in temperature can lengthen the growing season in a cool area and shorten it in a warm area. The response of vegetation to altered environments can range from tolerance to large impacts on health and productivity. When one considers the variety of ways people interact with the environment, the level of complexity greatly increases. Geographic analysis simplifies complexities of the physical world so that, progressively, the interconnectedness of people and features of the earth system can be better understood.

Particularly relevant geographic tools for climate impact analysis are spatial and temporal sampling of the earth system and statistical and process-based models. These provide observations of the variety of conditions that have existed and help us understand how observations relate to each other. Models also help to identify scenarios that may have existed in the past or will exist in the future. By applying a model across diverse environments, one can illuminate physical spatial gradients that are only clear from a

systems standpoint. In this dissertation we explore water and energy budgets using modern earth observation datasets, state of the science land simulation models, and a crop water balance model. The goal is to improve our understanding of climate-driven environmental stress in heterogeneous landscapes of sub Saharan Africa.

In Chapter 1, we explore spatial-temporal impacts of projected warming in the African Sahel. The goal is to provide decision makers with a sense of some of the constraints that may develop for rain fed agriculture due to temperature changes in the next 20 years. Rainfall is the most limiting factor for productivity in the Sahel, but there is much uncertainty as to how climate change will impact rainfall in the region. We consider a scenario in which climate conditions in 2026-2035 are similar to 2001-2010 except that global warming has increased temperature by the amount projected by the World Climate Research Programme Coupled Model Intercomparison Project Phase 5 (CMIP5) ensemble mean. We provide an outlook for how temperature changes would impact the crop water balance through its influence on atmospheric evaporative demand, or potential evapotranspiration, and how rain fed millet yields may respond to additional water stress. The projected change to potential evapotranspiration is estimated using historical statistical relationships from gridded weather data and CMIP5-projected changes to temperature. We place changes in context to local crop water budgets using the USGS GeoSpatial Water Requirement Satisfaction Index model, which is currently used for remotely monitoring crop productivity in Africa. We identify areas of the Sahel and crop growth stages that would experience most negative impacts under this scenario.

Chapter 2 uses energy budget variables simulated from a climate-land surface model experiment to identify factors that contribute to above average surface temperature in east

Africa. The purpose of the analysis is to provide information that could help remote monitoring of weather-driven vegetation stress. Surface heating is indicative of environmental conditions that are stressful for vegetation because it sometimes occurs when soil moisture is too low to support normal evaporation and plant photosynthesis. Vegetation that is not tolerant of higher temperature may experience a combination of heat and water stress, which can have large impacts to productivity. Land surface models are a potentially valuable resource for identifying when and where these conditions have occurred because they simulate energy and water fluxes for a variety of timescales and land cover types. We use output from an experiment in which the Noah land surface model v3.2 is forced with RFE 2.0 rainfall, a dataset that is currently used for monitoring in Africa. For areas in and near Kenya for a month of the long rains growing season, we examine modeled drivers of annual upwelling longwave radiation. We identify geographic variations in anomalous surface heating and the mechanisms responsible for warm and cool surface heat anomalies between 2002 and 2011.

In Chapter 3 we examine historical changes to rainfall and the potential impacts of these changes in Tanzania from 1982 to 2010. Widespread declines to March to May rainfall have been observed over the Greater Horn of Africa during this period. In Tanzania, rainfall declines have also been observed during other times of the year. The goal of this analysis is to identify where the declines may have influenced natural vegetation and agricultural productivity and water resources in Tanzania. For this analysis we use CHIRPS, a new 5.6 km resolution dataset based on station-observed and satellite-estimated rainfall. To get a sense of the general disagreement or agreement about changes to rainfall in the region we compare seasonal rainfall trends in CHIRPS to the trends in six other gridded rainfall

products. Previously, several studies reported declines to vegetation productivity for large areas of Tanzania. These were based on negative trends in satellite-observed vegetation index values from NASA GIMMS NDVI dataset. To determine if rainfall changes can explain some of these declines we compare interannual variability and historical trends in this NDVI dataset and CHIRPS. A model-based analysis is used to identify potential rainfall impacts to evapotranspiration, surface runoff, and maize yield potential. For these we use the Variable Infiltration Capacity hydrologic simulation model and the USGS GeoSpatial Water requirement Satisfaction Index model.

Chapter 1

Crop water stress in a warming Sahel: Anticipating impacts with potential evapotranspiration projections and a crop water balance model

Abstract

We explore spatial-temporal impacts of projected warming in the Sahel, an important agricultural region of sub-Saharan Africa, during the primary growing season. The goal is to provide decision makers with a sense of the constraints that may develop for rainfed agriculture due to temperature changes in the next 20 years. Potential evapotranspiration (PET) is projected for the 2026-2035 time period using a hybrid statistical method. In this approach CMIP5-projected warming is combined with locally-derived empirical relationships between PET and anomalous temperature. These are identified using a gridded historical record for 2001-2010. We model crop water stress to identify how millet yields may be impacted by temperature-induced PET changes.

Our results show that near-term warming could decrease average yields by 6-10% for rainfed millet. These declines would occur along the margins of current productive growing areas where farming is already constrained by low rainfall and infertile soil. Results also indicate more frequent low productivity seasons in these growing areas. Warming during August is the predominant driver, because the additional water stress from higher PET coincides with the millet reproductive phase. PET changes are mostly due to larger vapor pressure deficits with higher temperature. Based on the identified impact to moisture

demand, warmer temperatures will pose a substantial hazard to crop production in the Sahel in the next 20 years.

1.0 Introduction

One of the most critical aspects of future food security in Africa is how climate change will alter vegetation productivity in the Sahel (Batterbury and Warren, 2001; Devereux and Edwards, 2004). Climate-driven disruptions to productivity can have major environmental and social consequences. Most households in the semi-arid Sahel are highly dependent on the productivity of cropping and grazing lands, which in turn are reliant on a short and variable June-September rainy season (Rain, 1999; Sissoko et al., 2011). In the 1970's and 1980's, persistent drought transformed millions of people in the Sahel into environmental refugees (Myers, 2002). It is possible that in the 21st century climate-driven disruptions will be larger in scope and more frequent (Solomon, 2007; Giannini et al., 2013). The Sahel is warming at a faster rate than the global average, and by the end of the century, growing season temperature is projected to be higher than 20th century extremes (Battisti and Naylor 2009). Rapid population growth is exposing more people to climate hazards and increasing pressure on natural resources (Ramaswamy and Sanders, 1992). By 2050, Niger, one of the most impoverished countries in the world, will need to support an additional 32 to 44 million people, double to triple its 2010 population (PRB, 2010; UN, 2002; UN, 2007; Potts et al., 2011). Therefore a major goal of regional and international planners is to increase Sahelian communities' resilience to short term climate shocks and climate change (Adger et al., 2003; Dietz et al., 2004).

A fairly realistic range of climate change impact scenarios is needed to support food security planning in the Sahel (Paeth et al., 2009). This is a challenge because global climate models do not show consensus in projections for Sahelian rainfall (Druyan, 2011). Regional rainfall exhibits large natural variability on decadal timescales and it is unknown how the West African monsoon system will respond to future changes in atmospheric chemical and aerosol composition (Biasutti et al., 2008; Hein and De Ridder, 2006; Shanahan et al., 2009; Zhang et al., 2007). According to models compared in the Intergovernmental Panel on Climate Change 4th Assessment Report, the Sahel of the 21st century is wetter, drier, or no different from the recent past (Solomon, 2007). In Niger for instance, end of the century projections range between -25% and +49% (Burke et al., 2011). Despite these uncertainties, planners can prepare to some extent by being aware of the impacts that projected temperature changes could have on pastoral and agricultural activities in the region. Model projections for temperature are regarded with relatively higher confidence (Solomon, 2007). In the near-term, defined hereafter as the next 15-25 years, temperature changes will be mostly a consequence of greenhouse gas concentration increases that have already occurred (Neelin, 2011).

It can take more than a decade for major agriculture investments to produce returns and be fully adopted (Reilly and Schimmelpfennig, 2000), so it is important for adaptation programs to be proactive. Knowledge of climate risk 'hot spots', the areas where even small changes to climate would aggravate current problems, can help prioritize these investments within the region (Burton and van Aalst, 2004; Lobell et al., 2008). Food insecurity hot spots are generally identified by assessing projected scenarios with the context of historical observations. One example of this strategy is in Jankowska et al. (2012), which identifies

Mali's "front line" of vulnerability to near term hazards by exploring relationships between livelihoods, malnutrition, precipitation, and temperature. Combining near-term climate projections with knowledge of recent constraints to food production can give risk managers a sense of what to expect for certain agricultural regions in particular times of the growing season (Hellmuth et al., 2011). Using near-term projections is beneficial because some aspects of current climate can be compared or reasonably extrapolated.

Understanding how particular crops will respond to higher temperature is an essential component of adaptation to climate change (Thornton, 2012). While rainfall is the major limitation to crops in the Sahel, warmer air temperature can exacerbate plant water stress in drought years and limit yield potential in average rain years (Ong and Monteith, 1985). One concern is that warmer temperatures will harm crop development by more rapidly evaporating the soil moisture that plants rely upon between rainfall events. Evaporation rate increases exponentially with temperature according to the Clausius-Clapeyron relation. If warmer temperature is the main difference in climate, rainfall that was sufficient for agriculture in the past may not be sufficient in the future. Since 1975, growing season temperatures have increased by 0.6-1.0 °C in Mali, Burkina Faso, Niger, Chad, and Sudan (Funk et al., 2012a-e; Funk et al., 2011). Marshall et al. (2012) identified these trends as a potential cause of the recent decoupling between evapotranspiration and rainfall in the western Sahel. In the eastern Sahel Sheffield et al. (2012) found that increases in evaporative demand amplified plant stress during the late 20th century drying trend (Held et al., 2005; Zeng et al., 1999).

The goal of this paper is to explore how crop productivity may be impacted by near-term temperature changes by producing regional projections of near-term potential

evapotranspiration (PET). PET is the amount of water that atmospheric evaporative demand extracts from a saturated surface (Monteith, 1981). PET is commonly used for identifying agro-hydro-meteorological hazards (see e.g. Brown, 2008; Rind et al., 1990) because it is the expected rate evapotranspiration if soil moisture is not limiting. We focus on the role of temperature, because in the Sahel, a warming trend is projected with higher consensus between global climate models than are changes in other factors controlling PET (moisture and wind speeds) (Solomon, 2007). We use a hybrid statistical method to estimate the influence of above average temperature on PET and crop water stress. We model millet, a heat and drought resistant cereal crop important for food security in the Sahel (Suttie et al., 2005). Millet contributes to 20 to 50% of grain production in Sudan, Niger, and Burkina Faso (Leaky et al., 2009). Water stress in millet is symptomatic of major challenges to rainfed crop production. One third of millet production comes from crop areas that are vulnerable to climate variability and change, in part because farmers plant it when other staple crops will not produce (Ben Mohamed et al., 2002; Boschetti et al., 2013; Friborg et al., 1997).

2.0 Background

2.1 Potential evapotranspiration (PET) in the Sahel

When water resources cannot support potential evapotranspiration (PET), plants increase water use efficiency, but at the cost of less carbon fixation and photosynthesis (i.e. lower net productivity) (Hopkins and Hüner, 1995). Large disparity between soil moisture and PET is most detrimental to yields when it coincides with plant reproductive processes such as flowering and grain filling (Mahalakshmi et al., 1988; Sultan et al., 2005; Winkel et al.,

1997). The Sahel growing season (June to September, JJAS) is characterized by high levels of solar insolation and warm temperatures. This generally leads to high PET that fluctuates with monsoon activity and associated changes in cloud cover and near surface moisture. Figure 1 shows aridity, the ratio of precipitation to PET (P/PET), for JJAS. July-September precipitation in the southern Sahel is sufficient to balance PET and in the wettest areas is more than 1.25 times PET. The northern Sahel is more moisture limited, with evaporative demand greater than rainfall (aridity < 0.75).

2.2 Projecting PET

There is scientific consensus that warmer temperatures have and will continue to increase evaporation globally (Bates et al., 2008; Held and Soden, 2006). Regional patterns of observed and projected PET change are more ambiguous. Changes to other characteristics of the near surface atmosphere can amplify or suppress the impact of warming (Donohue et al., 2010; Gong et al., 2006; Rayner, 2007). Rates of PET will respond to changes in wind speed (McVicar et a., 2012), net radiation (Wild, 2009), atmospheric moisture, and air temperature. For PET projections a large amount of uncertainty comes from predicted moisture-related climate variables such as cloud cover and vapor pressure (Kay and Davies, 2008). There is a variety of formulas one can use to estimate PET, so PET projections are commonly produced by averaging output from multiple climate models using multiple formulas. Bias from combining these sources can cause PET estimates to diverge at global and regional scales and in some cases it determines the direction of change to water availability (Arnell, 1999; Kingston et al., 2009). New approaches to PET projections may reduce uncertainty in regional climate change impact assessments.

3.0 Data and Methods

We use a statistical model to estimate the additional PET that historically occurred during conditions that were warmer or cooler than average. The purpose is to use this as a guide for what changes to PET we might expect based on near-term average temperature projections. Projections tend to be small in magnitude compared to the historical range of daily temperature variability. Temperature is the only external predictor in the model. This approach accounts for the co-variation of surface radiative energy, humidity, and wind with anomalous temperature. Empirical relationships between anomalous temperature and PET are derived independently for each ~730 km^2 section of the study area using gridded land surface model simulations for 2001-2010. These locally-derived relationships are used to estimate the per-grid cell PET change that would occur given global climate model-predicted changes to air temperature between 2001-2010 and 2026-2035 periods. Warming-induced changes to crop water stress are assessed for rainfed millet using a simple crop water balance model.

3.1 Historical reference evapotranspiration

For our estimate of PET we use a version of the Food and Agriculture Organization of the United Nations Paper No. 56 Penman-Monteith (FAO-56 PM) formula (Allen et al., 1998) for reference evapotranspiration. Reference evapotranspiration (ET_o) and potential evapotranspiration are based on similar concepts but are not the same. PET assumes the surface is covered with water, which gives no resistance to evaporation, while ET_o assumes the surface has some (fixed) resistance to evaporation. Atmospheric variables drive ET_o variability when surface resistance parameters are held constant or are set to zero. In our scenario we assume that surface resistance is the same in 2001-2010 and 2026-2035.

The benefit of using ET_o or the Penman-Monteith equation (Monteith, 1964) on which it is based, is that both radiation and aerodynamic influences on atmospheric evaporative demand can be considered. Penman-Monteith is physically-based and includes all the parameters that govern energy exchange (Monteith, 1964; Allen et al., 1998). When meteorological data are available it is considered the choice model for PET (Sheffield et al., 2012) over the many alternatives (Lu et al., 2005). ET_o is denoted as 'reference' evapotranspiration because it is calculated with resistance parameters for a reference surface, usually well-watered grass crop of uniform height. Crop coefficients can then be used to modify ET_o for specific crop types and growth stages (Doorenbos and Pruitt, 1977). FAO-56 PM is the international standard for ET_o (Adeboye et al., 2009; Smith, 2000) and is actively used for monitoring growing conditions in the Sahel. The Famine Early Warning System (FEWS NET) use ET_o and rainfall data to identify areas where water stress may adversely impact yields. We use the same crop water balance model for this analysis (discussed in Section 3.3).

We use the California Irrigation Management Information System version of FAO-56 PM, which uses bulk surface resistance coefficients adapted from Walter et al. (2000) (CIMIS, 2009). FAO-56 PM separates evaporative demand into two main components: radiative energy and aerodynamic-driven ET_o [Eq. 1]. Net surface radiation dominates the first (energy) component, while the second (aerodynamic) component is driven by temperature, vapor pressure deficit (e_s-e_a), and wind speed.

$$ET_o = \frac{\Delta(R_n - G)}{\lambda[\Delta + \gamma(1 + C_d u_2)]} + \frac{\gamma \frac{37}{T_a + 273.16} u_2 (e_s - e_a)}{\Delta + \gamma(1 + C_d u_2)} \quad \text{[Eq. 1]}$$

Where

ET_o = grass reference evapotranspiration (mm h^{-1})

Δ = slope of saturation vapor pressure curve (kPa $°C^{-1}$) at T_a

R_n = net radiation (MJ m^{-2} h^{-1})

G = soil heat flux density (MJ m^{-2} h^{-1}) [= 0.1*R_n]

γ = psychrometric constant (kPa $°C^{-1}$)

T_a = mean hourly air temperature (°C)

u_2 = wind speed at 2 meters (m s^{-1})

e_s = saturation vapor pressure (kPa) at T_a

e_a = actual vapor pressure (kPa) at T_a

λ = latent heat of vaporization (MJ m^{-2} h^{-1})

C_d = bulk surface resistance and aerodynamic resistance coefficient [= 0.24]

Climate data used for FAO-56 PM is from the 0.25 degree GLDAS (Global Land Data Assimilation System) (Rodell et al., 2004) land surface state and flux product simulated with the Noah 2.7.1 land surface model (Ek et al., 2003). These data are made available by the NASA Goddard Earth Sciences Data and Information Services Center (http://disc.sci.gsfc.nasa.gov/). Noah 2.7.1 output are used to calculate 3-hourly ET_o (mm 3-hr^{-1}). All variables are then aggregated to daily daytime totals and averages. Daily anomalies are the difference between these data and 2001-2010 daily means, which are attained by fitting quadratic curves to JJAS data.

This particular GLDAS product was chosen, because forcing data are observation-derived fields rather than model-based reanalysis fields. Precipitation forcing is spatially and temporally disaggregated National Oceanographic and Atmospheric Administration (NOAA) Climate Prediction Center Merged Analysis of Precipitation (CMAP) fields, which are a blending of satellite and gauge observations. Atmospheric forcing data are NOAA Global Data Assimilation (GDAS) analysis fields (Derber et al., 1991). Radiation fluxes are derived with the Air Force Weather Agency's AGRicultural METeorological modeling system (AGRMET) method of combining satellite and station data.

3.2 Hybrid statistical PET projection

3.2.1 Statistical PET response to anomalous temperature (2001-2010)

We use a statistical model to estimate the PET response to temperature anomalies in the Sahel during JJAS. This model is designed under the assumption that near-term projected warming is analogous to a temperature perturbation from the mean climate. JJAS temperature changes projected by climate models for the Sahel between 2001-2010 and 2026-2035 are 0.4°C – 1.1 °C (Taylor et al., 2012), which is within the range of observed daily variability. We build the statistical model based on daily temperature anomalies observed during 2001-2010. 2001-2010 is a short record with but we have more confidence in data available for this period than longer ones.

The statistical model (Eq. 2) has two predictive components: a linear regression component *(βx(t))*, with daily temperature anomaly as the predictor, and an autoregressive component (*αy(t-1)*) to model observed first order PET anomaly persistence. Explicit modeling of one-day autocorrelation prevents overestimation of the PET response to temperature (*PET-T*).

An intercept term γ and model error ε are the third and fourth components. We use β (mm day^{-1} $°C^{-1}$), where it is statistically significant at the $95^{\%}$ confidence level, to estimate the impact of above average temperature on PET and crop water balance. For the purposes here, we explore the implications of a stationary β and projected warming through 2035.

$$y(t) = \alpha y(t\text{-}1) + \beta x(t) + \gamma + \varepsilon \qquad \text{[Eq. 2]}$$

Where

y(t) = Daily PET anomaly (mm)

α = PET autocorrelation coefficient for lag equal to one

β = Slope coefficient for temperature anomaly (mm day^{-1} $°C^{-1}$)

γ = Intercept term

ε = Model error

The statistical model is fit to each month of JJAS separately. Model parameters are estimated at each 0.25° by 0.25° grid cell using maximum likelihood. Model skill is estimated using the coefficient of determination (R^2). R^2 is the proportion of total observed variance explained by the model. Cross-validation is used to identify and remove areas from the analysis where model performance is unacceptable (cross-validated $R^2 < 0$). In cross-validation the model is iteratively trained on 9 of the 10 years and tested on the excluded year (Michaelsen, 1987). The contribution of temperature to *PET-T* is calculated by comparing R^2 of a partial model (no autocorrelation parameter) to that of the full statistical model.

We would expect, based on Equation 1, that the aerodynamic component of PET is the most important driver of *PET-T* because of the direct dependence of vapor pressure deficit on temperature. Variability in the surface radiation budget i.e. the radiation component of PET may also contribute to *PET-T*. To attribute β to radiative and/or aerodynamic controls of PET, we estimate the response of each component to temperature using simple linear regression. In the first regression model temperature predicts aerodynamic component anomalies (*adPET-T*); in the second model radiation component anomalies are predicted (*rdPET-T*). *adPET-T* represents the evaporative demand that is due to an increase in vapor pressure deficit. *rdPET-T* represents the evaporative demand due to an increase in net radiation.

3.2.2 Projected PET response to climate model-projected warming (2026-2035)

Projected changes to average near surface air temperature for the Sahel (ΔT) in June, July, August, and September are calculated as the difference between 2001-2010 to 2026-2035 monthly means as simulated by the World Climate Research Programme Coupled Model Intercomparison Project (CMIP5) (Taylor et al., 2012). For these periods, we use the CMIP5 multi-model ensemble mean of historical plus RCP4.5 greenhouse gas emissions scenario simulations. In the RCP4.5 scenario radiative forcing is stabilized by 2100 due to technological innovation and proactive emissions policy (Clarke et al., 2007; Smith and Wigley, 2006; Wise et al., 2009). The multi-model ensemble mean was downloaded as a 2.5° spatial resolution grid from the Earth System Grid Federation gateway (http://pcmdi9.llnl.gov/esgf-web-fe/) and is composed of the following 18 models (34 ensemble members): ACCESS1-0, ACCESS1-3, bcc-csm1-1, BNU-ESM, CanESM2,

CCSM4, CESM1-BGC, CESM1-CAM5, CMCC-CM, CNRM-CM5, CSIRO-Mk3-6-0, EC-EARTH, FGOALS-g2, FIO-ESM, GFDL-CM3, GFDL-ESM2G, GFDL-ESM2M, GISS-E.

For each month and 0.25° grid cell we use β from Equation 2 and ΔT to estimate the PET anomaly that historically would be associated with this deviation from average temperature. This model-estimated near future PET anomaly (ΔPET) is the same for all days of each month. For analysis and use in the crop water balance model, daily ΔPET and daily historical PET (PET_HIST) are each aggregated to 10-day and monthly totals. 10-day and monthly estimates of average PET for the 2026-2035 time period (PET_PROJ) are created from the sum of these fields (PET_HIST + ΔPET). The 10-day data are used for the crop water budget model that is discussed below.

3.3 Impact of projected PET on rainfed crop production

We use the USGS GeoSpatial Water Requirement Satisfaction Index model (GeoWRSI) (Senay and Verdin, 2003) to place projected PET changes in the context of climate-driven millet productivity. GeoWRSI is a spatially explicit simple bucket water balance model used for seasonal monitoring of crop moisture stress and yield in sub-Saharan Africa (see Tadesse et al., 2008, Verdin and Klaver, 2002, and http://chg.geog.ucsb.edu/products/geowrsi/index.html). GeoWRSI inputs are rainfall and PET in mm calculated for a reference crop using FAO-56 PM. GeoWRSI estimates overall crop water satisfaction by tracking moisture deficits through the growing season. Deficits occur when plant water use falls below the water requirement. Deficits indicate plant water stress and sub-optimal crop performance. Plant water use depends on rainfall, soil water surplus from the previous model time step, plant rooting depth, and water holding capacity

of the soil. Water requirements are determined by ET_o and a crop coefficient (*Kc*) that changes to reflect higher plant water needs in certain growth stages. Initial, vegetative, reproductive, and ripening growth stages are 14%, 24%, 38%, and 24% of the total growing season length, respectively. Millet water requirements are highest during the reproductive stage (*Kc* = 1), lowest during the initial stage (*Kc* = 0.3), and moderate for the vegetative and ripening stages (*Kc* = 0.3-0.7). WRSI, the overall crop water satisfaction, ranges from 50 to 100. WRSI = 50 indicates crop failure due to water stress, WRSI = 100 indicates no stress.

WRSI for millet is modeled for historical (2001-2010) and near future (2026-2035) periods with PET_HIST and PET_PROJ as respective inputs. To estimate the independent impact of ΔPET, 2001-2010 rainfall is used for historical and future periods. Recent rainfall climatology is as likely of a scenario for 2026-2035 as any model projection since Sahelian rainfall is difficult to predict and it is unclear how global warming will impact rainfall in this time frame (James and Washington, 2012). 2001-2010 was the wettest decade of the last 40 years (Peterson and Vose, 1997). Rainfall data for GeoWRSI are 10-day NOAA-CPC-FEWS NET Rainfall Estimates (RFE 2.0) (Xie and Arkin, 1997). RFE 2.0 was created specifically for drought monitoring in Africa and performs well in station validations for the Sahel growing season (Herman et al., 1997; Jobard et al., 2011). RFE 2.0 is available at the FEWS NET Africa Data Portal (http://earlywarning.usgs.gov/fews/africa/index.php). Start of season date is calculated within the GeoWRSI model using a rainfall accumulation threshold designed to reflect farmer decisions to wait for significant rain events before planting seed (see e.g. Marteau et al., 2011). We evaluate changes to average WRSI and the frequency of upper and lower 20^{th} percentile WRSI. To explain why WRSI changes we examine plant water deficits during the growth stages.

4.0 Results

4.1 Historical PET response to anomalous temperature

4.1.1 Statistical model skill

Figure 2 shows the statistical model R^2 for JJAS. The statistical model explained 30-50% of PET variability for much of the Sahel. Exceptions are dry regions in northern Mali, northern Niger, and northeastern Sudan. The model has most skill in predicting PET variability in July and August and in the eastern Sahel. Up to 70% of PET variability is explained in central Chad (July-August), southeastern Sudan (JJA), Eritrea (JJAS), and central Senegal and Mali (July). Moderate R^2 was expected, because the model predicts observed PET variability with essentially only one of the four meteorological variables important for PET. The West African monsoon, however, creates some degree of covariance because of its influence on summer temperature, moisture, and cloud cover. Model skill is mostly due to the predictive capacity of anomalous temperature rather than the autocorrelation parameter. The temperature parameter accounts for more than 75% of model skill south of 16°N in JJA and 14°N in September (not shown). This includes the areas of Chad, Sudan, Eritrea, and Mali where model skill is high.

4.1.2 PET response to anomalous temperature

Figure 3 shows monthly total PET anomalies associated with 1°C above average. These values are computed by scaling β from mm day^{-1} C$^{\circ -1}$to mm month^{-1}. Results are displayed where β is statistically significant at the 95$^{\%}$ confidence level. Figure 3 shows that for most of the Sahel, temperature has the strongest influence on PET in July and August. The June PET anomaly associated with a 1 °C anomaly is 5-9 mm for most of the Sahel. The June

anomaly is 10-20 mm in east Mauritania, central Mali, and pockets of the east Sahel in Sudan and Eritrea. July PET is 10-14 mm above average in Senegal, Mali, northern Burkina Faso, Nigeria, and southern Niger, and for ~2/3 of the region between 16° E and 40° E. The August PET anomaly is 10-14 mm in these areas and much of the central Sahel. In September the PET anomaly drops to 5-9 mm in central Mali, Burkina Faso, Niger north of 14° N, and Sudan; it remains at 10-14 mm in Senegal, southern Niger, Chad, and Eritrea.

4.1.3 Mechanism of PET response to anomalous temperature

Figure 4 shows the mechanisms driving the overall PET response to temperature (*PET-T*). In Figure 4a the JJAS mean of scaled β values from Figure 3 is plotted by aridity. Aridity > 0.35, meaning precipitation is > 0.35 PET, is a common indicator for where plant growth occurs in the Sahel (Le Houérou, 1989). Box plots show the median and inter-quartile range (IQR) of *PET-T*. Median JJAS *PET-T* is 10-14 mm month^{-1}, with high values decreasing non-linearly until aridity = 0.35. For aridity > 0.35, *PET-T* holds constant at 10 mm month^{-1}. *PET-T* is well constrained (IQR < 2 mm) for aridity > 0.35. For very arid areas, IQR < 5 mm. In Panel b *PET-T* is broken into radiative and advective controls. *rdPET-T* and *adPET-T* are the slope coefficients from simple linear regression models in which temperature anomalies predict radiation or aerodynamic component anomalies, respectively.

Comparison of Figure 4a and 4b shows that *adPET-T* accounts for most of *PET-T*. The magnitude of *adPET-T* is more than twice that of *rdPET-T* at most levels of climate aridity and *PET-T* is nearly identical to *adPET-T* for aridity < 0.35. For aridity > 0.35 *adPET-T* steadily declines to 6 mm month^{-1} at aridity = 1.8. *adPET-T* represents the physical constraint of evaporation rate by temperature. At warmer temperatures, the moisture

threshold at which air becomes saturated is higher. This increases the vapor pressure gradient between the moist surface and unsaturated near surface air and accelerates evaporation. Simultaneous below average specific humidity would enhance the vapor pressure deficit-temperature relationship. For aridity = 1.8 - 0.1 JJAS temperature increases from 27°C to 34 °C (not shown). Because saturation vapor pressure increases non-linearly with temperature, given a temperature anomaly of equal magnitude, we would expect to see a larger increase in evaporation rate in hotter areas. This explains the higher *adPET-T* magnitude in more arid, warmer zones. In general, the results show that drier areas experience stronger controls by *adPET-T*.

Increased vapor pressure deficit is the major driver of *PET-T*, but it is not the only factor. Despite moister areas having cooler temperatures, *PET-T* does not decrease for aridity = 0.35 - 1.8. We see in Figure 4b, from *rdPET-T*, that it is because the radiation component of PET positively responds to temperature. This response is due to covariance between net radiation and temperature anomalies. Temperature was a significant predictor of radiation component anomalies for approximately one third the study area. 80% of these samples are where aridity > 0.35. For aridity > 0.35 *rdPET-T* is 3-4 mm month^{-1} and IQR < 2 mm.

Figure 5 illustrates spatial-temporal aspects of *PET-T* mechanisms. The ratio of *adPET-T* to *PET-T* is plotted by grid cell for June, July, August, and September. The remaining fraction (= 1 - ratio) represents the *rdPET-T* contribution. Figure 5 shows that for most of the Sahel, *adPET-T* is the dominant driver of *PET-T* for June, July, August, and September (ratio > 0.6). Figure 5 also shows that *rdPET-T* only contributes to *PET-T* in JAS and its role is concentrated in the southern Sahel. Its contribution is greatest in August, when up to 40% of *PET-T* is due to *rdPET-T*. That *rdPET-T* is highest in the wettest areas and period of the

rainy season indicates rainfall processes might be influencing *rdPET-T* and to a some extent *PET-T*. Regional rainfall exhibits a similar spatial-temporal pattern with monsoon influence greatest during August and in the south (Sultan and Janicot, 2003). Variability in convective cloud cover might be responsible because it effectively blocks solar radiation, an important control of near surface air temperature.

4.2 CMIP5 projected warming (2026-2035)

Figure 6 shows the monthly change in temperature projected by CMIP5 models between 2001-2010 and 2026-2035 periods. For most of the Sahel, stronger warming occurs in June-July than in August-September. Between 10° N and 15° N (15° N and 20° N), average temperature increases ~0.7 °C (0.8 °C) in June-July and ~0.6 °C (0.7 °C) in August-September. The largest increases are mainly north of 15° N (0.9-1.1 °C, JJA). Models project the least warming (0.4-0.5 °C) in west Senegal (JJAS), central eastern Mali and northwest Burkina Faso (August-September), Lake Chad area (September), and east Sudan, Eritrea, and north Ethiopia (September). Between 10° N and 15° N the largest increases (0.8-0.9 °C, June-July) are in central Mali, north Burkina Faso, west and east Niger, and much of the eastern Sahel.

4.3 Projected impacts to millet water stress

Figure 7 shows average WRSI for 2001-2010 and the percent decline in WRSI to 2026-2035. In general, declines of 5% or less are projected in the southernmost Sahel. These are areas with rainfall in all months of JJAS and are the least water limited for both historical and near future periods. On the outskirt of the least water limited millet growing areas, WRSI is projected to decrease by 6-10%. This zone extends ~80-100 km to the north of

projected low impact areas from the Atlantic coast to west of Lake Chad. Larger declines (11-15%) are projected to the north of this moderate impact zone. In Sudan striking changes to WRSI can be seen in Figure 7, with moderate to large impacts projected for most areas where results are available. This feature is because rain isohyets are farther south in this part of the Sahel.

Figure 8 shows projected millet water deficit by growth stage. Decreases in average end of season WRSI are mainly due to water stress during millet's reproductive growth stage. Projected warming in late July, August, and early to mid-September is responsible. Millet requires a high amount of water during this stage ($Kc = 1$) for flowering and grain filling. End of season WRSI is strongly impacted by inadequate soil moisture during this stage. Projected PET does not change water deficit during the millet seedling (initial) stage. During the vegetative phase, small crop water deficits (2-4 mm in total) occur broadly across the Sahel. During the reproductive phase, deficits reach 7-10 mm within a large swath from central Senegal to north Burkina Faso and southwest Niger. The largest deficits are in the western Sahel (central Mali and north Burkina Faso) and in the eastern Sahel (southern and eastern Sudan). During the final growth stage, ripening, plant water needs rapidly decline ($Kc = 0.7$ to 0.3) and have less impact on yield (Winkel et al., 1995). Results show projected warming during late August and September will have a smaller impact on WRSI if millet is in the ripening stage at that time, which is the case for much of the study area according to model parameters. However, large water deficits during ripening can negatively impact WRSI, as illustrated by the projected 7-10 mm deficits in isolated areas of central Senegal, Mali, north Burkina Faso, southwest and southeast Niger, central Chad and along the northern edge of average millet production in Sudan and Eritrea.

Figure 9 shows projected changes to the frequency distribution of WRSI. In 2001-2010 areas with average WRSI near 100 (Fig. 7a) experienced good seasons (upper 20^{th} percentile of WRSI) 5 or more years of the 10 (Fig. 9a). Outside of these areas good seasons occurred 2-3 years of the 10. Fig. 9b shows that near-term warming will reduce good season frequency to 4 or 5 years of 10 in the most productive areas and elsewhere the frequency of good seasons will drop to 1 to 2 years of 10. Changes to the frequency of lower 20^{th} percentile seasons are more homogeneous (Fig. 9c,d).

5.0 Discussion

In this analysis we illustrated a scenario in which climate conditions are the same in 2026-2035 and 2001-2010 except that global warming has increased temperature by the amount projected by the CMIP5 ensemble mean. We used a simple crop water balance accounting model to estimate how changes to potential evapotranspiration may change the prevalence of water stress in rainfed millet. Soil or atmospheric water deficits during drought conditions cause C4 crops like millet to reduce stomatal conductance, which restricts photosynthesis and leads to lower yield (Leaky, 2009). There are many unknowns about future crop response to climate change in the Sahel. Rainfall, soil fertility, and breed-specific sensitivity to environmental stress will remain important determinants of crop productivity. Changes to crop water use efficiency might be important in the mid-century or later, depending on CO2 concentration and specific growing conditions. Free-air CO_2 enrichment experiments have shown that higher CO2 concentrations may benefit some C4 crops by allowing them to conserve soil moisture during drought periods and delay onset of severe water stress (Sage et al., 2003; Leaky, 2009 and references therein). The objective of this analysis was to create

a basic outlook for how crop water availability will change in the next 20 years due to projected warming.

Results show that higher evaporative demand will likely become a bigger problem for agriculture production in the near future than it has been in the recent decade. There is a strong link between PET and temperature in the Sahel. This is mainly because warmer air has a higher water holding capacity before saturation and this increases the vapor pressure deficit between the ground and the atmosphere. While the most intense warming is projected in the beginning of the growing season (June-July), results show that millet yields will be mainly impacted by higher crop water requirements during the middle of the growing season when the reproductive phase occurs. In the southern and eastern Sahel the statistical model showed PET is most responsive to temperature during July-August. Faster evaporation at higher temperature is the major driver of projected changes to JJAS PET.

Results show that near-term warming will disproportionately impact the more arid areas that currently experience moderate to severe water stress on average. In these zones soil moisture is inadequate to buffer the impact of higher PET. Small declines to average WRSI are projected in areas that typically exhibit minimal water stress. In addition to a lower WRSI on average, results show near-term warming will constrain regional millet productivity also by changing the frequency distribution of WRSI. For most of the Sahel study area poor seasons (lower 20^{th} percentile of WRSI) will become more frequent, from 2 years of 10 in 2001-10 (Fig. 9c) to 3 years of 10 in 2026-2035 (Fig. 9d). High frequency of poor seasons (4-5 years of 10) is projected in the northern cropping areas of central Mali and less spatially extensive locales in Niger, Chad, and Sudan. In combination, results project a larger

disparity between areas that can and cannot support rainfed millet without substantial risk of water stress.

It would be worthwhile to examine historical rainfall and temperature, insolation, and humidity relationships in more detail. We found that there is a positive statistical relationship between radiation and temperature anomalies in the rainiest time of the season in the southern Sahel, and this had some influence on the temperature-based PET projections. It is difficult to separate the influence of rainfall from PET projections because rainfall processes influence all characteristics of the near surface atmosphere. PET projections that use climate model projections of water vapor and cloud cover are highly uncertain for this reason. A wetter 2026-2035 period would probably ameliorate the moisture deficits that are projected here, as long as the timing rainfall events were similar. An extra 7-10 mm rainfall during the reproductive stage would be sufficient to prevent the projected stress from higher evaporative demand. A drier 2026-2035 period could be a major challenge to agricultural production because crops would receive less rainfall, grow in higher temperatures, and contend with higher evaporative demand. Whether climate is wetter or drier on average, warmer temperatures will lead to faster depletion of soil moisture between rainfall events.

6.0 Conclusion

We used a hybrid statistical approach to identify how near-term warming might impact rainfed agriculture in the semi-arid Sahel in the 2026-2035 period. Spatial heterogeneity of climate constraints to agriculture will lead to variable impacts of projected warming in the Sahel. We have estimated these impacts at a higher spatial resolution than can be achieved

with climate models alone. Our goal was to provide a resource for climate-related decision-support at local and sub-regional scales. For decision makers, high spatial resolution maps may be useful to determine risk, such as if investing in rainfed agriculture is a sustainable means of improving food security or if alternatives should be considered. We examined the sensitivity of an important component of the Sahel water balance, potential evapotranspiration, to above average temperature using gridded data from 2001-2010 (0.25° spatial resolution). We used this information to identify how and where CMIP5-projected warming would alter current geographic constraints to millet production.

Our method is unique in that the historical relationship between temperature and potential evapotranspiration is derived from local statistical regressions that account for observed feedbacks between temperature, humidity, wind, and net radiation. This impact assessment neglects the influence of projected rainfall because 21st century rainfall projections are uncertain for the Sahel. We elected instead to give disaster risk managers a sense of changes to expect by placing projected near-term warming, which climate models predict with more confidence, in the context of recent growing seasons. The method could be replicated for other areas where climate model projections for moisture variables are inconclusive or bias from conventional methods of PET projection obscures water resource estimation.

Results indicate that moisture constraints created by near-term warming will increase risk for crop production outside of current high yield potential zones. Warming projected for August is particularly hazardous because it coincides with a moisture-sensitive stage of millet growth. Projected 0.6-1 °C increases would contract the area where millet can be grown without yield loss due to water stress. Millet production potential in 2026-2035, as estimated with WRSI and assuming a repeat of 2001-2010 rainfall, is projected to be 6-15%

lower than in 2001-2010 in marginal growing areas. Declines of less than 5% are projected in areas that experienced minimal water stress in 2001-2010. Impact of near-term warming is greater in marginal cropping zones because average rainfall cannot compensate for increases to evaporation. Projected temperature changes translate directly into higher vapor pressure deficits in these areas.

If near-term warming will predominantly impact marginal cropping areas, as this analysis indicates, the implications are concerning for regional food security. Impacts to other staple crops like sorghum and maize may be worse because they are less drought resistant than millet. Population growth and yield stagnation in the region, along with recent hiatus from severe, long-lasting drought, have led to the expansion of farming into marginal areas (FAO, 2003; Olsson et al., 2005; Tappan et al., 2004). Increasing national-level millet production between 1980-2011 in Chad, Mali, Niger, and Sudan is largely due to extensification (Food and Agriculture Organization, 2003). In addition to the hazards temperature changes will create, farmers will also be dealing with land degradation from overuse by growing populations (Rain, 1999).

Improving food security in the Sahel in the face of climate change will be challenging. Demographics and food production systems are incredibly diverse in the Sahel and effective adaptation strategies will need to reflect this diversity (Lambin et al., 2001; Mortimore and Adams, 2001; Raynaut, 2001). This analysis has illustrated that the historical climate record can provide important information about future changes to agriculture constraints. Planners can use this scenario as an alternative to rainfall-based projections of near-term climate change impacts in the Sahel.

Acknowledgments

Thanks to Elena Tarnavskoy, Molly Brown, and Chris Funk for sharing the concept of making a temperature-based PET projection. Thanks to Michael Marshall for his edits and for downloading the GLDAS data and helping calculate daily ET_o with this data. Thanks to Joel Michaelsen for his help with the statistical modeling.

Chapter 2

Identifying sources of surface heating: Attribution of recent events in east Africa

Abstract

Surface heating can result from severe vegetation stress, suppression of latent or sensible heat flux by boundary layer conditions, increased radiative forcing, and other mechanisms. Identifying which of these is the source of surface heating is challenging because multiple physical processes offset each other to balance the surface energy budget. Energy and water fluxes simulated by land surface models provide a resource for diagnosing causes of surface heating and cooling at a variety of timescales. We use the Noah land surface model v3.2 to examine modeled drivers of annual surface heat variation and mechanisms responsible for heating during some drought events for a region in East Africa for 2002-2011. Upwelling longwave radiation (LWup) is used to quantify surface heat content and is estimated from surface energy balance terms. LWup variance in April 2002-2011 is attributed to radiative forcing (RF) or turbulent heat flux forcing (TF) for each grid cell and the regional pattern is examined with regression tree analysis. To identify the main cause of heating or cooling during annual events we use a simple ratio-based attribution method that quantitatively links LWup anomalies to anomalous RF and TF. Attributed LWup maps are used to examine several anomalous heating and cooling events in greater detail.

According to the simulation, radiative forcing, mainly through net shortwave radiation, is the main driver of April LWup anomalies for much of the region. Radiative forcing is most

important in wet and densely vegetated mountainous areas, such as Kenya's Rift Valley. LWup anomalies are closely linked to evapotranspiration in semi-arid areas with low density vegetation, such as eastern Kenya and southern Somalia. Major surface heating events corresponded with some drought events, but mechanisms that caused the heating were unique in several cases. For example, for a large area in northeast Kenya in 2005 surface heating was associated with below average evapotranspiration and anomalously warm air temperature. Surface heating occurred during severe drought conditions in 2011 and was attributed to high levels of insolation associated with below average cloud cover. Ratio-based attribution was useful for extracting summary information about complex physical processes and may be a practical approach for land model intercomparison.

1.0 Introduction

Changes to the climate system alter the pathways through which the Earth surface heats and cools (Chapin et al., 2011; Trenberth, 1998). Increased concentrations of greenhouse gases in the atmosphere are associated with higher air temperature and a hydrologic cycle with more rapid turnover (Solomon et al., 2007). These changes directly impact evaporation and precipitation, the main sources of moisture flux at the land-atmosphere interface. Changes to evaporation and atmospheric composition also influence cloud development, an important factor for radiative energy leaving and reaching the surface (Fairall et al., 2008; Ramanathan et al., 1995). The response of the climate system is in turn mediated by moisture and energy flux from the surface. Identifying the most important physical mechanisms involved in changes to the climate system can be something of a labyrinth. Linkages between them are circular and involve complex feedbacks. The basic situation, however, is straightforward. The surface must attain a new balance of energy given larger inputs of downwelling

longwave radiation, and it will do so by increasing its export of energy through warming and longwave radiation emission and through latent and sensible heat fluxes (Boer, 1993).

Getting an overall picture of what aspects of the surface energy budget are changing can be an analytical challenge. Multiple physical processes are active in balancing the energy budget and climate change can affect them all (Held and Soden, 2006; Wild et al., 2004). One approach is to focus on how physical processes collectively change surface heat content. Surface heat content is the 'leftover' energy that temporarily resides at the surface due to non-equal energy fluxes in and out of the surface. Increased heat content warms the surface, increasing surface temperature and emission of longwave radiation to the atmosphere. The surface cools in response to decreased heat content. In the IPCC AR4 report this instantaneous 'surface forcing' was described as a useful diagnostic tool for understanding changes in the heat and moisture surface budgets and the accompanying climate change (Solomon et al., 2007).

Understanding the geographic nature of anomalous surface heating- the environments in which it frequently occurs and the mechanisms involved- is important for anticipating its impacts at a variety of time scales. Surface heating associated with soil moisture deficits can lead to drought intensification (Chang and Wallace, 1987; Zampieri et al, 2009) and an amplified surface temperature response (Fischer et al., 2007ab). The impact these feedbacks have on vegetation productivity largely depend on ecosystem resilience to high temperature and on concurrent hydrometeorological conditions. For example, during the summer of 2003, the hottest summer in Europe in 500 years, biogeophysical characteristics were important factors for land and atmosphere interactions and regional impacts to vegetation productivity. Different impacts to growing season length enhanced growth in high elevation

areas and suppressed growth in low elevation areas (Jolly et al., 2005). In areas with well-watered and high biomass forests, where dense canopies used the excess solar radiation for metabolic energy and also shaded the understory, a muted surface heating response was observed. (Renaud and Rebetez, 2009). In semi-arid areas dominated by seasonal grassland, intercepted radiation led to rapid depletion of soil moisture which helped intensify and prolong the heat waves (Teuling et al., 2010). The most well understood hazards high temperature poses to crop yields are physiological stress from reduced efficiency or damage to photosynthetic tissues and reduced biomass through decreased plant growth duration (Al-Khatib and Paulsen, 1999; Ritchie and NeSmith, 1991; Tashiro and Wardlaw, 1989; Yoshida, 1972). High temperature has been shown to decrease wheat yields by 3 to 5% per 1 °C increase above 15 °C in wheat under controlled conditions and by larger amounts in field conditions (Choudhury and Wardlaw, 1978). Significant economic impacts of high temperature are also seen in livestock production systems, where heat stress reduces cattle fertility and increases their water requirements and susceptibility to disease and parasites (Howden and Turnpenny, 1997).

Establishing the most important weather and biophysical processes related to the potential for surface heating across geographic domains may benefit drought monitoring activities. Because higher than average surface temperature can be affiliated with reduced evapotranspiration, global surface temperature data from satellites are a promising resource for identifying vegetation stress (Garstang and Fitzjarrald, 1999). Thermally-based estimates of evapotranspiration are attractive because remotely sensed data provide repeat sampling and near global coverage. The estimates are based on a semi-consistent statistical relationship that is observed between satellite-observed surface temperature and vegetation

indices in some regions (e.g. Ts/VI methods, which are reviewed in Petropoulos et al. (2009)). However, use of these methods for monitoring remote regions is hindered by a lack of reference knowledge about historical drivers of surface temperature that influence the surface temperature-vegetation index slope. For example, Friedl and Davis (1994) found that the relationship between surface temperature and the Normalized Difference Vegetation Index depends on land cover type and does not always reflect changes to energy partitioning associated with evapotranspiration deficits. Karnieli (2010) showed that water-limited and energy-limited biomes exhibited slopes of opposite sign. Influence of soil moisture, incident radiation, wind speed, leaf area index, and energy partitioning on the slope have also been observed (Pierce and Congalton, 1988; Nemani and Running, 1989). Choudhury (1991) suggested that improving our ability to relate satellite temperature observations to the temperature determined by surface heat balance equations would lead to more effective use of satellite data for vegetation analysis. Similarly, a better understanding of how and where drought conditions have historically corresponded to surface heating might support identification of hazardous conditions for water resources and crop and rangeland productivity.

Land surface model (LSM) experiments are potentially a useful resource for investigating causes of abnormal surface heating and cooling. The ability of land surface models to provide spatially distributed information in near real time for regions with limited observation networks has generated considerable interest in using them for drought monitoring (Anderson et al., 2012). Land surface models simulate energy and water fluxes across the land-atmosphere interface at sub-daily to annual time steps based on atmospheric forcing data (Bonan, 2008). Surface energy balance variables are simulated based on

modeled physical processes and parameterized versions of the surface-atmosphere interface. LSMs can simulate the influence of vegetation morphological characteristics and soil type and texture on energy exchange (Choudhury, 1991). Coupled model experiments involve a land-atmosphere system in which simulated land surface processes influence the planetary boundary layer structure and thereby affect clouds and precipitation processes (Chen and Dudhia, 2001). Uncoupled model experiments do not allow for surface feedbacks but can provide physically-based energy flux and hydrometeorological data where it is otherwise unavailable. A major challenge to examining land-atmosphere processes across different geographic domains is the limited number of sites where surface energy fluxes and relevant variables are observed (Baldocchi, 2008). In sub Saharan Africa for example, approximately 11 observation sites measure surface fluxes with flux towers (Merbold et al., 2009) but records are generally intermittent. .

In this analysis we examine if anomalous surface heating during the rainy season can be consistently attributed to certain atmospheric or vegetative conditions. A potential link between drought events and surface heating is given particular attention. Figure 1 shows an example of how variations in soil moisture link surface water and energy budgets. When moisture is available, most of the surface-to-atmosphere heat transfer occurs through evaporation. This occurs in the Figure 1c, the wet soil example. Evaporation effectively removes heat from the surface, as indicated by the small magnitude of upwelling longwave radiation. For the moderate and dry soil (Figure 1b and 1a), progressively less energy transfer occurs through evaporation and more occurs through sensible heating. In some regions during drought conditions, dry soil leads to insufficient rates of surface-to-atmosphere heat transfer which results in surface heating and a larger magnitude of

upwelling longwave radiation (Figure 1a). In the Figure 1 example the amount of incoming solar energy is the same in all cases of soil wetness. In the real world, insolation and other weather conditions may be very different in drought periods vs. rainy (wet soil) periods. Using the atmospheric forcing data and the simulated data from a land model experiment allows us to identify and examine cases like these.

The goal of this analysis is to identify climate and geographic factors that are important for interannual variations in surface heating and cooling during the Long Rains (March-May) rainy season in East Africa. For this geographically diverse study area, we examine how monthly weather influences the surface energy budget and identify conditions that historically translated into anomalous surface heating or cooling. We use the Noah land surface model version 3.2 to examine modeled fluxes of the surface energy budget that have an effect on surface temperature. We also examine mechanisms responsible for surface heating during some drought events. Biogeophysical properties of the land surface are prescribed in the model according to a monthly climatology and do not produce feedbacks to atmosphere in this experiment. The analysis is for April 2002-2011 for the region in East Africa within 5 °N – 5°S, 33 °E – 43 °E, which mostly encompasses Kenya. Geographic variability is large in terms of elevation, vegetation density and land cover type. April is important for vegetation productivity because it is typically the wettest month of the Long Rains season. Favorable growing conditions are important for pastoralist communities in semi-arid areas and for rainfed fed crop production across the region.

We examine annual drivers of April mean upwelling longwave radiation (LWup) for 2002-2011. Upwelling longwave radiation is the essential measure used by satellites to estimate surface temperature, along with atmospheric corrections and emissivity estimates. LWup is

estimated using the surface energy balance equation using the following terms: Monthly mean shortwave net radiation (SWnet), longwave downwelling radiation (LWdown), latent heat flux (L), and sensible heat flux (H). Variables were output from a land surface model simulation experiment with the Noah model (Chen et al., 1996; Ek et al., 2003) in the United States Agency for International Development (USAID) Famine Early Warning Systems Network (FEWS NET) Land Data Assimilation System (FLDAS). LWup variance in April 2002-2011 is attributed to total radiative forcing (RF) (the sum of SWnet and LWdown), and total turbulent heat flux forcing (TF) (the sum of L and H), for each grid cell. Regression tree analysis is used to examine how the interannual variability of LWup for 2002-2011 varied through the East Africa region. We also identify the main source of heating or cooling in each year for each grid cell. For this we apply a method called ratio-based attribution, which identifies the fraction of each monthly LWup anomaly due to radiative energy and surface-to-atmosphere turbulent heat transfer. Attributed LWup maps and simulated surface energy balance variables are used to identify and discuss important mechanisms for anomalous heating and cooling events in the region.

2.0 Data

2.1 FLDAS Noah experiment

Data for 2002-2011 is simulated in an experiment from the United States Agency for International Development (USAID) Famine Early Warning Systems Network (FEWS NET) Land Data Assimilation System (FLDAS). The community Noah land surface model v3.2 (Chen et al., 1996; Ek et al., 2003) is forced in uncoupled mode with NOAA-CPC African Rainfall Estimation Algorithm 2.0 (RFE) rainfall (Xie and Arkin, 1997) and

National Center for Environmental Prediction (NCEP) Global Data Assimilation System (GDAS) meteorological data (Derber et al., 1991). This configuration was designed to simulate surface energy budget variables that complement the RFE rainfall record. RFE is a near-real time product that was developed for operational monitoring of growing conditions in Africa. FEWS NET uses 10-day accumulated RFE for drought monitoring activities. RFE is a blend of cloud top temperature from Meteosat 7 geostationary satellite infrared data, microwave data from Special Sensor Microwave/Imager (SSM/I) and Advanced Microwave Sounding Unit (AMSU), and WMO Global Telecommunication System (GTS) station data for satellite bias removal. These sources are merged for a daily rainfall estimate at 0.1° resolution. For sub-daily forcing of the land surface model RFE 2.0 was broken into 6-hourly estimates. Disaggregation was accomplished using a temporal weighting scheme that distributes RFE 2.0 daily total rainfall into sub-daily rainfall totals that are consistent with the temporal distribution of rainfall in the GDAS-CMAP product (Gottschalck et al., 2005). GDAS meteorological data come from surface, atmospheric, and satellite observations that are gridded for use in weather forecasting models such as the NCEP Global Forecast System.

Surface temperature was not used because it was not available in the FLDAS dataset as a monthly-averaged variable. Because monthly emissivity did not change between years in the simulation, interannual LWup variability would be similar to that of surface temperature. This was confirmed by comparing Noah land surface model-simulated surface temperature and calculated LWup from a similar dataset, the 0.25 degree monthly Global Land Data Assimilation System Noah simulation from NASA (GLDAS_NOAH025_M) (Rodell et al., 2004). LWup was calculated with the same method used in this analysis (detailed in Section

3.1). Figure 2 shows that upwelling longwave radiation and surface temperature are highly correlated in the GLDAS Noah dataset (R= 0.80-1). Upwelling longwave radiation anomalies are synonymous with anomalous surface temperature. An advantage to analysis with LWup is that it enables the impact of surface energy balance terms on surface heating and cooling to be examined based upon the magnitude of their anomalies (all are in units W m^{-2}).

The analysis domain for this paper is a region in East Africa from 5 °N – 5°S, 33 °E – 43 °E which encompasses Kenya and parts of Tanzania, Uganda, South Sudan, Ethiopia, and Somalia. We use surface energy budget terms and some atmospheric forcing variables that are output from the model as 24-hr averages. In this paper we analyze monthly mean data for April, the center month of the Kenyan 'Long Rains' season, for the period 2002-2011. Forcing data and surface parameters used for the FLDAS Noah simulation are listed in Table 1.

The East Africa region is shown in Figure 3. Figure 3a shows a regional map of April climatological daily rainfall, averaged over 2002-2011 with RFE 2.0 (Xie and Arkin, 1997). Figure 3b shows green vegetation fraction (as a percent) from NESDIS/NOAA (Gutman and Ignatov, 1998). Green vegetation fraction is the percent of each grid cell where midday downward insolation is intercepted by a photosynthetically active green canopy (Chen et al., 1996). It is an important land surface parameter used by the Noah model to calculate total evapotranspiration for each grid cell. As these maps show, rainfall and vegetation density are highly variable across the region. April rainfall is highest near Mount Kenya (central Kenya), Mount Meru and Kilimanjaro (north Tanzania) and near Lake Victoria. April rainfall is lowest in the zone from East Kenya to southeast Somalia and in very arid

northeast Kenya in the Chalbi Desert near Lake Turkana. Southern Ethiopia and areas in the region's southwest, including parts of Uganda, Kenya, and Tanzania, receive moderate rainfall in April. As seen in Figure 3b, vegetation density varies dramatically across the region, from near zero to 85% cover. Vegetation density is highest in the southwest and in coast Kenya and southern Ethiopia. The April pattern is similar to what an annual average would show because wet areas in April also receive rain through much of the year. The exception is in southern Ethiopia and the semi-arid east Kenya-southwest Somalia zone, where rain comes in two distinct and short seasons. In these areas April is one of the most productive months in terms of vegetation photosynthetic activity.

In this analysis only meteorological data are used to force the model, so annual differences in monthly mean upwelling longwave radiation are due to variations in weather and its impact to soil moisture. In the FLDAS experiment biological and reflective properties of the land surface do not change between years. Green vegetation fraction data (Gutman and Ignatov, 1998) and surface albedo data (Csiszar and Gutman, 1999) are NESDIS/NOAA 5-year monthly climatology grids, i.e. they vary in space and by month but not between years, that are derived from NOAA Advanced Very High Resolution Radiometer (AVHRR) satellite data. These datasets were designed for use in numerical weather prediction models. We used these climatological datasets because NASA's Land Information System, the platform used to run Noah and other models, is set up to ingest them. Using a monthly climatology instead of measured greenness and albedo introduces artificiality to the modeled surface energy budget and is a limitation of this analysis. Use of measured greenness data has been shown to improve partitioning between surface heating and evapotranspiration, which impacts the surface energy budget, planetary boundary layer evolution, cloud, and

convection. Advancements in land modeling are geared towards assimilating remotely sensed data and incorporating dynamic vegetation, where vegetation growth is modeled not prescribed, into models.

Table 1. Selected FLDAS Noah simulation variables

Variable	**Variable type**	**Source**
Mean rain rate	Forcing data	RFE 2.0 (Xie and Arkin, 1997)
Other meteorological variables	Forcing data	National Center for Environmental Prediction (NCEP) Global Data Assimilation System (GDAS) (Derber et al., 1991)
Elevation	Static parameter	GTOPO30 Global 30 Arc Second Elevation Dataset (Gesch et al., 1999)
Soil type	Static parameter	FAO Soils Database (Reynolds et al., 2000)
Vegetation type	Static parameter	University of Maryland 1 km vegetation classification (Hansen et al., 2000)
Green vegetation fraction	Monthly climatology	NESDIS/NOAA 0.144 degree monthly 5-year climatology green vegetation fraction from NCEP (Gutman and Ignatov, 1998)
Surface albedo	Monthly climatology	NESDIS/NOAA 0.144 degree monthly 5-year climatology surface albedo from NCEP (Csiszar and Gutman, 1999)

2.2 Noah Land Surface Model v3.2

Noah is a stand-alone one-dimensional column land surface model used for modeling physical processes of the hydrologic and energy cycle. The widely used Noah LSM forms the land component of the regional and global weather forecasting models at NCEP and of the Weather Research and Forecasting model (WRF) at the National Center for Atmospheric

Research (NCAR) (Chen and Dudhia, 2001; Zheng et al., 2013). Noah originally began as the Oregon State University land model (Mahrt and Ek, 1984; Pan and Mahrt, 1987), and after 30 years of evaluation and refinement, model physics continue to be improved by the land modeling community (see e.g. (Ek et al., 2003; Niu et al., 2011; Wei et al., 2012)). Sustained interest in improving Noah and recent experimentation with the model in regions outside the United States (e.g. (Anderson et al., 2012; Chen et al., 2010; Marshall et al., 2013; Patil et al., 2013; White and Toumi, 2012)) is largely due to the model's moderate complexity but good computational efficiency and reasonable simulation skill for a variety of geographic domains and time scales (Chen et al., 1996; Hogue et al., 2005; Jimenez et al., 2011; Mitchell et al., 2004; Robock et al., 2003; Xia et al., 2013; Xia et al., 2014).

The Noah model has an explicit vegetation canopy, soil hydrology, and soil thermodynamics. Figure 4 shows a schematic of the physical processes involved in Noah water and energy budget calculation. Precipitation not intercepted and held by the plant canopy goes directly into the soil and infiltrates through up to four soil layers. If the soil is saturated the water runs off the surface. Noah is a coupling of three main models: The Penman potential evaporation model from Mahrt and Ek (1984), a multilayer soil model (Mahrt and Pan, 1984), and a primitive single-layer canopy model (Pan and Mahrt, 1987) enhanced with resistance parameterizations (Jacquemin and Noilhan, 1990; Noilhan and Planton, 1989). Mahrt and Ek's (1984) Penman potential evaporation model is a modified version of the original 1948 Penman equation that allows for the stability condition of the boundary layer to influence turbulent water vapor transport. This form is convenient for use in atmospheric models because unlike more sophisticated potential evapotranspiration equations it does not require iterative procedures to estimate the influence of stability.

Surface temperature is not needed for the calculation and evaporation is only a function of atmospheric variables (Mahrt and Ek, 1984).

In Noah evapotranspiration is modeled as the sum of transpiration from the plant canopy, direct ("bare soil") evaporation of soil water from the uppermost soil layer, and direct evaporation of canopy-intercepted water. Bare soil evaporation is modeled such that moisture flux occurs at the rate defined by the Penman model (Mahrt and Ek, 1984) until soil moisture becomes low and a resistance parameter slows evaporation (Chen et al., 1996). Moisture and energy flux through canopy transpiration is defined by Penman and then scaled by green vegetation fraction and a canopy resistance term that depends on root zone soil moisture, with plant rooting depth dependent on vegetation type. Sensible heat flux is modeled from the gradient between ground and atmospheric surface temperatures plus a heat exchange coefficient that depends on parameterized roughness lengths for heat and momentum transfer and atmospheric stability (Chen et al., 2010). The coefficient is obtained from Monin-Obukhov similarity theory (Monin and Obukhov, 1954), which estimates the importance of thermal mixing (buoyancy) and mechanical mixing (wind shear) for near surface turbulence. Noah solves the surface energy balance and determines skin surface temperature for each grid cell using by applying a linearized surface energy balance equation using the combined soil/vegetation surface (Mahrt and Ek, 1984; Chen et al., 1996).

Skill for wet-season latent heat flux is conditional upon observed vegetation green-up being predictable by the monthly greenness climatology. Larger errors therefore tend to occur in semi-arid environments where real vegetation rapidly responds to rainfall (Kurkowski et al., 2003). Sensible heat flux, ground heat flux, and soil temperature in these environments are

simulated with higher skill (Hogue, 2003; Hogue et al., 2005) and could be improved with roughness length parameterization schemes outlined in Zheng et al. (2013).

3.0 Methods

3.1 Estimate monthly upwelling longwave radiation

Simulated upwelling longwave radiation (LWup) is used to quantify monthly mean surface heat content for each grid cell. LWup is calculated as a residual of a surface energy budget (Equation 1) using the following terms: Net solar radiation (SWnet), downwelling atmospheric longwave radiation (LWdown), latent heat flux (L), and sensible heat flux (H). Ground heat flux is excluded because of its small influence relative to L and H. It is negligible over a day because in most ecosystems heat is conducted down into the soil and balanced by heat conducted back up to the surface at night (Leuning et al., 2012; Chapin et al., 2011). Data are the annual April means of simulated 24-hr data.

Equation 1. Partial surface energy budget

$$LWup = SWnet + LWdown - L - H$$

Where

LWup is estimated upwelling longwave radiation emitted from the surface

SWnet is the shortwave radiation absorbed by the surface; it is insolation minus the radiation reflected by surface albedo

LWdown is the thermal radiation emitted by the atmosphere and absorbed by the surface

L is latent heat flux via evapotranspiration; it is the transfer of energy from the surface to the atmosphere by water phase change and is distributed by convection and atmospheric turbulence.

H is sensible heat flux; it the transfer of energy from the surface to the atmosphere by conduction and is distributed by convection and atmospheric turbulence

3.2 Identify drivers of anomalous upwelling longwave radiation

We use a two-tier approach to identify sources of LWup variability. Deviations from mean LWup are foremost attributed to variations in directional energy exchange between the atmosphere and surface. In doing so we first identify the major driver i.e. is warming caused by too much energy added or too little energy removed? From there we more closely examine the role of evapotranspiration, sensible heating, and radiative processes. Energy exchanges through all processes are related by complex feedbacks. Our goal is to identify the dominant factor that led to a warmer or cooler surface on average for the month.

Surface energy budget terms from Equation 1 are grouped by direction of energy flow. We use the grouped terms to match LWup anomalies to anomalous amount of incoming energy or anomalous amount of outgoing energy or both. This technique is used to identify the primary cause of surface heating or cooling for each year. We use this information to identify the main driver of LWup variability through 2002-2011 and to identify interesting events during 2002-2011. For these events, we examine fluxes in more detail to identify what happened. The grouping of flux terms is shown in Equation 2. SWnet and LWdown, the energy inputs, are summed for a collective estimate of atmospheric radiative forcing (RF), which is the source of incoming radiative energy. L and H, the main mechanisms for

heat transfer away from the surface, are summed for an estimate of turbulent heat flux forcing (TF).

Equation 2. Incoming and outgoing fluxes for the surface energy budget

$$RF = SWnet + LWdown$$

$$TF = L + H$$

$$LWup = RF - TF$$

Where

RF is radiative flux forcing, the main source of radiative energy input to the surface

TF is turbulent heat forcing, the main source of non-radiative energy transfer away from the surface

LWup, SWnet, LWdown, L, H, are from Equation 1

3.2.1 Regional drivers

We begin by examining the correlation between surface heating and evapotranspiration. Ts/VI methods of ET estimation assume an inverse relationship between these in water-limited vegetated areas. At interannual time scales we might also expect the relationship to be influenced by radiative forcing because net radiation is the source of surface energy. At each grid cell of the domain (5 °N – 5 °S, 33 °E – 43 °E) we calculate the Pearson correlation between April mean LWup and L, and LWup and RF, to identify where

evapotranspiration and/or radiative forcing strongly influence surface heating and cooling based on LWup. While these are simulated data, not observations, and have a short time span, correlation maps are useful for finding the relationship that the Noah land surface model simulates. Strong correlation between latent heat flux and LWup might support the use of Ts/VI methods in particular areas of the region based on modeled physical processes.

A more in-depth analysis of the geographic pattern of April LWup control is conducted for radiative forcing vs. turbulent heat flux forcing. LWup interannual variability is separated into incoming (RF-driven) and outgoing (TF-driven) energy components. In general we would expect turbulent heat flux forcing to have a larger influence than radiative forcing where soil moisture, wind, or atmospheric stability exhibit large annual fluctuations. We use a partitioning of sums of squared errors (variance) approach to identify RF or TF as the primary driver of April mean LWup at each grid cell. Then we use these results in a regression tree analysis to identify geographic characteristics that tend to be associated with areas where surface heating is driven primarily by annual variations in incoming radiation or by annual variations in aerodynamic energy transfer away from the surface (variability in non-radiation driven turbulent heat flux). Variance partitioning and regression tree methods are explained in Sections 3.2.1.1 and 3.2.1.2, respectively.

3.2.1.1. Partition LWup interannual variability

The variance of LWup is partitioned into the components of variability due to radiative forcing and due to turbulent heat flux forcing. The first step of LWup variance decomposition is to calculate the variance of RF, the variance of TF, and the covariance between RF and TF. In total, these terms sum to equal the variance of LWup, as shown in

Equation 3. This is similar to variance decomposition of the sum of two non-independent variables, with the difference being that the covariance term is subtracted. The covariance term is subtracted because LWup = RF-TF. LWup is controlled by the energy that still resides at the surface after accounting for towards-surface (RF) and away-from-surface (TF) energy flux.

Equation 3. Decompose LWup variance

$$Var(LWup) = Var(RF - TF) = var(RF) + var(TF) - 2*cov(RF,TF)$$

The second step of variance decomposition is to separate the right hand side of Equation 3 into a radiative forcing component and a turbulent heat flux forcing component. The fraction of LWup variability ascribed to each component is calculated by dividing each component by the LWup variance, as shown in Equation 4. This gives a fractional variance term for each that ranges from values less than 0 to greater than 1. These terms, $Var(LWup)_{RF}$ and $Var(LWup)_{TF}$ from Equation 4, sum to 1. This is similar to a method commonly used in regression analysis where the ratio of the explained variance to the total variance (R-squared value) is used to identify the fraction of the data that a model explains. Unlike regression analysis the fractional variance terms in Equation 4 are not orthogonal.

Equation 4. Fraction of LWup variance due to radiative forcing and turbulent heat flux forcing

$$Var(LWup)_{RF} = [var(RF) - cov(RF,TF)] / var(LWup)$$

$$Var(LWup)_{TF} = [var(TF) - cov(RF,TF)] / var(LWup)$$

We use the fractional variance term associated with turbulent heat flux forcing to identify

the primary factor for LWup interannual variability. This term, $Var(LWup)_{TF}$ from Equation 4, is here forth referred to as FracVar. FracVar between 0 and 1 gives and indication of how much LWup variability was due to non-radiation driven interannual variability in turbulent heat flux. FracVar near 1 means that essentially 100% of LWup variability is due to non-radiation driven TF variability, which is from aerodynamic factors such as wind, stability, and vapor pressure gradients. FracVar near 0 means that very little is due to TF and nearly all is driven by radiation. FracVar can be greater than 1 or less than 0 because of the impact of the covariance term. Covariance between RF and TF is positive. The covariance can be larger than the variance of TF when radiative forcing has large interannual variability and most of turbulent heat flux variability is due to fluctuations in energy input. In this case FracVar is negative. FracVar > 1 occurs when non-radiation drivers substantially influence TF variability and relatively low RF variability leads to small covariance. For FracVar > 1 and FracVar < 0, larger absolute values indicate stronger control of LWup variability by non-radiation driven turbulent heat flux forcing or radiative forcing, respectively.

3.2.1.2. Regression tree analysis

We use regression tree analysis to examine geographic attributes of TF-driven and RF-driven areas. Regression trees show the hierarchical order of importance of multiple predictor variables by successively splitting predicted data into smaller, more homogenous groups using binary classification rules. Regression tree analysis is a useful technique for multivariate environmental data analysis because relationships among environmental variables tend to be nonlinear and situationally dependent. Functional relationships (e.g. logistic, linear) often do not adhere for all cases. For example, the vegetation pattern of a landscape could be explained in part by aspect, but the relationships would likely vary at

different elevations (from Michaelsen et al., 1994). Unlike traditional regression methods that use a slope term to summarize each predictor-predictant relationship, regression tree analysis identifies the range of predictor values that best explains the variance of the data (usually with analysis of variance, ANOVA). The mean value of the predicted data for this range is reported. The regression tree process starts with the entire dataset, from which subsets are created, and then is iteratively applied to new subsets. The tree grows until new splits do not sufficiently increase explained variance. More extensive explanations of regression tree analysis including methods for predicting multiple variables and rules for selecting optimum trees can be found in Michaelsen et al. 1994 and Breiman et al. 1984.

Our regression tree uses ANOVA to explain the spatial pattern of FracVar with three variables (names in parentheses): Percent of surface cover by green vegetation (GreenVeg), mean daily rainfall (MeanRain), and the Pearson correlation between turbulent heat flux and latent heat flux (Correlation.TF.L). The regression tree analysis was conducted using the R language and environment for statistical computing and the R 'rpart', and 'RandomForest' packages. This combination of variables was identified using exploratory analysis. Models were built using combinations of predictor variables and were compared based upon model cross-validated R-squared value and ability to express hierarchical relationships that were physically meaningful. The selected model explains more than 50% of FracVar variance. Other variables tested were: Soil texture, elevation, surface albedo, correlation between rainfall and latent heat flux, mean latent heat flux, mean upwelling longwave radiation, and standard deviations of rainfall, radiative forcing and latent heat flux. The selected model was manually 'trimmed' to remove splits that had minimal contribution to model skill. The structure of the selected model was deemed stable by comparing it to output from a

RandomForest, which compares 500 trees made from bootstrapped samples of the data. The order of importance of the predictors remained the same and the mean square error reduction attributed to each predictor was similar across models.

GreenVeg is from the climatological greenness fraction surface parameter used by Noah in April (Figure 3b and Table 1). GreenVeg indicates whether latent heating is mainly through plant evapotranspiration or soil evaporation. If GreenVeg = 40, for example, plant evapotranspiration accounts for 40% of latent heating and evaporation from the soil accounts for the remaining 60%. MeanRain is the mean of 2002-2011 April RFE 2.0 data used as model forcing (Figure 3a and Table 1) and is used here to represent regional climate gradients. Correlation.TF.L indicates the extent to which evapotranspiration drives TF variability on an interannual basis. The following explains Correlation.TF.L in more detail. Heat transfer from the surface occurs preferentially through latent heating (evapotranspiration), and when evapotranspiration is limited, energy is either transferred away through sensible heating or used to heat the surface The strength of TF and L correlation depends on how much sensible heating occurs in this situation. Strong TF and L correlation occurs where, during conditions of below average evapotranspiration rate, energy is not quickly removed from the surface through an increase to sensible heating. Since sensible heat flux is not an effective means of surface energy transfer in this situation, turbulent heat flux interannual variability follows evapotranspiration interannual variability. Numerically, the sign and magnitude of evapotranspiration anomalies and total turbulent heat flux anomalies can only be similar if sensible heating remains at its mean rate. Otherwise, the TF anomaly is minimized. Weak or negative TF and L correlation indicates sensible heating is an active component of TF interannual variability. This occurs where

sensible heating is effective at removing energy in the situation explained above, and also where evapotranspiration varies little between years such as in very arid or very wet ecosystems.

3.2.2 Drivers of anomalous events

We identify surface heating and cooling events for each grid cell from annual April LWup anomalies. Each LWup anomaly (LWup') is attributed to one of the following: An anomalous rate of incoming energy, an anomalous rate of surface-to-atmosphere energy transfer, or a mixture of anomalous rates in both. Attribution is based upon the fraction of the LWup anomaly that is caused by turbulent heat flux. This is called ratio-based attribution, and is shown in Equation 5 and described in the paragraph below. Ratio-based attribution works by comparing the magnitude and the sign of upwelling longwave radiation anomalies to the magnitude and sign of turbulent heat flux anomalies and radiative forcing anomalies. Mean LWup, RF, and TF are calculated for 2002-2011 and subtracted from the data to get annual anomalies LWup', RF', and TF'. LWup anomalies are only attributed if they are in the lower or upper 25^{th} percentile of the data. This excludes LWup anomalies smaller in absolute magnitude than 3.6 W m^{-2}. Using a threshold minimizes the influence of erroneous energy budget imbalance from the model simulations, which ranged from 0-3 W m^{-2} using the monthly means. Distributions of the RF, TF and LWup anomalies are shown in Supplementary Figure 1 (Fig. S1). Histograms and quantile-quantile probability plots of 2002-2011 data from all grid cells shows that RF, TF and LWup anomalies are normally distributed.

Equation 5 shows turbulent flux forcing fraction f_{TF} and a radiative forcing fraction $f_{RF.}$

These represent the magnitude of each LWup' that is due to TF' and RF', respectively. The turbulent flux forcing fraction f_{TF} is calculated from the ratio of TF' to LWup'. After accounting for the difference in sign, f_{TF} indicates the extent to which anomalous turbulent flux is responsible for LWup'. TF is considered 100% responsible and the primary driver if TF' magnitude is equal or larger than LWup' and they have opposite sign ($f_{TF} = 1$). An example is when surface heating occurred because TF was below average and also because TF had a larger influence on LWup' than radiative forcing did. Likewise, RF is considered the primary driver ($f_{RF} =1$) when TF' and LWup' are of the same sign, e.g., surface heating occurred despite above average TF. A useful aspect of ratio-based attribution is that it shows when RF and TF have shared influence on LWup', with their respective proportions given by f_{TF} and f_{RF}. To show the location of anomalous heating events and the relative contribution of TF and RF, warm and cool LWup anomalies are each multiplied by f_{TF} and f_{RF}.

Equation 5. Ratio-based attribution

f_{TF} = -1 * TF' / LWup'

f_{TF} = 0 when $f_{TF} < 0$

f_{TF} = 1 when $f_{TF} > 1$

f_{RF} = 1- f_{TF}

Where

f_{TF} *is* the fraction of the surface heat anomaly due to anomalous turbulent heat flux

f_{RF} *is* the fraction of the surface heat anomaly due to anomalous atmospheric

radiative forcing

4.0 Results and Discussion

4.1 Regional controls of April LWup interannual variability

4.1.1 Correlation with radiative forcing and evapotranspiration

Figure 5 shows that for 2002-2011 annual variations of April upwelling longwave radiation are generally negatively associated with latent heat flux and positively associated with radiative forcing. Absolute magnitude of Pearson correlation between LWup and these variables is > 0.5 for many parts of the region. Besides these expected relationships (i.e. the surface warms from more radiation input and less evaporative cooling) the maps show an interesting and distinct spatial pattern of surface heat forcing within the 5 °N – 5 °S, 33 °E – 43 °E domain. Most areas exhibit a stronger LWup relationship with either radiative forcing or latent heat flux.

Areas west of 38° E exhibit a moderate to strong relationship between radiative forcing and LWup ($R > 0.6$) (Fig. 5a). To the east of 38° E in most areas radiative forcing is not a major driver of LWup ($R < 0.25$). LWup is moderately to strongly correlated with latent heat flux ($R < -0.6$) in northern Tanzania, southern Ethiopia and Somalia, and parts of north and east Kenya (Fig. 5b). This indicates evaporative cooling is an important factor for annual variations in surface heating in these areas. Low correlation between LWup and L is in some areas due to more net radiation partitioned to sensible heat fluxes. The degree to which this occurs is related to lower boundary layer conditions and the sensible heat response to these conditions as simulated by the Noah land surface model. In Section 4.1.2 we more closely examine the regional pattern of LWup control and consider the aggregate influence of latent

and sensible heating, turbulent heat flux, for surface to atmosphere energy transfer. In Section 4.2 we discuss drivers of large scale surface heating and cooling in selected years including atmospheric factors influential to energy partitioning.

Annual variations in radiative forcing are primarily due to net shortwave radiation. Because the model was forced with the same surface albedo in every April of 2002-2011, interannual variation in net shortwave radiation is due to variation in cloud cover and cloud–blocking of incoming solar radiation. The standard deviations of radiative forcing (RF = SWnet + LWdown), net shortwave radiation and downwelling longwave radiation are mapped in Figure 6. Comparison of Figure 6a and 6b shows the similarity between SWnet and RF variability for most areas of the region. Downwelling longwave radiation, which varies based on atmospheric temperature and water vapor content, only exhibits substantial interannual variability in climatologically wet areas in the southwest. LWdown and SWnet data are generally negatively correlated across the domain, which is expected because both are driven by water vapor and cloud cover (mean grid cell Pearson R = -0.53).

4.1.2 Regional pattern of LWup forcing and geographic attributes of TF- and RF-driven areas

The fraction of interannual April LWup variability driven by turbulent heat flux forcing (see Section 3.2.1) is mapped in Figure 7. In most areas west of 38 °E turbulent heat flux forcing has little or no measureable influence on April LWup variability. The amount of radiation coming into the surface is the dominant driver of surface heating and cooling. FracVar is < 0.25 in these areas, meaning that more than 75% of 2002-2011 LWup variability was due to radiative forcing. In southwestern areas where rainfall is high and vegetation is dense this is

in part due to consistently high rate of evapotranspiration. Turbulent heat flux has a larger influence on surface heating east of 38 °E and in pockets of northern Tanzania. TF control of LWup variance increases from 25% to 100% in these areas. Anomalous turbulent heat flux created most or all of the variability in LWup in the region from 39 °E to 42.5 °E and 5 °N to 3 °S, as shown by FracVar ≥ 1.

Regional FracVar values were classified with regression tree analysis based on the following geographic attributes: Percent of surface cover by green vegetation (GreenVeg), mean daily rainfall (MeanRain), and the Pearson correlation between turbulent heat flux and latent heat flux (Correlation.TF.L). Figure 8 shows the regression tree. From the top of the tree down, thresholds that best define the regional data are seen at the five classification splits. These splits explain 56% of the total spatial variability. The regression tree results show that the semi-arid and low vegetation density areas of lowland southeastern Kenya and southern Somalia are where a direct negative association between surface heating and non-radiation-driven evaporative cooling occurs, according to the FLDAS simulation. This is further explained in the discussion below.

The regression tree shows that an important criterion for turbulent heat flux control of surface heating is moderate to strong correlation between latent heating and total turbulent heat flux. This is important because it directly links TF-driven LWup variability to evapotranspiration. If L and TF are not positively correlated then evapotranspiration is not the main factor in outgoing energy flux. To see where this applies, thresholds from the 1st and 3rd tree splits are used to map TF and L correlation (Figure 9a). According to the 1st split LWup anomalies are caused by anomalous radiative forcing in 51% of the region where TF and L are weakly or negatively correlated ($R < 0.31$, mean FracVar < 0). As seen from

Figure 9a these are areas in Kenya 35 °E – 38 °E and along Kenya-northern Uganda and Kenya-southern Ethiopia borders. With exception of 1 °S – 4.5 °S and 34 °E – 35 °E evapotranspiration does not influence LWup in the western half of the region. Comparison of Figure 9a (L influence on TF) and Figure 7 (TF influence on LWup) shows evapotranspiration controls LWup through TF mainly in the eastern half of the region. These figures show similar spatial patterns with exception of near Lake Victoria, where evapotranspiration controls TF but TF does not control LWup. Strongest TF control of LWup occurs in the region from central Kenya to southern Somalia where TF and L are strongly correlated ($R > 0.58$, approx. 13% of region). Partial TF control in areas east of 37° E correspond to the border of moderate TF and L correlation ($R > 0.31$).

Regional topography and April vegetation density are shown in Figure 9b. GreenVeg is overlaid on a three-dimensional elevation surface (see Table 1). Dominant regional geographic features are an elevation gradient from west to east, with the mountainous Rift Valley dividing the Lake Victoria region from the eastern lowlands, and a spatial correspondence between elevation and vegetation density. The latter is primarily due to more convective rainfall in higher elevation areas. The regression tree identifies green vegetation density (GreenVeg) and April mean daily rainfall (MeanRain) as secondary explanatory variables for where TF controls LWup. In the 2nd tree split GreenVeg classifies an additional 21% of the domain and shows that TF exerts larger influence in areas with less than 38% green vegetation cover, such as in eastern lowland areas. Radiative forcing dominates LWup variability (mean FracVar < 0) in the Rift Valley and near Lake Victoria where vegetation density > 39%. Below the 3rd split the remaining 15% of domain area is classified based upon MeanRain. This split shows TF exerts primary control on LWup in

semi-arid zones that receive on average between 2.3-3.2 mm day^{-1}, which excludes low vegetation density areas near Lake Turkana.

4.2 Annual attributed surface heat anomalies

Drivers of annual April LWup anomalies were attributed using the method described in Section 2.2.2. Supplement Figure 2 (Fig. S2) shows LWup anomalies and the component of LWup anomalies attributed to turbulent heat flux forcing and radiative forcing for each year. A summary across the region of positive LWup anomalies and sources of annual heating is shown in Figure 10. For each year bar heights represent the percent of the region with LWup in the upper 25^{th} percentile (LWup' > 3.60 W m^{-2}). Bars 1-3 shows the percent attributed to radiative forcing (f <= 0), turbulent flux forcing (f >= 1), and a mix of RF and TF ($0 < f < 1$). Bar 4 shows the sum of these.

According to simulation the largest area (62% of the region) with anomalously high LWup occurred in 2005 (Figures 10 and S2). Other years with spatially extensive abnormal heating were 2003 and 2002, during which 39% and 30% of the region, respectively, had anomalously high LWup 2005 was unique in that a large area of heating was attributed to turbulent heat flux forcing, either as the sole driver (22% of region) or as a partial driver along with radiative forcing (21%). In 2002, 2003, and 2011 over 20% of the region exhibited anomalous heating attributed to radiative forcing. Figure 10 shows a notable difference between 2002-2006 and 2007-2011 in terms of area with warm LWup anomalies. Every year in the first part of the time period exhibits RF and TF-combined heating in 20% of the region or more. The overall low area with surface heating in 2007-2011 is due to several years with widespread cool LWup anomalies (2007, 2008, and 2010) (Fig. S2). In

general we find that heating and surface cooling events are associated with multiple factors and see no evident shift in forcing mechanism between 2002-2006 and 2007-2011. For example, evapotranspiration deficits occurred in multiple years but only led to turbulent heat flux-driven surface heating on a large scale in 2005. Sensible heating balanced moisture flux deficits in most other cases. Abnormal surface heating attributed to radiative forcing was associated with above average downwelling longwave radiation in 2002 and net shortwave radiation in 2003 and 2011. In the following sections we use the ratio-based attribution results, model forcing data, and model-simulated variables to discuss mechanisms that led to surface heating in April 2005 and 2011 and surface cooling in April 2007, 2008, and 2010.

4.2.1 The biggest heating event: 2005

The 2005 event shows that an important factor in the link between evapotranspiration and surface heating is the degree to which atmospheric conditions support effective energy partitioning. In April 2005 LWup was substantially higher than normal in 62% of the region. Below average turbulent heat flux was fully responsible for the abnormal warming in more than 20% of the region and had a partial role in another 25% of the region (Figure 10). Figure 11 shows the locations of anomalous LWup (11a) and the RF (11b) and TF (11c) components of these anomalies (same as in Fig. S2). The TF-driven warming in Kenya southeast of Lake Victoria and east of 38 °E and in southern Somalia and Ethiopia was associated with latent heat flux deficits that were 10-20 W m^{-2} and greater (Fig. 11d). Similar evapotranspiration deficits occurred across northeast Kenya and other areas as well, but deficits in those areas were matched by positive sensible heat flux anomalies (Fig. 11e).

Weak positive or absent sensible heat anomalies in northeastern areas of the region

ultimately led to TF-driven surface warming in April 2005. Atmospheric conditions led to a suppression of sensible heat transfer, which slowed energy removal from the surface and increased upwelling longwave radiation. This situation was unique to 2005, at least when considering the large area of the domain in which it occurred (Figure 10) Data indicate that sensible heating was suppressed by above average air temperature. Sensible heat flux is driven by the temperature gradient between the surface and the air. Across the region, mean air temperature was 0.5 to 2 °C above average in 2005 (Fig. 11f). Figure 6g shows that in some TF-driven heating areas (northeast and southeast of Lake Victoria) the difference between surface and air temperature was small (0-1.5 °C). Areas with air temperature anomalies < 0.5 °C exhibited larger differences (2-3.5 °C). Sensible heat flux is also driven by mechanical mixing of air in the lower boundary layer. We examined wind speed anomalies to see if this also was a factor but forcing data show near average wind speed in April 2005 (not shown). Thus we conclude that a combination of below average evapotranspiration and above average air temperature was responsible for TF-driven heating in April 2005. From our available data we were unable to attribute the cause of anomalous air temperature in 2005, but it would either be from warm air advection into the region or adiabatic warming due to subsidence.

Radiative forcing also contributed to surface warming in 2005. RF was responsible in east Uganda and northwestern Kenya for increasing LWup > 5 W m^{-2} and in some areas > 15 W m^{-2} from the 2002-2011 (Fig. 11b). Heating was mainly due to above average insolation and also downwelling longwave radiation in some areas. April mean net shortwave radiation was 5-20 W m^{-2} above average between 1 °S – 5 °N and 33 °E - 38 °E (Fig. 11h). North of Lake Victoria positive downwelling longwave radiation anomalies (5-15 W m^{-2}) also contributed

to radiative forcing (Fig. 11i). Positive downwelling radiation anomalies are consistent with a warmer than normal atmosphere and the air temperature anomalies seen in this month.

4.2.2 The worst drought: 2011

April 2011 was part of a severe and prolonged drought that affected over 13 million people in the Horn of Africa (Ledwith, 2011). Following a failed cropping season in October-December 2010, the 2011 Long Rains season began late and ended in May with low total seasonal rainfall. Poor crop production, high food prices, and political instability led to a regional crisis that resulted in high food insecurity in Kenya and Ethiopia and famine in Somalia (Funk, 2011; USAID FEWS NET, 2011). Given the importance of the 2010-2011 drought, and that rainfall was 40-160 mm below average in April for much of the region (Fig. 12c), we examine the factors that led to surface heating for more than 20% of this area (Fig. 10). Interestingly, ratio-based attribution shows surface heating was mainly due to radiative forcing (Fig. 12a, 12b), not evapotranspiration as would be expected from the rainfall deficits. Poor rainfall across central Kenya and northeastern areas of the domain reduced latent heat flux by 40 W m^{-2} below the April mean (Fig. 12e). However, according to the simulation energy partitioning was effective in April 2011 and large positive anomalies in sensible heating matched latent heat flux deficits (Fig. 12f). In total, turbulent heat flux was average and did not lead to TF-driven heating (Fig. S2).

Data show that surface heating during the 2011 drought was ultimately due to lack of cloud cover, which led to large (> 30 W m^{-2}) net shortwave radiation anomalies (Fig. 12d). In tropical regions clouds associated with convective rainfall effectively block insolation from reaching the surface (McGregor and Nieuwolt, 1998). Abnormally dry periods coincide with

high intensity solar radiation in some cases. Interannual variability of SWnet data corresponds to annual cloud cover because the land surface model was forced with surface albedo climatology. 2011 LWup anomalies (5-20 W m^{-2}) correspond to positive net shortwave radiation anomalies and 80-160 mm below normal April rain (Fig. 12b, 12c). Clear skies also led to below average downwelling longwave radiation due to a lower nightttime greenhouse effect (not shown). Rain deficits and enhanced incoming shortwave radiation occurred in many areas- in southern Ethiopia, northern Tanzania, and in Kenya's northwest and along the 36th meridian. Why all these areas did not exhibit above average LWup was not examined.

4.2.3. Surface cooling events: 2007, 2008, and 2010

Notable events with below average LWup are April 2007, 2008, and 2010 (S2). Figure 13 shows RBA results for 2007 and 2008 and the main source of cooling, which was below average net shortwave radiation. The radiative forcing component of LWup anomalies was 5-20 W m^{-2} west of 38 °E and parts of Ethiopia and Somalia in 2007 (Fig. 13a). In 2008 smaller magnitude anomalies occurred in similar locations and northern Kenya (Fig. 13c). Most of these radiative forcing anomalies were due to below average net shortwave radiation (Fig. 13b, 13d). An exception is the cool LWup anomaly area southwest of Lake Victoria in 2008. Here, below average downwelling longwave radiation (not shown) counterbalanced the weakly positive (< 10 W m^{-2}) net shortwave radiation anomalies. Downwelling longwave radiation and net shortwave radiation are physically linked through cloud radiative properties- clouds block insolation from the surface and emit thermal radiation towards the surface. In most cases LWdown anomalies were smaller in magnitude than SWnet anomalies.

April 2010 is an example of evaporative cooling of the surface due to above average latent heat flux. In eastern Kenya, southern Somalia, and southwest of Lake Victoria above-average turbulent heat flux lowered LWup 5-15 W m^{-2} below the April mean (Fig. 14b). Latent heat flux was enhanced by 10-40 W m^{-2} in these areas (Fig. 14d) by anomalously wet conditions. April rainfall was 20-160 mm above average (not shown). This event was a factor in results from the interannual variability analysis, which identified LWup variability as being strongly related to evapotranspiration in the region's eastern semi-arid lowlands. Similar to 2007, 2008, and the geographic analysis results, radiative forcing was the driver of 2010 LWup anomalies (-5 to -20 W m^{-2}) in western Kenya, Uganda, and part of southern Ethiopia (Fig. 14a). Cooling in these areas was mainly due to below average net shortwave radiation (Fig. 14c).

4.3. The geographic nature of anomalous surface heating

As noted in the Introduction surface temperature observations are sometimes used to indicate vegetation stress. Differences between ecosystems, such as the degree to which vegetation productivity is limited by energy or water, pose a challenge to making accurate thermally-based estimates of evapotranspiration. The results of this analysis shed some light upon the issue because the East Africa region has large gradients in climate and vegetation. Variance partitioning showed the spatial pattern of LWup control and the regression tree identified geographic factors to explain the pattern. Here, we more clearly visualize how factors controlling LWup change across the region's vegetation gradient. We look to the frequency of energy-driven and turbulent heat flux-driven events across the region's vegetation density gradient to identify energy-limited and water-limited biomes. For each grid cell, the number of anomalous upwelling longwave radiation events that were attributed

(using ratio-based attribution) completely to radiative forcing or non-radiative driven turbulent heat flux forcing is compared to the total number of anomalous events. Results are grouped according to the green vegetation fraction for each grid cell (in 5% vegetation cover increments). Boxplots summarize the distributions for each greenness interval. On the x-axis of Figures 15a and 15b is green vegetation fraction (0 to 1 is 0 to 100% cover). Figure 15a shows the frequency of events driven by radiative forcing. Figure 15b shows the frequency of events driven by non-radiative driven turbulent heat flux forcing. Box width indicates the number of grid cells in each greenness interval.

Several important points can be drawn from the frequency results shown in Figure 15. First, we see that the model shows ecosystem differences that are similar to what observed surface temperature and vegetation indices generally show. In wet and heavily vegetated areas the surface state is primarily driven by variations in energy, while in semi-arid and less vegetated areas water limitations become an important factor. In very arid areas water is too scarce to have a large role on the surface state. Figure 15a shows that surface heating and cooling is mostly energy-driven in places with more than 40% vegetation cover. For more than 50% of grid cells with a green vegetation fraction > 0.40 radiative forcing was the primary cause of anomalous LWup more than half the time. Comparison of Figure 15a and 15b shows that a transition zone occurs between areas with 25% and 40% vegetation cover, where LWup becomes less energy-driven and more aerodynamically-driven with decreased greenness. Figure 15b shows that it is in areas with 10% to 35% vegetation cover that turbulent heat flux control of LWup was most commonly seen. As showed in the regression tree analysis, evapotranspiration is the major driver of turbulent heat flux in low to moderate vegetation density areas. Therefore one is most likely to find surface heating induced by

vegetative drought in areas with 10% to 35% vegetation cover.

Another important point that is shown by Figure 15 is that knowledge of vegetation density in an area is not enough information to correctly identify the cause of every anomalous surface heating or cooling event. Weather introduces multiple meteorological factors that become important in some years and not important in others. The driver of anomalous LWup is more predictable for energy driven-biomes than transition or water-limited zones. The highest medians and upper quartiles, which reach frequencies of 55% to 80%, are for green vegetation fraction > 0.4 (Figure 15a). Even for these energy-driven biomes, anomalous LWup was caused by aerodynamic processes in at least one year of the eleven year period. There are long whiskers in Figure 15 boxplots, particularly for green vegetation cover from 5% to 45%. In these areas greenness is clearly not the only important factor: The frequency of RF-driven and TF-driven events ranges from 0% to 100% of the time. The occurrence of surface heating from vegetative drought is more likely in semi-arid areas than wet areas, but even in water-limited biomes less than 50% of the anomalous LWup events were attributed to anomalous turbulent heat flux.

5.0 Conclusion

5.1 Summary

We examined drivers of surface heating and cooling for a region of East Africa (5 °N – 5°S, 33 °E – 43 °E) using surface energy balance variables simulated by the Noah land surface model v3.2 for 2002-2011. The model was forced with rainfall data used for operational weather monitoring in Africa (RFE 2.0) and GDAS meteorological data. We used upwelling longwave radiation (LWup) estimated from a surface energy budget. Because surface

emissivity does not change between years in the model, interannual variability in upwelling longwave radiation and surface temperature would be similar. April LWup interannual variability and annual anomalies were linked to radiative forcing (RF) and turbulent heat flux forcing (TF), which are the pathways of incoming and outgoing energy. The purpose was to identify if hot surface conditions were due to more radiative energy being added or because surface energy was not being removed through high enough evapotranspiration and sensible heating rates. Results identified geographic patterns and the climate drivers of interesting surface heating and cooling events. Variance partitioning, regression tree analysis, and ratio-based attribution were used for the analysis.

According to variance partitioning and regression tree results, anomalous surface heating and cooling during April 2002-2011 was driven by evapotranspiration only in the semi-arid low elevation areas in the eastern part of the region (38 °E – 43 °E). The regional analysis showed that these are places with substantial latent heat flux variability that receive enough rainfall to support low density vegetation. In these areas soil evaporation is the primary mechanism for surface cooling because green vegetation covers less than 30% of the surface, but transpiration by vegetation is also important. In the greener and wetter mountainous areas interannual variability in surface energy balance variables are more strongly controlled by net incoming radiation. Abnormal surface heating is more commonly occurs from more energy being added to the surface than from moisture limitation to evapotranspiration rate. Regional differences in drivers of upwelling longwave radiation reflect spatial gradients between energy-driven and moisture-driven ecosystems.

Results of the ratio-based attribution showed that surface heating is a consequence of drought in the East Africa region, but important mechanisms vary based on characteristics of

the drought event. Drought events directly impact the surface energy budget by reducing evapotranspiration, but reductions in cloud cover associated with rainfall deficits can have a larger impact on surface heating than evapotranspiration deficits themselves. In many cases with evapotranspiration deficits the model simulated a sensible heating response that prevented LWup from increasing above average. In April 2005 however, the simulation showed surface heating that stemmed from suppression of evapotranspiration by rainfall deficits and suppression of sensible heating by anomalously warm air temperature. During the 2011 drought surface heating in April was attributed to high levels of solar radiation reaching the surface from anomalously clear skies. Cooling occurred from evaporative cooling and below average net shortwave radiation in several years (2007, 2008, and 2010).

5.2 Method evaluation, limitations, and future directions

Surface heat content is influenced by multiple energy fluxes whose covariance depends on atmospheric and land surface conditions. An inherent feature of modeled and observed surface temperature data is complex variability. To deal with these challenges we examined modeled upwelling longwave radiation instead of surface temperature and examined the surface energy budget foremost based on directional energy flux (RF is in, TF is out). This method of breaking anomalous LWup into RF and TF was successful in that it enabled interesting surface heating and cooling events to be identified and the geographic pattern of surface heat control to be established. A downside to this approach is that the influence of evapotranspiration, which many researchers are interested in, is not isolated at the first level of analysis. TF-forcing only leads to higher LWup if evapotranspiration deficits are accompanied by suppressed sensible heat flux. Variance partitioning results were somewhat redundant to the initial LWup-RF and LWup-L correlation analysis. However, the variance

approach helped with quantifying the role that reduced or enhanced rates of aerodynamic energy transfer away from the surface, i.e. non-radiation driven evapotranspiration and sensible heating, have on surface heating and cooling.

There are many important factors involved in surface energy and water budgets that were not examined in this analysis. Differences in vegetation type for example, such as shallow-rooted grasses vs. deep-rooted trees, can play a major role in the surface energy response to hydrometeorological conditions. A major limitation to the analysis is that aspects of the atmospheric-land modeling experiment are unrealistic. Green vegetation fraction, an important parameter for surface energy partitioning, is the same every year in the experiment despite the fact that actual plant cover is dynamic and depends on environmental conditions. Vegetation growth is highly responsive to seasonal rainfall in this region, which causes actual phenology and plant cover to differ between years. Surface albedo is another important parameter that is modeled as constant between years. Surface albedo determines the amount of solar radiation that is absorbed by the surface. Vegetation response to drought or very wet conditions can lead to increased albedo and less absorbed energy or decreased albedo and more absorbed energy, respectively. If albedo is highly variable this may influence results, as radiative energy input is an important driver of surface heating and cooling. This was an uncoupled model experiment, so land responses to hydrologic conditions did not produce feedbacks to the atmospheric state. Overall, it is important to remember that model simplification of the land surface comes at a cost to biological complexity and other important factors in land-atmosphere interactions.

We see potential for the ratio-based attribution method as a means of standardized intercomparison of land surface model experiments. This is because results depend on the

degree to which energy partitioning occurs, which is in turn dependent on the parameterizations used in the land model. Application of the method to multi-model simulations might help clarify the impact of different land model parameterizations for simulated surface heating. Using LWup with ratio-based attribution could be particularly useful for identifying unique events from a long time series dataset. A good candidate event to investigate further is April 2011, during which regional drought led to anomalous sensible heating according to the FLDAS Noah simulation. The spatial extent and intensity of anomalies is indicative of a major positive air temperature feedback by drought. Surface feedbacks to air temperature during 2011 could be examined with a coupled model simulation. In future analysis we would also like to quantify relationships between modeled upwelling longwave radiation and surface temperature and observed land surface temperature from Moderate Resolution Imaging Spectroradiometer Land Surface Temperature (MODIS LST). Comparisons of MODIS LST to data simulated by a set of widely used land surface models could identify common biases between models and also identify regions where biogeophysical processes are well understood.

The purpose of this analysis was to improve our understanding of the mechanisms that lead to increases in surface temperature. This is a timely goal, because changes that are occurring in the global climate system are markedly altering surface hydrology and energetics. While some changes are systematic, such as higher global temperature, geographic differences result in unique regional impacts. For this analysis we hoped to identify certain geographic features and atmospheric conditions that systematically lead to anomalous surface heating events in East Africa during the recent historical period. We developed a method to process energy flux data so that events and the primary driver of events can be identified. We found

that drought in this region can lead to surface heating through enhanced insolation associated with clear skies and through reduced evapotranspiration, and that the latter occurs mainly in areas with 10-35% vegetation cover. Anomalous heating and cooling events most commonly occur in areas with 40-75% vegetation cover due to variations in absorbed solar radiation. These general rules are accompanied by large variability between years and locations. Perhaps the most important finding is the variety of ways anomalous heating can be manifest by weather and hydrologic conditions. In the future, consideration of these factors may help to improve thermally-derived estimates of evapotranspiration.

Acknowledgements

Thanks to Amy McNally for conducting the Noah model simulation. Thanks to Chris Funk, Joel Michaelsen, and Leila Carvalho for guidance. Special thanks to Chris Still for his review.

Chapter 3

Impacts of rainfall declines on vegetation and hydrology in Tanzania between 1982 and 2010

Abstract

Declines in rainfall since the 1980s has been observed in multiple regions of Tanzania. These are associated with the well-documented March to May reductions over the Greater Horn of Africa and with declines during other times of the year. We seek to identify areas where rainfall declines may have impacted natural vegetation productivity, maize productivity, or water resources. Widespread declines to vegetation productivity have been reported based on satellite observations, but links between the vegetation declines and the rainfall declines have not been established.

Using CHIRPS, a new 0.05 degree resolution gridded rainfall product that blends station observations with satellite estimates of precipitation, we examine trends in October to May, October to February, and March to May rainfall for 1982 to 2010. Trends in six other gridded rainfall products and the NASA GIMMS Normalized Difference Vegetation Index (NDVI-3g) dataset are also examined. Trends in evapotranspiration and surface runoff at 0.25 degree resolution are estimated using the Variable Infiltration Capacity (VIC) hydrologic simulation model. Potential impacts to rain fed maize area explored using the USGS GeoSpatial Water requirement Satisfaction (GeoWRSI) model. We find that rainfall declines in central and northern Tanzania can explain observed vegetation declines. We

locate Tanzania's watersheds and agricultural areas that may have been most negatively impacted.

1.0 Introduction

Declines in rainfall in Tanzania in recent decades are in part due to a widespread reduction in March to May rainfall observed over the Greater Horn of Africa. Records show March to May rainfall has been in decline since the 1980s with an abrupt shift towards drought conditions after 1998 (Lyon et al., 2012; Williams and Funk, 2011; Funk et al., 2008). A growing set of evidence indicates that in Tanzania, rainfall also declined during other times of the year. This could have had major impacts to agriculture, natural ecosystem productivity, and regional livelihoods. Maize production is the most important agricultural activity in Tanzania and is a major factor in its economy (Thurlow and Wobst, 2003). Inadequate soil moisture is one of the main challenges to agriculture in semi-arid areas of Tanzania (Mongi et al., 2010; Barron et al., 2003; Gowing et al., 2003).

Multiple studies have documented changes to growing season rainfall in parts of Tanzania, including important maize production areas in the south and central-north regions (e.g. Estes et al., 2010). In the south yields are high due to wet climate. In Arusha and Shinyanga provinces, the declines are more concerning because of semi-arid climate and moderate to low maize yields (Rowhani et al., 2011). Studies have identified a general shift towards lower annual totals (Paavola, 2006), shorter seasons (Mary and Majule, 2009), and more extreme wet and dry events (Omondi et al., 2013). Mongi et al. (2010) and Mary and Majule (2009) showed that the observed changes were congruent with perceptions of local people.

Farmers reported that drought had become a bigger problem in recent decades and that rain fed agriculture had become more difficult because of it.

Declines to the March to May 'Long Rains' are attributed to changes to tropical circulation associated with enhanced sea surface temperature in the equatorial Indian-Pacific Ocean region. Williams and Funk (2011) identified a mechanism through which anthropogenic-driven warming in the Indian Ocean could have contributed to the rainfall declines. Lyon et al. (2012) proposed that the rainfall declines were due to a natural shift in the temperature gradient between the west equatorial Pacific and the central and east Pacific. According to Yang et al. (2014), CMIP5 model projections of East Africa rainfall should be used with caution because they do not simulate sea surface temperature patterns that are important for rainfall in the region. Therefore it is uncertain how the long rains will be in the future.

For Tanzania, a more complete understanding of the spatial patterns of rainfall trends and the implications of these trends for agriculture, natural ecosystem productivity, and regional livelihoods is needed. A challenge thus far has been sparse station data in gridded precipitation datasets (Rowhani et al., 2011). Climatic Research Unit data (CRU, New et al. 2002), for example, only uses rainfall observations from three climate stations for the entire country. Coarse resolution data does not adequately represent Tanzania's geography and complex rainfall regime. Some areas in Tanzania have single rainfall season. Others have two seasons that are influenced by different regional and large-scale climate drivers. Interannual variability in October to December rainfall is influenced by the El Nino-Southern Oscillation (Ogallo 1988; Hastenrath et al., 1993; Nicholson and Kim, 1997; Nicholson and Selato, 2000) and the Indian Ocean Dipole (Saji et al. 1999; Abram et al., 2008). March to May rainfall is linked to convective activity in the tropical Indo-Pacific

Ocean region, but drivers of interannual variability are complex and not well understood (Williams and Funk, 2011 and references therein). In addition to supporting a rapidly growing human population, rainfall in both these seasons is important for the rich diversity of Tanzania's natural ecosystems. Improved climate data could better support planning within the country and identification of at-risk areas.

In this paper we conduct a geographic assessment of historical changes to Tanzania's growing season rainfall and eco-hydrology. Our goal is to identify areas in Tanzania where rainfall declines may have impacted crop yields, natural vegetation productivity, or water resources. We use a new gridded rainfall product that was designed for monitoring drought impacts where surface data is sparse. The Climate Hazards Group InfraRed Precipitation with Stations (CHIRPS) dataset has high spatial resolution (0.05° latitude x 0.05° longitude) and is available at monthly, decadal (10-day), pentad (5-day), and daily time steps. It is based on a high quality climatology grid, infrared satellite observations, and station data from multiple sources (Funk et al., 2014). We use CHIRPS data to examine changes to Tanzania vegetation productivity and surface hydrology between 1982 and 2010. Multiple datasets are available for comparison for this period.

We begin with an introduction to Tanzania's geographic and seasonal patterns of rainfall. Tanzania has three major cropping seasons so we use the CHIRPS data to explain where each of these is located. We also review what some earlier studies reported in terms of rainfall trends and trends in satellite-observed vegetation productivity. We begin the analysis by examining trends in October to May, October to February, and March to May rainfall using CHIRPS. Then we ask if the changes shown in CHIRPS are also shown in other rainfall products. We compare CHIRPS trends to trends in six other gridded rainfall

products. We use an independent record of vegetation productivity, the GIMMS NDVI-3g dataset, to identify if trends in satellite-observed Normalized Difference Vegetation Index could be related to the rainfall declines. Impacts to the water balance are examined using evapotranspiration and surface runoff simulated from the Variable Infiltration Capacity (VIC) hydrologic simulation model (Liang et al. 1994). We use the GeoWRSI model (Senay and Verdin, 2003), which is actively used for monitoring cropping activities in Africa by the Famine Early Warning Systems Network (FEWS NET), to identify if rainfall changes may have intensified or introduced new limitations to maize production related to water stress. Finally, we discuss the level of confidence we have in regard to these vegetation and hydrology impacts.

2.0 Background

2.1 Tanzania rainfall and cropping seasons

A map of Tanzania's administrative zones (provinces) is provided in Figure 1.

Tanzania has a complex rainfall pattern. Annual rainfall ranges from less than 400 mm to greater than 1400 mm (Figure 2). Rain primarily falls between October and May, with a pronounced dry period around February in northern Tanzania. Tanzania's semi-arid region extends southwest from the Tanzania-Kenya border through north-central and central Tanzania, from 2 °S-9 °S and 34 °E-38 °E. Annual rainfall is 300 mm to 600 mm. The lowest rainfall totals occur in the northern part of this region, in Arusha and eastern Manyara provinces, and between Iringa and Dodoma provinces around 7 °S. The semiarid region is punctuated by areas with topography that receive higher amounts of rainfall. Mount

Kilimanjaro (3°4'S, 37°21'E), the highest free-standing mountain in the world (5,895 m elevation), is the most extreme example and is one of the wettest areas in Tanzania.

The east arm of the East African Rift Valley extends from Kenya through Tanzania's semi-arid region around 35 °E to Lake Nyasa at the Tanzania-Malawi border. There it meets the western arm of the East African Rift, which forms the long Lake Tanganyika along the Tanzania-Democratic Republic of the Congo border. A large plateau at approximately 1000 m elevation is between the east and west arms of the Rift. From 35 °E to the west across the central region plateau, rainfall increases from 600 mm to 1000 mm. Areas near Lake Victoria receive more than 1200 mm. East of the Rift is a low coastal plain. Most areas in east and southern Tanzania receive 800 mm to 1200 mm rainfall. Sections of Ruvuma and Iringa provinces near Lake Nyasa in the southwest receive more than 1200 mm.

Tanzania's agroclimatic areas fall into two major categories- those with unimodal rainfall and those with bimodal rainfall. Central and southern Tanzania have a single rainy season are that begins between October and December and ends around May. Planting for the unimodal season starts around November and harvest occurs in May or June. A dry period occurs around February. In northern and eastern Tanzania this dry period is accentuated and separates rainfall into two seasons. Planting for the 'short rains' minor cropping season, known as Vuli, starts in October or November and harvest occurs in late January to February. Planting for the 'long rains' major cropping season, often called Masika, follows the Vuli season in late February to March and harvest occurs in July or August (FAO/WFP, 1998). For most of Tanzania seasonal rainfall tapers off in May or June and is followed by a four to five month dry period. The lean season, when income and supply from the previous

season runs low, lasts from October to January in bimodal areas and from November to March in unimodal areas (FEWS NET).

Figure 3 shows the areas that receive rainfall during October to February and March to May. Greater than 80% annual rainfall occurs between October and May in Tanzania. Areas in central, west, and southern Tanzania receive 60-80% of their annual rainfall between October and February. Annual totals in northern and eastern areas are influenced by rainfall accumulated during the short rains and the long rains. March and April are the wettest months in these areas. The long rains account for more than 50% of annual rainfall in parts of northern provinces Arusha, Kilimanjaro, Manyara and eastern provinces Tanga, Pwani, Morogoro, and Lindi. Short rains have larger accumulations than the long rains in Kagera and Mwanza provinces near Lake Victoria and along transition zones between bimodal and unimodal areas. This variety of seasonal patterns is shown for several places in Figure 4. Bukoba, in the far northwest near Lake Victoria, has much higher rainfall than Arusha, which is in north-central Tanzania. In Arusha the long rains season is prominent. Shinyanga, in central Tanzania, has a dry season from June to September and steady rainfall for most of December to April. Mbeya, in southern Tanzania, has a much wetter unimodal season.

2.2 Previously identified rainfall and NDVI trends in Tanzania

Paavola (2006) examined historical rainfall for Morogoro Province in inland southeast Tanzania. Morogoro is semi-arid to wet with a long rainy season from December to May with the peak in March and April. Annual rainfall was reported to have declined since the 1950s with a potential increase to interannual variability. Paavola shows rainfall between 1922 and 2005 for Morogoro town (6.8 °S, 37.7 °E). The observations come from the

Global Precipitation Dataset, Climatic Research Unit, School of Earth and Environment, University of East Anglia, UK, and the Tanzania Meteorological Agency. The time series shows lower rainfall since the 1980s. A period of stronger decline can be seen after the late 1990s.Mary and Majule (2009) presented convergence between rainfall observations and local perception about changes to growing season rainfall in the Manyoni district of Singida province in semi-arid central Tanzania. Rainfall data were from the Tanzania Meteorological Department. Between 1922 and 2007 the season had shortened in duration due to less rain at the onset (October/November) and at the end (April/May) of the season. More pronounced declines had occurred since 1982. Changes to the distribution also suggested increasing drought frequency within the season. Mary and Majule report that rainfall declines and increased variability have been noticeable enough to trigger an adaptation response by farmers. They plant a number of crop varieties and species on the same land to reduce the risk associated with increased drought (Climate Change Secretariat, 2010; Mary and Majule 2009).

The UNDP Climate Change Country Profile from McSweeney et al. (2010a and 2010b) summarized national trends using gridded rainfall data from the Climatic Research Unit (1961-2000, 0.5° resolution) (New et al. 2002), University of Delaware (1961-2006, 0.5° resolution) (Matsuura and Willmott, 2007), and Global Precipitation Climatology Centre (1960-1979, 2.5° resolution) (Adler et al., 2003). The document reports statistically significant decreases to the national average for annual, June to September, and March to May rainfall. MAM rainfall had the largest decline at 4 mm mo^{-1} (6%) per decade. The annual trend was 2.8 mm mo^{-1} (3.3%) per decade, with largest declines in southern Tanzania. Estes et al. (2010) examined trends in several climate variables from the Princeton

Global Forcing gridded product (Sheffield et al., 2006) for the period 1979 to 2010. They limited analysis in Tanzania to three zones where the data were bias-corrected by global summary of the day (GSOD) station data. They found declines in the ratio of rainfall to potential evapotranspiration in all three. Decreases in rainfall were responsible in the zone near Mara-Arusha-Kilimanjaro provinces and in the zone near Mbeya province in the south.

Omondi et al. (2013) reported significant decreases in annual total precipitation at three locations in Tanzania using daily station data. These were for 1961 to 1991 at Bukoba and Mwanza, which are to the west and south of Lake Victoria, and for 1971 to 2009 at Dar es Salaam along the east coast. For Dodoma in central Tanzania, a linear trend over the 1971 to 2009 period showed significant increases. Time series of Dodoma show that the increasing trend is mainly due to more intense rainfall in the wettest days between the mid-1990s and the mid-2000s. In the 2000s the data show a declining trend in the annual maximum 5-day rainfall accumulation.

Two studies used the NDVI-3g dataset produced by NASA's Global Inventory Modeling and Mapping Studies (GIMMS) group to identify trends in the region. Kim et al. (2013) showed decreasing trends in NDVI for the 1982 to 2006 period and detailed statistical properties of the NDVI trends (e.g. abrupt, long-term, hockey-stick, etc.). Their results show declines in much of Tanzania north of 8 °S and west of 38° E and in smaller areas farther south. In total, 36% of Tanzania showed a declining trend. Most of the trends in the central-northwest were associated with a change point that occurred during the 1990s or the 2000s. Vrieling et al. (2013) used NDVI-3g to calculate trends in the length of growing period from 1981 to 2011. They found significant declining trends that were associated with a later start to the growing season. Julien et al. (2009) analyzed an earlier version of GIMMS (1981-

2003) and also obtained negative length of growing period trends in Tanzania. The cause of the NDVI declines was not examined in these papers.

3.0 Data and Methods

3.1 Climate Hazards Group InfraRed Precipitation with Stations (CHIRPS)

The CHIRPS dataset extends from 1981 to present. It has spatial resolution of 0.05° latitude x 0.05° longitude and is available at monthly, decadal (10-day), pentad (5-day), and daily (for Africa) time steps. The CHIRPS methodology blends in situ observations with unbiased satellite rainfall estimates (Funk et al., 2014). Biases in monthly rainfall estimates from several satellite datasets are removed using a 0.05° resolution global gridded precipitation monthly climatology. The Climate Hazards Precipitation Climatology, CHPclim (Funk et al., 2012), was created using historical station data and geostatistical relationships (e.g. between rainfall and elevation, longitude, and latitude) to model spatial gradients. Station data are blended with the unbiased satellite product, the Climate Hazards InfraRed Precipitation (CHIRP), at pentad and monthly timescales. Blending at each 0.05 degree CHIRP grid cell involves up to five neighboring stations, with higher weights for stations that are closer. CHIRP grid cells that have multiple stations end up with values that are a weighted combination of all sources.

In Tanzania, station data in CHIRPS comes from a variety of sources including the Tanzania Meteorological Agency, NCDC Global Summary of the Day (GSOD), WMO Global Telecommunication System (GTS), and Global Historical Climate Network (GHCN2). A problem that CHIRPS shares with other rainfall products in Africa is a decline in reporting meteorological stations after the late 1980s. Figure 5 shows the high density of station data

that was available in the 1980s in Tanzania compared to the much lower coverage in the 2000s. We are using a more recent version (version 1.9) than the version that is available to the public (version 1.8). CHIRPS version 1.9 is an interim product designed to improve upon data quality issues in version 1.8. A subset of station data from the Tanzania Meteorological Agency was found to be irregular compared to neighboring stations. It was determined that the differences were due to reporting in tenths of inches instead of millimeters and a conversion of 2.54 was applied to these data in version 1.9. A new version of CHIRPS is planned for release in 2015. It will have more historical station data and higher quality control in Tanzania and elsewhere.

3.2 Rainfall trend analyses and inter-product comparison

Rainfall trends are estimated using the Theil-Sen single median method, which is a non-parametric technique of linear regression (Sen 1968; Thiel 1959). The Theil-Sen method gives the median value of the difference between all combinations of data points. Theil-Sen is more accurate than least squares linear regression in the case of outliers and skewed or heteroscedastic data (Siegel 1982). Statistical significance is computed using the Mann-Kendall (Kendall's tau) test for a monotonic trend in a time series, which is based on rank correlation between the time series and a time vector (Mann 1945).

Trends are calculated for 1982 to 2010 using seasonal rainfall accumulations in the eight rainfall datasets listed in Table 1. For CHIRPS, October to May, October to February, and March to May rainfall trends are examined. For all the rainfall datasets we examine October to February and March to May trends. CHIRPS and CHIRP are resampled to 0.25° resolution for the comparison. We compare the products based on the percent change in

rainfall per decade. Between-product differences in the percent change are in part influenced by differences in the product means. The main difference between their seasonal means is that the coarser resolution data (GPCP, CMAP, and NCEP/NCAR R1) do not resolve regional rainfall gradients within the country, such as the dry corridor through northern and central Tanzania.

It should be noted that these rainfall products are not independent since some of the products use data from the same sources. CHIRPS and University of Delaware both use station data from GHCN2. CHIRPS and Princeton both use Global Precipitation Climatology Project (GPCP) and Tropical Rainfall Measuring Mission (TRMM). We include CHIRP trends in the comparison to show if trends in CHIRPS originate from station data or from other sources. The difference between CHIRPS and CHIRP is that CHIRP does not have stations reporting through the data period. Trends in CHIRP come from estimates derived from satellite infrared sensors. Trends in CHIRPS come from estimates that are driven mainly by station reports and where stations do not report, from the combination of interpolated station data and satellite data.

Table 1. Gridded datasets used in the analysis

Dataset	Abbreviation	Resolution	Information and access	Citation
Climate Hazards Group InfraRed Precipitation with Station data	CHIRPS	0.05° latitude x 0.05° longitude	Version 1.9. The most up-to-date publically available CHIRPS (version 1.8) can be downloaded here: ftp://chg-ftpout.geog.ucsb.edu/pub/org/chg/products/CHIRPS-latest	Funk et al., 2014
CHIRPS without station data	CHIRP	0.05° latitude x 0.05° longitude	ftp://chg-ftpout.geog.ucsb.edu/pub/org/chg/products/CHIRP/monthly/	Funk et al., 2014
GPCP Version 2.2 Combined	GPCP	2.5° latitude × 2.5° longitude	http://www.esrl.noaa.gov/psd/data/gridded/data.gpcp.html	Adler et al., 2003

Precipitation Data Set (Final)				
GPCC Global Precipitation Climatology Centre	GPCC	GPCC Global Precipitation Climatology Centre	http://www.esrl.noaa.gov/psd/data/gridded/data.gpcc.html	Schneider et al., 2011
CPC Merged Analysis of Precipitation	CMAP	2.5° latitude × 2.5° longitude	http://www.esrl.noaa.gov/psd/data/gridded/data.cmap.html	Xie and Arkin, 1997
University of Delaware Precipitation	U. Delaware	0.5° latitude x 0.5° longitude	http://www.esrl.noaa.gov/psd/data/gridded/data.UDel_AirT_Precip.html	Matsuura and Will mott, 2007
Global Meteorological Forcing Dataset for Land Surface Modeling	Princeton	0.25° latitude x 0.25° longitude	http://rda.ucar.edu/datasets/ds314.0/ Downloaded from: http://hydrology.princeton.edu/data/pgf/0.25deg/daily/	Sheffield et al., 2006
NCEP/NCAR Reanalysis 1	NCEP/NCAR R1	2.5° latitude × 2.5° longitude	http://www.esrl.noaa.gov/psd/data/gridded/data.ncep.reanalysis.surface.html	Kalnay et al., 1996
GIMMS AVHRR Global NDVI-Third generation	NDVI-3g	0.0833° latitude × 0.0833° longitude	Downloaded February 2013 from NASA ftp site. Current download site: http://ecocast.arc.nasa.gov/data/pub/gimms/3g/	Pinzon and Tucker, 2014

3.3 NDVI trend analysis

Annual mean normalized difference vegetation index (NDVI) is used as a proxy for annual vegetation productivity due to its relationship to photosynthetic activity. NDVI is a ratio of reflectance in the visible and near infrared portions of the electromagnetic spectrum and represents canopy absorption of photosynthetic active radiation (Sellers 1985; Tucker and Sellers, 1986). We use the NDVI-3g product from the NASA Global Inventory Monitoring and Modeling System (GIMMS) group (Pinzon and Tucker, 2014) (Table 1). NDVI-3g (1981-2012) is an extended and improved version of earlier GIMMS NDVI which comes

from NOAA's Advanced Very High Resolution Radiometer (AVHRR) data. NDVI-3g improvements account for issues related to calibration loss, orbital drift, and volcanic eruptions. This dataset was described in Pinzon and Tucker (2014) as having low uncertainty (on the order of ±0.005 in NDVI units) and is therefore suitable for detection of seasonal and inter-annual climate forcings.

Our goal with NDVI-3g is to establish if some of the declines reported in Kim et al. (2013) and Vrieling et al. (2013) in Tanzania could be due to changes in rainfall. Annual mean NDVI was calculated using the bi-monthly NDVI-3g data for the November to October period. Seasonal curves using bi-monthly NDVI data showed that the vegetative season generally begins in November in Tanzania following the arrival of seasonal rains in October. Green-up occurs later in areas with later starts to the rainy season. After June to August, depending on the region, NDVI values gradually declines to a minimum around October. To determine the degree to which annual vegetation productivity from NDVI responds to October to May rainfall accumulations we compute the Pearson correlation coefficient between these values at each grid cell. Maps of these values are used to identify where NDVI-3g may show a vegetation response to rainfall during the 1982 to 2010 period.

We conduct a per-pixel trend analysis on annual mean NDVI. We also examine time series of areal averages of the data for some areas with declining trends. For these analyses we convert annual mean NDVI into standardized anomalies. Standardized anomalies are deviations from the 1982-2010 mean that are divided by the 1982-2010 standard deviations. Using standardized anomalies is helpful for cross-dataset comparisons when the data variables not always linearly related or are unitless. At each grid cell linear regression is

used to estimate the linear change in NDVI between 1982 and 2010. For comparison, the same methodology was applied to October to May rainfall totals from CHIRPSv9.

3.4 Hydrology analysis

We use the Variable Infiltration Capacity (VIC) hydrologic simulation model (Liang et al. 1994) to explore the potential hydrologic impacts of the CHIRPS rainfall trends. The VIC model, which is described in detail in Njissen et al. (1997, 2001a, 2001b), has been used to study climate impacts to large river basins in the US and around the world (e.g. Nijssen et al. 2001c). It is currently used for monitoring water budgets and drought in Africa by the Land Surface Hydrology Group at Princeton University. In our experiment VIC iss forced with a daily version of CHIRPS that is spatially aggregated to 0.25° latitude x 0.25 ° longitude resolution. Other atmospheric forcings for the model come from the Princeton University dataset (Table 1). We examine changes to simulated annual evapotranspiration and surface runoff. Daily data for these variables were summed to the month then averaged over the October to September water year. The VIC model calculates the moisture fluxes for each grid cell independently. Evapotranspiration is from canopy evaporation, evaporation from bare soils, and transpiration (Liang et al, 1994). VIC uses a standalone routing model that is based on a representation of reservoirs and streams (Njissen et al., 2001c). Trends in runoff at each grid cell would occur from changes to local and upstream runoff changes. Trends in runoff do not account for influence of groundwater-surface water interactions on stream flow because this is not modeled in VIC (Trambauer et al., 2013). Evapotranspiration and runoff trends were calculated at each grid cell using the Theil-Sen method and statistical significance was identified using Kendall's tau ($p < 0.05$). The model was initialized on

January 1982. Several years of outputs were omitted from the analysis to account for model spin up. Trends were calculated for the 1984 to 2009 period.

To identify where changes in surface runoff could be important for water resources we overlay a map of the major water basins in Tanzania on the trend results. We created this shapefile by combining two sources. The base map was the USGS HydroSHEDS Drainage Basin (Beta) 30 second version which was downloaded from http://hydrosheds.cr.usgs.gov/dataavail.php. This map has many small scale basins, so we used ArcMap version 10.1 to aggregate them into nine major water basins. These are the major basins according to Tanzania's Ministry of Water. They are described in Table 2. Detailed descriptions of the basins and the map used for aggregation of HydroSHEDS data can be found at http://maji.go.tz/basins/index.php. The shapefile for river outlines came from the USGS Hydro1K dataset and was downloaded at http://www.fao.org/geonetwork/srv/en/metadata.show?id=30934&currTab=simple. The shapefile of major lakes was from the Global Lakes and Wetlands Database (GLWD-Level1) and was downloaded at http://www.wwfus.org/science/data.cfm.

We conduct an additional VIC experiment to test if changes in temperature are contributing to the evapotranspiration and runoff trends. Princeton data show significant increases in annual mean air temperature between 0.1 °C and 0.5 °C per decade in Tanzania (not shown), which could influence evapotranspiration and runoff by increasing evaporative demand. We remove any long term trends that are present in the Princeton temperature data using the method from Hamlet et al., 2005. In the de-trended data the mean of each month is equal to the climatological mean but daily variability remains the same as in the original data. The

VIC model is run again using the de-trended temperature data. Trends are recalculated using evapotranspiration and runoff from this experiment.

Table 2. Tanzania's nine major water basins

Text from http://maji.go.tz/basins/nine.php

ID	Name	Basin description
1	Lake Victoria Basin	A source of the White Nile River
2	Internal Drainage Basin	Internal drainage basins of Lake Eyasi, Manyara and Bubu Complex. Rainfall varies greatly from year to year.
3	Pangani Basin	Major water uses are domestic, irrigation, industries, hydropower, livestock, fisheries, recreation, transportation
4	Wami/Ruvu Basin	Basin consists of wide plains and large mountain ranges and consists of two main river systems, the Wami and the Ruvu, and coastal rivers south of Dar es Salaam
5	Rufiji Basin	The climate in the basin differs from the coast (two rainy seasons) to the highlands in the upper part of the catchment (unimodal rainfall). Land use in the Basin is agriculture, mining, forestry, livestock keeping, fishing, wild life, navigation, and human settlements.
6	Ruvuma River and Southern Coast Basin	Basin is comprised of five major independent rivers that drain into the Indian Ocean. Ruvuma River is shared by Tanzania and Mozambique.
7	Lake Nyasa Basin	Lake Nyasa is shared by Tanzania, Malawi, and Mozambique. The Tanzania side of the basin has a drainage area of 37,000 km^2 (28% of the total drainage area in the lake).
8	Lake Rukwa Basin	Major water uses are domestic water supply for urban centers Mbeya and Sumbawanga and for smaller towns and rural areas. Also for smallholder irrigation. Important source in the dry season despite poor water quality.
9	Lake Tanganyika Basin	The Tanzania side of the basin contributes 60% of the total runoff to Lake Tanganyika. The main river is the Malagarasi. Its main tributaries are Moyowosi River from the north and Igome River from the east.

3.5 Maize water stress analysis

We use the United States Geological Survey (USGS) GeoSpatial Water Requirement Satisfaction Index model (GeoWRSI) (Senay and Verdin, 2003) to place rainfall changes in

context of rainfed maize. We seek to identify the areas where maize yield potential may have declined due to increased levels of water stress. GeoWRSI is a spatially explicit simple bucket water balance model that is used for seasonal monitoring of crop moisture stress and yield in Africa (Tadesse et al., 2008, Verdin and Klaver, 2002, and http://chg.geog.ucsb.edu/products/geowrsi/index.html). GeoWRSI estimates overall crop water satisfaction by tracking moisture deficits through the growing season. It provides an estimate of the yield potential of the crop given how much water was available for growth. End of season WRSI of 100 mean high potential (no stress). WRSI of 50 means crop failure due to high stress. Deficits in soil moisture throughout the season can influence yield potential and WRSI but the largest impacts occur when the crop is water stressed during the reproductive (flowering) stage.

We modeled three seasons with the GeoWRSI model for 1982 to 2010: The unimodal season (October to May), the short rains season (October to February), and the long rains season (March to June). GeoWRSI was forced with a 10-day version of CHIRPS at 0.05° resolution. The other climate forcing variable, potential evapotranspiration, came with the GeoWRSI model. Originally it was calculated from NOAA Global Data Assimilation (GDAS) analysis fields (Derber et al., 1991) using the FAO-56 PM equation from Allen et al., 1998. In our experiment rainfall is the primary factor in annual differences in WRSI because we used 10-day climatological means (2000-2010) for potential evapotranspiration in every year. Spatial variations are from rainfall, soil characteristics, and the length of growing period at each grid cell. For length of growing period we used maps that come with the GeoWRSI installation file. The start of season is calculated using a 3-dekad rainfall-accounting method that was developed at the Agriculture-Hydrology-Meteorology

(AGRHYMET) Regional Center in Niamey, Niger (AGRHYMET, 1996) and is the standard method for GeoWRSI. If there is at least 25 mm rainfall during three consecutive dekads (10-day periods) and at least 20 mm fall during the 2nd and 3rd dekads in this window, the season is determined to have started.

For three regions in Tanzania we visually examine historical changes in mean monthly rainfall and crop water use in each of the four stages of crop growth. Several studies have reported a shift towards drought conditions in East Africa in 1999 (Lyon et al., 2012; Williams and Funk, 2011; Funk et al., 2008). Therefore we break the WRSI time series into two historical periods: Period 1 is 1982 to 1998 and Period 2 is 1999 to 2010. Differences in mean WRSI and mean start of season date for each period are calculated and tested for statistical significance. We used the Welch's t-test (Welch, 1947) to test the hypothesis that the two populations have equal means. Welch's test is similar to Student's t-test but is used when the variance of the two populations differ, which was the case for most of the WRSI time series. We also conduct a linear trend analysis at a per-pixel basis using WRSI for the short rains, long rains, and unimodal seasons.

4.0 Results

4.1 Changes to rainfall according to CHIRPS

Based on the CHIRPSv9 product, rainfall during the October to May season declined throughout much of Tanzania during the 1982-2010 period. Figure 6 shows trends in seasonal-accumulated rainfall in terms of the percent change per decade. For the plots the Theil-Sen slope was multiplied by 10 and divided by the 1982-2010 mean at each grid cell. Significance at the 95th percent confidence level is shown in the plots by stippling. Figure 6a

shows that October to May rainfall totals declined by 6-10% per decade in northern Tanzania in Arusha, Manyara, Kilimanjaro, and Tanga provinces and in southern Tanzania in Morogoro, Iringa, and Ruvuma provinces. Some places in these areas show significant declines of 10-14% per decade. 6-10% per decade declines are also in northwest, central and coastal Tanzania. Trends are significant along the northwest and southwest borders, in Shinyanga province in central Tanzania, and in the areas with 10-14% per decade declines. Smaller declines of 2-6% per decade are seen in most other areas of the country.

Characteristics of changes to the wet season are more clearly shown by the trends in October to February and March to May rainfall (Figure 6). Drying trends are seen in both of these periods. With the exception of the Arusha-Manyara-Kilimanjaro area, changes to October to February rainfall are more substantial. Shinyanga and Singida in central Tanzania and Morogoro and Ruvuma in southern Tanzania have significant declines of 14-18% in the first part of the wet season. In the Arusha-Manyara-Kilimanjaro area it is March to May rainfall trends that are significant. The data indicate that the Vuli, Masika, and unimodal rainy seasons have all experienced declines in rainfall. In some areas the estimated trends amount to seasonal declines of 30% or more through the 1982-2010 period.

4.2 Comparison of CHIRPS with other gridded datasets

4.2.1 Rainfall

Figure 7 shows the percent change in rainfall per decade for October to February for the rainfall products in Table 1. Rainfall declines are shown in light green to red colors. Rainfall increases are shown in blues. For October to February rainfall, CHIRPS, GPCP, GPCC, CMAP, U. Delaware, Princeton, and NCEP/NCAR R1 all show declines. Similar to CHIRPS, GPCC and CMAP show declines over most of the country. There is general

agreement between products that rainfall declined in the southern region. Statistically significant ($p < 0.05$) negative trends are in southern Tanzania in CHIRPS, GPCP, GPCC, CMAP, U. Delaware, and Princeton products. Declines in the northeast and central region are also a common feature but trends are not significant. For the northeast region, CHIRPS, GPCP, CMAP, and NCAR/NCEP R1 show negative trends. CHIRPS, GPCP, CMAP, and U. Delaware show rainfall declines in central region. Near Lake Victoria, GPCC and Princeton have positive trends. CHIRPS and CMAP show declines in this area. CHIRP shows almost no trends except for a negative trend in the south and a positive trend in the central-north.

Figure 8 shows trend results for March to May. CHIRPS March to May declines are less spatially extensive than October to February declines. CHIRPS March to May trends are largest in the northern region around Arusha, Manyara and Tanga provinces. CHIRPS, GPCP, CMAP, and NCEP/NCAR R1 all show significant negative trends in the same area and throughout the northern and central regions. Negative trends in Manyara area and along Tanzania's east coast are in GPCC, Princeton, and U. Delaware products. In western Tanzania, GPCP, CMAP, CHIRP, and NCEP/NCAR R1 show negative trends. Positive trends are in parts of the southern region in Princeton, U. Delaware, GPCC, and CHIRP.

4.2.2 Satellite observations of vegetation productivity

Figure 9 shows the NDVI annual mean and the Pearson correlation coefficient at each pixel for 1982 to 2010 data. The Pearson correlation shows the degree to which vegetation productivity from NDVI responds to October to May rainfall on an interannual basis. Isohyets for mean October to September rainfall (400 mm interval) are overlaid on both these maps. The main area for moderate vegetation productivity ($NDVI \leq 0.5$) is in central

and northern-central Tanzania. This area receives less than 800 mm rainfall annually. Mount Kilimanjaro can be clearly seen along the northern border as the area with 0.7 NDVI encircled by two isohyets. High productivity areas (0.7 NDVI to 0.8 NDVI) are mainly seen in places with greater than 800 mm rainfall. These are along the coast, and in areas near Lake Victoria and western Tanzania, and between the 1200 mm and 1600 mm isohyets in the south. It is common for patterns in mean NDVI to be similar to patterns in rainfall. For NDVI to respond to interannual fluctuations in rainfall or to long term changes in rainfall, the vegetation must be water-limited. Davenport and Nicholson (1993) compared an earlier version of NDVI based on AVHRR to in situ rainfall observations in East Africa for 1982 to 1985. They found NDVI to be sensitive to interannual fluctuations in rainfall in areas with less than approximately 1000 mm per year or 200 mm per month. The correlation map in Figure 9b shows a similar pattern. In much of Tanzania's central and northern areas which have less than 1000 mm annual rainfall, annual mean NDVI and October to February rainfall is moderately positively correlated ($R > 0.4$). Strong correlation ($R = 0.6$-1.0) mainly occurs in areas that receive less than 800 mm rainfall. In these areas it is reasonable to believe that the NDVI-3g product may show declining trends in vegetation productivity that are a response to declining trends in rainfall.

Results from the NDVI and rainfall linear trend analyses are shown in Figure 10. Slope coefficients are multiplied by 10 to show changes in terms of the number of standard deviations per decade. Stippling in Figure 10a shows where NDVI trends were statistically significant (p-value < 0.05). Significance stippling was omitted from Figure 10b. NDVI-3g shows a large area of significant declines in central Tanzania. Significant declines are also seen in areas of western, southern and northern Tanzania in Arusha province. For the most

part, trends in NDVI are spatially coherent. We focus on the widespread declines in the central and northern region. In some of these areas results show decreases in NDVI by 0.4 to 0.8 per decade which equates to a change of 1 to 2 standard deviations over the 1982 to 2010 period. In the same general region, the CHIRPS trends are of similar magnitude. Significant increases to NDVI were found in a large swath between 6 °S and 11 °S and west of Lake Victoria. Based on the correlation results these areas receive high amounts of rainfall and are not strongly water-limited. We do not examine the cause of these NDVI increases.

Three areas of the central region and an area of Arusha province are examined further. These areas are shown by box outlines in Figure 10. Location and extent of these boxes were selected based on declining NDVI and rainfall trends and by NDVI and rainfall climatology. The purpose of the boxes is for examining NDVI and rainfall time series in more detail. They are not meant to be independent samples from the region. Boxes in the central region (from west to east, Shinyanga-Tabora West, Shinyanga-Tabora Central and Singida) differ due to a west to east rainfall gradient. Shinyanga-Tabora West is the wettest area. The box in Arusha province was selected because the NDVI trend indicated substantial changes to vegetation productivity- the trend is large compared to mean NDVI values in that area. For each of these boxes NDVI data and rainfall data was averaged and converted to standardized anomalies. Linear regression was conducted with these values. Figure 11 shows the time series, the rainfall and NDVI correlation, and the estimated rate of change (in standard deviations per year) for each box. Statistical significance of trends is denoted with an asterisk. Pearson correlation between rainfall and NDVI is also shown. Years are labelled by the year the season began. For example, 1997 rainfall and NDVI are for the 1997/98 season which begins in October for rainfall and November for NDVI.

The plots show very similar interannual variability in NDVI (November to October mean) and rainfall (October to May total). Correlation between NDVI and rainfall time series in Shinyanga-Tabora West, Shinyanga-Tabora Central, Singida, and Arusha are 0.65, 0.83, 0.83, and 0.76, respectively (Figure 11). Several features in the extracted time series appear responsible for the declining linear trends. These are a wetter period in the 1980s than the more recent period, a very wet and productive year in 1997 that is presumably due to the strong 1997-1998 El Nino, and multiple years with below average rainfall and NDVI values after 1997.

In Shinyanga-Tabora West (3°S – 6 °S/31 °E – 32.25 °E), all the years with rainfall or NDVI that was higher than one standard deviation above the mean, the wet or productive years, occurred before 1999. The NDVI and rainfall time series both show significant declines of 0.05 standard deviations per year. Interannual correspondence between NDVI and rainfall is clear with exception of 2004 through 2009. In Shinyanga-Tabora Central (3.5 ° S – 5.25 °S / 32.25 °E – 34.25 °E) NDVI and rainfall both show significant declining trends that have similar magnitude. As in west Shinyanga-Tabora, all of the most productive or wet years, based on a one standard deviation threshold, occurred before 1999. Between 1984 and 1990 there was a prolonged period of above average rainfall and NDVI compared to the rest of the time series. This period, a wet 1997, and a dry 2010 appear to explain some of the trend. In Singida (4°S – 6.5 °S / 34.25 °E – 35.25 °E) rainfall and NDVI trends are similar in magnitude but the NDVI trend is not significant at $p < 0.05$. In 1997 rainfall and NDVI were both 2.5 standard deviations above the mean. 1997 was also a wet and productive year in Shinyanga-Tabora area but the year is more outstanding in Singida. Box 3

also shows higher NDVI and rainfall values in the 1980s than in the 1990s and 2000s, with exception of 1997.

The Arusha box (2.25 °S – 3.25 °S / 36.25 °E – 37 °E) shows declining trends for rainfall and NDVI that are similar magnitude to each other but neither trend is statistically significant. The trend magnitudes are a decline of 0.03 standard deviations per year, which is change of less than 1 standard deviation over the 1982 to 2010 period. The most productive or wet years occurred between 1984 and 2000. The highest rainfall and NDVI values occurred in 1997. The two years following this event show low productivity despite near average rainfall. 2008, the driest year in the time series, led to very low productivity. Rainfall and NDVI were 1.5 to 2 standard deviations below the mean in 2008.

4.3 Impacts to surface hydrology

The percent change per decade for rainfall and evapotranspiration and the magnitude of change to surface runoff (in mm mo^{-1} per decade) are shown in Figure 12. These trends were calculated over the 1984 to 2009 period. At an annual time scale the changes to rainfall are most substantial in northeastern Tanzania, from Arusha and Manyara provinces to the coast. Dark red colors indicate changes that are roughly equivalent to a 35 to 45 percent decline over the 1984 to 2009 period. Even larger declines appear over Mt. Kilimanjaro and in Tanga province near the Usambara Mountains. Central areas of Morogoro province also shows up in dark red. Country-wide, annual rainfall trends are similar to those for October to May (Figure 6). Comparison of rainfall and evapotranspiration trends shows that the rainfall declines translated directly into evapotranspiration reductions for much of Tanzania's northeast and eastern areas. Evapotranspiration declines are also seen in central Tanzania. These declines may explain why NDVI-3g shows declines in vegetation productivity in

central Tanzania and the Arusha area. Comparatively smaller impact of rainfall declines on evapotranspiration in the central region indicates a difference in ecohydrology or factors related to other climate variables. However, rainfall appears to be the primary factor in evapotranspiration and runoff trends in Tanzania as there were no major changes to results when the model was forced with de-trended temperature data.

Results show major changes to hydrology in Tanzania's water basins. Surface runoff trends in some of Tanzania's major water basins (see Table 2 for their description) between 1 °S and 6°S and in the southern region are roughly equivalent to a 50% decline in runoff over the 1984 to 2009 period. Decreases in runoff in many areas are significant and large relative to the historical mean. Figure 12 maps the location of per-pixel surface runoff trends in mm mo^{-1} per decade and is overlaid with the major basins and river network. We also aggregate runoff for the basin level and show monthly mean runoff for 1984 to 2009 for several basins (Figure 13). The runoff trends imply a decrease in the total amount of flow through some river networks and less inflow to wetlands and lakes downstream. This would translate into longer dry periods for seasonal water sources and potentially, impacts to lake water levels. The major cause of the runoff trends appears to be rainfall. Evapotranspiration decreased in these areas.

As seen in Figure 12, rainfall on and near Tanzania's central plateau flows through the Lake Victoria Basin, the Internal Drainage Basin of the north-central region, and the Lake Tanganyika Basin. Substantial declines to runoff magnitudes are seen in the southern drainage area of the Lake Victoria Basin. Declining trends are seen in the Internal Drainage Basin watersheds that supply Lake Eyasi and the smaller Lake Manyara. The Lake Tanganyika Basin shows declines that are largest near the headwaters of the Moyowosi

River, a main tributary of the Malagarasi River that flows into Lake Tanganyika. Most of the Malagarasi's tributaries show declines, which may be important for Lake Tanganyika since 60% of its water comes from Tanzania's side of the basin. The impact of rainfall declines in the southern region are seen at the headwaters of the Ruvuma River and near tributaries of the Rufiji River. The largest declining trends in the Rufiji Basin are were not identified as statistically significant. These are near the Kilombero Valley floodplain, one of Africa's largest wetlands and a World Heritage Site (Kangalawe and Liwenga, 2005). Lake Rukwa has a history of large fluctuations in lake levels due to variability in its intermittant streams. Drainage into Lake Rukwa from the east and south side of the basin shows non significant and declining trends. In the northeast, declining runoff is in the Pangani Basin near the coast and also near Mount Kilimanjaro.

Basin-total runoff declined by 13 to 16 percent per decade in Tanzania's Internal Drainage Basin (-21.82 mm mo^{-1}, $p < 0.05$), Ruvuma River and Southern Coast Basin (-10.32 mm mo^{-1}, $p < 0.05$), and Lake Nyasa (Lake Malawi) basin (-4.75 mm mo^{-1}, $p < 0.05$) (Table 3). Lake Tanganyika basin had the largest absolute magnitude trend (-32.24 mm mo^{-1}, $p < 0.1$). Figure 13 shows total basin runoff for these basins.

Table 3. Surface runoff trends for Tanzania water basins

Basin	Trend (Theil-Sen slope in mm mo^{-1} yr^{-1})	Change (per decade) relative to the 1984-2009 mean
1 Lake Victoria	-15.82	-5.9%
2 Internal Drainage Basin	-21.81*	-16.4%
3 Pangani Basin	-8.44	-13.9%

4 Wami/Ruvu Basin	2.01	4.4%
5 Rufiji Basin	-21.39	-9%
6 Ruvuma River and Southern Coast Basin	-10.32*	-13.9%
7 Lake Nyasa Basin	-4.75*	-16.3%
8 Lake Rukwa Basin	-6.7	-4%
9 Lake Tanganyika Basin	-32.24	-9%

* Denotes significance at $p < 0.05$

4.4 Impacts to maize water stress

Here we examine WRSI model output for the short rains season (October to February), long rains season (March to June), and unimodal season (October to May). Primarily we explore the changes to WRSI and the causes of these changes at a regional level. We follow with examination of the per-pixel linear trend analyses. Figure 14 shows 1982 to 2010 mean WRSI in northern Tanzania and central and southern Tanzania. In the northern region WRSI values for the short and long rains were averaged. Regional-level examination is for three regions: two in northern Tanzania and one in central Tanzania. The extent of each region is shown by the yellow-black outlines in Figure 14. Table 4 lists details about the regions. In northern Tanzania, areas west of 34°E are grouped as Region 1 and areas east of 34 °E are grouped as Region 2. The short rains and long rains seasons begin earlier and last longer in Region 1 than in Region 2. Mean WRSI in Figure 14 shows maize yield potential as generally average in Region 1. Region 2 has mainly areas with mediocre to average potential due to water stress. Places in Region 2 with good to very good potential are near the coast and Mount Kilimanjaro. Declining rainfall trends are in all regions but trends in Region 2 are larger than in Region 1. Region 3 is a subset of Tanzania's central-northern area with a

unimodal season where per-pixel trend results show a particularly strong declining trend in WRSI. Maize yield potential is average to mediocre in Region 3. Within Region 3 water stress is a bigger problem in eastern areas.

Figure 15 shows time series of standardized WRSI anomalies for the short and long rains seasons in Region 1 and Region 2 and for the unimodal season in Region 3. Years are labelled by the year the season began. For example, WRSI for the 1997 long rains season corresponds the season that began in March 1997. WRSI for the 1997 short rains and unimodal seasons corresponds to seasons that began around October 1997. Two main features are visible in the time series. First, there was a period of above average maize potential in the 1980s. Second, in Region 2 (March to May season) and Region 3, many of values are below average in the more recent years. These features were also seen in the NDVI time series. We grouped the data into two periods: Period 1 from 1982 to 1998 and Period 2 from 1999 to 2010. We chose the two periods based on the previously documented shift in 1999 towards lower rainfall. In Figure 15 Period 1 is shown as open circles and Period 2 as filled circles. Figure 16 provides a more detailed look at growing season rainfall in Period 1 and Period 2. Mean monthly rainfall during 1982 to 1998 and 1999 to 2010 is shown for each region. For the northern regions the biggest difference in monthly rainfall is in April. April rainfall in Period 1 was wetter by approximately 40 mm. October, November, and February rains were also wetter in Period 1. Region 2, the more water stressed region, shows a decline in May rainfall as well. In Region 3, December through February rainfall and April and May rainfall totals are lower in Period 2 than in Period 1. There are some months with higher rainfall in Period 2. These are March in all three regions, September in Region 1, and November in Region 3. Figure 16 shows only a marginal

difference in October rainfall in Region 3, but on average the growing season start date was 2 dekads later in Period 2. According to the Welsh t-test this difference was not statistically significant. Regions 1 and 2 also did not have significant differences in season onset.

Results vary by region in terms of rainfall impacts on crop water use. Figure 17 shows the amount of water used via evapotranspiration by the crop during its four main growth stages for Period 1 (in gray) for Period 2 (in green). These values are compared to the average amount of water required for no crop stress to occur (in white). The amount required depends on how much water is needed to support biological processes and to satisfy atmospheric evaporative demand. The amount of water evapotranspired is lower than the amount required when plants close stomata to prevent water loss. This slows photosynthesis and plant and grain development. Figure 17 shows, for Region 1, a small decline in evapotranspiration during the maize ripening stage of the short rains season and no differences in other times. The impact of rainfall changes was small compared to the water limitations that maize typically faces during the middle to end of the growing season in this region. WRSI for the short rains and the long rains seasons in Region 1 are very similar in Period 1 and Period 2 (Table 4). For Region 2, small declines are seen during the short rains during the flowering and ripening stages. These did not translate into significant declines to WRSI. Larger declines occurred during the long rains season: On average, maize water stress during flowering increased by about 50% in Region 2 (Figure 17). Soil moisture deficits in late April through June are responsible for the evapotranspiration declines in flowering and ripening stages. The long rains WRSI shows average yield potential in Period 1 and mediocre yield potential in Period 2. The difference in mean WRSI was not significant but the p-value was low ($p=0.07$).

Region 3 is different from Regions 1 and 2 in that it was selected based on the presence of declining trends in WRSI in that area. A larger amount of water is required during the flowering stage here than in Regions 1 and 2 because the entire growing period is 6 months long. Figure 17 shows an approximate 50% decrease in evapotranspiration between Period 1 and Period 2 during flowering In Region 3. The flowering stage is typically between mid-February and mid-April in this region. Depending on how long soil moisture is stored in this area, rainfall declines in January, February, and April could be responsible for the increase in water stress. Changes in rainfall during April and May contributed to evapotranspiration reductions during the ripening stage. WRSI for both periods shows average yield potential although mean WRSI was lower in Period 2 than in Period 1. The difference was not significant but the p-value was low (p=0.06).

Table 4. Regions analyzed with GeoWRSI

Region	Season	Start of season (1982-2010 mean)	Length of growing period	Mean WRSI (1982-1998)	Mean WRSI (1999-2010)	Welsh Two Sample t-test p value
1	October-February	October 11th	120 days	86.8	85.7	0.67
1	March-June	March 1st	140 days	75.2	75.7	0.81
2	October-February	October 11th	100 days	65.1	62.7	0.65
2	March-June	March 11th	110 days	81.9	76.6	0.07
3	October-May	October 11th	180 days	85.3	80.2	0.06

Results from the per-pixel linear regression trend analysis on WRSI for the short rains, the long rains, and the unimodal season are shown in Figure 18. From these maps one can pinpoint the areas in Regions 1, 2, and 3 where changes to WRSI are concentrated. The

slope of the trend is shown in terms of the percent decline in WRSI over the entire 1982-2010 period. Empty pixels show where there were too many years with no start to the season to conduct the analysis. The companion figure to each trend plot shows the R-squared value of the linear trend. Declines in short rains WRSI are in Kagera province and in northern Tanga province in the West Usambaras Lushoto Mountain Reserve. The long rains season has declines of 20% or more in the Arusha-Manyara-Kilimanjaro-Tanga area. Trends in these areas explain 11% to 30% of the historical variability. In northern Kanga and Arusha provinces there are increasing trends also with R-squared values between 0.11 and 0.30. For the unimodal season the declining trends are concentrated in the Shinyanga-Tabora-Manyara-Singida-Dodoma area. The linear trends show declines of 20% in the Lake Eyasi area. Trends explain 20% to 40% of the historical variability there.

5.0 Discussion

Comparison of 1982 to 2010 trends in the CHIRPS product to other rainfall products showed that trend magnitudes for seasonal rainfall totals are relatively consistent across datasets and are consistent with the findings of previous studies. Rainfall declines in Tanzania during October to February and March to May of 1982-2010 were a common feature of all the products compared. Rainfall during each of these periods is important locally for the annual total and the short rains, long rains, and unimodal cropping seasons. Multiple products showed negative trends for March to May rainfall in areas of central and northern Tanzania. Multiple products showed statistically significant negative trends in October to February rainfall in southern Tanzania. October to February and March to May rainfall declines are on the order of 5% to 20% per decade. It should be noted that some of

the products compared are not independent because they use the same station data sources. Also, there were differences in the spatial extent of trends.

Results using CHIRPS and the GeoWRSI model showed that reductions in rainfall during critical growth stages could have led to increased water stress for maize in rainfed areas of central Tanzania and in northeast Tanzania during the long rains season. At a regional average the differences were not significant. However, the per-pixel trend maps showed that changes to maize yield potential were substantial in areas of Shinyanga, Arusha, Singida, Dodoma, Manyara, and in neighboring provinces. These are areas that receive 300mm to 700 mm annual rainfall. Shinyanga and Arusha are important contributors to national maize production (Rowhani et al., 2011), so yield declines in these areas could impact domestic food supply and the economy. No major changes to water stress were identified in high production areas of the southern region. Long term records for regional and local level yields would be helpful for identifying signs of increased crop water stress in the central and north-central region. Farmer access to agricultural inputs, pests and disease, and climate extremes are some of the many factors that influence yields. In terms of delayed onset of the growing season, which was reported in Mary and Majule (2009) in Singida province and by Vrieling et al. (2013) for larger areas, we found that the average date of onset was later in the more recent period in central and northeast Tanzania (long rains). We also examined per-pixel trends in the onset date (not shown) and found delays of one to two months in Singida and Manyara. However, no changes in the onset date were statistically significant.

Our purpose in analyzing evapotranspiration and runoff trends from CHIRPS and the VIC model was to identify where hydrologic impacts would have been most apparent. Validation is important for confirming authenticity of these trends. Hydrologic simulation models in

general do not represent all the processes that are important in the terrestrial water budget in semi-arid areas (Trambauer et al., 2013). This would include parts of central and northern Tanzania. The VIC model is useful in that channel networks are represented in the model, but runoff simulated by the model has not been validated in these basins. Most validations of VIC output are in the mountainous western United States or at much larger spatial scales than are used here. Finally, the meteorological data used to run hydrologic models can be a major source of error. For CHIRPS, poor quality station data could potentially create erroneous trends.

We are confident in saying that based on the data analyzed here, rainfall declines reduced vegetation productity between 1982 and 2010. VIC evapotranspiration and NDVI-3g both show statistically significant declines in the central region, e.g. Shinyanga, Tabora and Singida, in the northern region, e.g. Arusha, Tanga, and near Mount Kilimanjaro, in the southern region in Ruvuma, and along some sections of the east coast. Interannual variations in rainfall and NDVI were found to be similar in these areas. A closer look at Arusha area and the central region time series showed that rainfall and NDVI trends were mainly driven by a wet and productive period in the 1980s and generally below average conditions after the 1997-98 El Nino event.

Substantial declines to surface runoff were estimated using the VIC model. Given the magnitude of trends and importance of water resources in Tanzania the surface runoff trends deserve to be examined more fully. Observed stream flow records, accounts from experts in the region, or some other form of validation are needed to confirm these trends. Along some river networks we identified trends of 20% per decade. Declines to rainfall over the central region plateau impacted drainage into the Lake Victoria Basin, the Internal Drainage Basin

of the north-central region, and the Lake Tanganyika Basin. Rainfall declines over the southern highlands impacted drainage into the two major rivers, the Ruvuma River and the Rufiji River. Rainfall declines also impacted the Kilombero Valley floodplain, an important resource for wildlife and tourism. Overall, total runoff declined by 9 to 16% per decade in several Tanzania watersheds (Lake Tanganyika, Lake Nyasa, Ruvuma River and Southern Coast, and the Internal Drainage basin). Drainage in these basins provides 50-60% of total inflow into Lake Tanganyika and Lake Nyasa (Lake Malawi). It also supports biologically-rich wilderness areas, hydroelectric power stations, and provides drinking water for communities. Rapid growth of human population, expansion of cropland and increase in livestock population pose a major threat to the sustainability of water resources in the Eastern Rift Valley Lakes zone (Yanda and Madulu, 2005), and declines in the inflow of water would exacerbate these issues.

The CHIRPS dataset uses rainfall observations from more than 25 stations in Tanzania, and is based on a fine resolution (0.05°) climatology grid. We have concerns about the lower number of reporting stations after the 1980s and about the quality of some of the stations used in CHIRPS. We did not examine how these influence trends in the data. The next version of CHIRPS (anticipated release: 2015) will have more station data in this region and will be useful for future comparison. In spite of these concerns, CHIRPS was found to be a very useful product for geographic assessment of impacts. The variety of temporal resolutions was useful for running a hydrologic simulation model and a crop model. Its high resolution provides much in the way of spatial detail about the rainfall trends. Based on agreement with NDVI-3g in Arusha area and in the central region, regional details from CHIRPS seem authentic there. CHIRPS trends in the southern region (Mbeya, Irigina, south

Morogoro) could not be corroborated with NDVI-3g because vegetation is not water-limited enough for the NDVI signal to reflect water stress.

6.0 Conclusion

We conducted a geographic assessment of the impacts that changes to rainfall between 1982 and 2010 may have had in Tanzania. Rainfall trends we examined have been well-documented in previous studies, but until now, trend assessments have been at local scales or with coarse resolution. Our goal was to identify areas where the rainfall declines may have impacted natural vegetation productivity, maize productivity, and water resources. For this a high resolution gridded precipitation dataset was needed. We used CHIRPS, a new gridded rainfall product that has high spatial resolution blends station observations with satellite estimates of precipitation (Funk et al., 2014).

October to February and March to May trends show rainfall declines between 5% and 20% per decade. Trends of similar magnitude were seen in multiple rainfall products. We were able to show with CHIRPS data that negative trends in GIMMS NDVI-3g vegetation index can be directly attributed to declines in October to May rainfall. These are primarily in the central region and in the northeast region near Arusha. We used CHIRPS to run experiments with the Variable Infiltration Capacity (VIC) hydrologic model and the USGS GeoSpatial Water Requirement Satisfaction Index (GeoWRSI) model. Evapotranspiration trends from VIC closely mimic the spatial pattern and intensity of CHIRPS annual rainfall declines. GeoWRSI results showed that the abrupt decline in March to May rainfall after 1999 increased the possibility of water stress during yield-sensitive stages in central and northeast maize production areas. Based on the findings of other studies we tested if the data showed a

later start to the growing season in central Tanzania. After 1999, the growing season did start later on average but the difference was not statistically significant.

Declines in October to May rainfall have important implications for water resources. Three major drainage basins showed significant declines in annual runoff due to rainfall declines during October to May in the central region. These basins feed Lake Victoria, Lake Tanganyika, Lake Nyasa, and seasonal lakes in the semi-arid northern Tanzania. Since rapid population growth is already increasing competition for water in this region, continuation of the declines could have major consequences. In southern Tanzania near Mbeya, Irigina, and southern Morogoro, declines to annual rainfall are also from reductions in October to February and March to May rainfall. Impacts to rainfed maize were not identified here, presumably because rainfall is still quite high. We did find declines to evapotranspiration and to surface runoff that feeds the Ruvuma River, the Rufiji River, and the Kilombero Valley floodplain, an important resource for wildlife and tourism.

Based on the general agreement between CHIRPS trends, previously documented localized rainfall trends, and trends in other gridded rainfall products, it is clear that Tanzania has experienced substantial changes to rainfall in recent decades. We have identified spatial and temporal details about these trends and impacts to vegetation and hydrology. We hope that future studies will provide evidence for confirming or negating the modeled trends. In central and northern Tanzania, observed vegetation declines indicate that rainfall declines substantially altered the natural landscape. Attention should be given to understand how livelihoods in the region may have been affected.

Acknowledgements

Thank you to the UC Santa Barbara Climate Hazards Group for their contributions. Shraddahanand Shukla ran the VIC model and made the trend plots for the rainfall inter-product comparison. Diego Pedreros ran the GeoWRSI model. Pete Peterson made the CHIRPS station data figure. Chris Funk, Pete Peterson, and Marty Landsfeld provided CHIRPS version1.9.

Conclusion

Energy and water cycles are sensitive to changes in weather and climate. Factors that influence evapotranspiration are particularly important because this process involves a large exchange of energy between water and the environment, which connects energy and water budgets, and because it is a strong determinant of vegetation productivity. We explored some of these factors in this dissertation research. In Chapter 1 we showed how increased rate of evaporation at higher air temperature influences how much water is available for plants. In Chapter 2, we showed how annual climate variability and energy exchange processes affect surface temperature. In Chapter 3 we showed the widespread impacts that regional-scale rainfall changes can have on evapotranspiration, vegetation productivity, and hydrology.

In our study areas, the African Sahel and east Africa, moisture and radiation are particularly important to the surface energy budget. Insolation and downwelling longwave radiation provide the radiative energy required for evaporation and surface heating. What happens to energy and water at the surface depends on heat and moisture gradients and on the stability and amount of mechanical mixing in the boundary layer. These factors are naturally connected as part of the climate system, so changes to one produce a reaction in multiple others. This connection makes analysis of the energy and water budgets a non-trivial venture. To deal with complexity we grouped fluxes by their mechanistic type, for example, into radiative and non-radiative processes in Chapters 1 and 2. In these chapters we evaluated the influence of these processes as a whole. In Chapter 2 we used this strategy to identify specific fluxes that had importance impacts on the overall energy budget.

A recurrent theme of results was that mechanisms of energy exchange fluctuate in different weather conditions and across ecosystems. In the Sahel we found that evaporative demand is higher on days with above average temperature because of a larger vapor pressure gradient, but that net radiation also plays a role during the wettest time of the season. We speculated this was because cloud cover would be an important factor for cooling air temperature during this time. To explore how surface energy balance and surface temperature is influenced by interannual variations in radiation and evapotranspiration, we focused on the area in and around Kenya. This region in east Africa has high heterogeneity in terms of climate types and experienced several major drought events since 2001. We found that insolation is the primary driver of surface heat anomalies during April, the rainiest month of the long rains season. In semi-arid areas heat and moisture gradients and turbulence are also important. The importance of rainfall for surface energy and water budgets was most clearly shown in the analysis of post-1982 rainfall declines in Tanzania. The magnitude and timing of rainfall reductions are important to ecohydrology in many places, but the most visible impacts have been in semi-arid areas.

Pronounced sensitivity of semi-arid and marginal productivity areas to variations in weather and climate was shown throughout the dissertation research. Warming temperatures may increase evaporative demand by 10 mm mo^{-1} $°C^{-1}$ throughout the Sahel, but impacts to agriculture would most likely occur in the more marginal productivity areas where low and erratic rainfall is already a challenge. Vegetation in semi-arid central and north central Tanzania responded negatively to less convective activity over east Africa in recent decades, according to a satellite-observed vegetation index record. In the semi-arid areas in Kenya, Somalia, and Ethiopia, we identified several cases of widespread moisture stress and above

average surface temperature, which can be damaging to vegetation, between 2001 and 2011. In the 2005 drought, anomalous heating was linked to below average evapotranspiration and in the 2011 drought, it was linked to above average insolation.

The geographic pattern of high sensitivity in semi-arid areas has important implications for efforts to increase resilience to climate change in Africa. There is much uncertainty as to how climate change will impact rainfall in the Sahel and east Africa. Rainfall in both these regions is influenced by sea surface temperature gradients in the Pacific, Indian, and Atlantic Oceans that interact with weather systems on the continent. In east Africa, climate models have trouble simulating historical observed variability, and in the Sahel, it is uncertain how future atmospheric aerosol concentrations will influence the Inter Tropical Convergence Zone. Fortunately this uncertainty is not as limiting to planning as it would seem. As shown in this research, negative effects of higher temperature and more frequent drought would be seen first in the marginal growing areas of Africa. Climate change will disproportionally affect communities where weather and climate variability have historically impacted vegetation productivity and water resources. It is important that planners focus on these communities because climate change has or will make it more difficult for them to sustain their livelihoods. These communities may also offer strategies for dealing with extreme climate. A wide variety of adaptation strategies will be necessary to help people deal with climate-related challenges.

We close the dissertation with a discussion about the merits and disadvantages of three models we used and ideas for research in the future. We used a simple crop water balance accounting model (GeoWRSI) and two complex models that simulate energy and water fluxes between the atmosphere and land surface (Noah and VIC). The land surface models

were run in uncoupled mode, i.e. the land surface state did not produce feedbacks to the atmosphere.

In terms of ease of interpretation, the GeoWRSI model was the best. It does not account for many important biogeophysical factors for plant growth and productivity, but the model is simple enough that modeled impacts to plant stress can be easily traced back to stress during particular growth stages and/or changes to the onset of seasonal rainfall. This is useful model feature for identifying basic ways in which historical and future changes to rainfall or evaporative demand will influence the plant water supply. In terms of annual variations in vegetation phenology, the GeoWRSI model was more realistic than our land surface model simulations. It uses accumulated rainfall to model when vegetation begins growing each season. The land surface model simulations used a prescribed phenology.

Based on our experience with the model, we have several suggestions for future GeoWRSI work. Foremost, validation of GeoWRSI output with historical yield observations would increase confidence in model results. The GIMMS NDVI-3g product (1981-2011) might be helpful in water-limited areas if yield data are not available. In Chapter 3 we found convergence between this product, CHIRPS rainfall, and maize WRSI trends in some areas of Tanzania. Second, GeoWRSI has an option for modeling rangeland productivity, which could be useful in the semi-arid areas of Africa, but there has been no research published using GeoWRSI rangeland output. This indicates that the model needs more attention before its use. Comparison to other rangeland models would be a good place to begin. Calibrating the model to observed productivity might help. NDVI-3g could be a good resource for this because African rangelands are mainly in semi-arid areas. Third, multiple mechanisms of crop response to projected rainfall and temperature changes could be modeled if crop

phenology was temperature-dependent in GeoWRSI (when appropriate). Efforts to amend the model could be worthwhile if there is sufficient knowledge about the phenology of maize varieties grown in a region and if the model were run at higher temporal frequency with daily or 5-day data, for example.

Land surface models (LSMs) are useful for studying climate impacts to regional energy and water budgets. There are very few in situ observations for surface energy fluxes available in Africa. Flux towers are only in a handful of places and tend to have short observation periods. LSMs have benefits and drawbacks. A major benefit of LSM data is that the energy budget terms are simulated based on basic physical mechanisms of energy exchange. Variability is a response to the forcing data and to other terms, so one can get a complete picture of what happened on the ground during droughts and for time periods as long as forcing data are available. For instance, we used the VIC hydrologic simulation model to analyze evapotranspiration and surface runoff during the last three decades. The downside to using LSM-simulated data is that the picture you get may not be accurate. Uncertainties in LSM data come from the forcing data and the parameterizations that model use to simplify complex processes involved in land-atmosphere interactions. In the future we would like to experiment more with climate models and land surface models to determine how closely they represent observed vegetation-climate relationships. One of the less realistic aspects of our simulated data was that the modeled seasonal cycle of vegetation cover did not change from year to year. In semi-arid areas vegetation green up and cover largely depends on rainfall. It may be worthwhile to create a more realistic gridded record of vegetation phenology to use in historical simulations and to explore assimilation of remotely sensed data for forecast simulations with LSMs.

As one question is answered, many new ones are born in its place. Managing and conducting research is therefore a challenging and rewarding experience. In this dissertation we examined impacts of climate variability on energy and water budgets and vegetation productivity in several regions of Africa. In the future we will work toward a more in depth understanding of these topics. Some potential research ideas were discussed above. More generally, the goal is to advance our understanding of how society interacts with the natural world. A major unknown is how future climate change will interact with continued human population growth and unsustainable use of natural resources. At the foundation of Geography is the importance of place- that places are unique and yet their physical qualities are connected to a larger system. This makes it a useful tool for exploring these problems. We look forward to using and expanding on the knowledge we gained to help find solutions for the future.

References

Abram, N. J., Gagan, M. K., Cole, J. E., Hantoro, W. S., & Mudelsee, M. (2008). Recent intensification of tropical climate variability in the Indian Ocean. Nature Geoscience, 1(12), 849-853.

Adeboye, O.B., Osunbitan, J.A., Adekalu, K.O., Okunade, D.A. (2009) Evaluation of FAO-56 Penman-Monteith and temperature based models in estimating reference evapotranspiration using complete and limited data, application to Nigeria. Agricultural Engineering International: CIGR Journal.

Adger, W.N., Huq, S., Brown, K., Conway, D., Hulme, M. (2003) Adaptation to climate change in the developing world. Progress in Development Studies 3, 179-195.

Adler, R.F., G.J. Huffman, A. Chang, R. Ferraro, P. Xie, J. Janowiak, B. Rudolf, U. Schneider, S. Curtis, D. Bolvin, A. Gruber, J. Susskind, and P. Arkin (2003). The Version 2 Global Precipitation Climatology Project (GPCP) Monthly Precipitation Analysis (1979-Present). J. Hydrometeorology, 4,1147-1167.

AGRHYMET. (1996). Methodologie de suivi des zones a risque. AGRHYMET FLASH, Bulletin de Suivi de la Campagne Agricole au Sahel, Centre Regional AGRHYMET, B.P. 11011, Niamey, Niger, Vol. 2, No. 0/96, 2 pages.

Al-Khatib, K., & Paulsen, G. M. (1999). High-temperature effects on photosynthetic processes in temperate and tropical cereals. Crop Science, 39(1), 119-125.

Allen, R.G., Pereira, L.S., Raes, D., Smith, M. (1998) Crop evapotranspiration-Guidelines for computing crop water requirements-FAO Irrigation and drainage paper 56. FAO, Rome 300, 6541.

Anderson, W. B., Zaitchik, B. F., Hain, C. R., Anderson, M. C., Yilmaz, M. T., Mecikalski, J., & Schultz, L. (2012). Towards an integrated soil moisture drought monitor for East Africa. Hydrology & Earth System Sciences Discussions, 9(4).

Arnell, N.W. (1999) The effect of climate change on hydrological regimes in Europe: a continental perspective. Global Environmental Change 9, 5-23.

Baldocchi, D. (2008). TURNER REVIEW No. 15.'Breathing'of the terrestrial biosphere: lessons learned from a global network of carbon dioxide flux measurement systems. Australian Journal of Botany, 56(1), 1-26.

Barron, J., Rockstrom, J., Gichuki, F., Hatibu, N. (2003). “Dry spell analysis and maize yields for two semi-arid locations in East Africa”, Agric.Meteorol., 117: p. 23 - 37.

Bates, B., Kundzewicz, Z.W., Wu, S., Palutikof, J. (2008) Climate change and water. Intergovernmental Panel on Climate Change (IPCC).

Batterbury, S., Warren, A. (2001) The African Sahel 25 years after the great drought: assessing progress and moving towards new agendas and approaches. Global Environmental Change 11, 1-8.

Biasutti, M., Held, I.M., Sobel, A.H., Giannini, A. (2008) SST forcings and Sahel rainfall variability in simulations of the twentieth and twenty-first centuries. Journal of Climate 21, 3471-3486.

Boer, G. J. (1993). Climate change and the regulation of the surface moisture and energy budgets. Climate Dynamics, 8(5), 225-239.

Bonan, G. B., 2008. Ecological climatology: concepts and applications, 2nd ed., Cambridge University Press, 568 pp. (ISBN:9780521693196)
Boschetti, M., Nutini, F., Brivio, P.A., Bartholomé, E., Stroppiana, D., Hoscilo, A. (2013) Identification of environmental anomaly hot spots in West Africa from time series of NDVI and rainfall. ISPRS Journal of Photogrammetry and Remote Sensing 78, 26-40.

Breman, H., Groot, J.J.R., van Keulen, H. (2001) Resource limitations in Sahelian agriculture. Global Environmental Change 11, 59-68.

Brown, M. E., & Chourlarton, R. (2008). Famine early warning systems and remote sensing data. Berlin/Heidelberg: Springer.

Brown, M. E., & Funk, C. C. (2008). Food security under climate change.

Bureau, P.R., (2010) 2010 World Population Data Sheet. Population Reference Bureau, Washington, D.C.

Burke, M., Dykema, J., Lobell, D., Miguel, E., Satyanath, S., (2011) Incorporating climate uncertainty into estimates of climate change impacts, with applications to US and African agriculture. National Bureau of Economic Research.

Burton, I., van Aalst, M. (2004) Look before you leap: a risk management approach for incorporating climate change adaptation into World Bank operations. World Bank Envirnoment Department.

California Irrigation Management Information System, (2009) PM equation, http://wwwcimis.water.ca.gov/cimis/infoEtoPmEquation.jsp, May 8 2013.

Chang, F. C., & Wallace, J. M. (1987). Meteorological conditions during heat waves and droughts in the United States Great Plains. Monthly Weather Review, 115(7), 1253-1269.

Chapin III, F. S., Chapin, M. C., Matson, P. A., & Vitousek, P. (2011). Principles of

terrestrial ecosystem ecology. Springer. pp 93-122.

Chen, F., Mitchell, K., Schaake, J., Xue, Y., Pan, H.L., Koren, V., Duan, Q.Y., Ek, M., Betts, A. (1996) Modeling of land surface evaporation by four schemes and comparison with FIFE observations. Journal of Geophysical Research: Atmospheres (1984-2012) 101, 7251-7268.

Chen, F., & Dudhia, J. (2001). Coupling an advanced land surface-hydrology model with the Penn State-NCAR MM5 modeling system. Part I: Model implementation and sensitivity. Monthly Weather Review, 129(4), 569-585.

Chen, Y., Yang, K., Zhou, D., Qin, J., Guo, X. (2010) Improving the Noah Land Surface Model in Arid Regions with an Appropriate Parameterization of the Thermal Roughness Length. Journal of Hydrometeorology 11, 995-1006.

Choudhury, B. J. (1991). Multispectral satellite data in the context of land surface heat balance. Reviews of Geophysics, 29(2), 217-236.

Chowdhury, S. I., & Wardlaw, I. F. (1978). The effect of temperature on kernel development in cereals. Crop and Pasture Science, 29(2), 205-223.

Clarke, L., Edmonds, J., Jacoby, H., Pitcher, H., Reilly, J., Richels, R., (2007) Scenarios of Greenhouse Gas Emissions and Atmospheric Concentrations, Sub-report 2.1A of Synthesis and Assessment Product 2.1 by the U.S. Climate Change Science Program and the Subcommittee on Global Change Research. Department of Energy, Office of Biological & Environmental Research, Washington, D.C.

Climate Change Secretariat. (2010). *Climate Change: Impacts, Vulnerabilities and Adaptation In Developing Countries*. Retrieved from CAKE: http://www.cakex.org/virtual-library/579

Csiszar, I., Gutman, G. (1999) Mapping global land surface albedo from NOAA AVHRR. Journal of Geophysical Research: Atmospheres (1984-2012) 104, 6215-6228.

Davenport, M. L., & Nicholson, S. E. (1993). On the relation between rainfall and the Normalized Difference Vegetation Index for diverse vegetation types in East Africa. International Journal of Remote Sensing, 14(12), 2369-2389.

Derber, J.C., Parrish, D.F., Lord, S.J. (1991) The new global operational analysis system at the National Meteorological Center. Weather and Forecasting 6, 538-547.

Devereux, S., Edwards, J. (2004) Climate Change and Food Security. IDS Bulletin 35, 22-30.

Dietz, A.J., Ruben, R., Verhagen, A., Dietz, T., Ruben, R., Verhagen, J., Dittoh, S., KonatÃ©, M., Millar, D., Ofori-Sarpong, E., Saley, H., Sylla, N., (2004) Climate Change Preparedness in West Africa, The Impact of Climate Change on Drylands. Springer Netherlands, pp. 403-408.

Donohue, R.J., McVicar, T.R., Roderick, M.L. (2010) Assessing the ability of potential evaporation formulations to capture the dynamics in evaporative demand within a changing climate. Journal of Hydrology 386, 186-197.

Doorenbos, J., Pruitt, W., (1977) Crop water requirements, Irrigation and Drainage paper. Food and Agriculture Organization, Rome, p. 144.

Druyan, L.M. (2011) Studies of 21st Century precipitation trends over West Africa. International Journal of Climatology 31, 1415-1424.

Ek, M.B., Mitchell, K.E., Lin, Y., Rogers, E., Grunmann, P., Koren, V., Gayno, G., Tarpley, J.D. (2003) Implementation of Noah land surface model advances in the National Centers for Environmental Prediction operational mesoscale Eta model. J. Geophys. Res 108, 8851.

Estes, L. D., Chaney, N. W., Herrera-Estrada, J., Sheffield, J., Caylor, K. K., & Wood, E. F. (2014). Changing water availability during the African maize-growing season, 1979–2010. Environmental Research Letters, 9(7), 075005.

Famine Early Warning Systems Network. (2014). Tanzania: Weather, Climate, and Agriculture-Seasonal Calendar, Typical Year. 3 Nov 2014. http://www.fews.net/east-africa/tanzania/

Fairall, C. W., Uttal, T., Hazen, D., Hare, J., Cronin, M. F., Bond, N., & Veron, D. E. (2008). Observations of cloud, radiation, and surface forcing in the equatorial eastern Pacific. Journal of Climate, 21(4).

Fischer, E. M., Seneviratne, S. I., Lüthi, D., & Schär, C. (2007a). Contribution of land-atmosphere coupling to recent European summer heat waves. Geophysical Research Letters, 34(6).

Fischer, E. M., Seneviratne, S. I., Vidale, P. L., Lüthi, D., & Schär, C. (2007b). Soil Moisture–Atmosphere Interactions during the 2003 European Summer Heat Wave. Journal of Climate, 20(20).

Food and Agriculture Organization, (2003) FAOSTAT agriculture data, http://faostat3.fao.org/home/index.html, May 8 2013.

Food and Agriculture Organization of the United Nations/World Food Programme. (1998). Crop and Food Security Assessment Mission to Tanzania Special Report. Online Resource. 3 Aug 1998. http://www.fao.org/docrep/004/w9479e/w9479e00.htm#E62E1

Friborg, T., Boegh, E., Soegaard, H. (1997) Carbon dioxide flux, transpiration and light response of millet in the Sahel. Journal of Hydrology 188â€“189, 633-650.

Friedl, M. A., & Davis, F. W. (1994). Sources of variation in radiometric surface temperature over a tallgrass prairie. Remote Sensing of Environment, 48(1), 1-17.

Funk, C. (2011) We thought trouble was coming, Nature, 576, 7, doi:10.1038/476007a.

Funk, C., Dettinger, M. D., Michaelsen, J. C., Verdin, J. P., Brown, M. E., Barlow, M., & Hoell, A. (2008). Warming of the Indian Ocean threatens eastern and southern African food security but could be mitigated by agricultural development. Proceedings of the National Academy of Sciences, 105(32), 11081-11086.

Funk, C., Eilerts, G., Verdin, J., Rowland, J., Marshall, M., (2011) A Climate Trend Analysis of Sudan, U.S. Geological Survey Fact Sheet, p. 6.

Funk, C., Michaelsen, J., Marshall, M.T., (2012a) Mapping Recent Decadal Climate Variations in Precipitation and Temperature across Eastern Africa and the Sahel, in: Wardlaw, B.D., Anderson, M.C., Verdin, J.P. (Eds.), Remote Sensing of Drought: Innovative Monitoring Approaches, p. 331.

Funk, C.C., Peterson, P.J., Landsfeld, M.F., Pedreros, D.H., Verdin, J.P., Rowland, J.D., Romero, B.E., Husak, G.J., Michaelsen, J.C., and Verdin, A.P. (2014). A quasi-global precipitation time series for drought monitoring: U.S. Geological Survey Data Series 832, 4 p., http://pubs.usgs.gov/ds/832.

Funk, C., Rowland, J., Eilerts, G., Adoum, A., White, L., (2012b) A Climate Trend Analysis of Niger, U.S. Geological Survey Fact Sheet, p. 4.

Funk, C., Rowland, J., Eilerts, G., Adoum, A. and White, L., (2012c) A Climate Trend Analysis of Burkina Faso, U.S. Geological Survey Fact Sheet, p. 4.

Funk, C., Rowland, J., Eilerts, G., Adoum, A. and White, L., (2012d) A Climate Trend Analysis of Chad, U.S. Geological Survey Fact Sheet, p. 4.

Funk, C., Rowland, Jim, Adoum, Alkhalil, Eilerts, Gary, and White, Libby, (2012e) A climate trend analysis of Mali, U.S. Geological Survey Fact Sheet, p. 4.

Garrity, D. P., Akinnifesi, F. K., Ajayi, O. C., Weldesemayat, S. G., Mowo, J. G., Kalinganire, A., Larwanou, M., Bayala, J. (2010). Evergreen Agriculture: a robust approach to sustainable food security in Africa. Food Security, 2(3), 197-214.

Garstang, M., & Fitzjarrald, D. R. (1999). Observations of surface to atmosphere interactions in the tropics. Oxford University Press.

Gesch, D.B., Verdin, K.L., Greenlee, S.K. (1999) New land surface digital elevation model covers the Earth. Eos, Transactions American Geophysical Union 80, 69-70.

Giannini, A., Biasutti, M., Held, I.M., Sobel, A.H. (2008). A global perspective on African climate. Clim. Change 90, 359–383.

Giannini, A., Salack, S., Lodoun, T., Ali, A., Gaye, A.T., Ndiaye, O. (2013) A unifying view of climate change in the Sahel linking intra-seasonal, interannual and longer time scales. Environmental Research Letters 8, 024010.

Gong, L., Xu, C.-y., Chen, D., Halldin, S., Chen, Y.D. (2006) Sensitivity of the Penman-Monteith reference evapotranspiration to key climatic variables in the Changjiang (Yangtze River) basin. Journal of Hydrology 329, 620-629.

Gottschalck, J., Meng, J., Rodell, M., & Houser, P. (2005). Analysis of multiple precipitation products and preliminary assessment of their impact on global land data assimilation system land surface states. Journal of Hydrometeorology, 6(5), 573-598.

Gowing, J.W., Young, M.D.B., Hatibu, N., Mahoo H.F., Rwehumbiza, F., Mzirai, O.B. (2003). Developing Improved Dryland Cropping Systems For Maize In Semi-Arid Tanzania. Part II. Use of a Model to Extrapolate and Add Value to Experimental Results, Exp. Agric., 9(3): 293-306.

Gregory, P. J., Ingram, J. S., & Brklacich, M. (2005). Climate change and food security. Philosophical Transactions of the Royal Society B: Biological Sciences, 360(1463), 2139-2148.

Gutman, G., Ignatov, A. (1998) The derivation of the green vegetation fraction from NOAA/AVHRR data for use in numerical weather prediction models. International Journal of Remote Sensing 19, 1533-1543.

Hamlet, A. F., Mote, P. W., Clark, M. P., & Lettenmaier, D. P. (2005). Effects of temperature and precipitation variability on snowpack trends in the Western United States*. Journal of Climate, 18(21), 4545-4561.

Hansen, M.C., DeFries, R.S., Townshend, J.R.G., Sohlberg, R. (2000) Global land cover classification at 1 km spatial resolution using a classification tree approach. International Journal of Remote Sensing 21, 1331-1364.

Hastenrath, S. (2001). Variations of East African climate during the past two centuries. Climatic change, 50(1-2), 209-217.

Hein, L., De Ridder, N. (2006) Desertification in the Sahel: a reinterpretation. Global Change Biology 12, 751-758.

Held, I.M., Delworth, T.L., Lu, J., Findell, K.L., Knutson, T.R. (2005) Simulation of Sahel drought in the 20th and 21st centuries. Proceedings of the National Academy of Sciences of the United States of America 102, 17891-17896.

Held, I.M., Soden, B.J. (2006) Robust responses of the hydrological cycle to global warming. Journal of Climate 19, 5686-5699.

Hellmuth, M.E., Mason, S.J., Vaughan, C., van Aalst, M.K., Choularton, R., (2011) A Better Climate for Disaster Risk Management. International Research Institute for Climate and Society (IRI), Columbia University, New York.

Herman, A., Kumar, V.B., Arkin, P.A., Kousky, J.V. (1997) Objectively determined 10-day African rainfall estimates created for famine early warning systems. International Journal of Remote Sensing 18, 2147-2159.

Hogue, T.S. (2003) A multi-criteria evaluation of land-surface models and application to semi-arid regions.

Hogue, T.S., Bastidas, L., Gupta, H., Sorooshian, S., Mitchell, K., Emmerich, W. (2005) Evaluation and Transferability of the Noah Land Surface Model in Semiarid Environments. Journal of Hydrometeorology 6, 68-84.

Hopkins, W.G., Hüner, N.P.A. (1995) Introduction to plant physiology. J. Wiley New York.

Howden, S. M., & Turnpenny, J. (1997, December). Modelling heat stress and water loss of beef cattle in subtropical Queensland under current climates and climate change. In Modsim'97 International Congress on Modelling and Simulation, Proceedings, 8–11 December, University of Ta smania, Hobart (pp. 1103-1108). Modelling and Simulation Society of Australia, Canberra, Australia.

Jacquemin, B., Noilhan, J.l. (1990) Sensitivity study and validation of a land surface parameterization using the HAPEX-MOBILHY data set. Boundary-Layer Meteorology 52, 93-134

James, R., Washington, R. (2012) Changes in African temperature and precipitation associated with degrees of global warming. Climatic Change, 1-14.

Jankowska, M.M., Lopez-Carr, D., Funk, C., Husak, G.J., Chafe, Z.A. (2012) Climate change and human health: Spatial modeling of water availability, malnutrition, and livelihoods in Mali, Africa. Applied Geography 33, 4-15.

Jimenez, C., Prigent, C., Mueller, B., Seneviratne, S.I., McCabe, M.F., Wood, E.F., Rossow, W.B., Balsamo, G., Betts, A.K., Dirmeyer, P.A. (2011) Global intercomparison of 12 land surface heat flux estimates. Journal of Geophysical Research 116, D02102.

Jobard, I., Chopin, F., Berges, J.C., Roca, R. (2011) An intercomparison of 10-day satellite precipitation products during West African monsoon. International Journal of Remote Sensing 32, 2353-2376.

Jolly, W. M., Dobbertin, M., Zimmermann, N. E., & Reichstein, M. (2005). Divergent vegetation growth responses to the 2003 heat wave in the Swiss Alps. Geophysical Research Letters, 32(18).

Julien, Y., & Sobrino, J. A. (2009). Global land surface phenology trends from GIMMS database. International Journal of Remote Sensing, 30(13), 3495-3513.

Kalnay, E., Kanamitsu, M., Kistler, R., Collins, W., Deaven, D., Gandin, L., ... & Joseph, D. (1996). The NCEP/NCAR 40-year reanalysis project. Bulletin of the American meteorological Society, 77(3), 437-471.

Kangalawe, R. Y., & Liwenga, E. T. (2005). Livelihoods in the wetlands of Kilombero Valley in Tanzania: Opportunities and challenges to integrated water resource management. Physics and Chemistry of the Earth, Parts A/B/C, 30(11), 968-975.

Karnieli, A., Agam, N., Pinker, R. T., Anderson, M., Imhoff, M. L., Gutman, G. G., ... & Goldberg, A. (2010). Use of NDVI and Land Surface Temperature for Drought Assessment: Merits and Limitations. Journal of Climate, 23(3).

Kay, A.L., Davies, H.N. (2008) Calculating potential evaporation from climate model data: A source of uncertainty for hydrological climate change impacts. Journal of Hydrology 358, 221-239.

Kim, D. Y., Thomas, V., Olson, J., Williams, M., & Clements, N. (2013). Statistical trend and change-point analysis of land-cover-change patterns in East Africa. International Journal of Remote Sensing, 34(19), 6636-6650.

Kingston, D.G., Todd, M.C., Taylor, R.G., Thompson, J.R., Arnell, N.W. (2009) Uncertainty in the estimation of potential evapotranspiration under climate change. Geophys. Res. Lett. 36, L20403.

Kurkowski, N.P., Stensrud, D.J., Baldwin, M.E. (2003) Assessment of implementing satellite-derived land cover data in the Eta Model. Weather & Forecasting 18.

Lambin, E.F., Turner, B.L., Geist, H.J., Agbola, S.B., Angelsen, A., Bruce, J.W., Coomes, O.T., Dirzo, R., Fischer, G., Folke, C., George, P.S., Homewood, K., Imbernon, J., Leemans, R., Li, X., Moran, E.F., Mortimore, M., Ramakrishnan, P.S., Richards, J.F., Skånes, H., Steffen, W., Stone, G.D., Svedin, U., Veldkamp, T.A., Vogel, C., Xu, J. (2001) The causes of land-use and land-cover change: moving beyond the myths. Global Environmental Change 11, 261-269.

Le Houérou, H. (1989) The Grazing Land Ecosystems of the African Sahel. Springer, New York.

Leakey, A. D. (2009). Rising atmospheric carbon dioxide concentration and the future of C4 crops for food and fuel. Proceedings of the Royal Society B: Biological Sciences, 276(1666), 2333-2343.

Leuning, R., Van Gorsel, E., Massman, W. J., & Isaac, P. R. (2012). Reflections on the surface energy imbalance problem. Agricultural and Forest Meteorology, 156, 65-74.

Lobell, D.B., Burke, M.B., Tebaldi, C., Mastrandrea, M.D., Falcon, W.P., Naylor, R.L. (2008) Prioritizing Climate Change Adaptation Needs for Food Security in 2030. Science 319, 607-610.

Liang, X., Lettenmaier, D. P., Wood, E. F., & Burges, S. J. (1994). A simple hydrologically based model of land surface water and energy fluxes for general circulation models. Journal of Geophysical Research: Atmospheres (1984–2012), 99(D7), 14415-14428.

Lyon, B., Barnston, A., DeWitt, D.G. (2014). Tropical Pacific forcing of a 1998–99 climate shift: Observational analysis and climate model results for the boreal spring season. Climate Dyn., 43, 893–909, doi:10.1007/s00382-013-1891-9.

McGregor, G. R., & Nieuwolt, S. (1998). Tropical climatology: an introduction to the climates of the low latitudes (No. Ed. 2). John Wiley & Sons Ltd.

McSweeney, C., New, M. & Lizcano, G. (2010a). UNDP Climate Change Country Profiles: Tanzania. Available: http://country-profiles.geog.ox.ac.uk/ [Accessed 9 May 2014].

McSweeney, C., New, M., Lizcano, G. & Lu, X. (2010b). The UNDP Climate Change Country Profiles Improving the Accessibility of Observed and Projected Climate Information for Studies of Climate Change in Developing Countries. Bulletin of the American Meteorological Society, 91, 157-166.

Mahalakshmi, V., Bidinger, F.R., Rao, G.D.P. (1988) Timing and intensity of water deficits during flowering and grain-filling in pearl millet. Agronomy journal 80, 130-135.

Mahrt, L., Ek, M. (1984) The influence of atmospheric stability on potential evaporation. Journal of climate and applied meteorology 23, 222-234.

Mahrt, L., Pan, H. (1984) A two-layer model of soil hydrology. Boundary-Layer Meteorology 29, 1-20.

Mann, H.B. (1945). Nonparametric tests against trend. Econometrica, 13, 245-259.

Marshall, M., Funk, C., Michaelsen, J. (2012) Examining evapotranspiration trends in Africa. Climate Dynamics 38, 1849-1865.

Marshall, M., Tu, K., Funk, C., Michaelsen, J., Williams, P., Williams, C., Ardö, J., Boucher, M., Cappelaere, B., de Grandcourt, A., Nickless, A., Nouvellon, Y., Scholes, R., Kutsch, W. (2013). Improving operational land surface model canopy evapotranspiration in Africa using a direct remote sensing approach. Hydrology and Earth System Sciences, 17(3), 1079-1091.

Marteau, R., Sultan, B., Moron, V., Alhassane, A., Baron, C., Traoré, S.B. (2011) The onset of the rainy season and farmersâ€™ sowing strategy for pearl millet cultivation in Southwest Niger. Agricultural and Forest Meteorology 151, 1356-1369.

Mary, A. L., and A. E. Majule. (2009). "Impacts of climate change, variability and adaptation strategies on agriculture in semi arid areas of Tanzania: The case of Manyoni District in Singida Region, Tanzania." *African Journal of Environmental Science and Technology* 3.8 (2009): 206-218.

Matsuura, K., & Willmott, C. J. (2009). Terrestrial precipitation: 1900–2008 gridded monthly time series. Center for Climatic Research Department of Geography Center for Climatic Research, University of Delaware.

Merbold, L., Ardö, J., Arneth, A., Scholes, R. J., Nouvellon, V., De Grandcourt, A., ... & Michaelsen, J., Schimel, D. S., Friedl, M. A., Davis, F. W. and Dubayah, R. C. (1994), Regression Tree Analysis of satellite and terrain data to guide vegetation sampling and surveys. Journal of Vegetation Science, 5: 673–686. doi: 10.2307/3235882

Mitchell, K.E., Lohmann, D., Houser, P.R., Wood, E.F., Schaake, J.C., Robock, A., Cosgrove, B.A., Sheffield, J., Duan, Q., Luo, L., Higgins, R.W., Pinker, R.T., Tarpley, J.D., Lettenmaier, D.P., Marshall, C.H., Entin, J.K., Pan, M., Shi, W., Koren, V., Meng, J., Ramsay, B.H., Bailey, A.A. (2004) The multi-institution North American Land Data Assimilation System (NLDAS): Utilizing multiple GCIP products and partners in a continental distributed hydrological modeling system. Journal of Geophysical Research: Atmospheres 109, D07S90.

Mohamed, A. B., Van Duivenbooden, N., & Abdoussallam, S. (2002). Impact of climate change on agricultural production in the Sahel–Part 1. Methodological approach and case study for millet in Niger. Climatic Change, 54(3), 327-348.

Mongi, H., Majule, A. E., & Lyimo, J. G. (2010). Vulnerability and adaptation of rain fed agriculture to climate change and variability in semi-arid Tanzania. African Journal of Environmental Science and Technology, 4(6).

Monin, A.S., Obukhov, A. (1954) Basic laws of turbulent mixing in the surface layer of the atmosphere. Contrib. Geophys. Inst. Acad. Sci. USSR 151, 163-187.

Monteith, J. L. (1964) Evaporation and environment. Symp. Soc. Exp. Biol. 19, 205–234

Monteith, J.L. (1981) Evaporation and surface temperature. Quarterly Journal of the Royal Meteorological Society 107, 1-27.

Mortimore, M.J., Adams, W.M. (2001) Farmer adaptation, change and 'crisis' in the Sahel. Global Environmental Change 11, 49-57.

Mougin, E. (2009). Precipitation as driver of carbon fluxes in 11 African ecosystems. Biogeosciences, 6(6).

Myers, N. (2002) Environmental refugees: a growing phenomenon of the 21st century. Philosophical Transactions of the Royal Society of London. Series B: Biological Sciences 357, 609-613.

Nations, U., (2002) Niger: Projections Démographiques des Nations Unies, Révision de 2002. UNDP, New York.

Nations, U., (2007) World Population Prospects: The 2006 revison. UN, New York, pp. 362-363.

Neelin, J.D. (2011) Climate change and climate modeling. Cambridge University Press.

Nemani, R. R., & Running, S. W. (1989). Estimation of regional surface resistance to evapotranspiration from NDVI and thermal-IR AVHRR data. Journal of Applied meteorology, 28(4), 276-284.

Nicholson, S. E., & Kim, J. (1997). The relationship of the El Nino-Southern oscillation to African rainfall. International Journal of Climatology, 17(2), 117-135

Nicholson, S. E., & Selato, J. C. (2000). The influence of La Nina on African rainfall. International Journal of Climatology, 20(14), 1761-1776.

Nicholson, S.E. (2001). Climatic and environmental change in Africa during the last two centuries. Clim. Res. 17, 123–144.

Nijssen, B., Lettenmaier, D. P., Liang, X., Wetzel, S. W., & Wood, E. F. (1997). Streamflow simulation for continental-scale river basins. Water Resources Research, 33(4), 711-724.

Nijssen, B., O'Donnell, G.M., Lettenmaier, D.P., Lohmann, D., Wood, E.F. (2001a). Predicting the discharge of global rivers. Journal of Climate 14, 3307–3323.

Nijssen, B., Schnur, R., Lettenmaier, D.P. (2001b). Global retrospective estimation of soil moisture using the variable infiltration capacity land surface model, 1980-93. Journal of Climate 14, 1790–1808.

Nijssen, B., Schnur, R., & Lettenmaier, D. P. (2001c). Global retrospective estimation of soil moisture using the variable infiltration capacity land surface model, 1980-93. Journal of Climate, 14(8), 1790-1808.

Niu, G.-Y., Yang, Z.-L., Mitchell, K.E., Chen, F., Ek, M.B., Barlage, M., Kumar, A., Manning, K., Niyogi, D., Rosero, E., Tewari, M., Xia, Y. (2011) The community Noah land surface model with multiparameterization options (Noah-MP): 1. Model description and evaluation with local-scale measurements. Journal of Geophysical Research: Atmospheres 116, D12109.

Noilhan, J., Planton, S. (1989) A simple parameterization of land surface processes for meteorological models. Monthly Weather Review 117, 536-549.

Olsson, L., Eklundh, L., Ardö, J. (2005) A recent greening of the Sahel--trends, patterns and potential causes. Journal of Arid Environments 63, 556-566.

Omondi, P. A. O., Awange, J. L., Forootan, E., Ogallo, L. A., Barakiza, R., Girmaw, G. B., ... & Komutunga, E. (2014). Changes in temperature and precipitation extremes over the Greater Horn of Africa region from 1961 to 2010. International Journal of Climatology, 34(4), 1262-1277.

Ong, C.K., Monteith, J.L. (1985) Response of pearl millet to light and temperature. Field Crops Research 11, 141-160.

Paavola, J. (2008). Livelihoods, vulnerability and adaptation to climate change in Morogoro, Tanzania. Environmental Science & Policy, 11(7), 642-654.

Paeth, H., Born, K., Girmes, R., Podzun, R., Jacob, D. (2009) Regional Climate Change in Tropical and Northern Africa due to Greenhouse Forcing and Land Use Changes. Journal of Climate 22, 114-132.

Pan, H.L., Mahrt, L. (1987) Interaction between soil hydrology and boundary-layer development. Boundary-Layer Meteorology 38, 185-202.

Patil, M.N., Kumar, M., Waghmare, R.T., Dharmaraj, T., Mahanty, N.C. (2013) Evaluation of Noah-LSM for soil hydrology parameters in the Indian summer monsoon conditions. Theoretical and Applied Climatology, 1-10.

Penman, H. L. (1948). Natural evaporation from open water, bare soil and grass.*Proceedings of the Royal Society of London. Series A. Mathematical and Physical Sciences*, *193*(1032), 120-145.

Peterson, T.C., Vose, R.S. (1997) An overview of the Global Historical Climatology Network temperature database. Bulletin of the American Meteorological Society 78, 2837-2849.

Petropoulos, G., Carlson, T. N., Wooster, M. J., & Islam, S. (2009). A review of Ts/VI remote sensing based methods for the retrieval of land surface energy fluxes and soil surface moisture. Progress in Physical Geography, 33(2), 224-250.

Pierce, L. L., & Congalton, R. G. (1988). A methodology for mapping forest latent heat flux densities using remote sensing. Remote sensing of environment, 24(3), 405-418.

Pinzon, J. E., & Tucker, C. J. (2010). GIMMS 3g NDVI set and global NDVI trends. In Second Yamal Land-Cover Land-Use Change Workshop Arctic Centre (Rovaniemi, March).

Potts, M., Gidi, V., Campbell, M., Zureick, S. (2011) Niger: Too little, too late. International perspectives on sexual and reproductive health 37, 95-101.

Rain, D. (1999) Eaters of the Dry Season: Circular Labor Migration in the West African Sahel. Westview Press, Boulder, Colorado.

Ramanathan, V., Subasilar, B., Zhang, G. J., Conant, W., Cess, R. D., Kiehi, J. T., Grassi, H., & Shi, L. (1995). Warm pool heat budget and shortwave cloud forcing: A missing physics?. Science, 267(5197), 499-503.

Ramaswamy, S., Sanders, J.H. (1992) Population pressure, land degradation and sustainable agricultural technologies in the Sahel. Agricultural Systems 40, 361-378.

Raynaut, C. (2001) Societies and nature in the Sahel: ecological diversity and social dynamics. Global Environmental Change 11, 9-18.

Rayner, D.P. (2007) Wind Run Changes: The Dominant Factor Affecting Pan Evaporation Trends in Australia. Journal of Climate 20, 3379-3394.

Reilly, J., Schimmelpfennig, D. (2000) Irreversibility, uncertainty, and learning: portraits of adaptation to long-term climate change. Springer.

Renaud, V., & Rebetez, M. (2009). Comparison between open-site and below-canopy climatic conditions in Switzerland during the exceptionally hot summer of 2003. Agricultural and forest meteorology, 149(5), 873-880.

Reynolds, C.A., Jackson, T.J., Rawls, W.J. (2000) Estimating soil water-holding capacities by linking the Food and Agriculture Organization Soil map of the world with global pedon databases and continuous pedotransfer functions. Water Resources Research 36, 3653-3662.

Rind, D., Goldberg, R., Hansen, J., Rosenzweig, C., Ruedy, R. (1990) Potential evapotranspiration and the likelihood of future drought. Journal of Geophysical Research: Atmospheres 95, 9983-10004.

Ritchie, J. T., & NeSmith, D. S. (1991). Temperature and crop development. In Modeling plant and soil systems, Vol. 31 (eds Hanks, J. & Ritchie, J.T.), American Society of Agronomy, 5-29.

Robock, A., Luo, L., Wood, E.F., Wen, F., Mitchell, K.E., Houser, P.R., Schaake, J.C., Lohmann, D., Cosgrove, B., Sheffield, J. (2003) Evaluation of the North American Land Data Assimilation System over the southern Great Plains during the warm season. Journal of Geophysical Research: Atmospheres (1984-2012) 108.

Rodell, M., Houser, P.R., Jambor, U., Gottschalck, J., Mitchell, K., Meng, C.J., Arsenault, K., Cosgrove, B., Radakovich, J., Bosilovich, M. (2004) The global land data assimilation system. Bulletin of the American Meteorological Society 85, 381-394.

Sage, R. F., & Kubien, D. S. (2003). Quo vadis C4? An ecophysiological perspective on global change and the future of C4 plants. Photosynthesis research, 77(2-3), 209-225.

Saji, N. H., Goswami, B. N., Vinayachandran, P. N., & Yamagata, T. (1999). A dipole mode in the tropical Indian Ocean. Nature, 401(6751), 360-363.

Sellers, P. J. (1985). Canopy reflectance, photosynthesis and transpiration. International Journal of Remote Sensing, 6(8), 1335-1372.

Sen, P.K. (1968) Estimates of Regression Coefficient Based on Kendall's tau. J. Am. Stat. Ass. 63, 324, 1379-1389.

Senay, G.B., Verdin, J. (2003) Characterization of yield reduction in Ethiopia using a GIS-based crop water balance model. Canadian Journal of Remote Sensing 29, 687-692.

Schmidhuber, J., & Tubiello, F. N. (2007). Global food security under climate change. Proceedings of the National Academy of Sciences, 104(50), 19703-19708.

Schneider, U., Becker, A., Finger, P., Meyer-Christoffer, A., Rudolf, B., Ziese, M. (2011): GPCC Full Data Reanalysis Version 6.0 at 0.5°: Monthly Land-Surface Precipitation from Rain-Gauges built on GTS-based and Historic Data. DOI: 10.5676/DWD_GPCC/FD_M_V6_050

Shanahan, T.M., Overpeck, J.T., Anchukaitis, K.J., Beck, J.W., Cole, J.E., Dettman, D.L., Peck, J.A., Scholz, C.A., King, J.W. (2009) Atlantic forcing of persistent drought in West Africa. Science 324, 377-380.

Sheffield, J., Goteti, G., Wood, E. F. (2006). Development of a 50-yr high-resolution global dataset of meteorological forcings for land surface modeling, J. Climate, 19 (13), 3088-3111

Sheffield, J., Wood, E.F., Roderick, M.L. (2012) Little change in global drought over the past 60 years. Nature 491, 435-438.

Siegel, A.F. (1982) Robust Regression Using Repeated Medians. Biometrika, 69, 1, 242-244.

Sissoko, K., Keulen, H., Verhagen, J., Tekken, V., Battaglini, A. (2011) Agriculture, livelihoods and climate change in the West African Sahel. Regional Environmental Change 11, 119-125.

Smith, M. (2000) The application of climatic data for planning and management of sustainable rainfed and irrigated crop production. Agricultural and Forest Meteorology 103, 99-108.

Smith, S.J., Wigley, T.M.L. (2006) Multi-Gas Forcing Stabilization with the MiniCAM. Energy Journal, pp 373-391.

Solomon, S. (Ed.). (2007). Climate change 2007-the physical science basis: Working group I contribution to the fourth assessment report of the IPCC (Vol. 4). Cambridge University Press.

Stige, L.C., Stave, J., Chan, K.-S., Ciannelli, L., Pettorelli, N., Glantz, M., Herren, H.R., Stenseth, N.C. (2006). The effect of climate variation on agro-pastoral production in Africa. Proc. Natl. Acad. Sci. U.S.A. 103, 3049–3053.

Sultan, B., Baron, C., Dingkuhn, M., Sarr, B.t., Janicot, S. (2005) Agricultural impacts of large-scale variability of the West African monsoon. Agricultural and Forest Meteorology 128, 93-110.

Sultan, B., Janicot, S. (2003) The West African monsoon dynamics. Part II: Thepreonset and onset of the summer monsoon. Journal of Climate 16, 3407-3427.

Suttie, J.M., Reynolds, S.G., Batello, C. (2005) Grasslands of the world. Food and Agriculture Organization of the United Nations (FAO).

Tadesse, T., Haile, M., Senay, G., Wardlow, B.D., Knutson, C.L. (2008) The need for integration of drought monitoring tools for proactive food security management in sub-Saharan Africa. Natural Resources Forum 32, 265-279.

Tappan, G.G., Sall, M., Wood, E.C., Cushing, M. (2004) Ecoregions and land cover trends in Senegal. Journal of Arid Environments 59, 427-462.

Tashiro, T., & Wardlaw, I. F. (1989). A comparison of the effect of high temperature on grain development in wheat and rice. Annals of Botany, 64(1), 59-65.

Taylor, K.E., Stouffer, R.J., Meehl, G.A. (2012) An Overview of CMIP5 and the Experiment Design. Bulletin of the American Meteorological Society.

Teuling, A. J., Seneviratne, S. I., Stöckli, R., Reichstein, M., Moors, E., Ciais, P., others, & Wohlfahrt, G. (2010). Contrasting response of European forest and grassland energy exchange to heatwaves. Nature Geoscience, 3(10), 722-727.

Theil, H. (1950). A rank invariant method for linear and polynomial regression analysis. Nederl. Akad. Wetensch. Proc. Ser. A 53, 386-392 (Part I), 521-525 (Part II), 1397-1412 (Part III).

Thornton, P.K., (2012) Recalibrating food production in the developing world: Global warming will change more than just the climate, CCAFS Policy Brief no. 6. CGIAR Research Program on Climate Change, Agriculture and Food Security (CCAFS)

Thurlow, J., & Wobst, P. (2003). Poverty-focused social accounting matrices for Tanzania (No. 112). International Food Policy Research Institute (IFPRI).

Trambauer, P., Maskey, S., Winsemius, H., Werner, M., & Uhlenbrook, S. (2013). A review of continental scale hydrological models and their suitability for drought forecasting in (sub-Saharan) Africa. Physics and Chemistry of the Earth, Parts A/B/C, 66, 16-26.

Trenberth, K. E. (1998). Atmospheric moisture residence times and cycling: Implications for rainfall rates and climate change. Climatic change, 39(4), 667-694.

Tucker, C. J., & Sellers, P. J. (1986). Satellite remote sensing of primary production. International journal of remote sensing, 7(11), 1395-1416.

USAID FEWS NET (2011) – United States Agency for International development, Famine Early Warning System Network, East Africa: Past year one of the driest on record in the eastern Horn, http://www.fews.net/east-africa/special-report/tue-2011-06-14, last access: 1 Apr 2014

Verdin, J., & Klaver, R. (2002). Grid-cell-based crop water accounting for the famine early warning system. Hydrological Processes, 16(8), 1617-1630.

Verdin, J., Funk, C., Senay, G., & Choularton, R. (2005). Climate science and famine early warning. Philosophical Transactions of the Royal Society B: Biological Sciences, 360(1463), 2155-2168.

Vrieling, Anton, Jan de Leeuw, and Mohammed Y. Said. (2013). "Length of growing period over Africa: Variability and trends from 30 years of NDVI time series."*Remote Sensing* 5.2 (2013): 982-1000.

Walter, I.A., Allen, R.G., Elliott, R., Jensen, M.E., Itenfisu, D., Mecham, B., Howell, T.A., Snyder, R., Brown, P., Echings, S., (2000) ASCE's standardized reference evapotranspiration equation.

Wei, H., Xia, Y., Mitchell, K.E., Ek, M.B. (2012) Improvement of the Noah land surface model for warm season processes: evaluation of water and energy flux simulation. Hydrological Processes 27, 297-303.

Welch, B. L. (1947). "The generalization of "Student's" problem when several different population variances are involved". Biometrika 34 (1–2): 28–35. doi:10.1093/biomet/34.1-2.28. MR 19277.

White, R., Toumi, R. (2012) A tightly bound soil-water scheme within an atmosphere-land-surface model. Journal of Hydrology 452-453, 51-63.

Williams, A. P., & Funk, C. (2011). A westward extension of the warm pool leads to a westward extension of the Walker circulation, drying eastern Africa. Climate Dynamics, 37(11-12), 2417-2435.

Wild, M., Ohmura, A., Gilgen, H., & Rosenfeld, D. (2004). On the consistency of trends in radiation and temperature records and implications for the global hydrological cycle. Geophysical Research Letters, 31(11).

Winkel, T., Renno, J.-F.o., Payne, W.A. (1997) Effect of the timing of water deficit on growth, phenology and yield of pearl millet (Pennisetum glaucum (L.) R. Br.) grown in Sahelian conditions. Journal of Experimental Botany 48, 1001-1009.

Wise, M., Calvin, K., Thomson, A., Clarke, L., Bond-Lamberty, B., Sands, R., Smith, S., Janetos, A., Edmonds, J. (2009) Implications of Limiting CO2 Concentrations for Land Use and Energy. Science, 1183-1186.

Xia, Y., Ek, M., Sheffield, J., Livneh, B., Huang, M., Wei, H., Feng, S., Luo, L., Meng, J., Wood, E. (2013) Validation of Noah-Simulated Soil Temperature in the North American Land Data Assimilation System Phase 2. Journal of Applied Meteorology & Climatology 52, 455-471.

Xia, Y., Sheffield, J., Ek, M.B., Dong, J., Chaney, N., Wei, H., Meng, J., Wood, E.F. (2014) Evaluation of multi-model simulated soil moisture in NLDAS-2. Journal of Hydrology 512, 107-125.

Xie, P., Arkin, P.A. (1997) Global precipitation: A 17-year monthly analysis based on gauge observations, satellite estimates, and numerical model outputs. Bulletin of the American Meteorological Society 78, 2539-2558.

Yanda, P. Z., & Madulu, N. F. (2005). Water resource management and biodiversity conservation in the Eastern Rift Valley Lakes, Northern Tanzania. Physics and Chemistry of the Earth, Parts A/B/C, 30(11), 717-725.

Yang, W., Seager, R., Cane, M. A., & Lyon, B. (2014). The East African long rains in observations and models. Journal of Climate, (2014).

Yoshida, S. (1972). Physiological aspects of grain yield. Annual Review of Plant Physiology, 23(1), 437-464.

Zampieri, M., D'Andrea, F., Vautard, R., Ciais, P., de Noblet-Ducoudré, N., & Yiou, P. (2009). Hot European Summers and the Role of Soil Moisture in the Propagation of Mediterranean Drought. Journal of Climate, 22(18).

Zaitchick, B.F., Habib, S., Anderson, M., Ozodogan, M., Alo, C., (2010) A Land Data Assimilation System for hydrologic studies in countries of the Nile basin, 8th International Conference of the African Association of Remote Sensing for the Environment, Addis Ababa, Ethiopia.

Zeng, N., Neelin, J.D., Lau, K.M., Tucker, C.J. (1999) Enhancement of interdecadal climate variability in the Sahel by vegetation interaction. Science 286, 1537-1540.

Zhang, X., Zwiers, F.W., Hegerl, G.C., Lambert, F.H., Gillett, N.P., Solomon, S., Stott, P.A., Nozawa, T. (2007) Detection of human influence on twentieth-century precipitation trends. Nature 448, 461-465.

Zheng, D., Van Der Velde, R., Su, Z., Booij, M.J., Hoekstra, A.Y. (2013) Assessment of Roughness Length Schemes Implemented within the Noah Land Surface Model for High Altitude Regions. Journal of Hydrometeorology.

Figures

Chapter 1

Figure 1

Aridity by month for the June-September rainy season. Aridity is the ratio of average precipitation *P* (mm) to potential evapotranspiration *PET* (mm) over the 2001-2010 time period. Aridity is computed with RFE2.0 rainfall, GLDAS Noah LSM 2.7.1 data, and FAO-56 PM equation for reference evapotranspiration. Areas in light blue are drier while areas in dark blue are wetter.

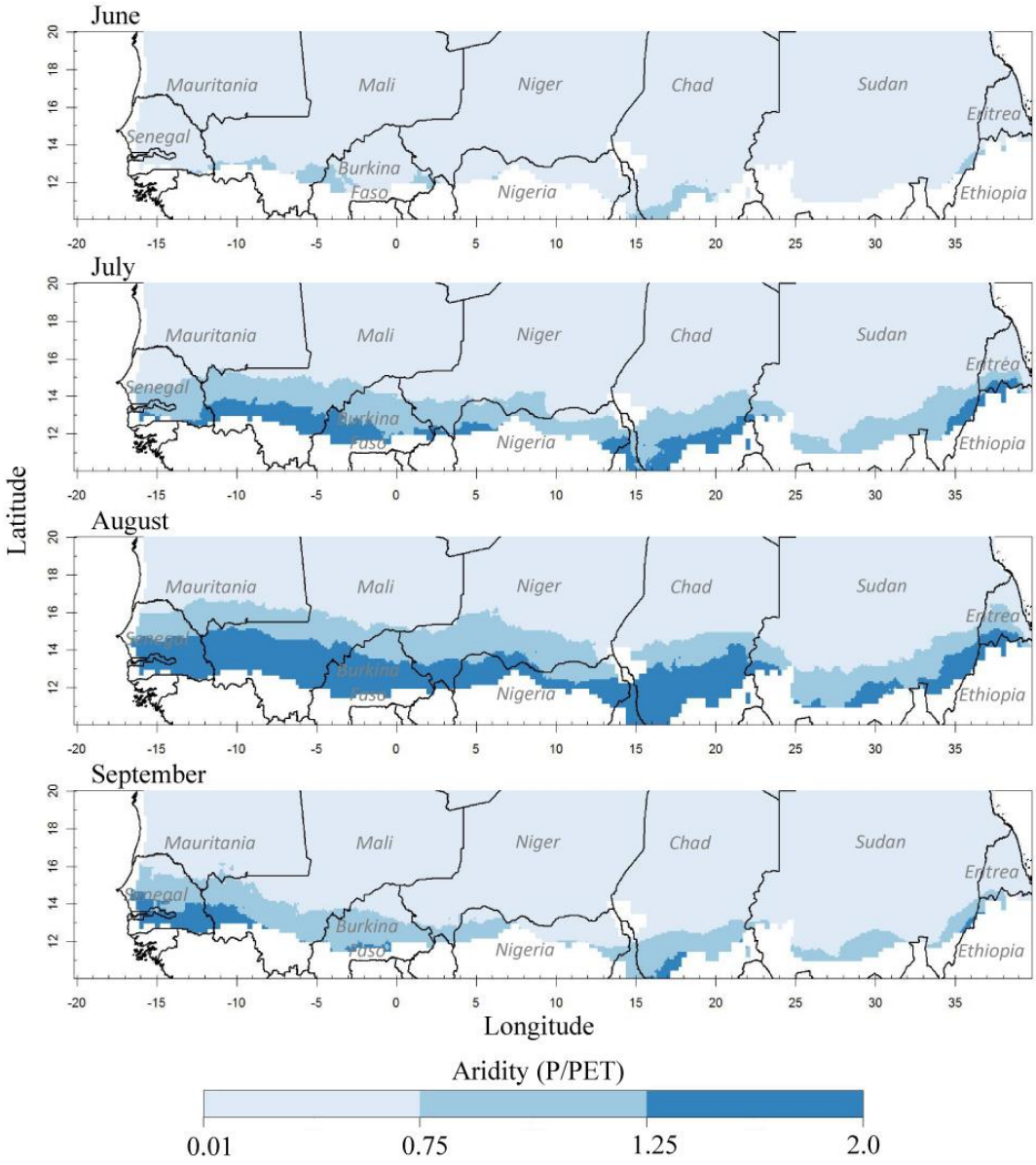

Figure 2

Fraction of PET variability explained by the statistical model (R^2). The statistical model uses the current temperature anomaly and the PET anomaly from the previous day to predict daily PET anomalies. The model is fit to each month of JJAS separately. Shown where cross-validated $R^2 > 0$

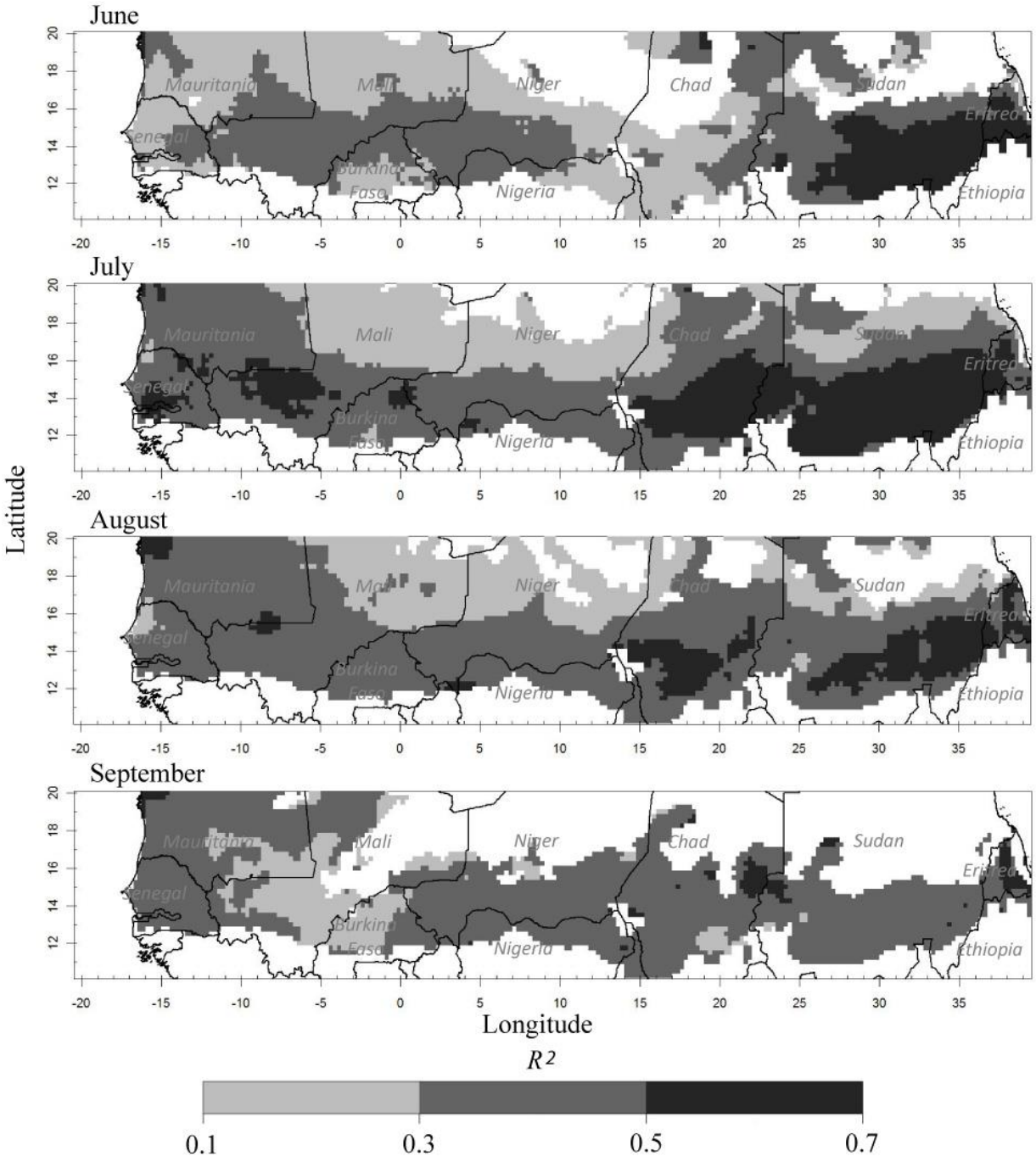

Figure 3

Potential evapotranspiration response to above average temperature (*PET-T*). The monthly total potential evapotranspiration (PET) anomaly (mm) associated with 1 °C above average is plotted. Anomalies are derived from local statistical regressions between temperature and PET with 2001-2010 data (β from Eq. 2). The model accounts for feedbacks between temperature, humidity, wind, and net radiation. Values are shown that were statistically significant at the 95% confidence level and cross-validated $R^2 > 0$.

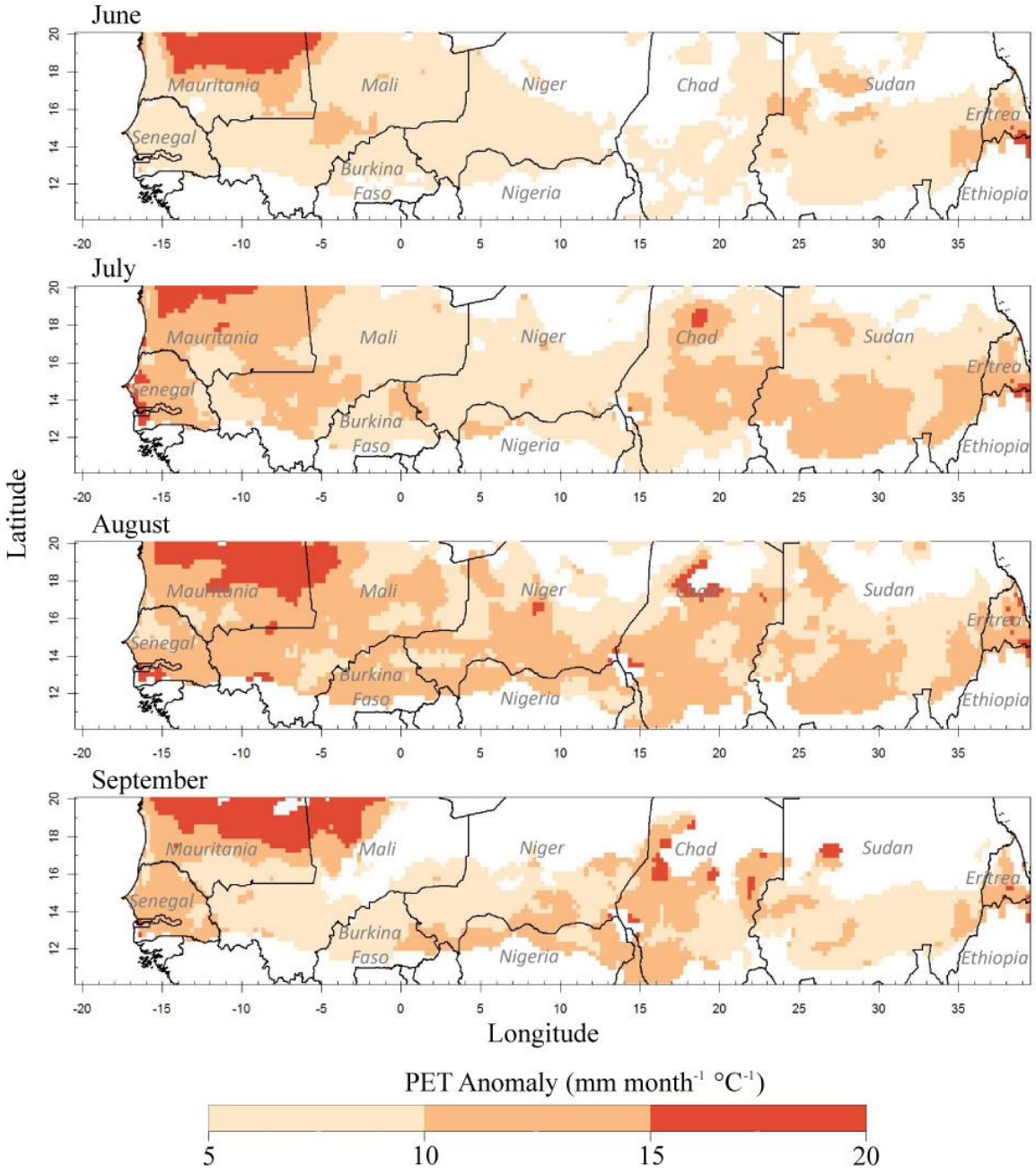

Figure 4

Mechanisms of overall potential evapotranspiration response to above average temperature (*PET-T*) as a function of mean June-September (JJAS) aridity. Aridity, which is described and mapped by month in Figure 1, is plotted on the x-axis. Boxplot whiskers show 1.5 times the inter-quartile range. a) JJAS mean *PET-T* (See Fig. 3 caption). b) Response of aerodynamic (*adPET-T)* and radiation (*rdPET-T*) components of PET to above average temperature. *adPET-T* and *rdPET-T* are estimated using simple linear regression. Sample size is based on statistical significance of these regressions.

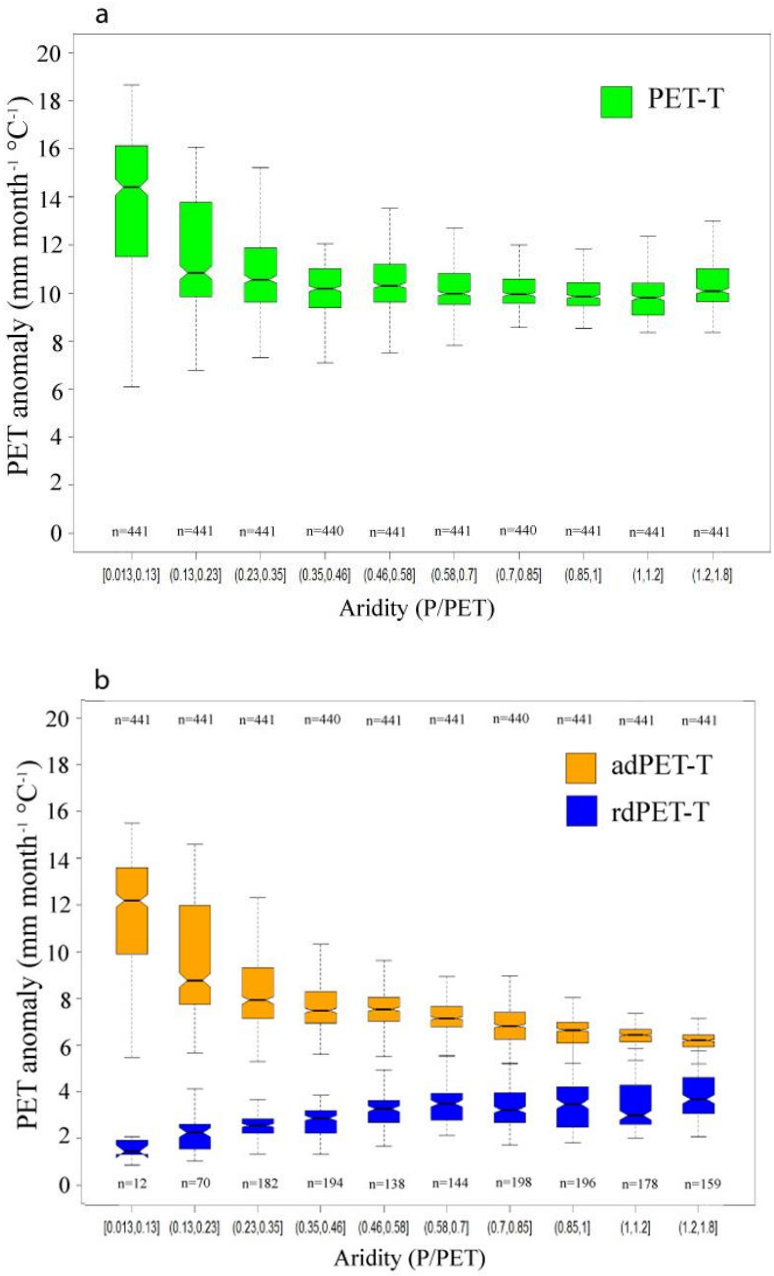

Figure 5

Extent to which vapor pressure deficit is the driver of monthly potential evapotranspiration response to above average temperature (*PET-T*). Plotted ratio values are the fraction of *PET-T* due to the PET aerodynamic component response to temperature (*adPET-T*); the remainder (1-ratio) is due to the PET radiation component response (*rdPET-T*). Values are shown where *PET-T* is statistically significant at 95% confidence level and cross-validated $R^2 > 0$

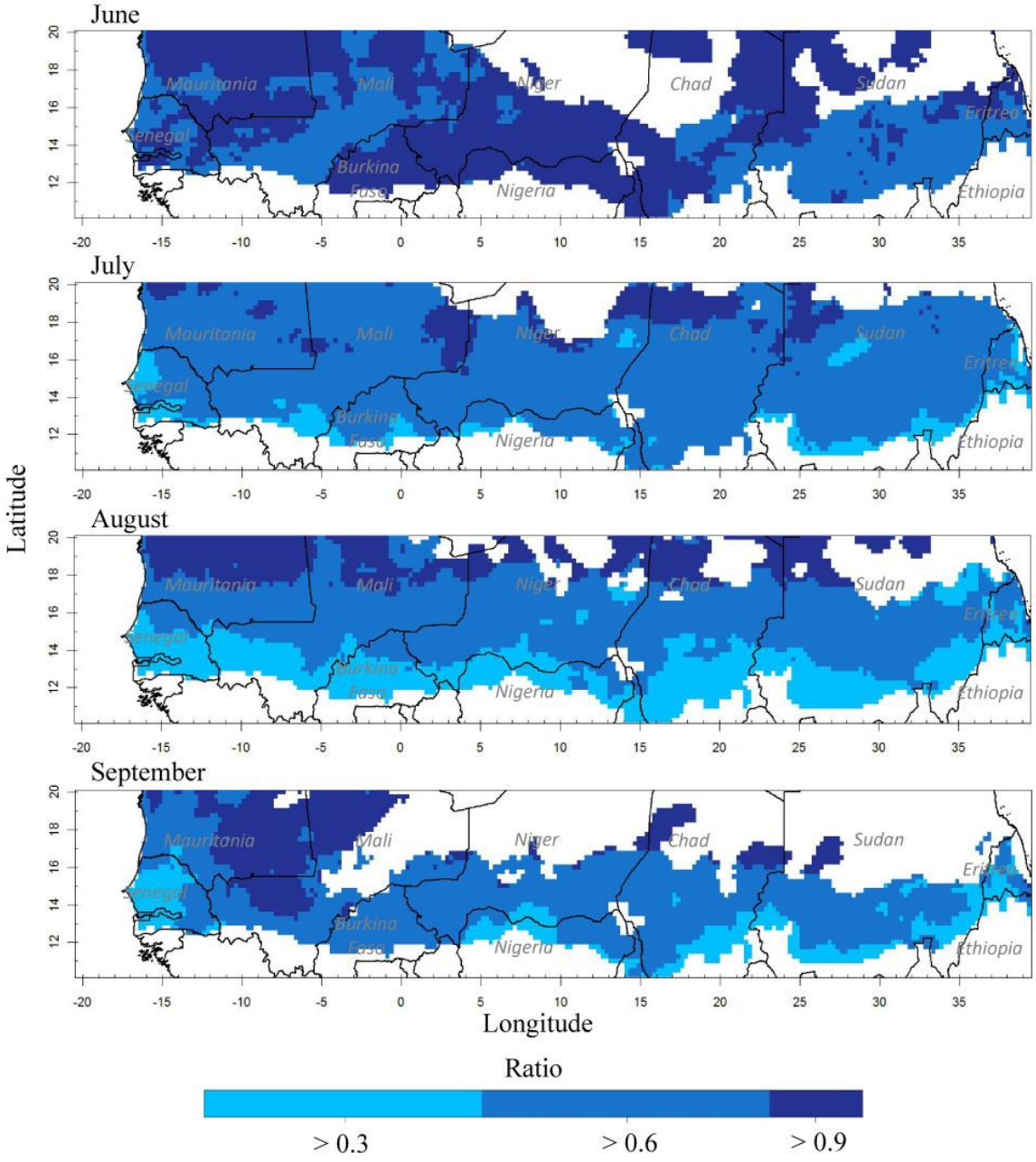

Figure 6

Projected monthly temperature change between 2001-2010 and 2026-2035 time periods. June-September temperature projections are from the World Climate Research Programme Coupled Model Intercomparison Project (CMIP5) multi-model ensemble mean of historical plus RCP4.5 greenhouse gas emissions scenario simulations. Models are listed in Section 3.2.2.

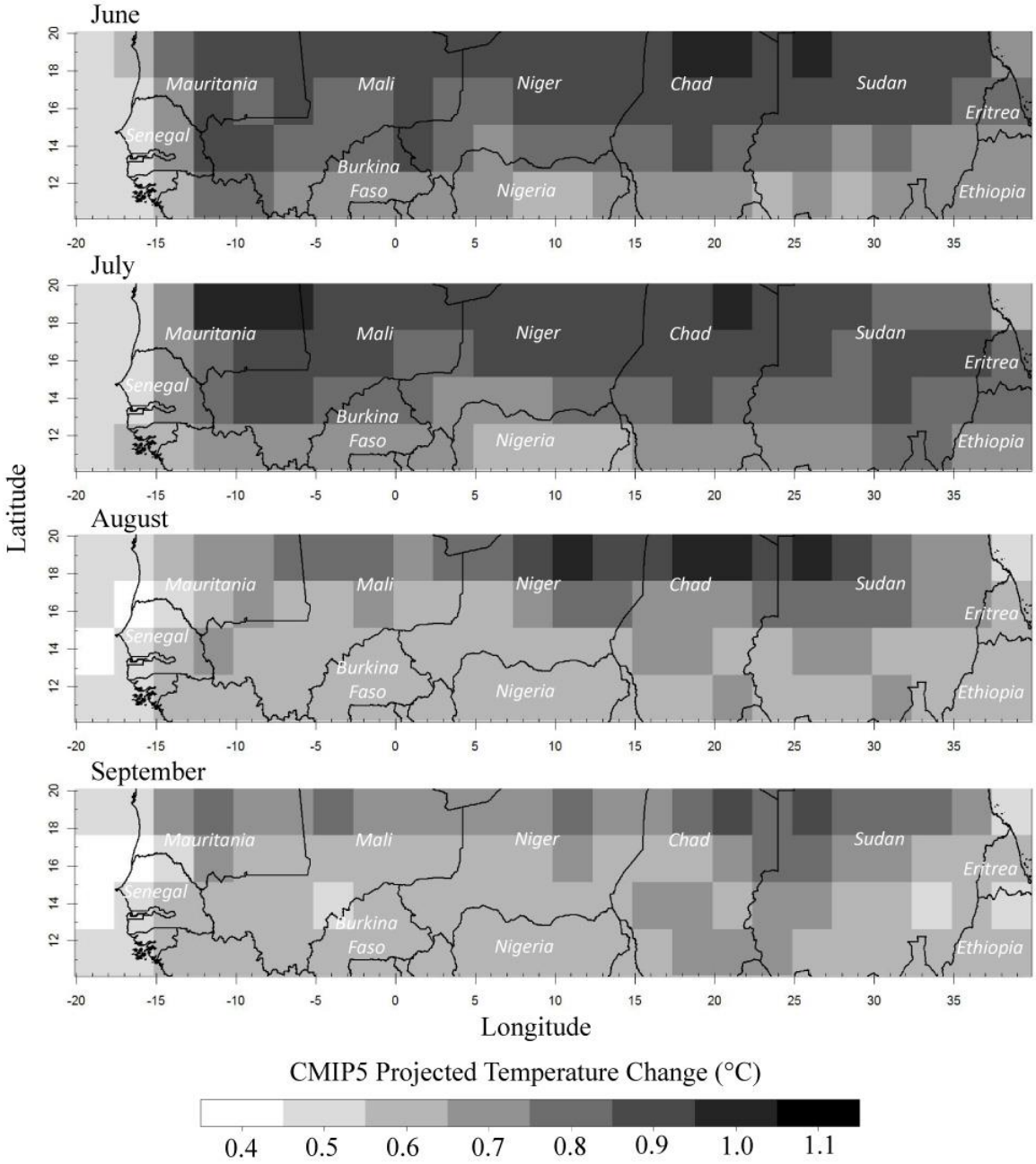

Figure 7

Projected impact of regional warming on millet water stress. a) Average millet WRSI for 2001-2010. b) Projected change to WRSI by 2026-2035 (percent difference; all values are negative). Calculated with rainfall for 2001-2010, potential evapotranspiration for 2001-2010 and 2026-2035, and the USGS GeoSpatial Water Requirement Satisfaction Index model (GeoWRSI)

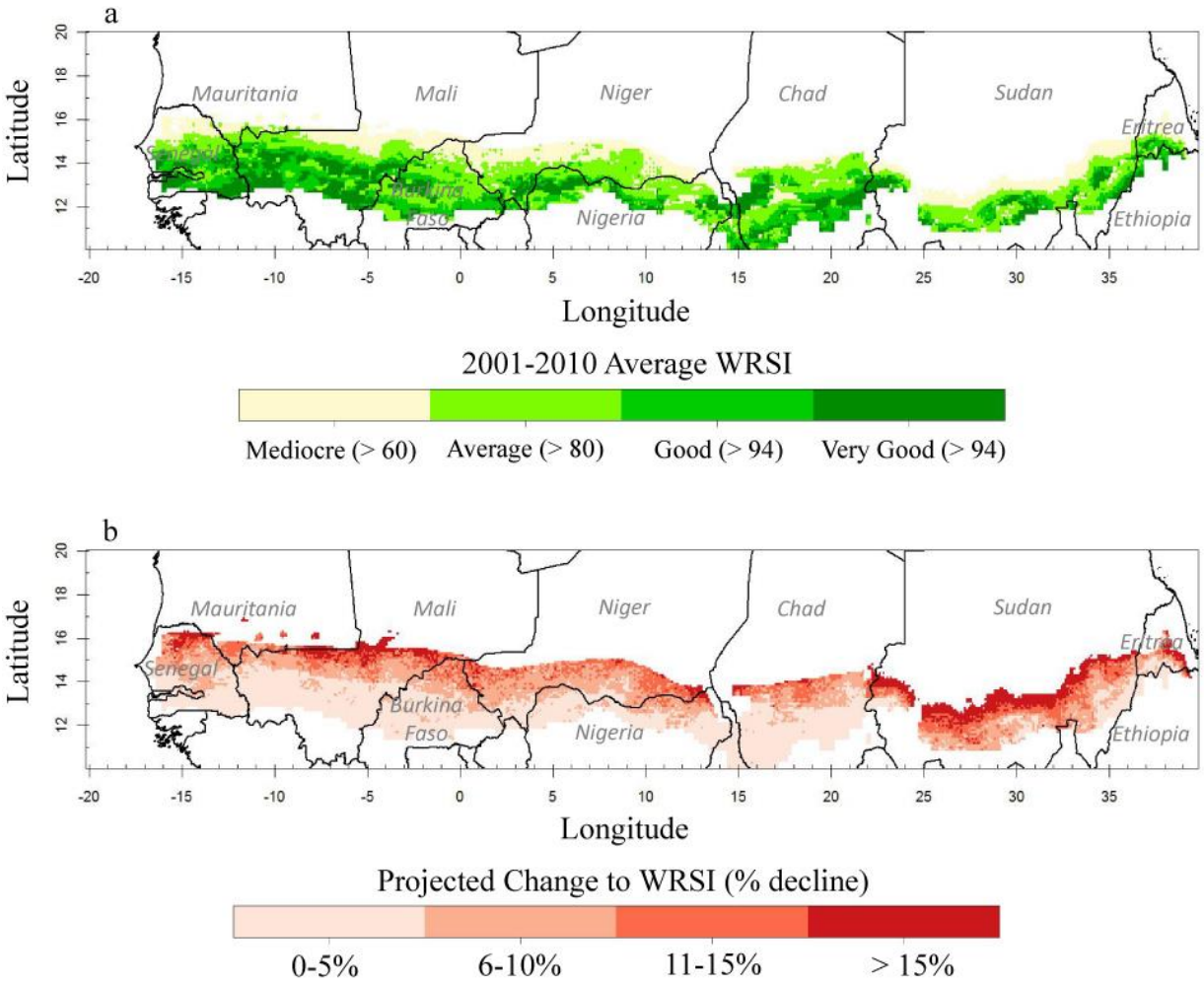

Figure 8

Projected water deficit during initial, vegetative, reproductive, and ripening stages of millet growth for the 2026-2035 period. Deficits are due to the impact of near-term warming on plant water balance. Calculated with rainfall for 2001-2010, potential evapotranspiration for 2001-2010 and 2026-2035, and the USGS GeoSpatial Water Requirement Satisfaction Index model (GeoWRSI)

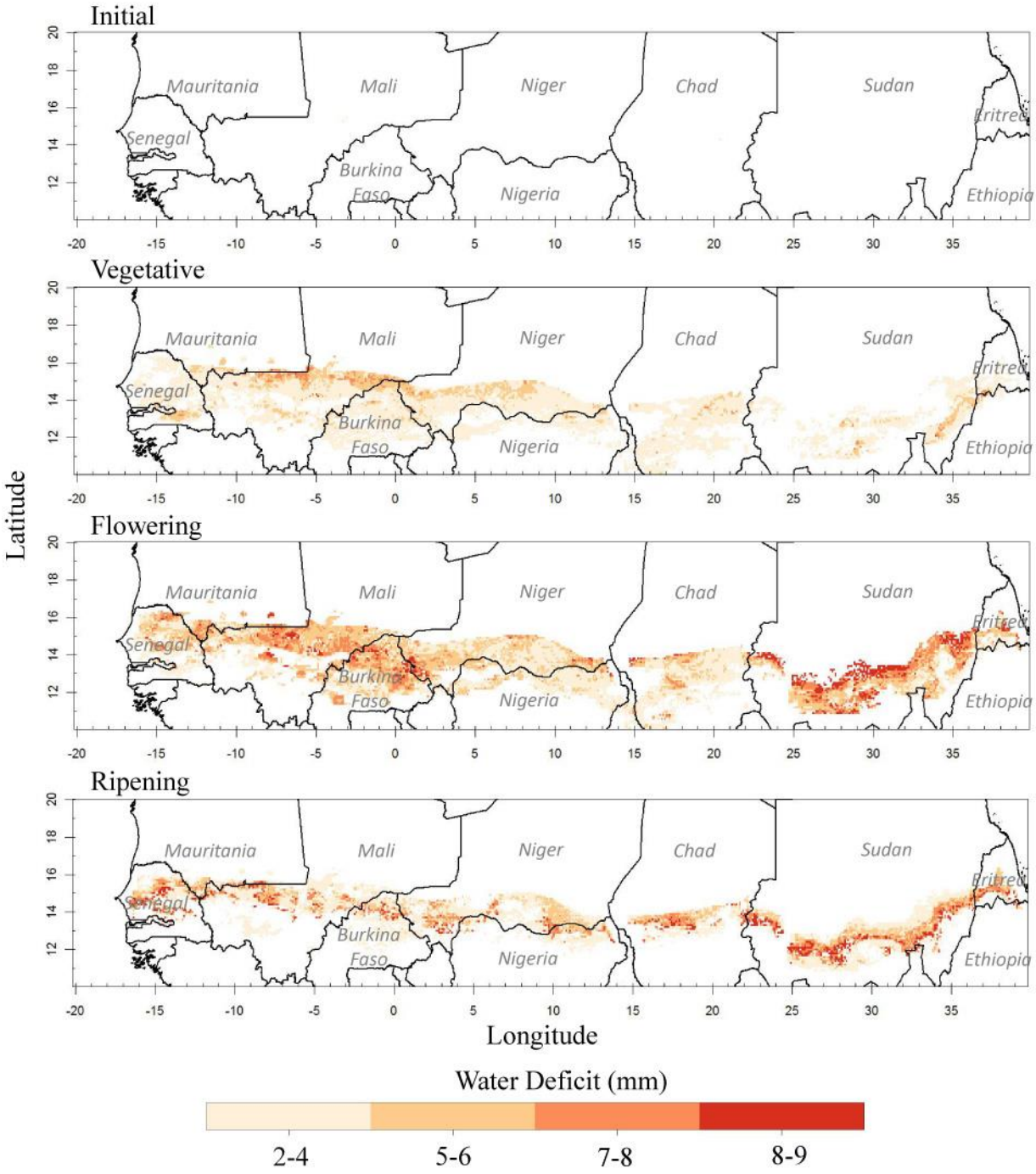

Figure 9

Projected changes to the frequency of good and poor growing seasons in the Sahel due to near-term warming. Upper and lower 20th percentile end of season millet WRSI (WRSI) values are calculated for 2001-2010. Top two panels show frequency of good growing seasons (upper 20th percentile WRSI) for (a) 2001-2010 and (b) 2026-2035. Bottom two panels show frequency of poor growing seasons (lower 20th percentile WRSI) for (c) 2001-2010 and (d) 2026-2035

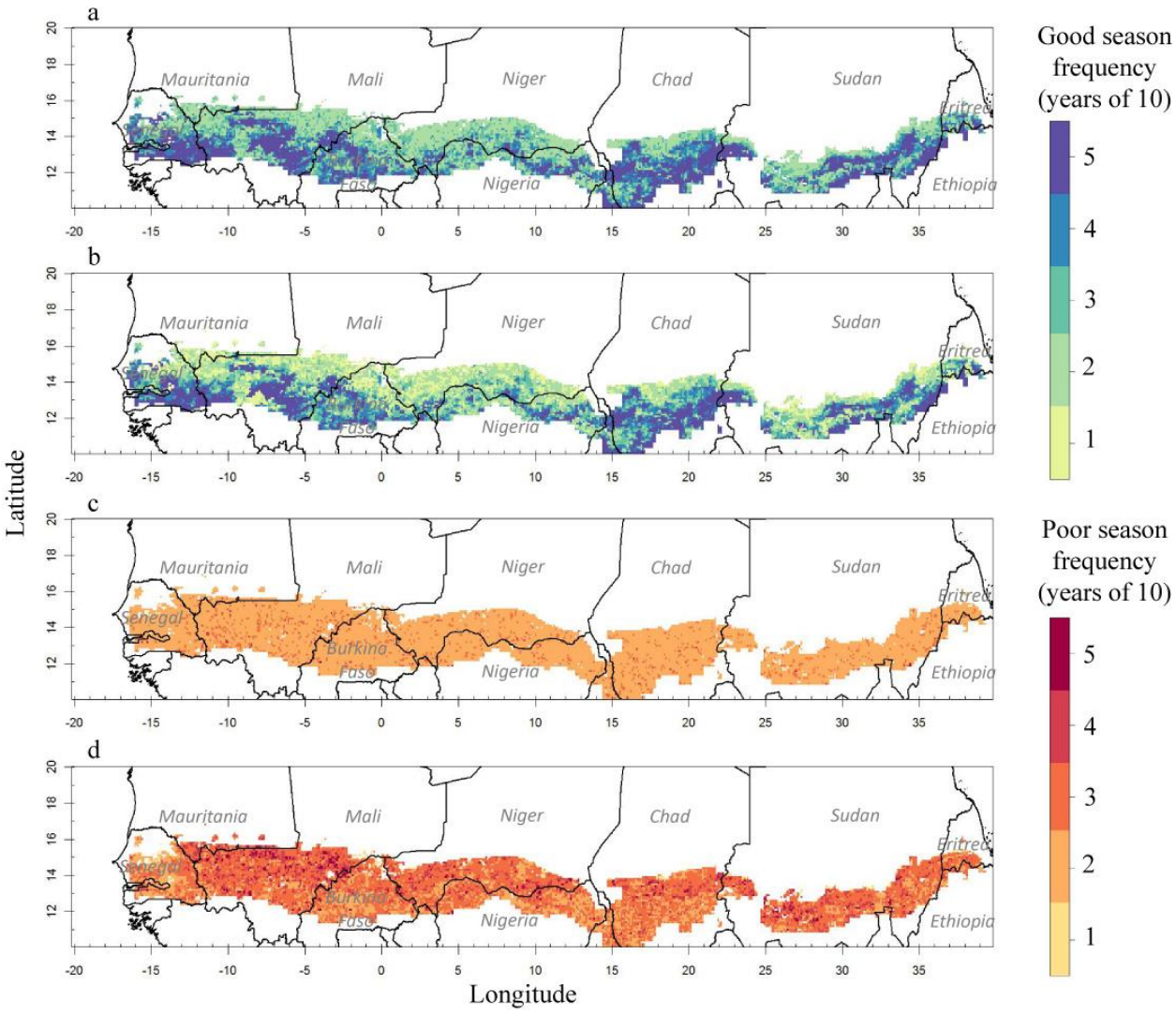

Chapter 2

Figure 1

Influence of soil moisture on the surface energy budget. Processes involved in heat transfer to and from the surface are shown in the case of (a) dry soil, (b) moderately dry soil, and (c) wet soil. Each panel shows radiative fluxes through incoming solar radiation, the influence of surface albedo, and upwelling longwave radiation. Panels also show non-radiative heat transfer through conduction and turbulent mixing (evaporation and sensible heating). Figure from The Comet Program https://www.meted.ucar.edu/nwp/model_physics/print.htm

When soil is wet, most energy leaves the surface through evaporation and cools the surface. A decline in soil moisture forces less energy transfer through evaporation and more energy transfer through sensible heating. Sensible heating is much less effective at removing heat from the surface than evaporation, so declines in soil moisture can lead to a warmer surface, as shown by higher emission of upwelling longwave radiation in the dry soil example.

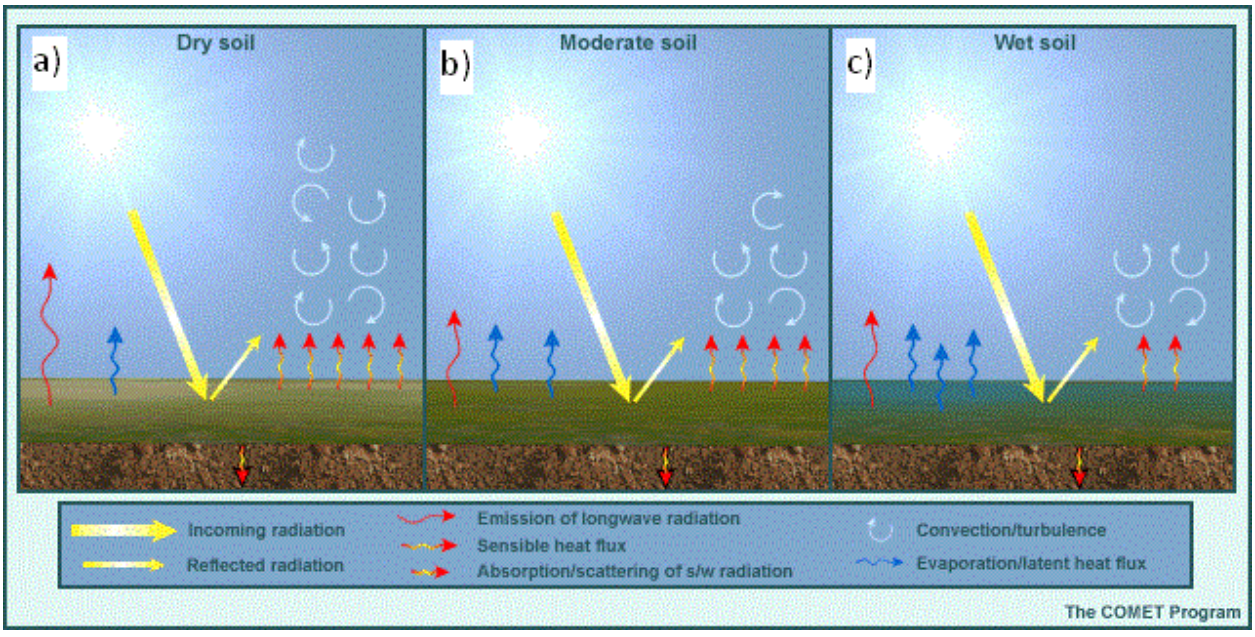

Figure 2

Relationship between upwelling longwave radiation and surface temperature. The map shows pearson correlation between April mean upwelling longwave radiation and surface temperature from the 0.25° monthly Global Land Data Assimilation System Noah dataset for the 2002-2011 period (GLDAS_NOAH025_M, Rodell et al., 2004).

In the FLDAS output monthly average surface temperature was not available, so we use upwelling longwave radiation to examine annual deviations in surface heating. In this figure we show that upwelling longwave radiation calculated from land surface model output has very similar interannual variability as the land surface model's surface temperature output. The data used to create this figure is from a NASA GLDAS land surface model experiment that also uses the Noah land model. Upwelling longwave radiation was calculated using the same method as was used with the FLDAS data.

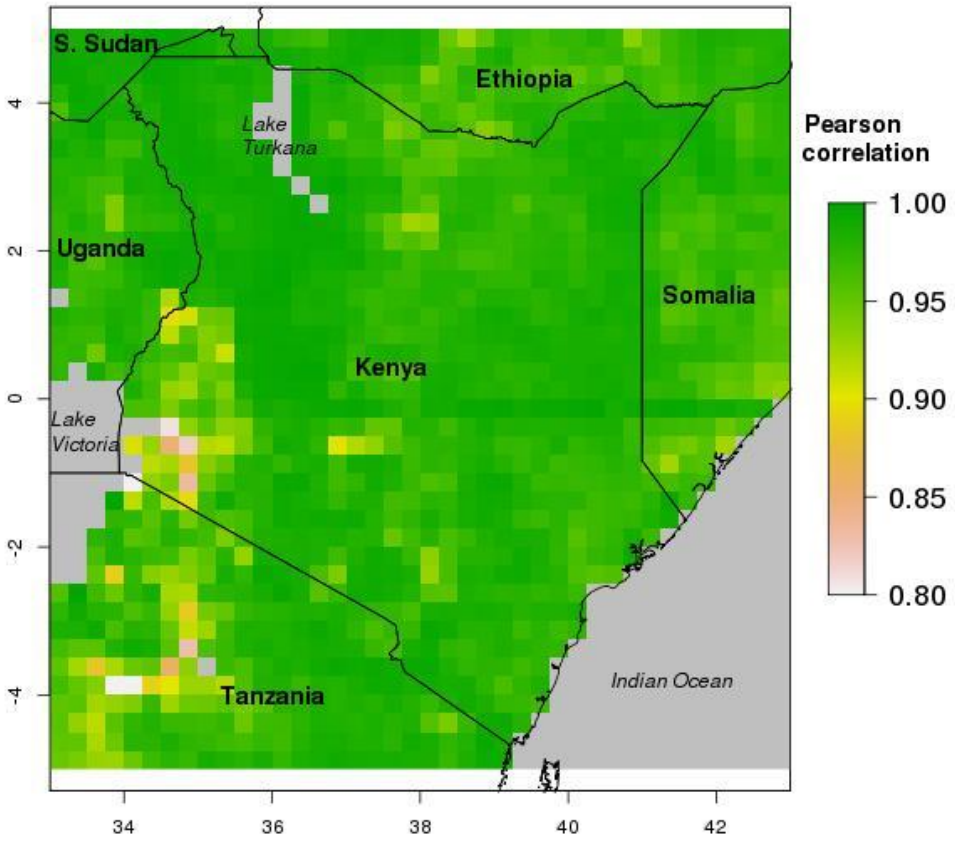

Figure 3

April rainfall and vegetation density in the East Africa domain. (a) Mean April daily rainfall (mm day^{-1}) and (b) mean April green vegetation fraction (shown as a percent).Data from RFE 2.0 (Xie and Arkin, 1997) and NCEP (Gutman and Ignatov, 1998)

a)

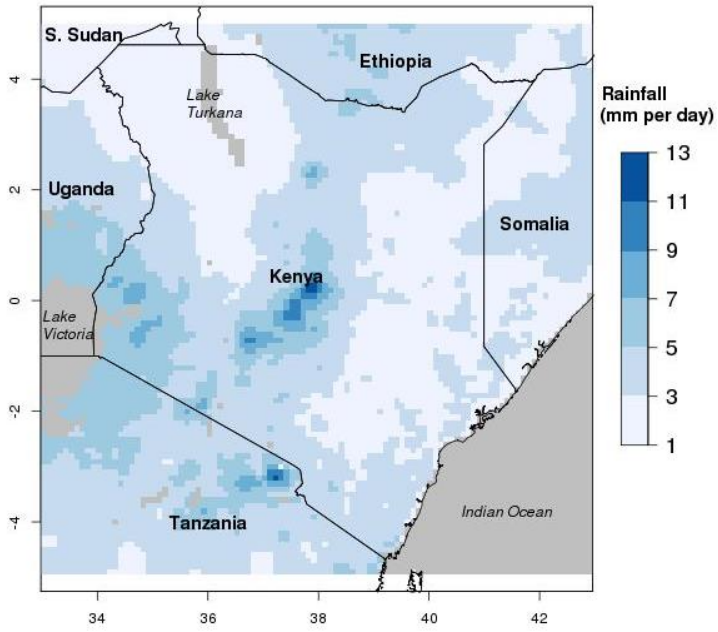

b)

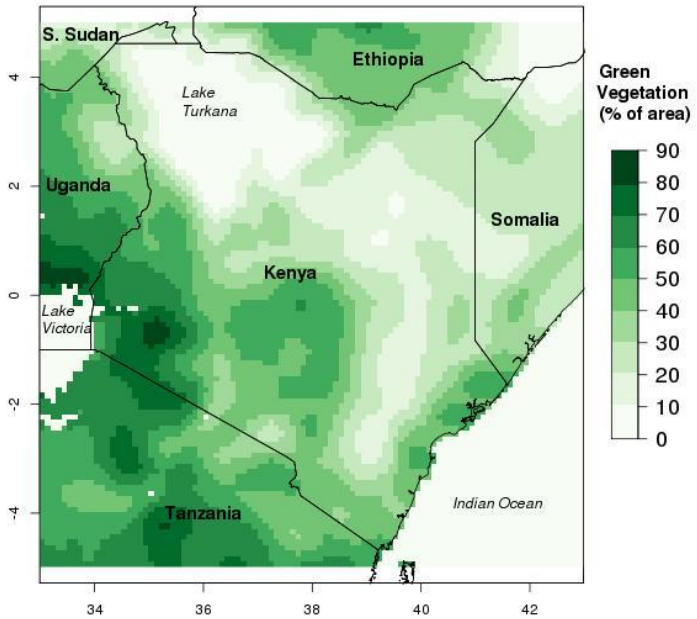

Figure 4

Noah Land Surface Model. This schematic shows hydrologic processes that are simulated in the Noah land surface model. Our analysis examines the influence of radiative and turbulent energy transfer processes on the surface energy budget through the lens of surface heating and cooling. The energy budget is intimately linked to dynamics in the surface water budget. In the FLDAS experiment, atmospheric data (precipitation, humidity, insolation, downwelling longwave radiation, etc.) from RFE 2.0 (Xie and Arkin, 1997) and NCEP's Global Data Assimilation System (GDAS) (Derber et al., 1991) are used to force the Noah land surface model v3.2 (Chen et al., 1996; Ek et al., 2003) in uncoupled mode.

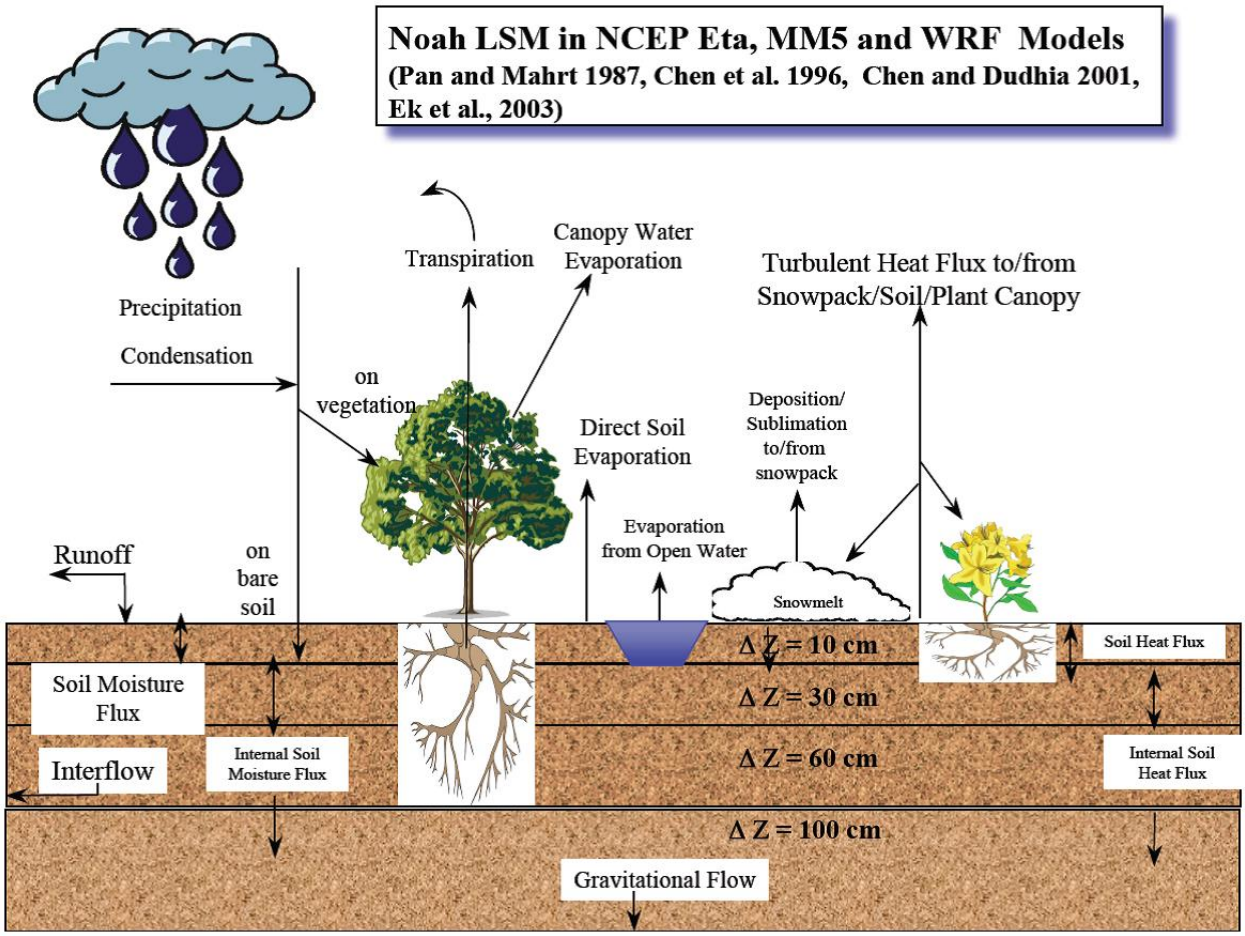

Figure 5

Surface heating correspondence to radiative forcing and evapotranspiration, 2002-2011. Mapped Pearson correlation between upwelling longwave radiation, LWup, and (a) radiative forcing, RF, and (b) latent heat flux, L. Data are monthly means for April from the FLDAS Noah simulation.

a)

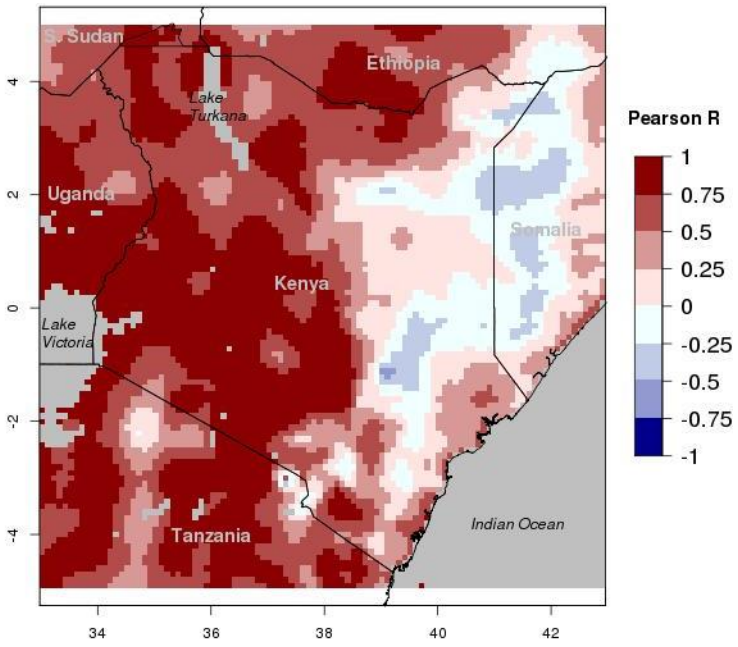

b)

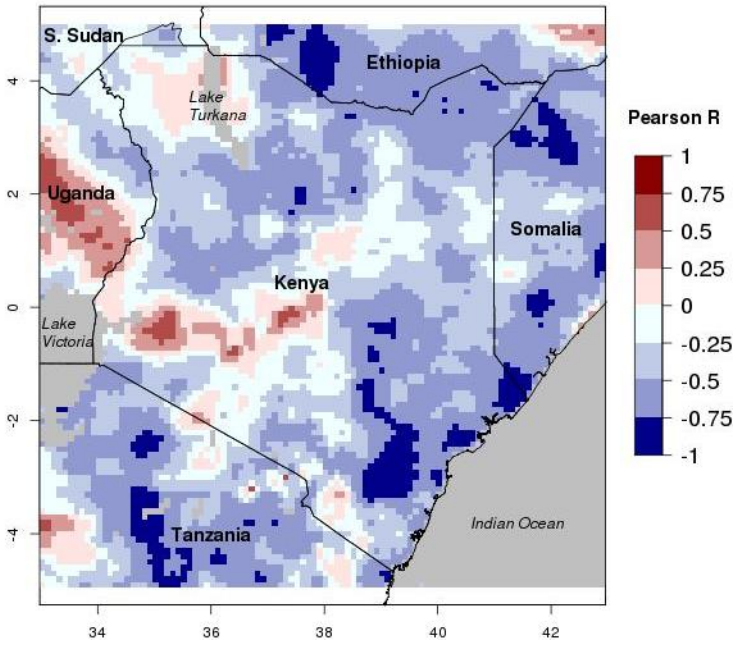

Figure 6

Radiative forcing interannual variability is driven by insolation. Maps show the standard deviations of April mean (a) radiative forcing (RF = SWnet + LWdown), (b) net shortwave radiation and (c) downwelling longwave radiation for 2002-2011. Data from the FLDAS experiment.

a)

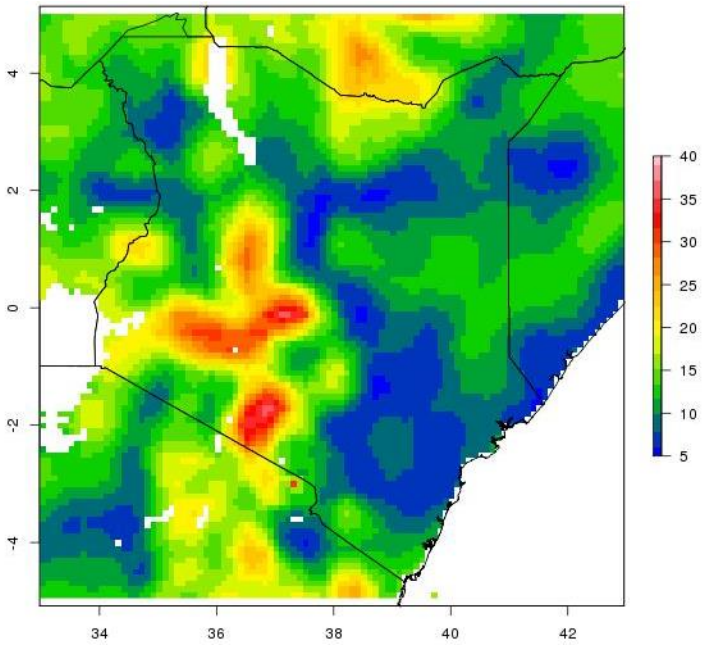

b)

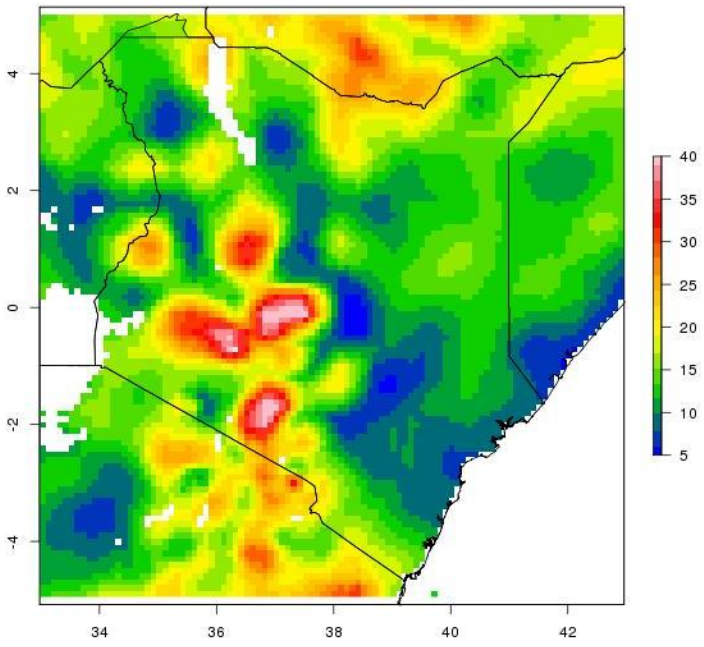

c)

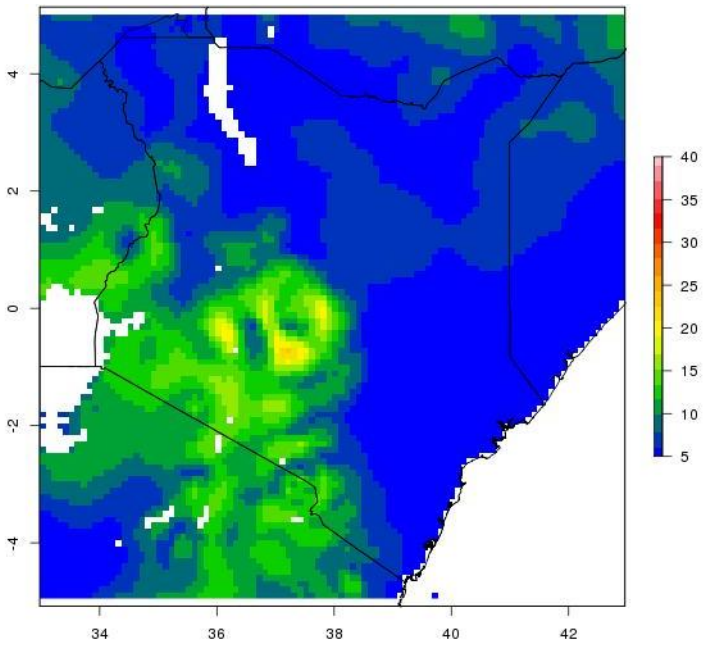

Figure 7

Major driver of annual variation in upwelling longwave radiation varies geographically. Overall influence of turbulent heat flux (TF) on interannual surface heat variability, 2002-2011. The ratio of turbulent flux forcing to upwelling longwave radiation (LWup) variability is mapped. Ratio values < 0 means TF had no influence on LWup, from 0 to 1 indicate percent of TF control (0-100%), and > 1 means TF had full control of LWup variability, outweighing any influence by radiative forcing (RF). Ratio = [Var(TF) – Cov(TF,RF)] / Var(LWup). Data are monthly means for April from the FLDAS Noah v3.2 LSM simulation.

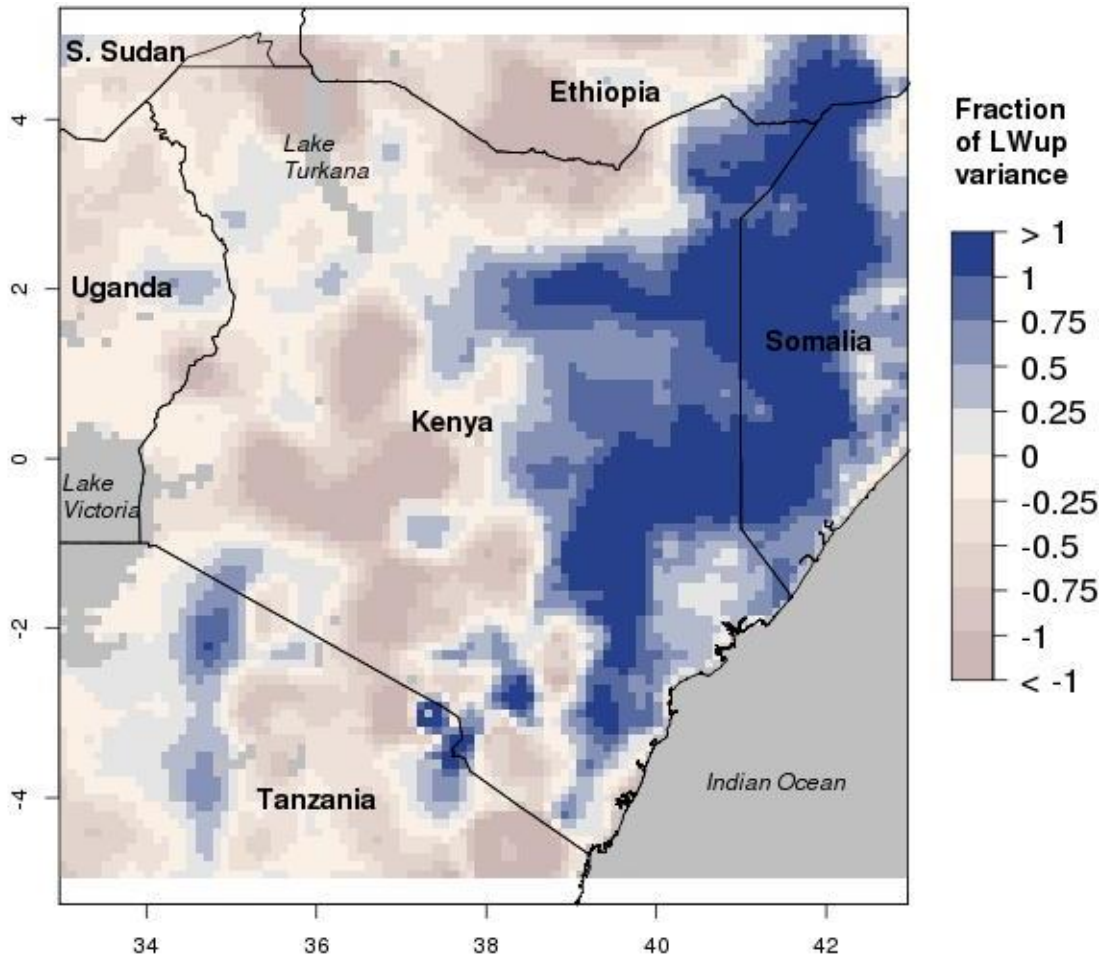

Figure 8

Regression tree classification of geographic variability. Classification of the region by primary driver of surface heating. The regression tree shows the thresholds that best define the regional pattern of upwelling longwave radiation (LWup) forcing (Figure 1). Explanatory variables are Pearson correlation between annual April turbulent heat flux and latent heat flux (Correlation.TF.L), mean April green vegetation density (GreenVeg, %), and mean daily April rainfall (MeanRain, mm day^{-1}). Labels show number of grid cells that fall into each group, their mean value, and the percent of total areal coverage of the 10° x 10° east Africa domain. Values correspond to Figure 1, where < 0 means TF has no influence on LWup, from 0 to 1 shows the percent of LWup variability driven by T , and > 1 means TF fully controlled LWup variability.

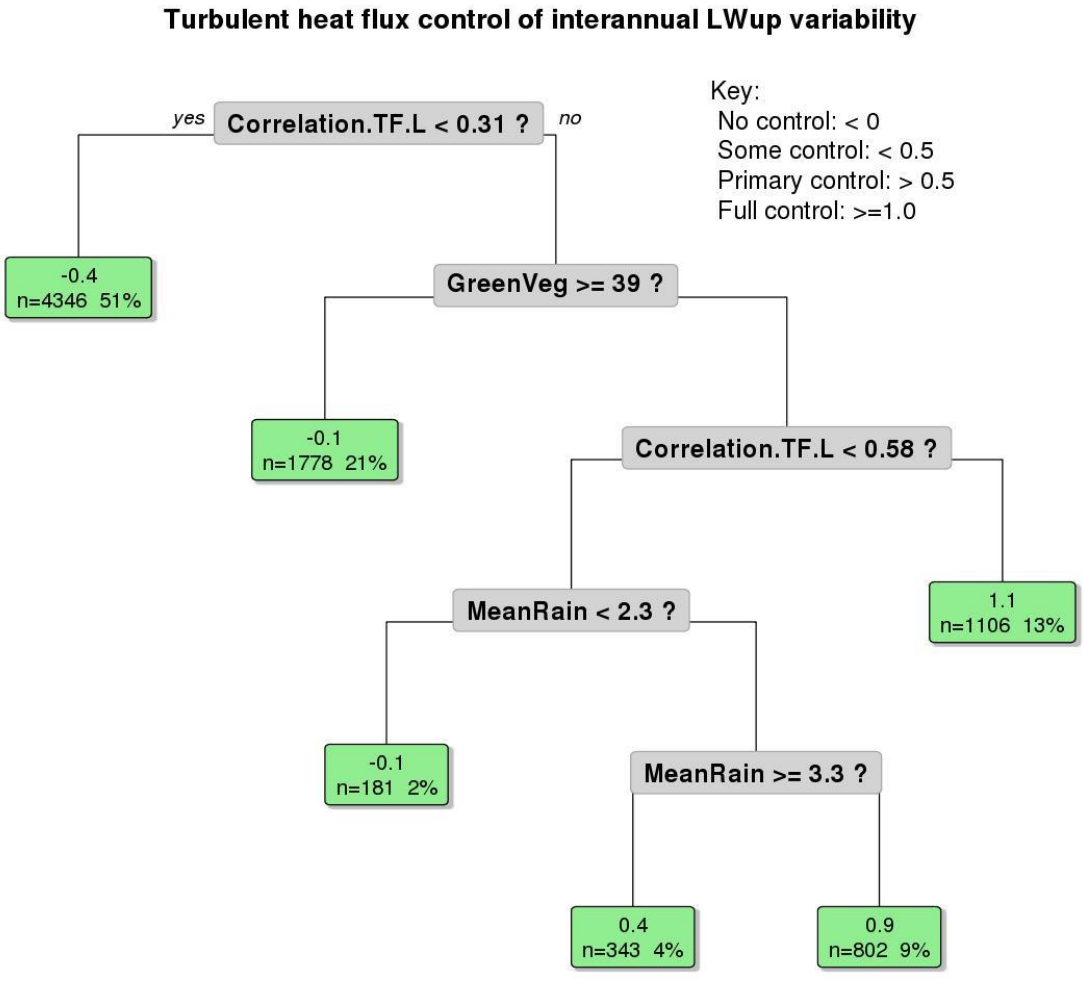

Figure 9

Geographic attributes that correspond to the regional pattern of LWup forcing. Map a shows the Pearson correlation between annual April turbulent heat flux and latent heat flux (Correlation.TF.L) using thresholds defined by the regression tree. In b, mean April green vegetation density (%) is overlaid on a 3D elevation surface. Elevation is exaggerated 1000x.

a)

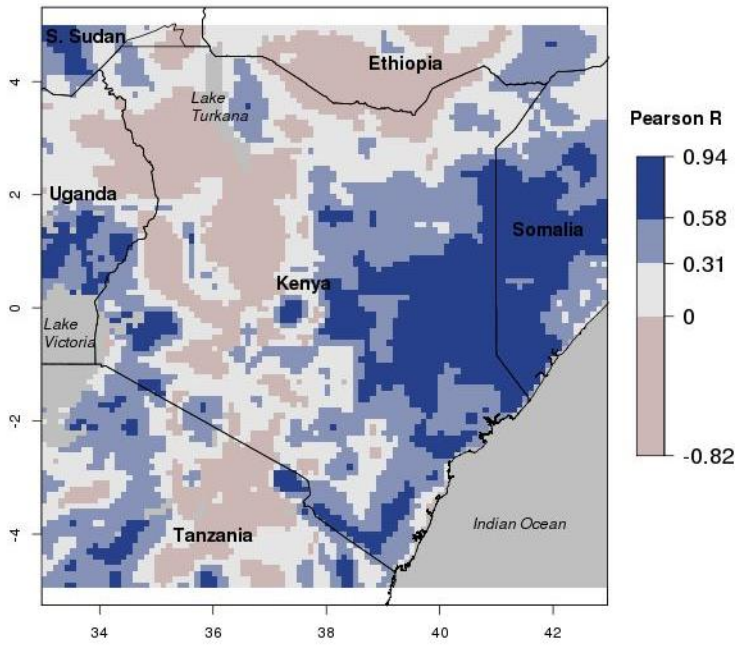

b)

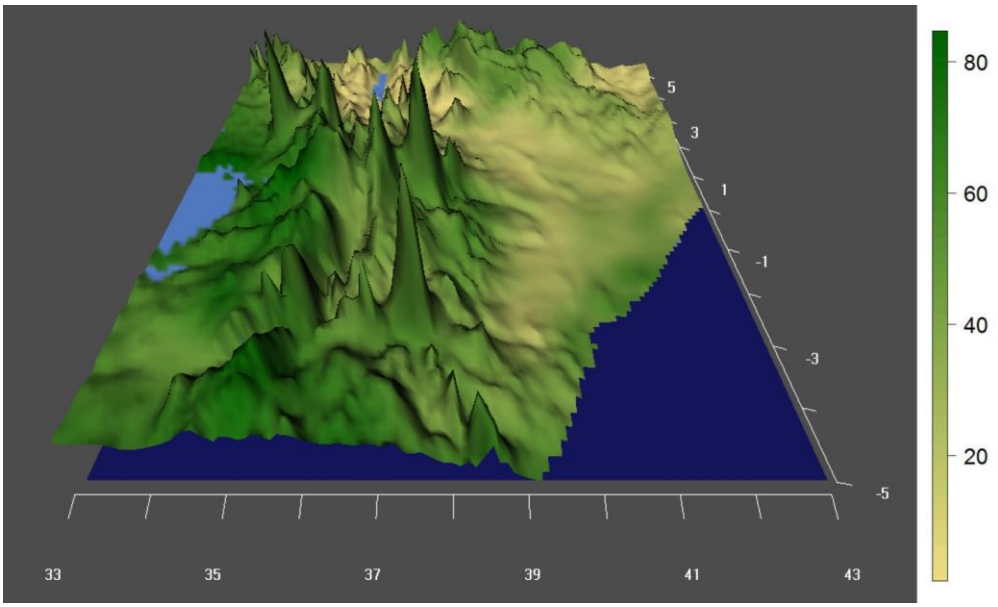

Figure 10

Instances of large and small-scale anomalous heat events during 2002-2011. Bar charts show the area that exhibited anomalous surface heating in each April of 2002-2011 and the responsible forcing. Anomalous surface heating is defined as > 75th percentile upwelling longwave radiation. Area is plotted in terms of the percent of the domain (33 °E – 43 °E, 5 °N – 5 °S) with LWup above this threshold. Bars show the total area with heating (purple) and the area attributed to radiative forcing, RF (orange), turbulent heat flux forcing, TF (green), and a mix of both RF and TF (blue).

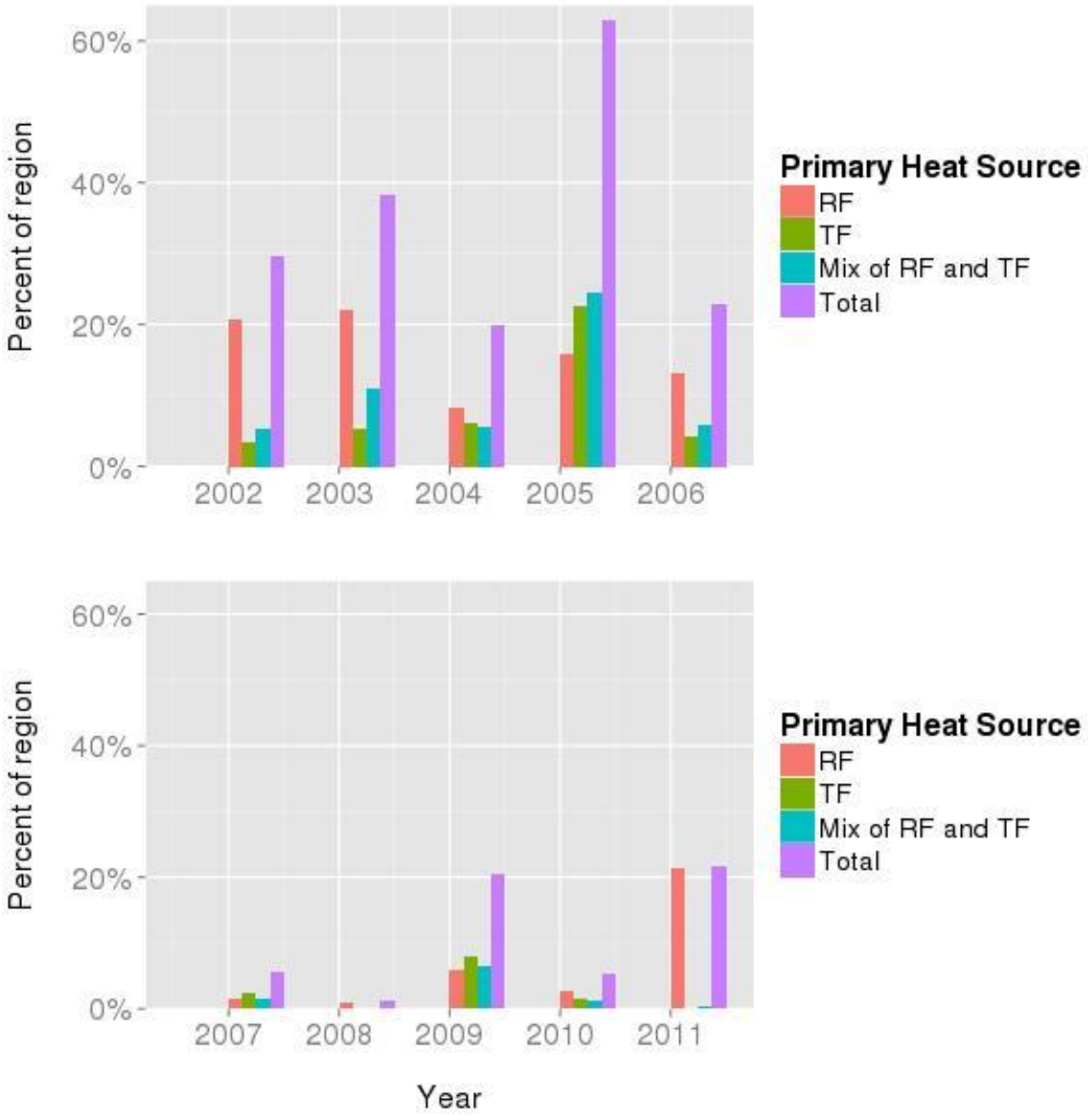
60%
40%
20%
0%
Percent of region
2002
2003
2004
2005
2006
Primary Heat Source
RF
TF
Mix of RF and TF
Total
60%
40%
20%
0%
Percent of region
2007
2008
2009
2010
2011
Year
Primary Heat Source
RF
TF
Mix of RF and TF
Total

Figure 11

Factors for surface heating in April 2005. Panels show atmospheric and energy flux variables that were influenctial in generating large-scale anomalous surface heating in April 2005. a) Upwelling longwave radiation, LWup, anomaly, (W m^{-2}), b) LWup anomaly attributed to radiative forcing (W m^{-2}), c) LWup anomaly attributed to turbulent heat flux forcing (W m^{-2}), d) Latent heat flux anomaly (W m^{-2}), e) Sensible heat flux anomaly (W m^{-2}), f) Air temperature anomaly (°C), g) Surface temperature minus air temperature (°C), h) Net shortwave radiation anomaly (W m^{-2}), i) Downwelling longwave radiation anomaly (W m^{-2}). Data for d and e are from GLDAS Noah 0.25° resolution monthly simulation (GLDAS_NOAH025_M) from http://disc.sci.gsfc.nasa.gov/hydrology/data-holdings. All other data from FLDAS Noah simulation.

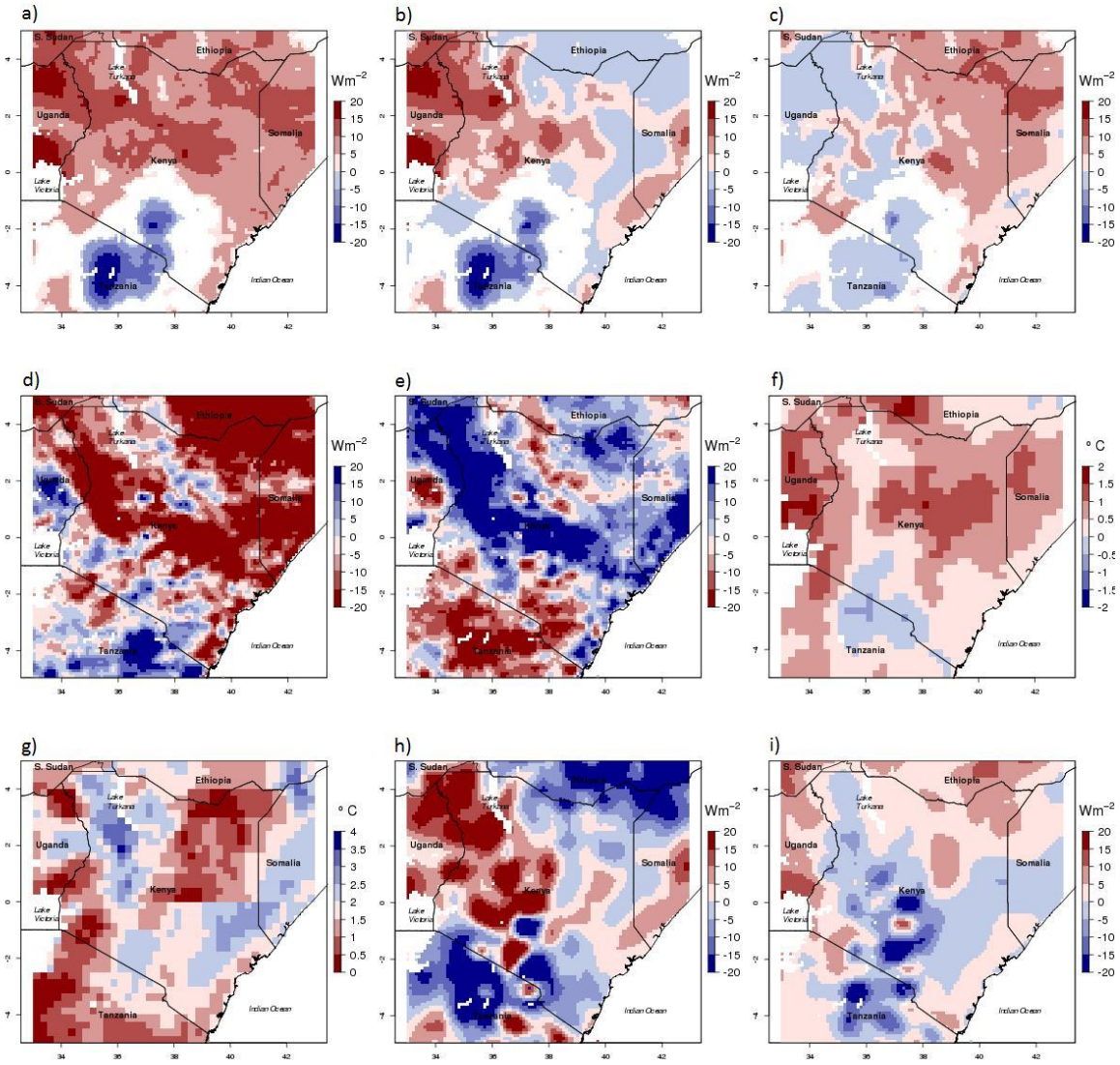

Figure 12

Drought-related surface heating in April 2011. Panels show factors that lead to anomalous surface heating in some parts fo east Africa during the 2011 drought. a) Upwelling longwave radiation, LWup, anomaly, (W m^{-2}), b) LWup anomaly attributed to radiative forcing (W m^{-2}), c) rainfall anomaly (mm mo^{-1}), d) Net shortwave radiation anomaly (W m^{-2}), e) Latent heat flux anomaly (W m^{-2}), f) Sensible heat flux anomaly (W m^{-2}). Data from FLDAS Noah simulation.

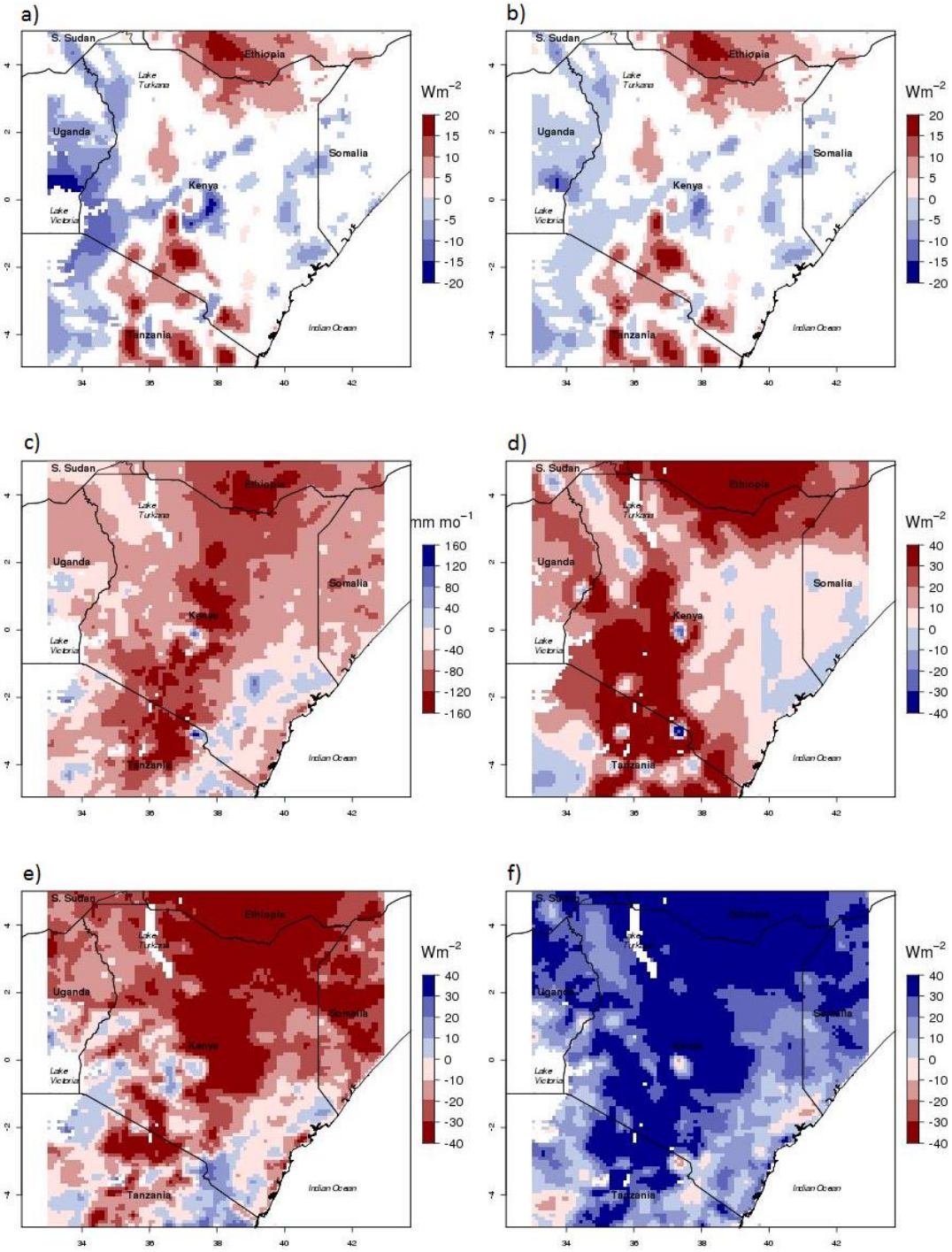

Figure 13

Radiation-driven surface cooling events in April 2007 and 2008. Panels show the location and intensity of anomalous surface cooling in April 2007 and 2008 and how the cooling corresponded to below average net shortwave radiation. Upwelling longwave radiation anomaly attributed to radiative forcing (W m^{-2}) and net shortwave radiation anomaly (W m^{-2}) for April 2007 (a and b) and April 2008 (c and d). Data from FLDAS Noah simulation.

.

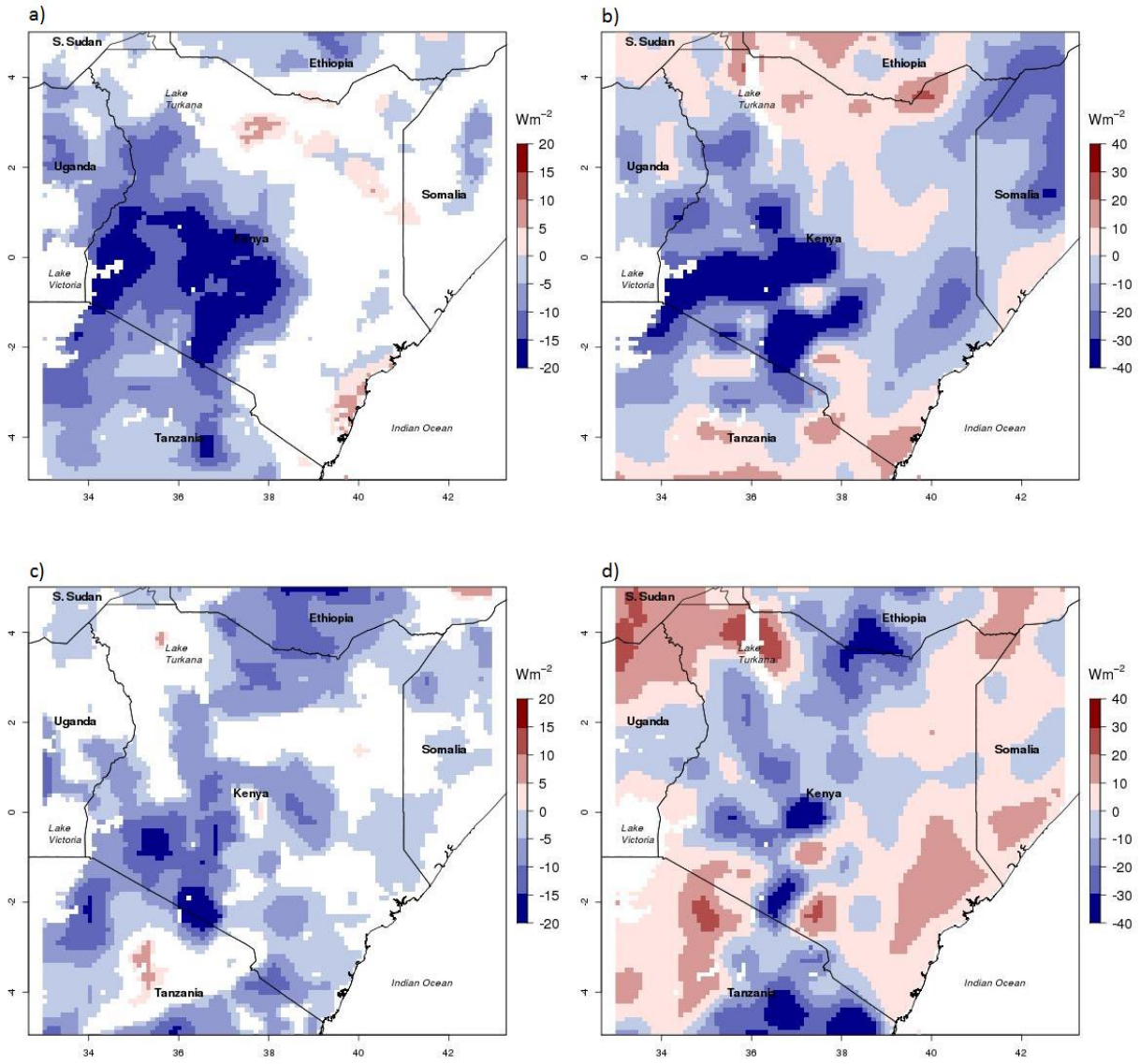

Figure 14

Widespread evaporative cooling in April 2010. In April 2010 high evaporation rates played a major role in the anomalous surface cooling that occurred throughout the region. Below average net shortwave radiation was also an important factor. Panels show the anomalous upwelling longwave radiation attributed to these factors. a) radiative forcing (W m^{-2}) and b) turbulent heat flux forcing (W m^{-2}), c) Net shortwave radiation anomaly (W m^{-2}), d) Latent heat flux anomaly (W m^{-2}). Data from FLDAS Noah simulation.

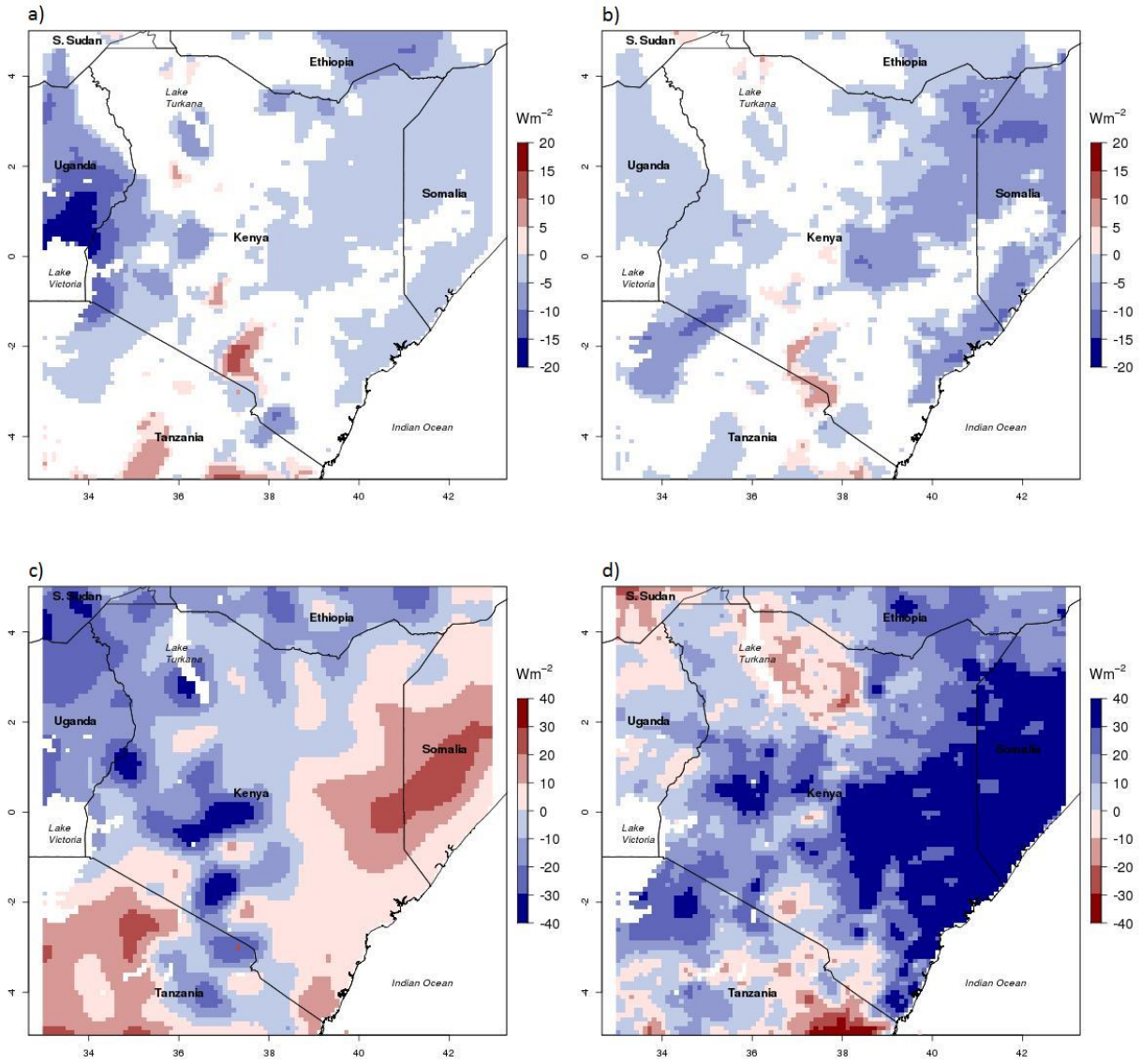

Figure 15

Identifying the cause of surface heating using vegetation density. The frequency of radiation-driven (a) and turbulent heat flux-driven (b) anomalous surface heating and cooling events (2002-2011) are displayed as a function of vegetation density using boxplots. The plots show that in wet and heavily vegetated areas the surface energy state is primarily driven by variations in energy and that in semi-arid and less vegetated areas variations in water supply become important factor. This is similar to relationships seen in observed surface temperature and vegetation index data. It is important to note the wide range of scenarios that can occur within an ecosystem type, and that it is differences in atmospheric conditions that are responsible. Data from the FLDAS experiment.

a)

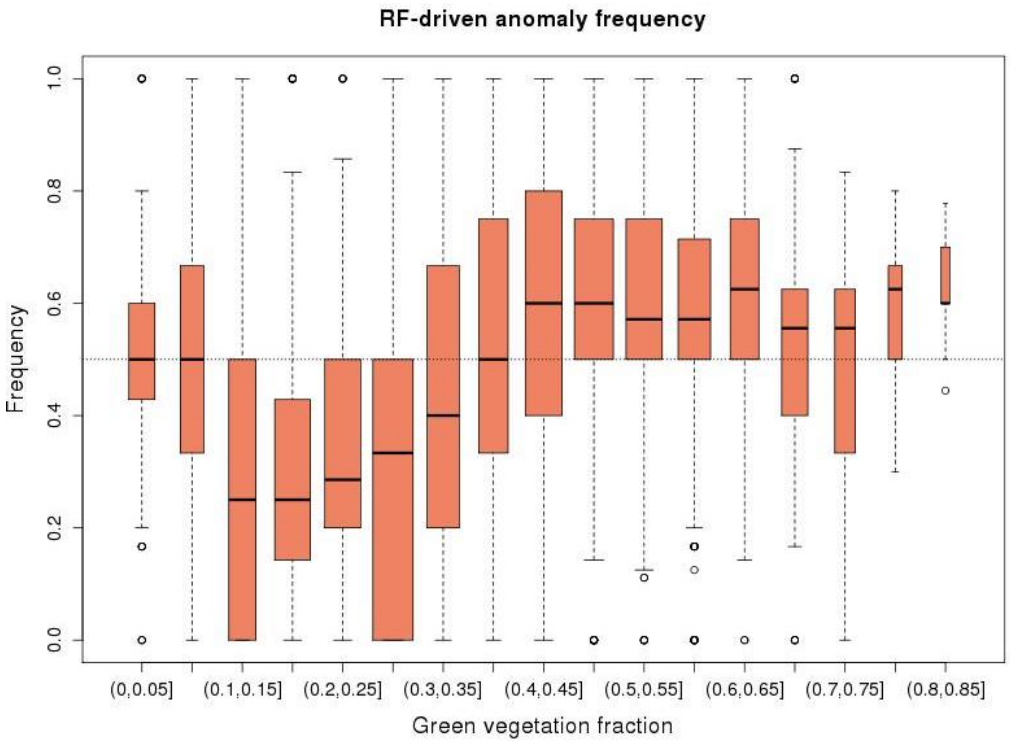

b)

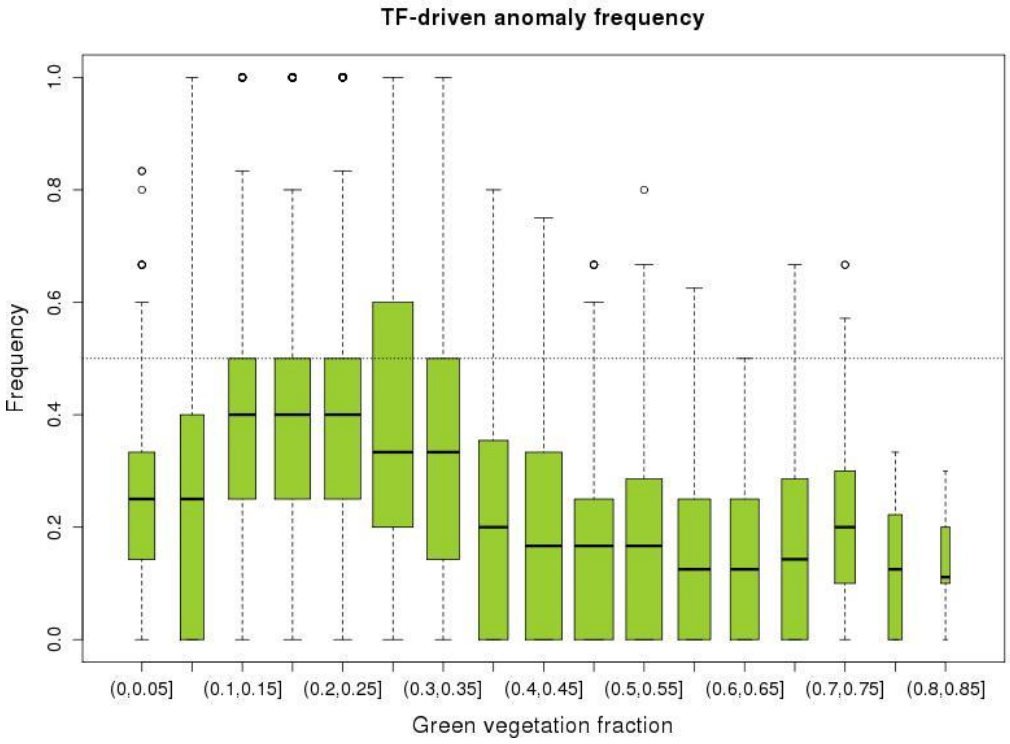

Supplement

Figures S1 and S2 are below the captions

Figure S1 caption: Distribution of anomalies. Data statistics show variables used in ratio-based attribution are approximately normally distributed. Histogram plots and normal quantile-quantile plots of (a,b) radiative forcing (RF) anomalies, turbulent heat flux (TF) anomalies (c,d), and upwelling longwave radiation (LWup) anomalies (e,f).

Figure S2 caption: Ratio-based attribution of anomalous upwelling longwave radiation, LWup. Column a shows LWup anomalies (W m^{-2}) for each April of 2002-2011 (rows 1-10). Ratio-based attribution is used to attributed LWup anomalies to radiative forcing, RF, and/or turbulent heat flux forcing, TF. Only LWup anomalies in upper or lower 25^{th} percentile ($|LWup'| > 3.6$ W m^{-2}) are attributed and mapped. The RF-component of LWup anomalies is shown in column b (W m^{-2}). The TF-component of LWup anomalies is shown in column c (W m^{-2}). Data from FLDAS Noah simulation.

S1. Distribution of anomalies

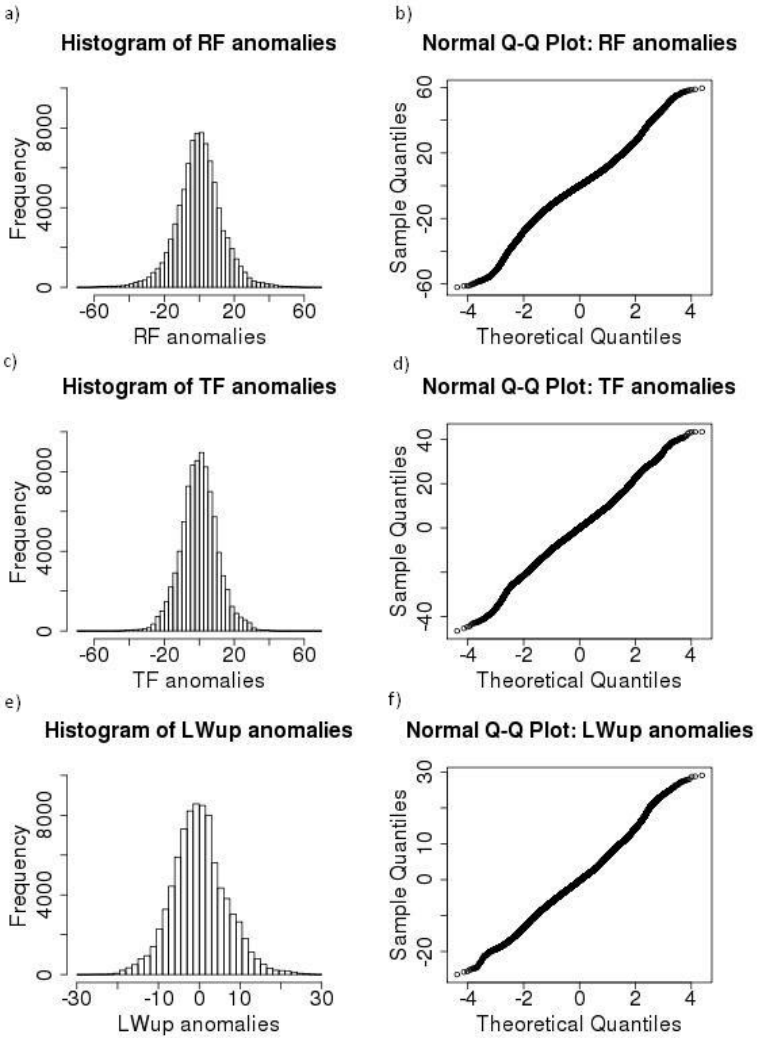

S2. Ratio-based attribution of anomalous upwelling longwave radiation, LWup.

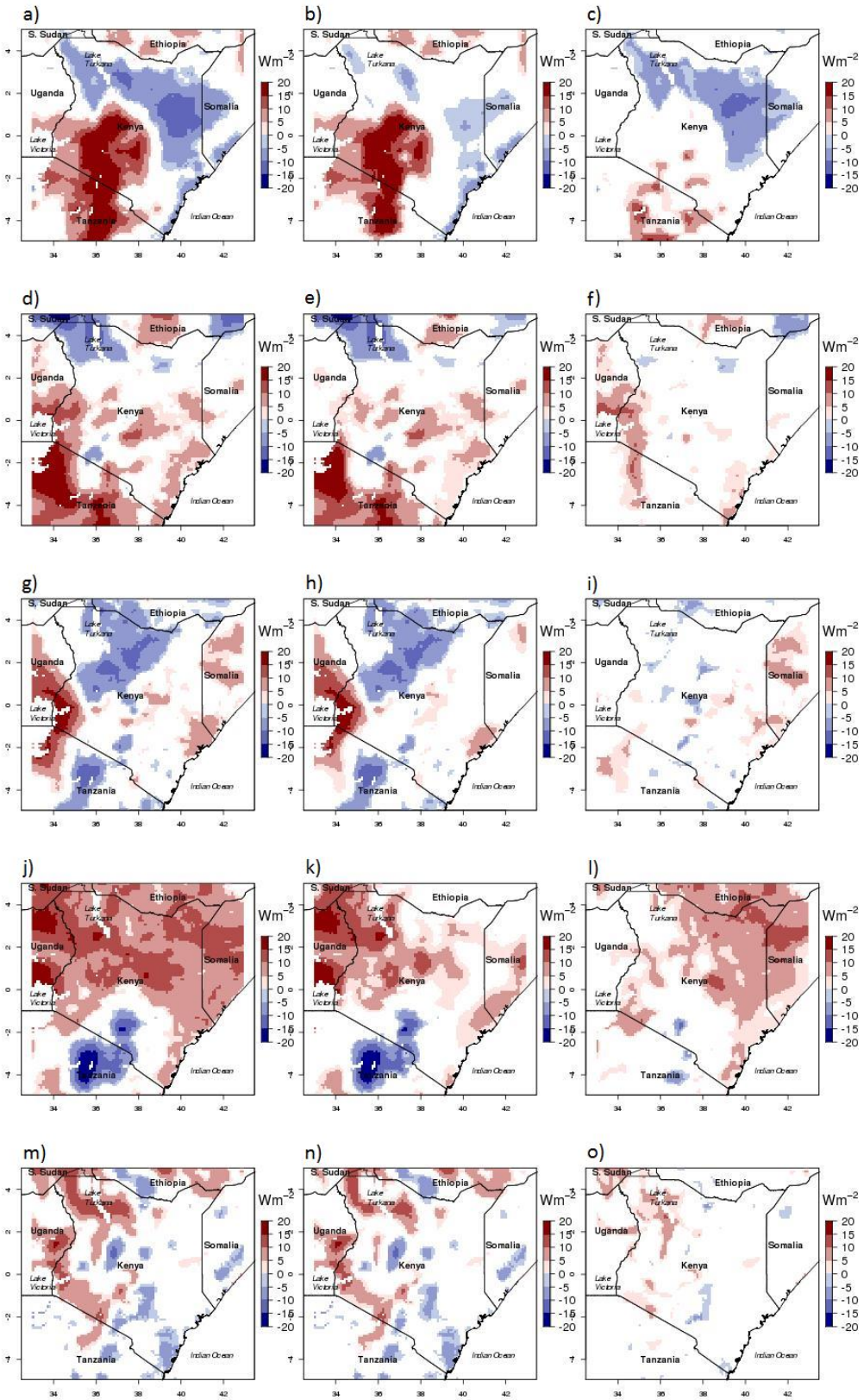

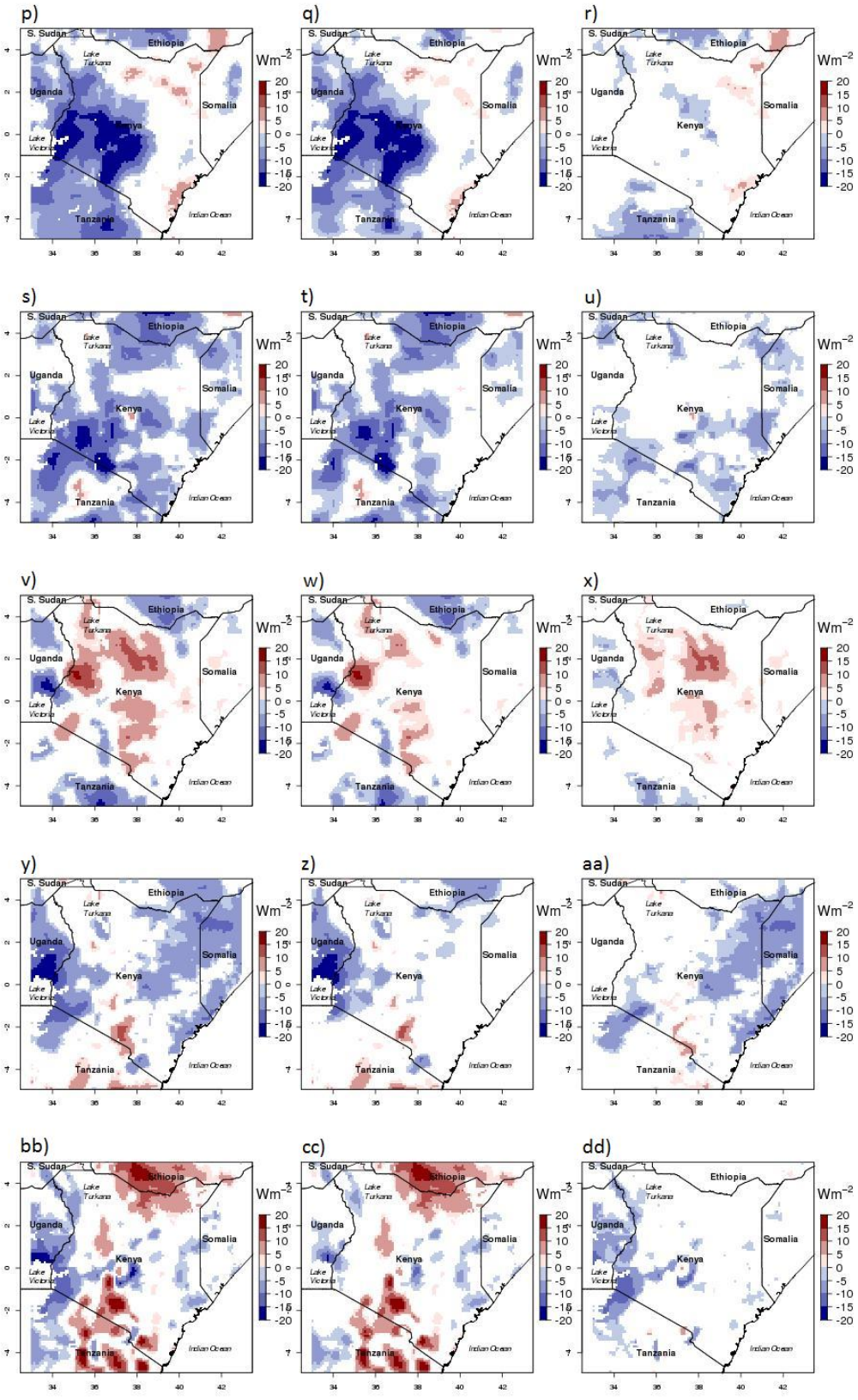
p)
q)
r)
s)
t)
u)
v)
w)
x)
y)
z)
aa)
bb)
cc)
dd)
S. Sudan
Ethiopia
Lake Turkana
Uganda
Somalia
Kenya
Lake Victoria
Tanzania
Indian Ocean
Wm^{-2}
20
15
10
5
0
-5
-10
-15
-20
34
36
38
40
42
4
2
0
-2
-4

Chapter 3

Figure 1

Level 1 administrative zones in Tanzania. Global Administrative Unit Layers from FAO.

Figure 2

Tanzania physical geography. Annual rainfall (a) and elevation (b). Rainfall calculated using CHIRPS. Elevation from http://upload.wikimedia.org/wikipedia/commons/8/87/Tanzania_Topography.png.

a)

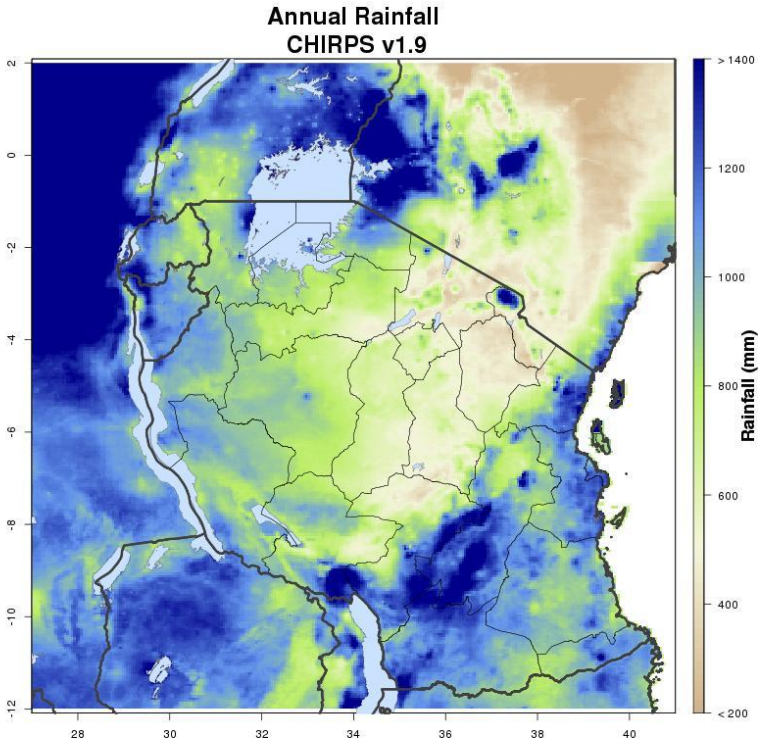

b)

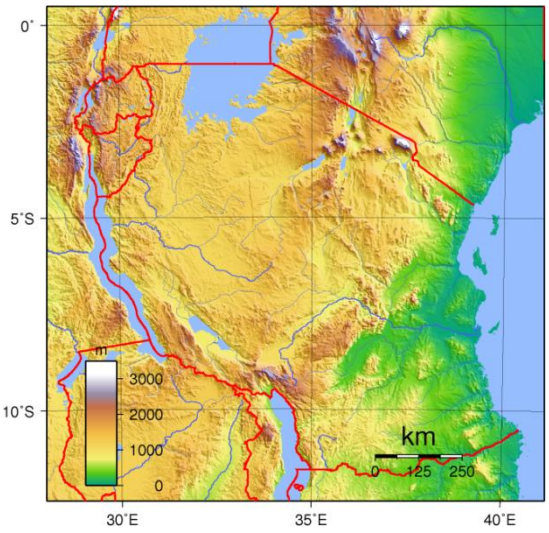

Figure 3

Seasonal rainfall in Tanzania. The percent of annual rainfall received during October to February (a) and during March to May (b). Calculated with CHIRPS data.

a)

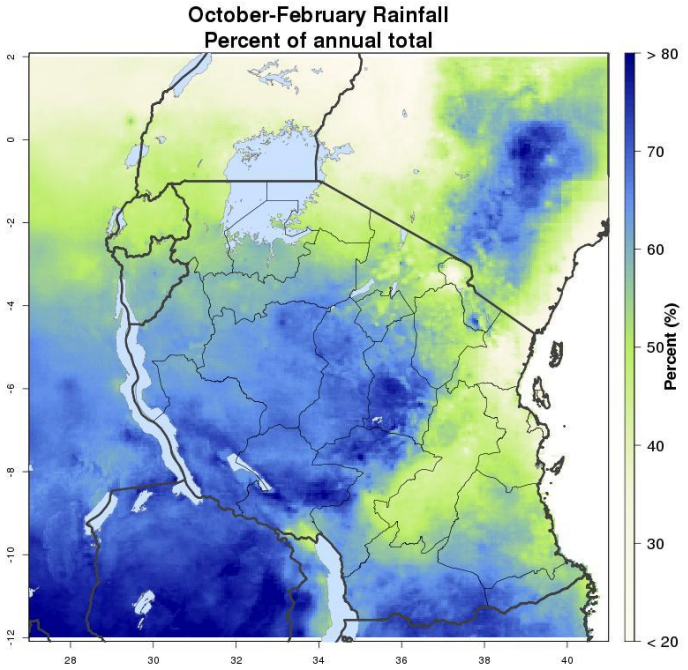

b)

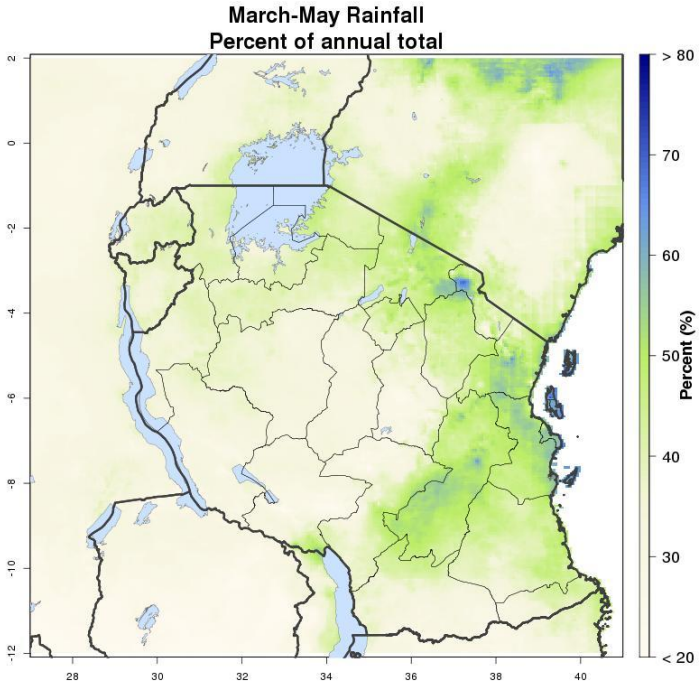

Figure 4

Monthly rainfall in selected areas. Mean monthly rainfall for 1982-2010 at Bukoba (a), Arusha (b), Shinyanga (c), and Mbeya (d). Calculated with CHIRPS data.

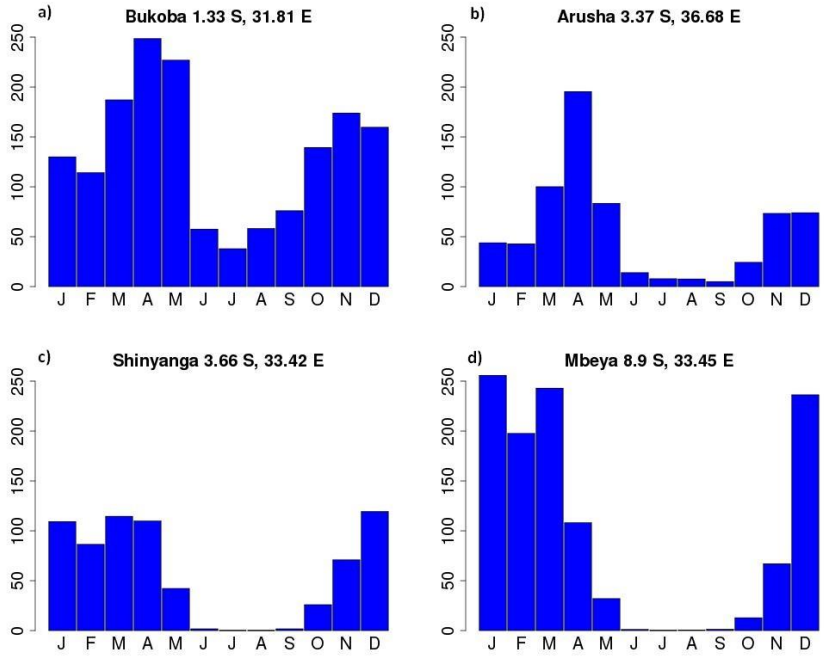

Figure 5

Stations used in CHIRPS in 1982 and 2010. From Pete Peterson, UC Santa Barbara Climate Hazards Group.

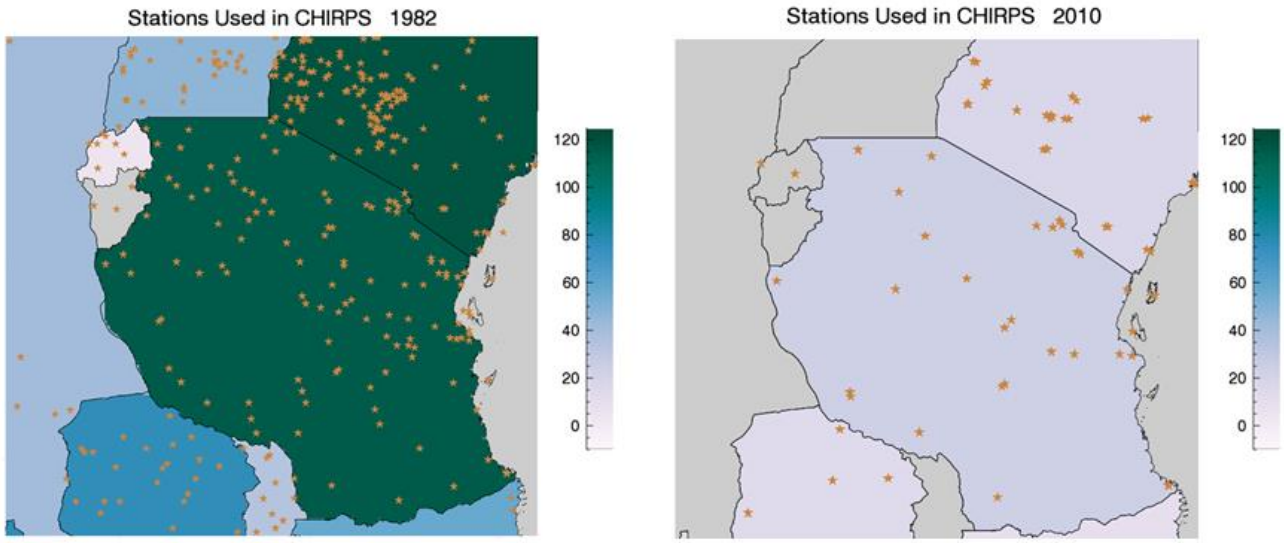

Figure 6

Rainfall trends in CHIRPS, 1982-2010. Percent change to season total per decade for October to May (a), October to February (b), and March to May (c). Gray stippling shows significance at $p < 0.05$.

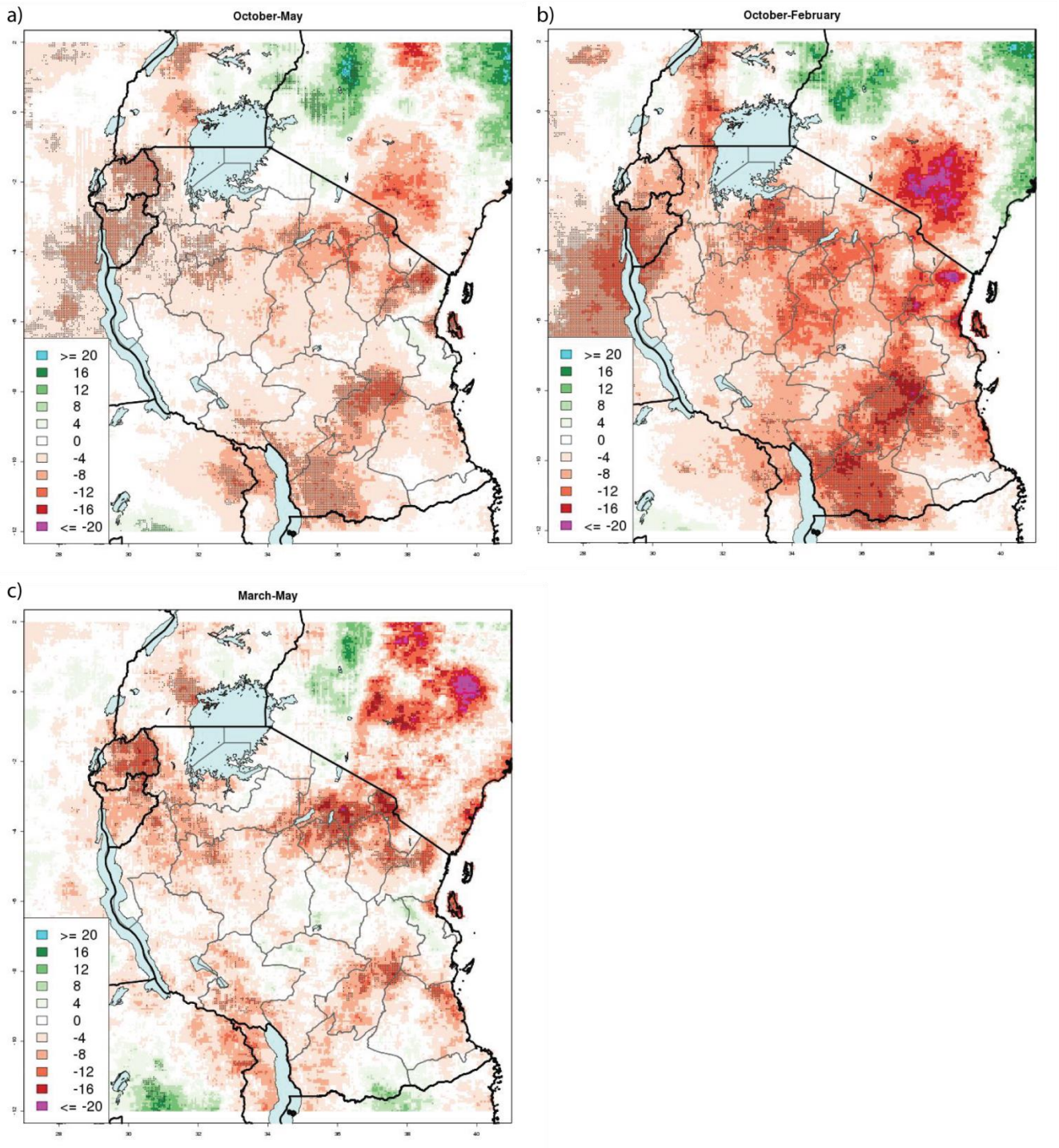

Figure 7

October to February rainfall trends (1982-2010) in several rainfall datasets. Percent change to season total per decade for the datasets in Table 1. Stippling shows significance at $p < 0.05$ for both positive and negative trends. Figure from Shraddahanand Shukla, UC Santa Barbara Climate Hazards Group.

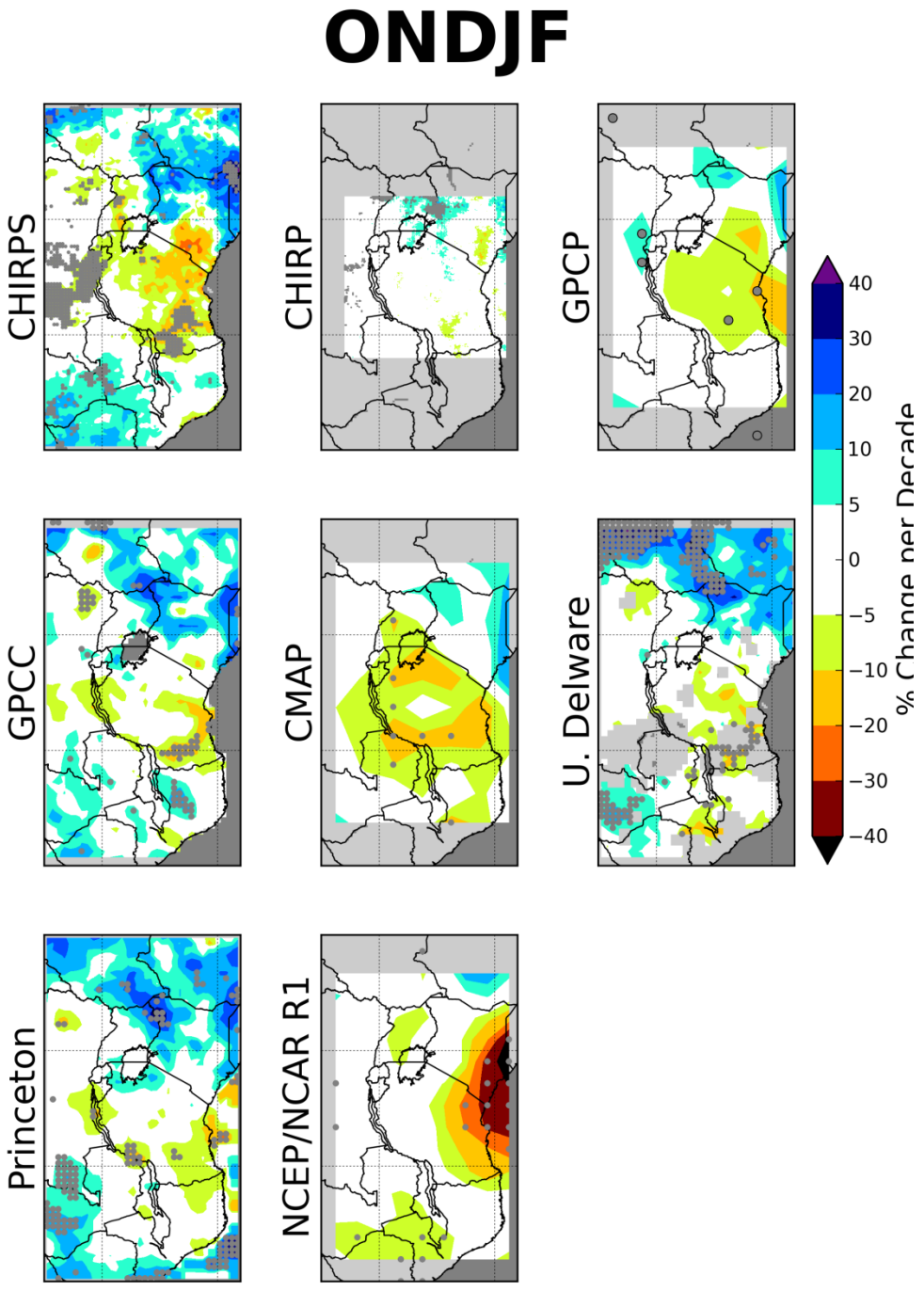

Figure 8

October to February rainfall trends (1982-2010) in several rainfall datasets. Percent change to season total per decade for the datasets in Table 1. Stippling shows significance at $p < 0.05$ for both positive and negative trends. Figure from Shraddahanand Shukla, UC Santa Barbara Climate Hazards Group.

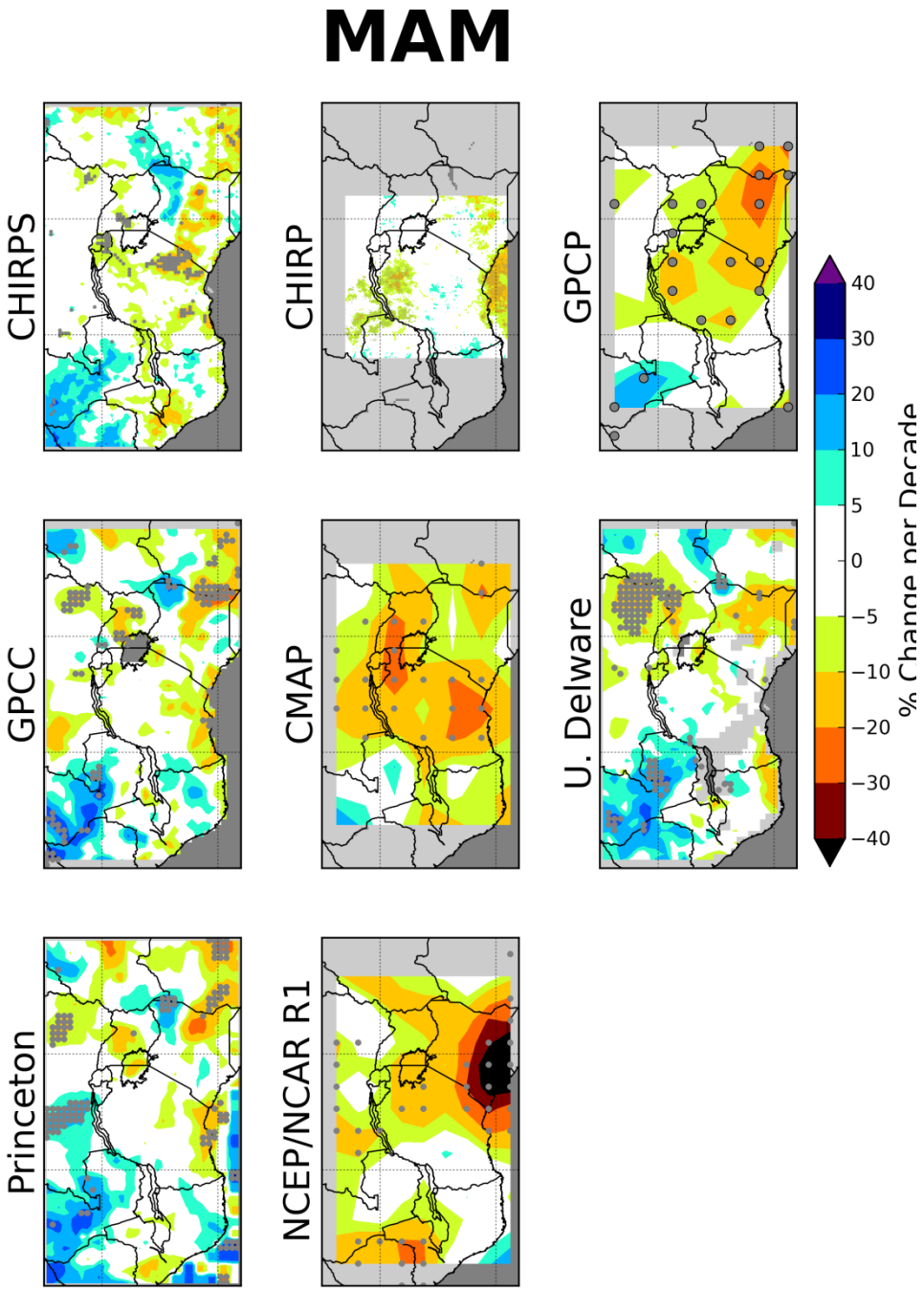

Figure 9

Relationship between vegetation productivity and rainfall, 1982-2010. November to October mean Normalized Difference Vegetation Index (NDVI) from GIMMs NDVI-3g (a). Pearson correlation between October to May rainfall (CHIRPS) and November to October mean NDVI (NDVI-3g) (b).

a)

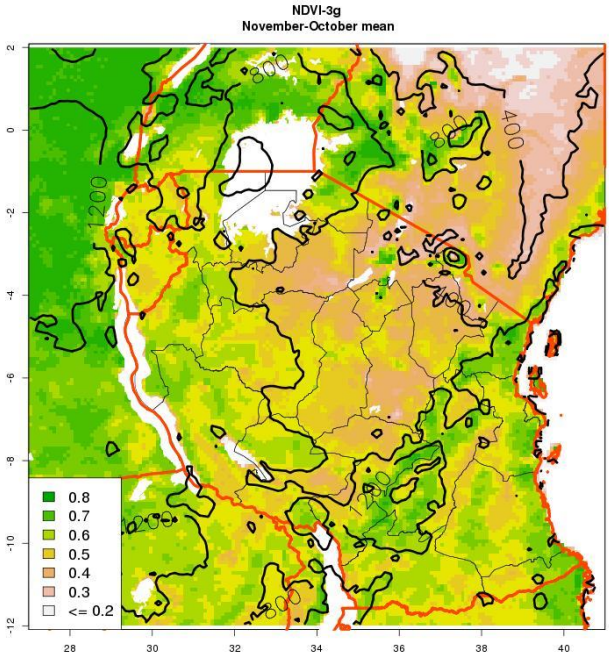

b)

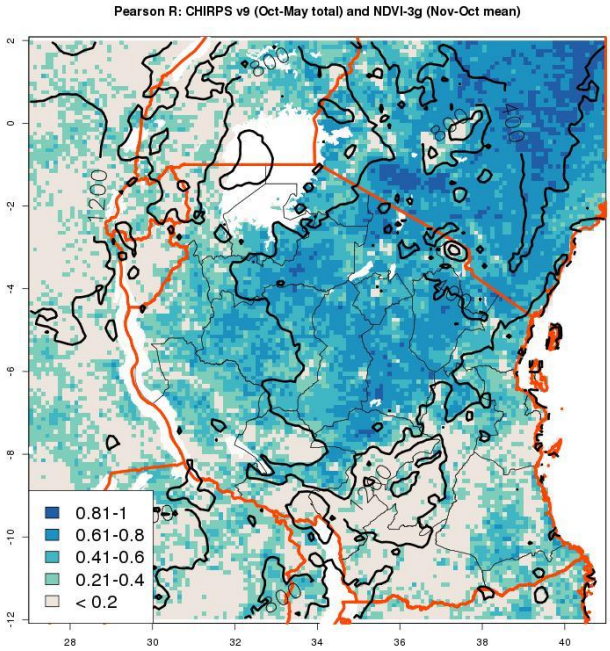

Figure 10

Trends in vegetation productivity and rainfall, 1982-2010. Trends in standardized anomalies for (a) November to October mean NDVI (NDVI-3g) and (b) October to May rainfall (CHIRPS). The four boxes show where areal averages are extracted for time series analysis. Boxes from west to east: Shinyanga-Tabora West (3°S – 6 °S/31 °E – 32.25 °E), Shinyanga-Tabora Central (3.5 ° S – 5.25 °S / 32.25 °E – 34.25 °E), Singida (4°S – 6.5 °S / 34.25 °E – 35.25 °E), Arusha (2.25 °S – 3.25 °S / 36.25 °E – 37 °E).

a)

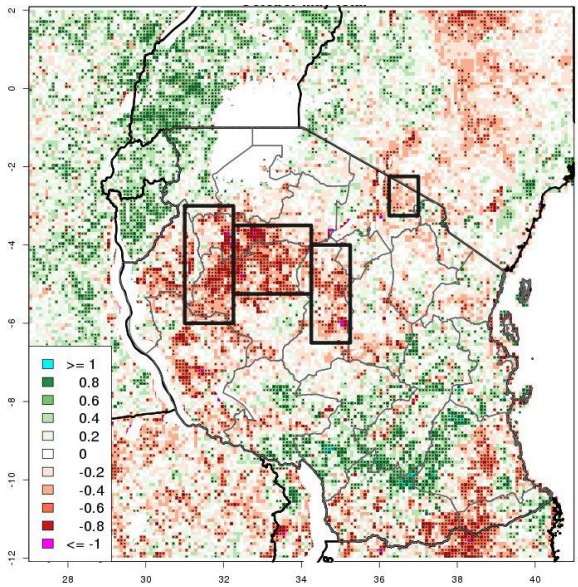

b)

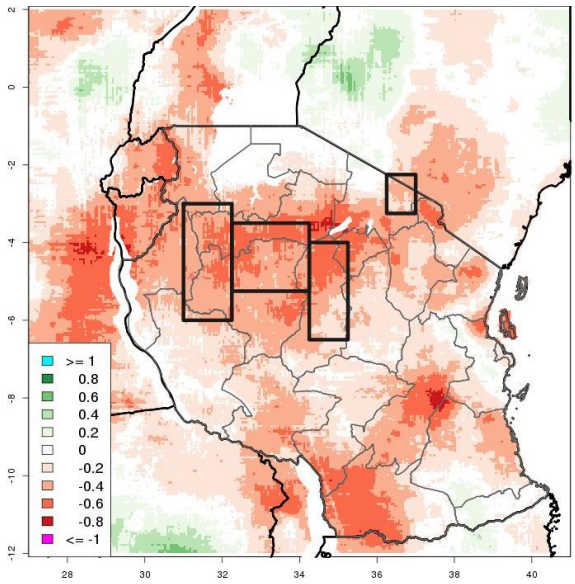

Figure 11

NDVI and rainfall time series of standardized anomalies for the boxes shown in Figure 11: Shinyanga-Tabora West (a), Shinyanga-Tabora Central (b), Singida (c), and Arusha (d). Plots show a linear trend equation for each NDVI and rainfall time series.

a)

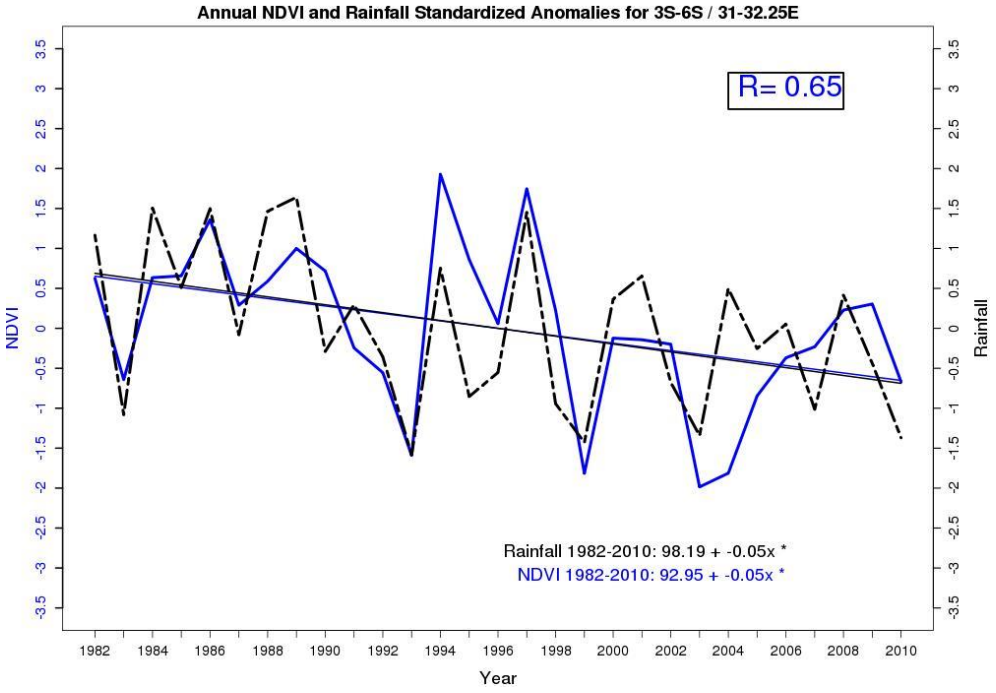

b)

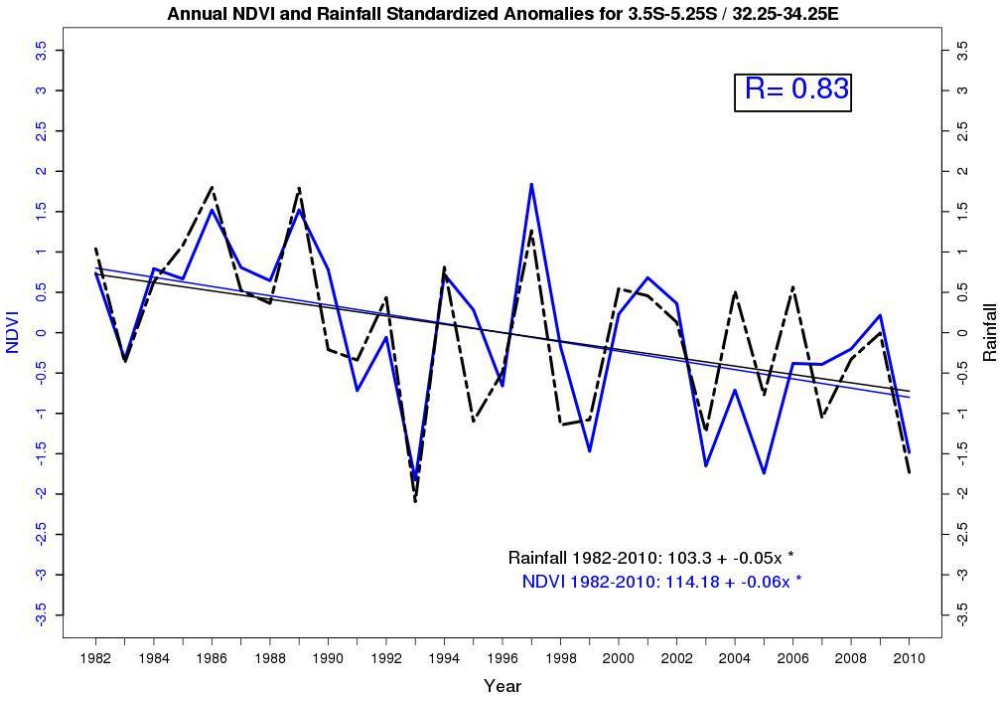

c)

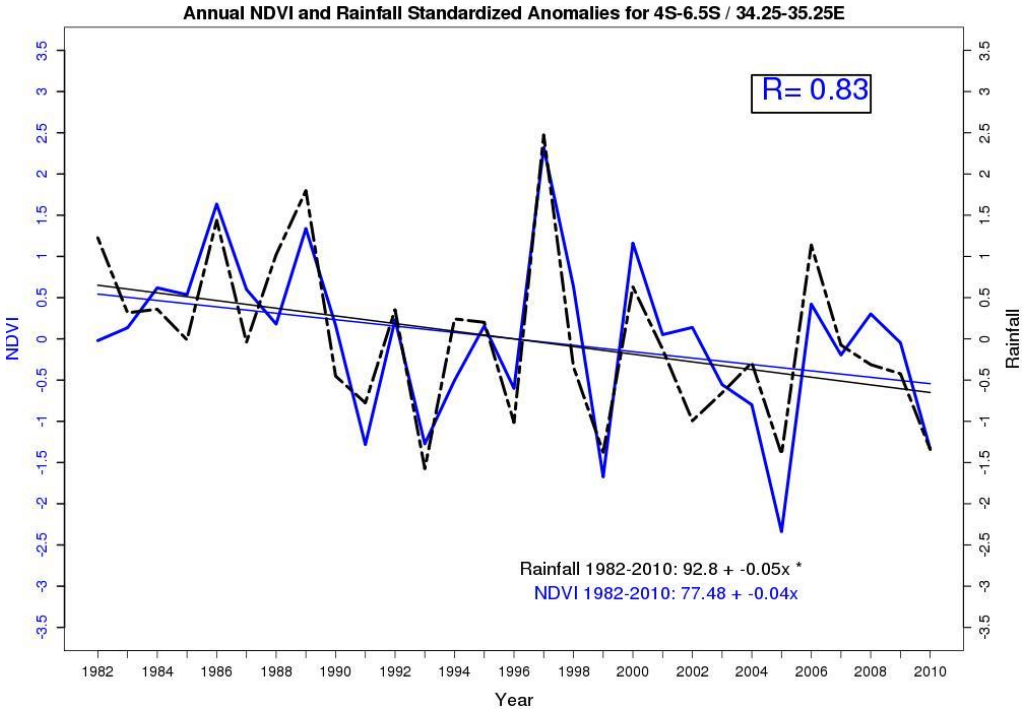
Annual NDVI and Rainfall Standardized Anomalies for 4S-6.5S / 34.25-35.25E
R= 0.83
Rainfall 1982-2010: 92.8 + -0.05x *
NDVI 1982-2010: 77.48 + -0.04x
NDVI
Rainfall
Year

d)

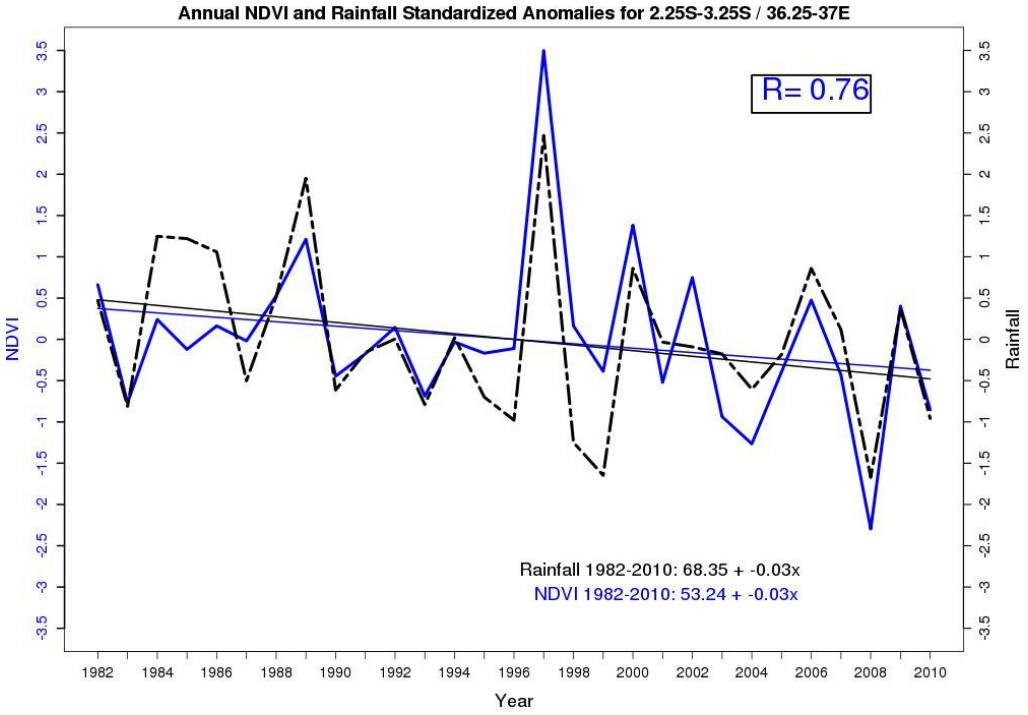
Annual NDVI and Rainfall Standardized Anomalies for 2.25S-3.25S / 36.25-37E
R= 0.76
Rainfall 1982-2010: 68.35 + -0.03x
NDVI 1982-2010: 53.24 + -0.03x
NDVI
Rainfall
Year

Figure 12

Trends in hydrology, 1984-2009. Percent change per decade to annual (October to September) rainfall (a), evapotranspiration (b), and magnitude of surface runoff trend (mm per decade) (c). Data simulated in the 0.25 ° CHIRPS-Princeton-VIC hydrologic model experiment. Stippling shows significance at $p < 0.05$. Major drainage basins (Table 2) are shown in 12c.

a, b)

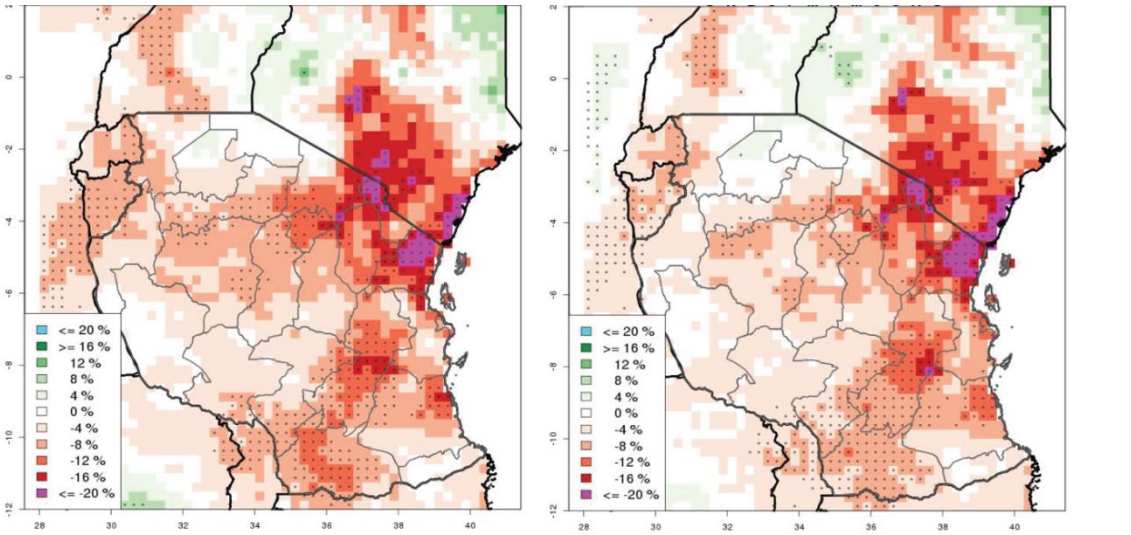

c)

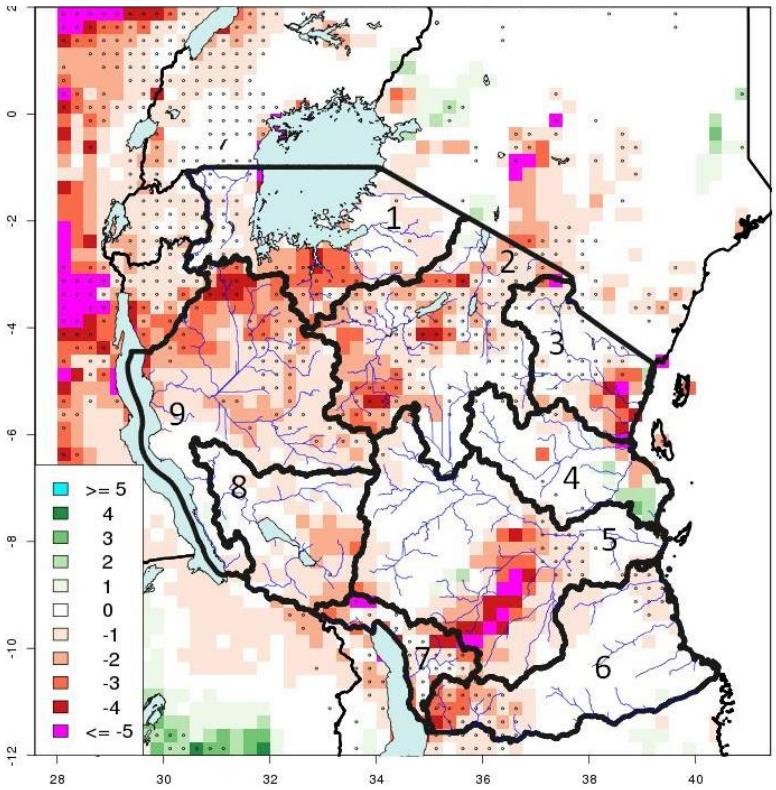

Figure 13

Surface runoff in Tanzania water basins, 1984-2009. Per-pixel simulated runoff is summed for total runoff (in mm mo-1) for the following basins: a) Internal Drainage Basin, b) Ruvuma River and Southern Coast Basin, c) Lake Nyasa basin, d) Lake Tanganyika basin. Text shows the Theil-Sen slope (mm mo-1 yr^{-1}) and the magnitude of the slope compared to the 1984-2009 mean (in percent change per decade). Asterisk denotes trend significance at $p< 0.05$. Data is from the 0.25 ° CHIRPS-Princeton-VIC hydrologic model experiment.

a)

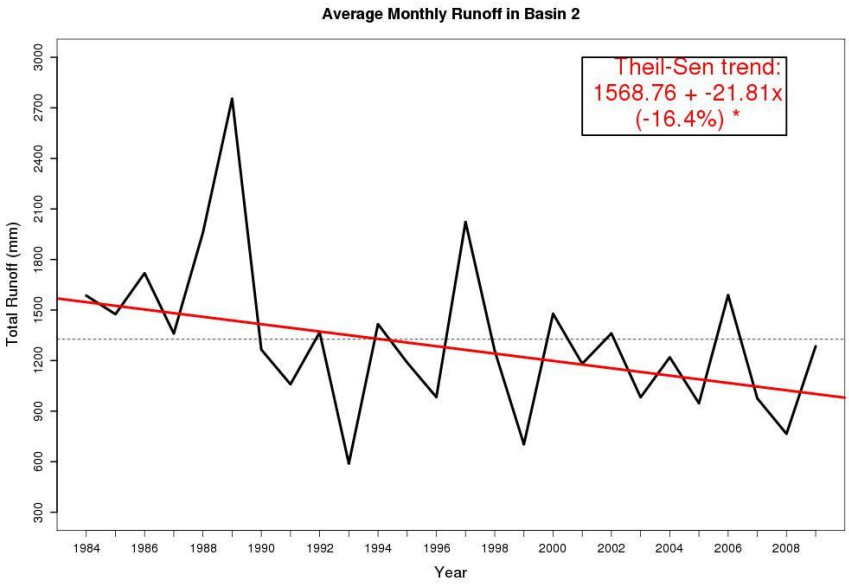

b)

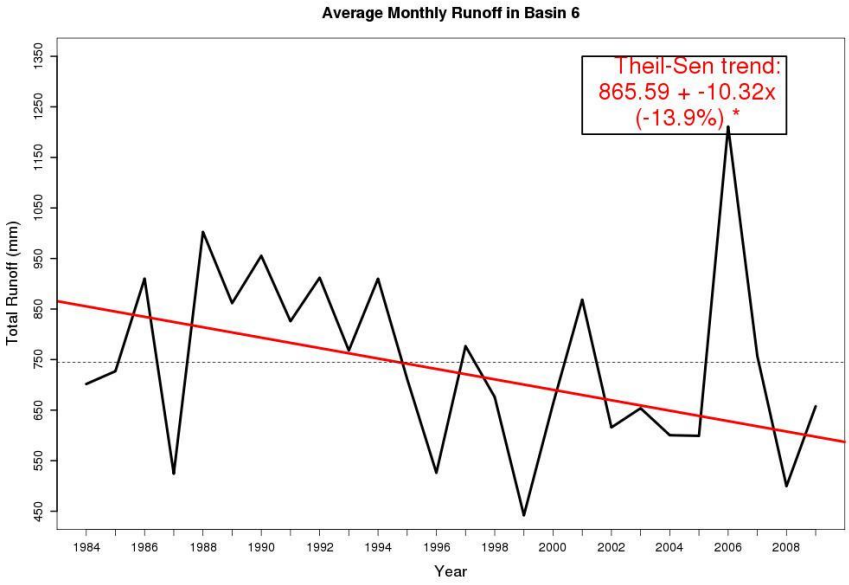

c)

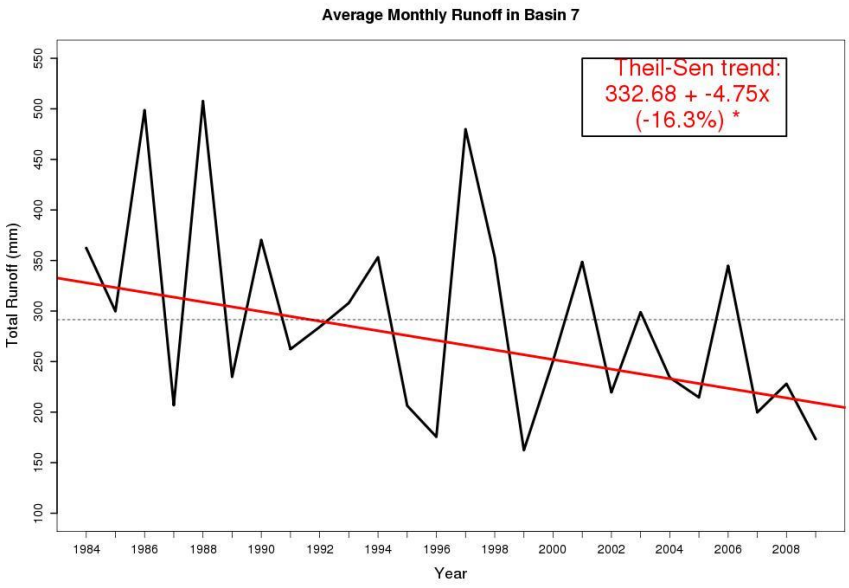
Average Monthly Runoff in Basin 7
Theil-Sen trend:
332.68 + -4.75x
(-16.3%) *
Total Runoff (mm)
100
150
200
250
300
350
400
450
500
550
1984
1986
1988
1990
1992
1994
1996
1998
2000
2002
2004
2006
2008
Year

d)

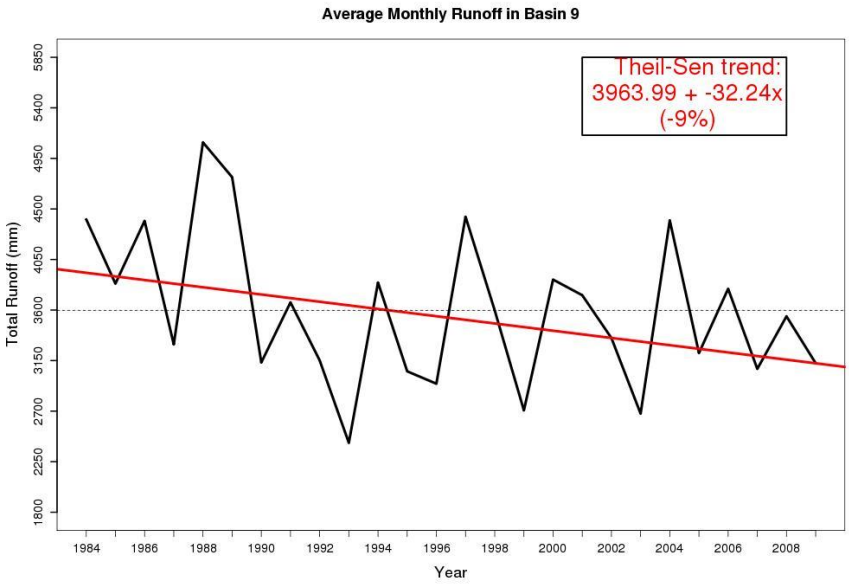
Average Monthly Runoff in Basin 9
Theil-Sen trend:
3963.99 + -32.24x
(-9%)
Total Runoff (mm)
1800
2250
2700
3150
3600
4050
4500
4950
5400
5850
1984
1986
1988
1990
1992
1994
1996
1998
2000
2002
2004
2006
2008
Year

Figure 14

Yield potential for rainfed maize in Tanzania. For northern (a) and central/southern (b) Tanzania, the 1982-2010 mean Water Requirement Satisfaction Index (WRSI). WRSI is calculated from the USGS GeoSpatial Water Requirement Satisfaction Index (GeoWRSI) model using CHIRP rainfall data. Three regions of interest are outlined in yellow/black.

a)

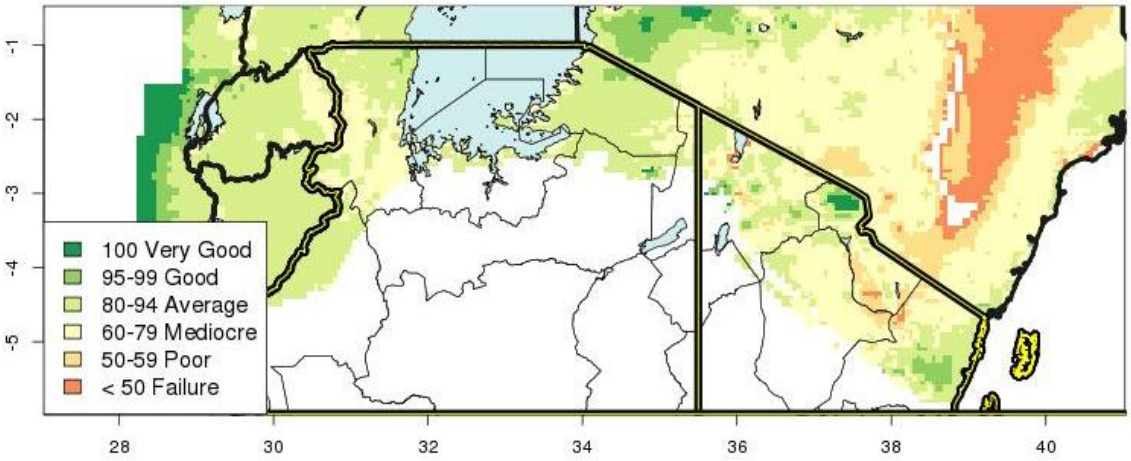

b)

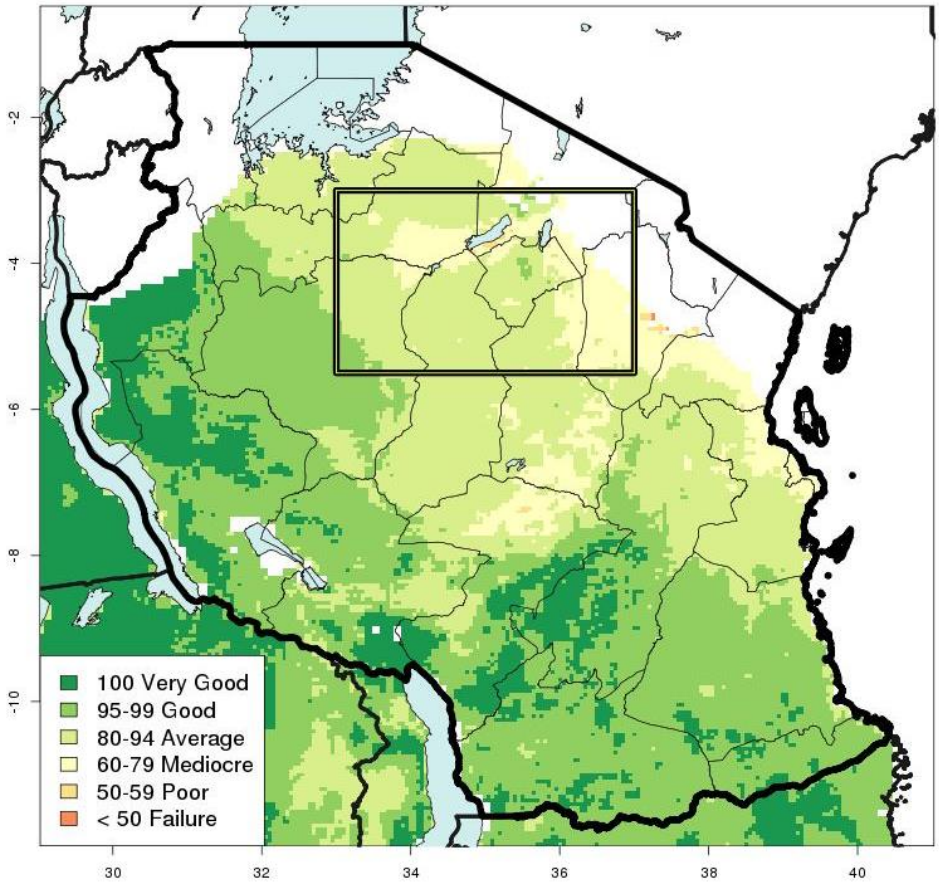

Figure 15

Time series of standardized WRSI anomalies for 1982-2010. For Region 1, the short rains and long rains seasons (a,b). For Region 2, the short rains and long rains seasons (c,d). For Region 3, the unimodal October to May season (e).

a,b)

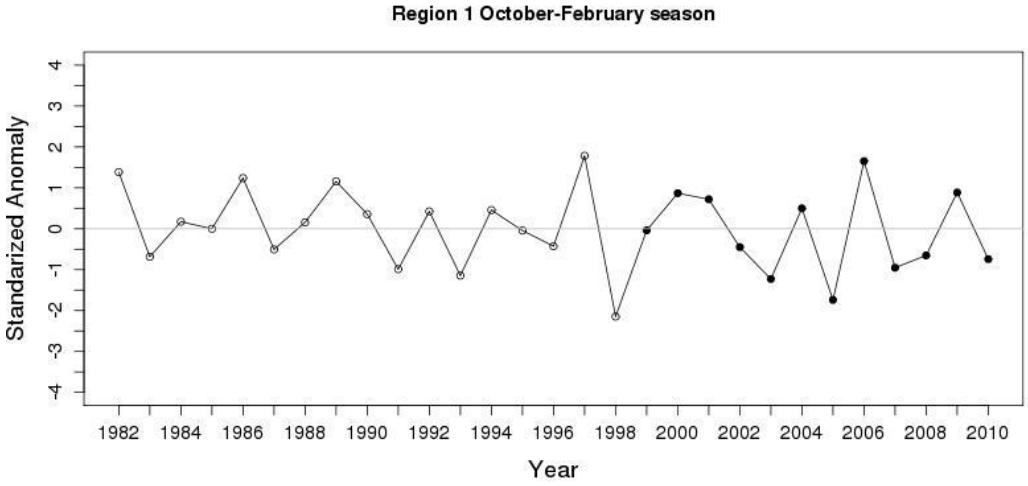

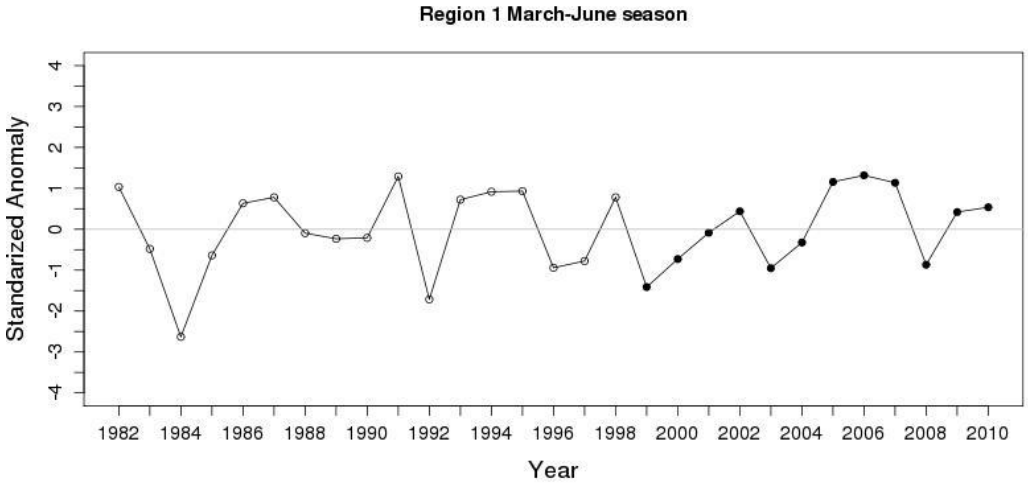

c,d)

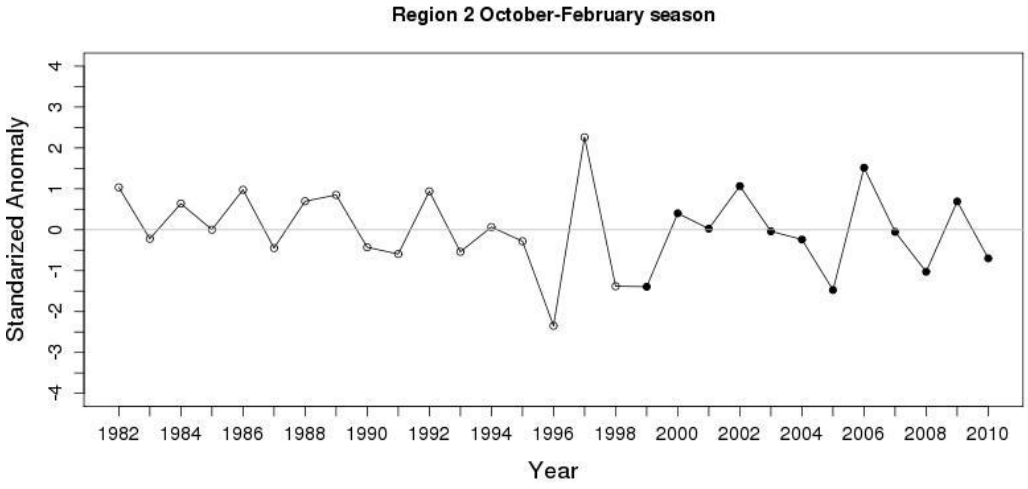
Region 2 October-February season
Standarized Anomaly
4
3
2
1
0
-1
-2
-3
-4
1982
1984
1986
1988
1990
1992
1994
1996
1998
2000
2002
2004
2006
2008
2010
Year

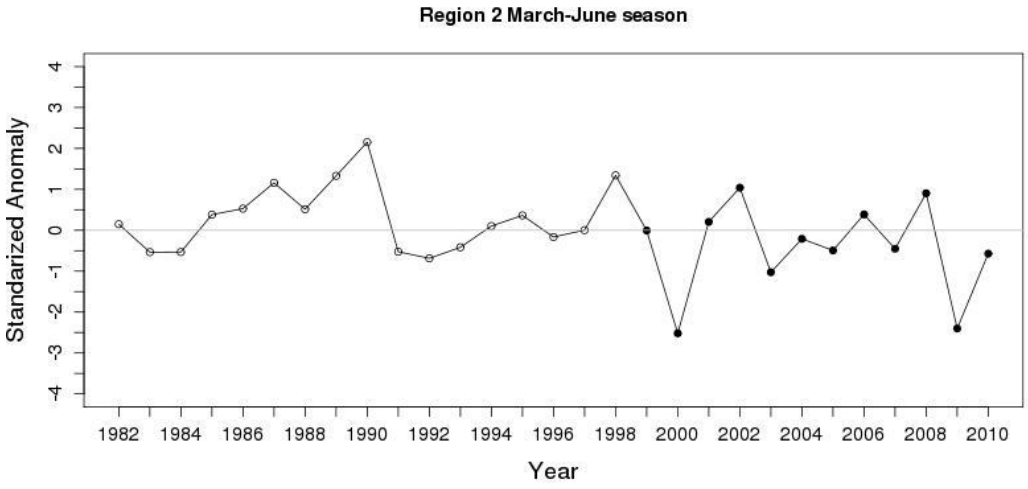
Region 2 March-June season
Standarized Anomaly
4
3
2
1
0
-1
-2
-3
-4
1982
1984
1986
1988
1990
1992
1994
1996
1998
2000
2002
2004
2006
2008
2010
Year

e)

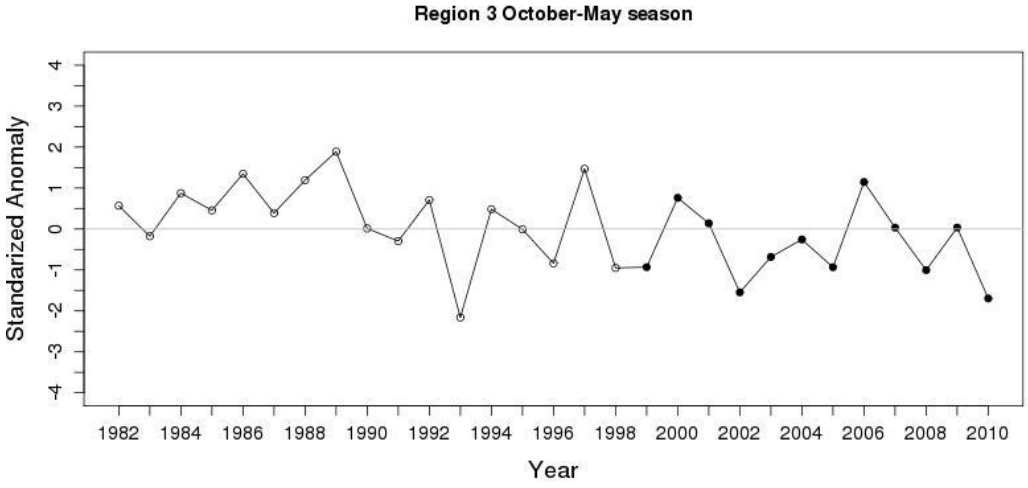
Region 3 October-May season
Standarized Anomaly
4
3
2
1
0
-1
-2
-3
-4
1982
1984
1986
1988
1990
1992
1994
1996
1998
2000
2002
2004
2006
2008
2010
Year

Figure 16

Regional rainfall during 1982-1998 and 1999-2010. Mean monthly rainfall for Region 1, Region 2, and Region 3 are plotted for years 1982-1998 in gray and 1999-2010 in blue hashes. Calculated with CHIRPS.

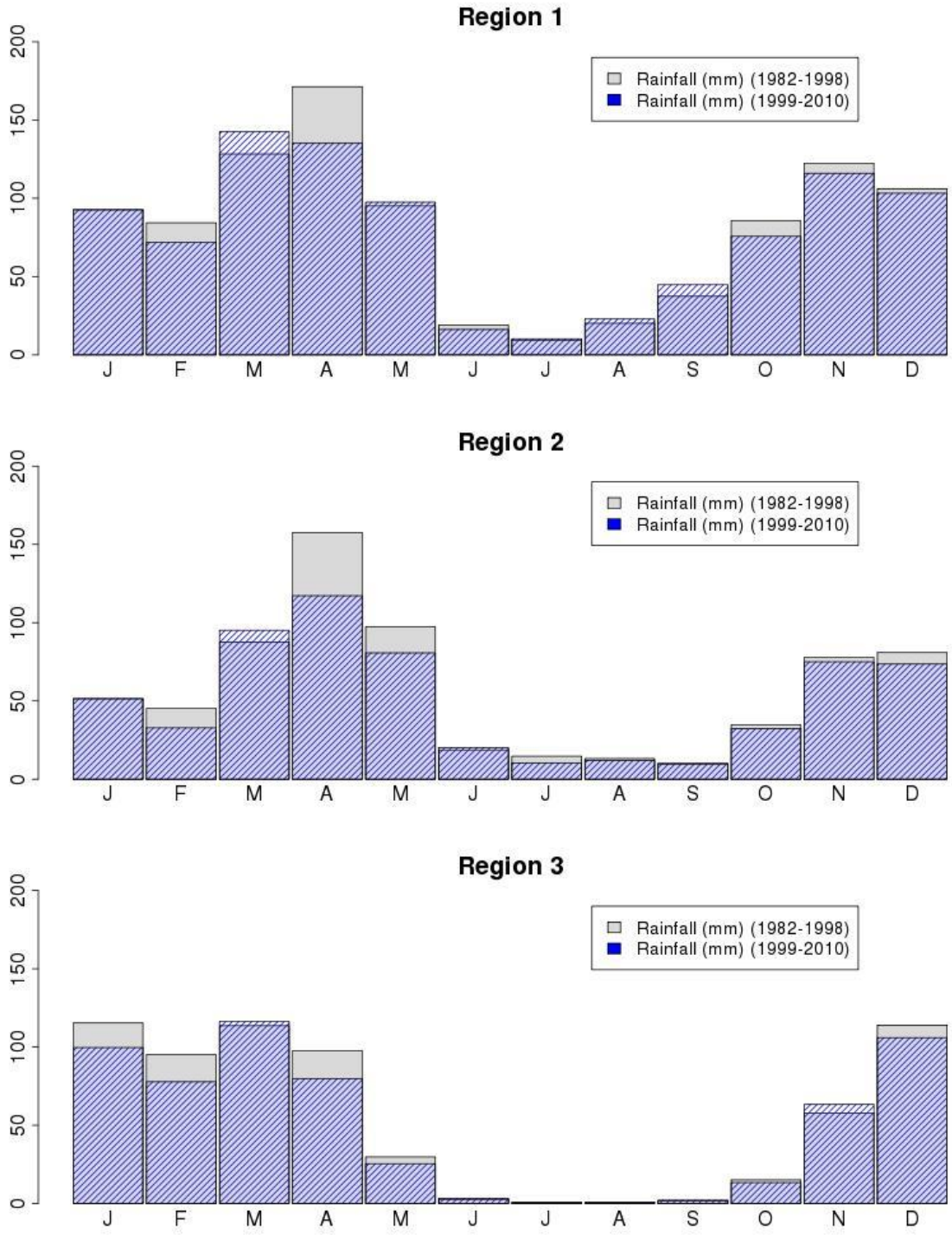

Figure 17

Regional crop water use during 1982-1998 and 1999-2010. For Regions 1, 2, and 3, the amount of water used by the crop during major growth stages is plotted for years 1982-1998 in gray and for 1999-2010 in green. The average amount of water required for no water stress to occur is plotted in white.

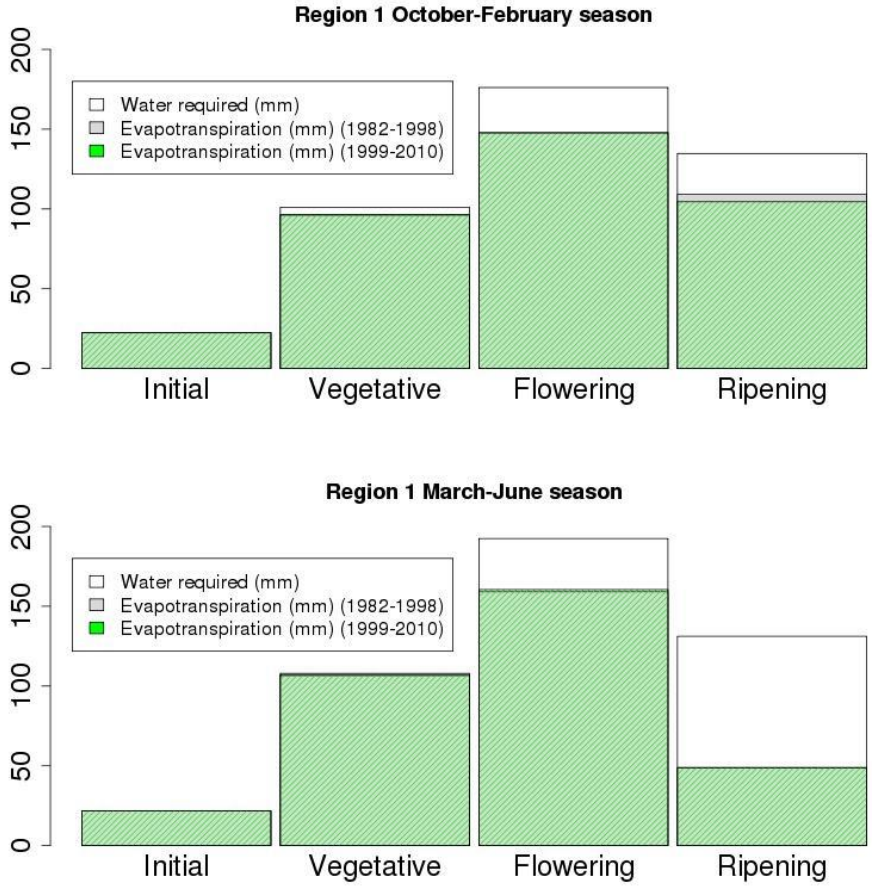

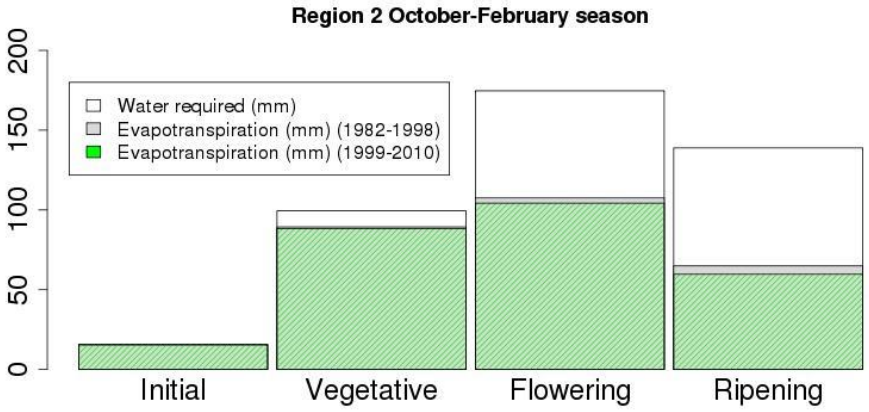
Region 2 October-February season
Water required (mm)
Evapotranspiration (mm) (1982-1998)
Evapotranspiration (mm) (1999-2010)
0
50
100
150
200
Initial
Vegetative
Flowering
Ripening

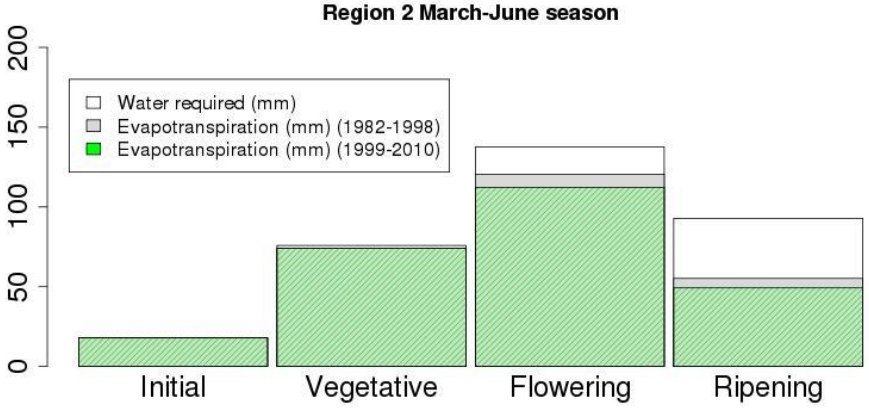
Region 2 March-June season
Water required (mm)
Evapotranspiration (mm) (1982-1998)
Evapotranspiration (mm) (1999-2010)
0
50
100
150
200
Initial
Vegetative
Flowering
Ripening

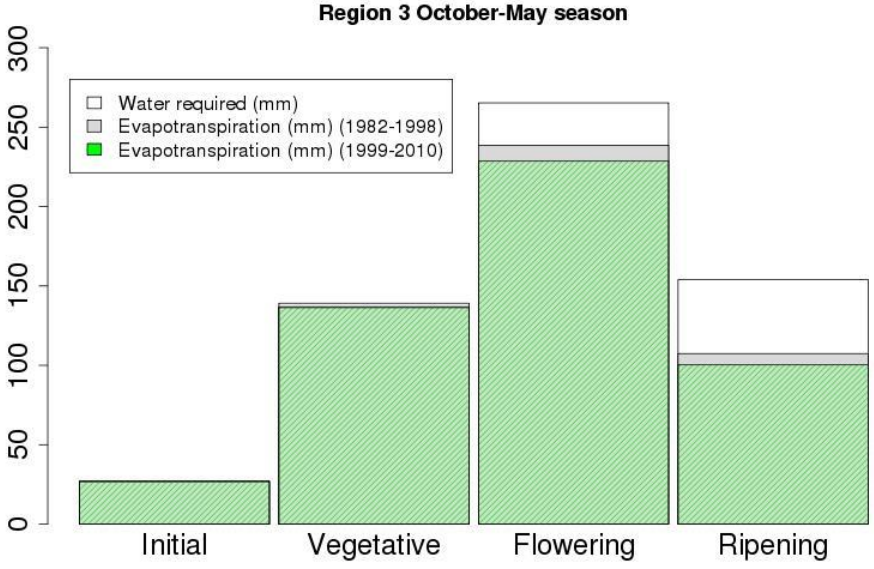
Region 3 October-May season
Water required (mm)
Evapotranspiration (mm) (1982-1998)
Evapotranspiration (mm) (1999-2010)
0
50
100
150
200
250
300
Initial
Vegetative
Flowering
Ripening

Figure 18

Trends in maize water stress, 1982-2010. Percent decline to Water Requirement Satisfaction Index (WRSI) over the 1982-2010 period and the R-squared values for the linear trends. For the short rains season (a,b), the long rains season (c,d) and the unimodal October to May season (e,f). Calculated with the USGS GeoWRSI model and CHIRPS data.

a)

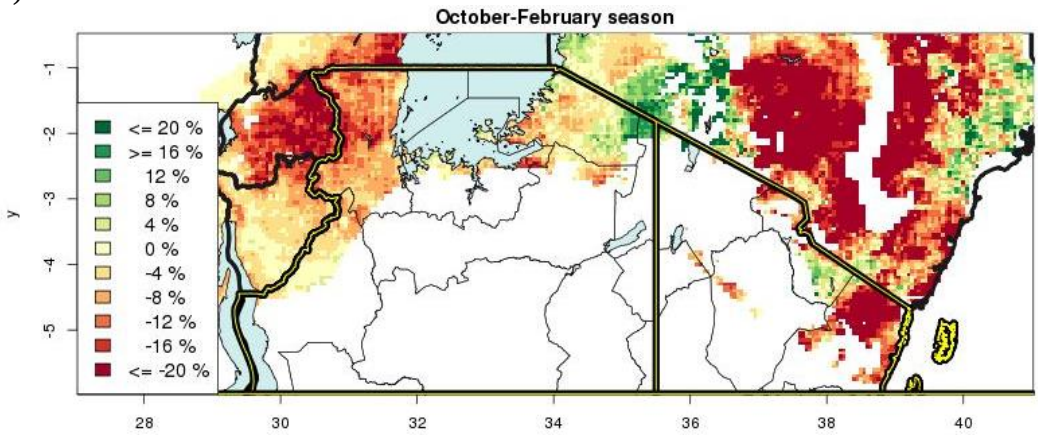

b)

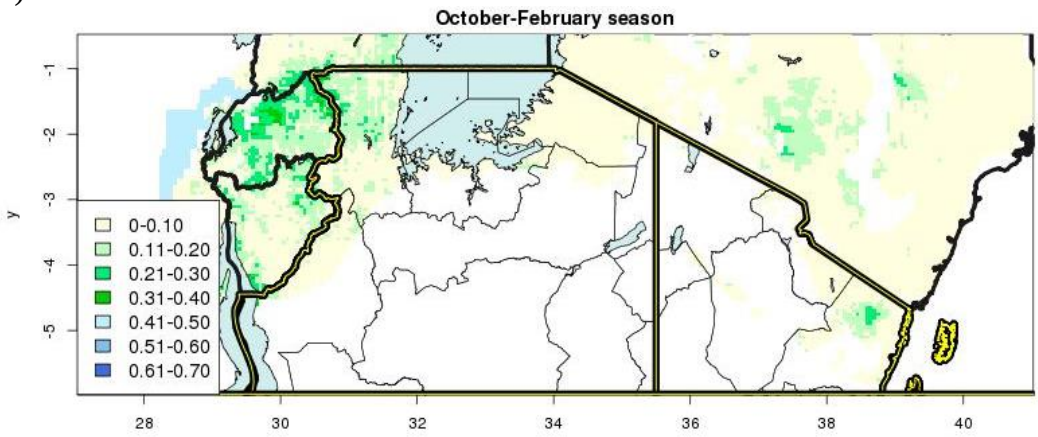

c)

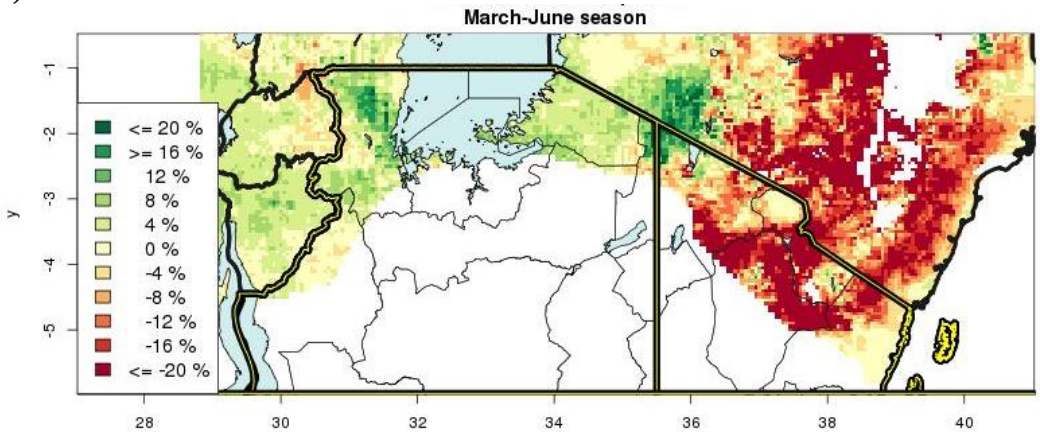

d)

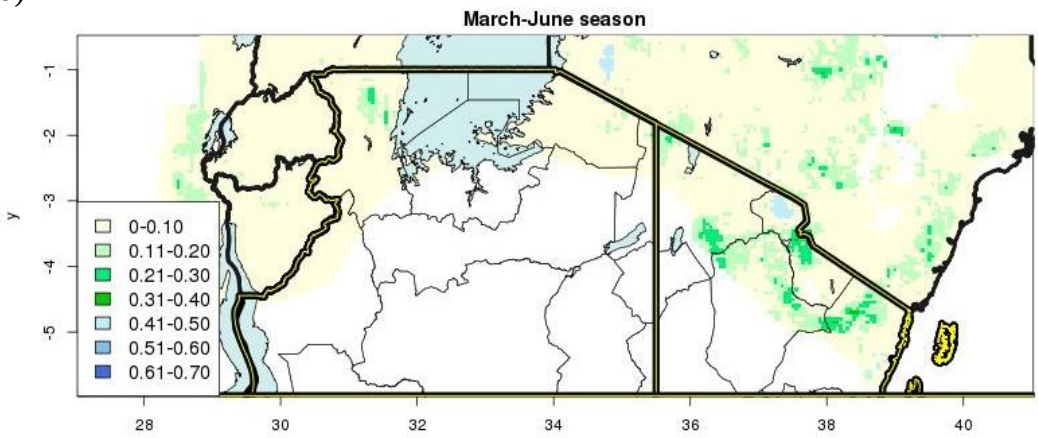
March-June season
0-0.10
0.11-0.20
0.21-0.30
0.31-0.40
0.41-0.50
0.51-0.60
0.61-0.70
y
-1
-2
-3
-4
-5
28
30
32
34
36
38
40

e)

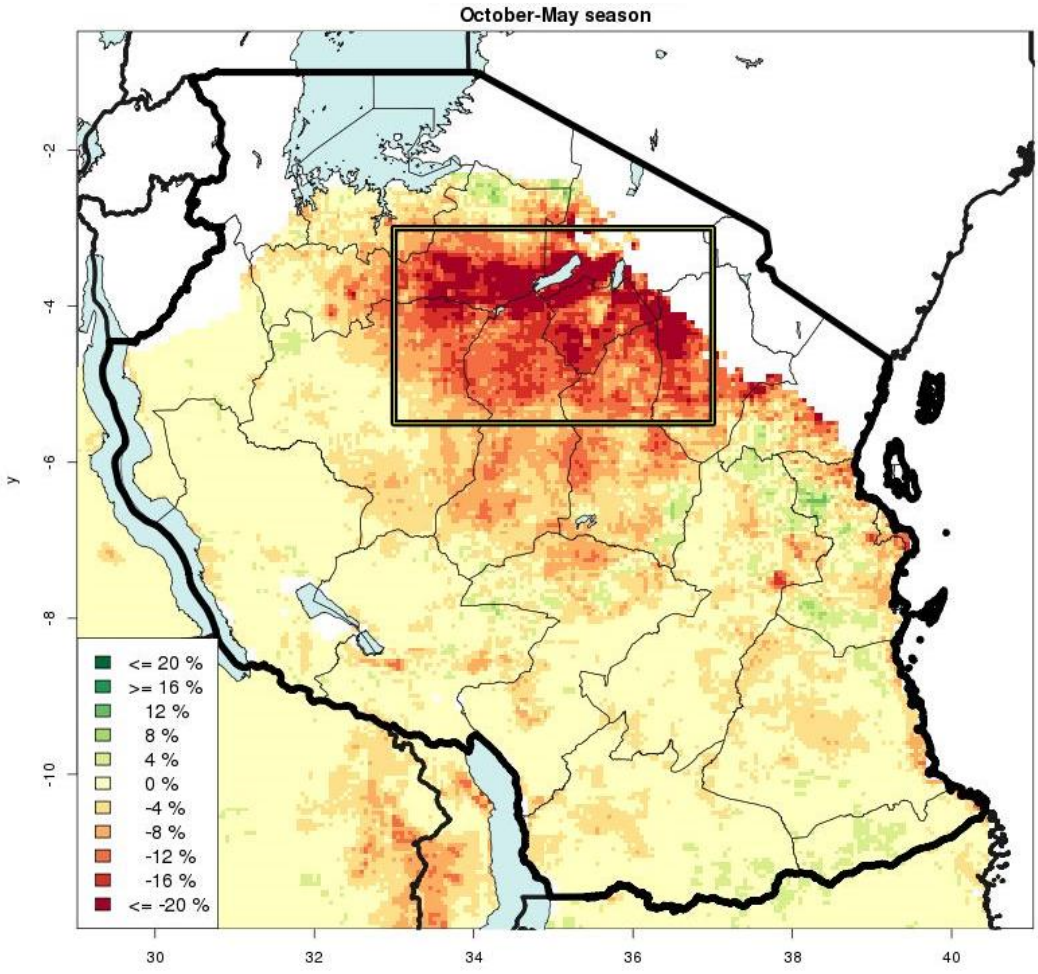
October-May season
<= 20 %
>= 16 %
12 %
8 %
4 %
0 %
-4 %
-8 %
-12 %
-16 %
<= -20 %
y
-2
-4
-6
-8
-10
30
32
34
36
38
40

f)

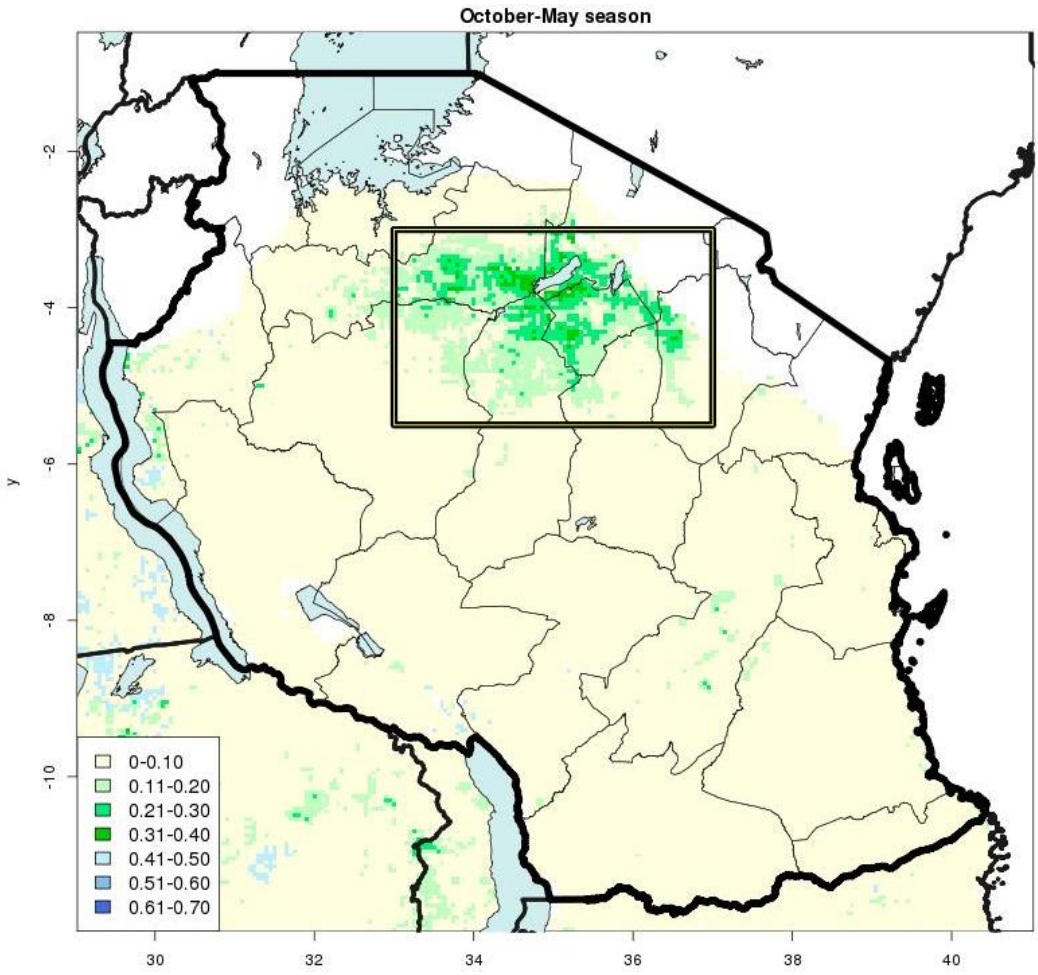
October-May season
y
-2
-4
-6
-8
-10
30
32
34
36
38
40
0-0.10
0.11-0.20
0.21-0.30
0.31-0.40
0.41-0.50
0.51-0.60
0.61-0.70